Investigation of Buoyant Plume Wind Enhancement

Esmaeel Eftekharian

A thesis submitted to fulfil the requirements of the degree of
Doctor of Philosophy

Centre for Infrastructure Engineering (CIE)

WESTERN SYDNEY
UNIVERSITY

November 2019

ABSTRACT

Bushfires are a natural disaster that has a devasting effect on nature and mankind. The vulnerability of buildings to bushfires has caused enormous loss of property and in extreme conditions, loss of life. It is well known that bushfires invade building structures via three mechanisms, namely embers, thermal radiation, and flame contact. Based on recent bushfire field surveys and numerical simulations, bushfire enhanced wind has also been identified to be a major contributor to building damage. Wind enhancement by bushfires can have a destructive impact on buildings arising from the increasing pressure load on structures downstream of the bushfire front as well as the increasing velocity of embers carried by wind during bushfire attacks. However, the mechanisms involved in this phenomenon are not yet fully understood.

This study aims to (1) fundamentally understand the interaction of longitudinal wind velocity with vertical buoyant plume that leads to enhancement of wind velocity downstream of the buoyant source; (2) quantify the effects of fire intensity, wind velocity, terrain slope, and different fire sources on wind enhancement by fire; and (3) develop correlations between the enhanced wind flow characteristics and these contributing factors.

This study used FireFOAM, an open-source computational fluid dynamics solver, to numerically solve thermo-fluid governing equations based on Large Eddy Simulation (LES). A module has been developed and implemented within the FireFOAM solver to compute and extract the identified parameters to help explain the phenomenon of wind enhancement by fire. To determine the effects of each contributing factor, the stepwise method in which one parameter is subjected to change while the others are maintained constant was used. The numerical model was validated against two sets of experimental data, namely, a buoyant diffusion fire plume in still air and a buoyant diffusion fire plume in cross-wind conditions. The reliability of the FireFOAM LES was checked by LES uncertainty analysis which includes the resolved fraction of the kinetic energy of turbulence, the ratio of the grid spacing to the Kolmogorov scale, and turbulent spectra at characteristic locations.

The numerical analysis commenced with simulation of the interaction of wind and a dimensionally finite source of fire, called a point source fire. Results revealed that when wind interacts with fire, a longitudinal negative pressure gradient is generated within the fire plume region downstream of the fire source where the flow density is lower than that of ambient condition. This fire-induced pressure gradient causes flow acceleration and consequently results in enhancement of wind in longitudinal direction (parallel to the wind direction). The results generated in this thesis substantiated that this generation of the fire-induced pressure gradient is the main reason why wind enhancement occurs during fire-wind interaction. It was also found that with the increase of fire intensity corresponding to the fire heat release rate per unit area for a point source fire, the fire-induced pressure gradient and consequently wind enhancement increases.

In addition to the impacts of fire intensity, the effects of free-stream wind velocity on the enhancement of wind by fire were also studied. To this end, a number of simulations were performed under constant point source fire intensity but different free-stream wind velocities. An appropriate normalization approach was developed based on the free-stream dynamic pressure. Consequently, the fire-induced pressure gradient was normalized to describe the effects of free-stream wind velocity on wind enhancement by fire. Results showed that with an increase of free-stream wind velocity under constant fire intensity, the normalized fire-induced pressure gradient decreases, which causes a comparative reduction in wind enhancement by fire.

The effect of fire source configuration on wind enhancement by fire is another parameter studied in this thesis. The width of the bushfire front can be assumed as infinite and as such, can be treated as a line fire source. Hence the computational domain approximates a truncated section of an infinitely wide bushfire front. A study was carried out to compare wind enhancements by fires of point and line sources. Simulations were performed under the same free-stream wind velocity and fire heat release rate per unit area for both line and point source fires. It was found that the longitudinal fire-induced pressure force induced by a line fire source is much greater, hence resulting in a stronger wind enhancement, than a point source. Vertical flow distribution analysis was also performed for the two simulated cases. The results reveal that in contrast to the longitudinal flow enhancement, vertical flow enhancement by a point fire source is higher than that for a line fire source. This finding is attributed to the more intensified vertical fire-induced pressure gradient and buoyancy forces in the point source configuration than the line source case.

Developing correlations for wind enhancement by fire based on the main contributing factors corresponding to fire intensity and wind velocity is one of the main practical findings of this research study. In this regard, a series of simulations with different combinations of free-stream wind velocity and line fire intensity was performed to develop correlations for wind enhancement. Two relevant non-dimensional groups, namely, Froude number and normalized fire intensity, were utilized to respectively quantify the impacts of free-stream wind velocity and fire intensity on wind enhancement. A correlation was developed to determine the maximum wind enhancement and the corresponding location as a function of Froude number and normalized fire intensity. Furthermore, the concept of wind enhancement plume line was defined as a line along which the local wind enhancement occurs at a given longitudinal location downstream of the fire source. A correlation was also developed for this case. It was also found that after wind hits the maximum value at a certain location downstream of the fire source, it undergoes a gradual decay along the wind enhancement plume line for which a correlation was also developed as a function of normalized longitudinal direction.

In this thesis, the effect of terrain slope on wind enhancement caused by a line source fire has been presented. A number of simulation scenarios were performed for practical values of terrain upslope and downslope. It was observed that upslope terrain intensifies wind enhancement whereas downslope terrain reduces wind enhancement. The simulation results revealed that in upslope terrain cases, the buoyancy force component parallel to the sloped surface amplifies the fire-induced pressure force and consequently intensifies wind flow. However, in the downslope cases, the component of buoyancy parallel to the sloped surface opposes the wind flow and consequently mitigates the wind velocity. It was also found that a steeper gradient in upslope and downslope terrain respectively causes an increase and a reduction in wind enhancement by fire.

In summary, this research provides a fundamental explanation for enhancement of horizontal wind with a vertical buoyant plume by the development of a theoretical framework based on fire-induced force and acceleration analysis. The developed fire-induced force analysis and acceleration theory were employed and the effects of wind velocity, fire intensity, fire-source configuration, and terrain slope on the enhanced wind by fire were studied. Trends between the studied contributing factors were analyzed and correlations were developed for fire-wind enhancement flow characteristics.

ACKNOWLEDGMENTS

First and foremost, I would like to express my sincere gratitude and special appreciation to my supervisors: Dr. Yaping He, Professor Kenny Kwok and Associate Professor Ming Zhao for their continuous support during my PhD journey, for their patience, motivation, immense knowledge, and insight. I would like to thank them for providing me with the opportunity to broaden my horizons knowledge and intuition. Their instrumental guidance has helped me to successfully overcome every challenge and improve my research skills.

I would like to thank Western Sydney University for provision of scholarship as well as travel fund supports during my PhD candidature period. I would like to also thank my colleagues and friends at the Centre for Infrastructure Engineering for their care, companionship, and support, who all made a peaceful, collaborative and joyful environment.

Finally, I would like to extend my deepest appreciation to my family for their unconditional, deep and genuine love, without whom I would not be here. To my mum, for her dedication, infinite love, and compassion. To my dad for his all-time support, patience, motivation, and encouragement. To my siblings for their emotional support and always being there for me.

STATEMENT OF AUTHENTICATION

The work presented in this thesis is, to the best of my knowledge and belief, original except as acknowledged in the text. I hereby declare that I have not submitted this material, either in full or in part, for a degree at this or any other institution.

Esmaeel Eftekharian [redacted]

ANTHOLOGY OF DISSEMINATION

The present thesis is prepared based on publications. There are five published journal papers included in the thesis:

Published articles:

1. **Esmaeel Eftekharian,** Yaping He, Robert H. Ong, Kenny C. S. Kwok, Jianping Yuan, Investigation of fire-driven cross-wind velocity enhancement. *International Journal of Thermal Sciences.* 2019; Volume 141, Pages 84-95.
https://doi.org/10.1016/j.ijthermalsci.2019.03.033.

2. **Esmaeel Eftekharian,** Maryam Ghodrat, Yaping He, Robert H. Ong, Kenny C. S. Kwok, Ming Zhao, Numerical analysis of wind velocity effects on fire-wind enhancement. *International Journal of Heat and Fluid Flow*2019; Vol 80, Article No, 108471.
https://doi.org/10.1016/j.ijheatfluidflow.2019.108471

3. **Esmaeel Eftekharian**, Maryam Ghodrat , Yaping He, Robert H. Ong, Kenny C. S. Kwok, Ming Zhao, Numerical analysis of the effect of fire source configuration on fire-wind enhancement. *Heat Transfer Engineering*. 2019; Volume 42, Issue 1, Pages 1-20.
https://doi.org/10.1080/01457632.2019.1685249

4. **Esmaeel Eftekharian**, Maryam Ghodrat, Yaping He, Robert H. Ong, Kenny C. S. Kwok, Ming Zhao, Correlations for fire-wind enhancement flow characteristics based on LES simulations. *International Journal of Heat and Fluid Flow*. 2020; Volume 82, Article number: 108558.
https://doi.org/10.1016/j.ijheatfluidflow.2020.108558

5. **Esmaeel Eftekharian,** Maryam Ghodrat, Yaping He, Robert H. Ong, Kenny C. S. Kwok, Ming Zhao, Bijan Samali, Investigation of terrain slope effects on wind enhancement by a line source fire. *Case Studies in Thermal Engineering*. 2019; Volume 14, Article No, 100467. https://doi.org/10.1016/j.csite.2019.100467.

The journal articles have been published under my name, Esmaeel Eftekharian, as the first and corresponding author, and I was responsible for preparing the first full draft of each paper.

The following conference papers are also prepared and presented based on the studies undertaken during this research project.

1. **Esmaeel Eftekharian**,, Yaping He, Kenny C. S. Kwok, Robert H. Ong, “Numerical analysis of heat effects on fire wind enhancement”, *Nineteenth Australasian Wind Engineering Society Workshop*, April 4-6, 2018, Torquay, Victoria.

2. **Esmaeel Eftekharian**, Maryam Ghodrat, Yaping He, Kenny C. S. Kwok, Robert H. Ong, “Numerical Investigation of fire intensity effects on fire wind enhancement”, *The 7th International International Symposium on Computational Wind Engineering*, June 18-22, 2018, Seoul, Republic of Korea.

3. **Esmaeel Eftekharian**, Maryam Ghodrat, Yaping He, Robert H. Ong, Kenny C. S. Kwok, Bijan Samali, “Numerical Simulation of the effects of slope terrain on fire-wind enhancement”, *25th Austrialian Conference on Mechanics of Structure and Materials*, Dec 4-7, 2018, Brisbane, Australia.

4. **Esmaeel Eftekharian**, Maryam Ghodrat, Yaping He, Robert H. Ong, Kenny C. S. Kwok, “CFD investigation of cross-flow effects on fire-wind enhancement”, *21st Australasian Fluid Mechanics Conference*, Dec 10-13, 2018, Adelaide, Australia.

TABLE OF CONTENTS

ABSTRACT III
ACKNOWLEDGMENTS VI
STATEMENT OF AUTHENTICATION VII
ANTHOLOGY OF DISSEMINATION VIII
TABLE OF CONTENT X
LIST OF TABLES XII
LIST OF FIGURES XIII
NOMENCLATURE XVII
CHAPTER 1. INTRODUCTION 21
1.1. Background 21
1.1.1 The problem of bushfires 21
1.1.2 Bushfire attack mechanism 22
1.2. Research problem 24
1.3. Objectives of the research project 26
1.4. Overview of research methodology 26
1.5. Significance of the research 27
1.6. Thesis content 28
1.7. Publications generated from the current study 29
CHAPTER 2. LITERATURE REVIEW ON FUNDAMENTALS OF FIRE DYNAMICS 31
2.1. Heat of combustion and heat release rate 31
2.2. Plume structure and orientation 32
2.2.1. Flame and buoyancy 32
2.2.2. Flame characteristics of free-standing fires 35
2.2.3. The effects of wind 37
2.3. Other characteristics of flame and effect of wind 44
2.3.1. Flame spread on solid fuel surface 44
2.3.2. Flame oscillation 46
2.4. Summary 47
CHAPTER 3. INVESTIGATION OF FIRE-DRIVEN CROSS-WIND VELOCITY ENHANCEMENT 48
3.1. Abstract 49
3.2. Introduction 50
3.3. The numerical modeling approach 52
3.3.1. The modeling software and the governing equations 52
3.3.2. Geometrical model and simulation conditions 55
3.4. Results and discussion 56
3.4.1. Grid Sensitivity analysis 56
3.4.2. Results of validation 57
3.4.3. Results of fire-wind interaction 61
3.5. Conclusions 71
CHAPTER 4. NUMERICAL ANALYSIS OF WIND VELOCITY EFFECTS ON FIRE-WIND ENHANCEMENT 72
4.1. Abstract 73
4.2. Introduction 74
4.3. Numerical modeling 76
4.3.1. Simulation method 76
4.3.2. Geometrical model and simulation conditions 77
4.4. Validation and numerical setting 78
4.4.1. Validation 78
4.4.2. Grid sensitivity analysis 78
4.4.3. Details of LES analysis and uncertainties 79
4.4.4. Vortex method and turbulent intensity 81
4.5. Fire-wind interaction simulation results and discussion 82

4.5.1. The effects of fire-induced forces 82
4.5.2. Longitudinal changes in longitudinal velocity profile 91
4.6. Conclusion 95
CHAPTER 5. NUMERICAL ANALYSIS OF THE EFFECTS OF FIRE SOURCE CONFIGURATION ON FIRE-WIND ENHANCEMENT 97
5. 1. Abstract 98
5. 2. Introduction 99
5. 3. Numerical modeling 102
5. 4. Validation 103
5. 5. Geometric model and simulation condition 104
5. 6. Results and discussion 107
5.6.1. Grid sensitivity analysis 107
5.6.2. Fire-wind interaction simulation results and discussion 107
5.6.3. Enhancement of wind by fire in longitudinal direction 107
5.6.4. Vertical velocity distribution 114
5. 7. Conclusion 120
CHAPTER 6. CORRELATIONS FOR FIRE-WIND ENHANCEMENT FLOW CHARACTERISTICS BASED ON LES SIMULATIONS 121
6.1. Abstract 122
6.2. Introduction 123
6.3. Fire-wind interaction 124
6.4. Numerical Modelling 128
6.4.1. Overall methodology and simulation strategy 128
6.4.2. Modeling software and governing equation 128
6.5. Computational domain and simulation condition 129
6.6. Numerical uncertainty analysis 130
6.6.1. Grid sensitivity analysis 130
6.6.2. LES uncertainty analysis 131
6.6.3. Validation 132
6.7. Results and discussion 132
6.8. Conclusion 151
CHAPTER 7. INVESTIGATION OF TERRAIN SLOPE EFFECTS OF WIND ENHANCEMENT BY A LINE SOURCE FIRE 152
7.1. Abstract 153
7.2. Introduction 154
7.3. Numerical approach 157
7.4. Model descriptions and boundary conditions 157
7.4.1. Grid sensitivity analysis 159
7.4.2. Model validation 159
7.5. Results and discussion 159
7.5.1. Upslope wind 159
7.5.2. Downslope wind 161
7.5.3. comparison of upslope and downslope 164
7.6. Conclusion 167
7.7. Acknowledgment 167
CHAPTER 8. CONCLUSION 168
CHAPTER 9. REFERENCES 171
Appendix A1 186
Appendix A2 199
Appendix A3 216
Appendix A4 238
Appendix A5 256

LIST OF TABLES

Table 2-1 values of κ and λ coefficients for temperature and velocity profile (Zang et al. 2014) .. 37
Table 3-1. Input parameters for different simulation scenarios. 56
Table 4-1 Demonstration of different simulation scenarios.......... 77
Table 5-1. Description of simulation scenarios 106
Table 6-1. List of simulation scenarios based on free-stream wind velocity and fire line intensity. 130
Table 6-2 Data related to the maximum wind enhancement predicted by CFD and the developed correlation for different simulation scenarios. 139
Table 7-1. Variation of maximum wind velocity enhancement and the corresponding location for different slope angles (degrees). 165

LIST OF FIGURES

Figure 1-1 Bushfire attack mechanisms (NSWRFS 2006) 22
Figure 1-2 Trees fallen due to strong wind after bushfire attack (Lambert 2010) 23
Figure **1-3** Longitudinal velocity profiles downstream of the fire. z^* and u^* are respectively, non-dimensional height and longitudinal velocity. Fire source is located at *x*=0. (He et al. 2011a) 24
Figure **1-4** Schematic view of fire in cross-flow showing the common terminologies used in this research studies 25
Figure 2-1 Introducing different regions for (a) flame length and (b) flame temperature profile for line source of fire (Zang et al. 2014) 37
Figure 2-2 Schematic view of the control volume and the acting force, considered by (Fang et al. 2016) 40
Figure 2-3 Four vertical structures of jet in cross-flow suggested by (Fric & Roshko 1994) 43
Figure 2-4 Fire front shape under (a) no slope condition with 120s interval (b) slope degree of 30 ∘with 15s interval (Silvani, Morandini & Dupuy 2012) 45
Figure 2-5 time-averaged velocity vector for five consecutive instantaneous velocities for (a) horizontal fire and (b) up-slope fire. 46
Figure 3-1 Schematic views of the computational domain for (a) validation (b) cross-wind fire scenarios. 55
Figure 3-2 vertical distribution of normalized (a) horizontal velocity (b) density for different grid sizes at *X*=6*D* when *Q*=580 kW. 57
Figure 3-3 Comparison of the normalized centreline velocity profile of the current study with numerical and experimental data available in the literature 58
Figure 3-4 Schematic of Hirano and Kinoshita's experimental configuration (Hirano & Kinoshita 1975)... 59
Figure 3-5 Comparison between experiment (Hirano & Kinoshita 1975) and CFD of the velocity profiles taken downstream the boundary layer of methanol-air diffusion flame, u_∞ = 0.5 m/s. 60
Figure 3-6 Comparison between experiment (Hirano & Kinoshita 1975) and CFD of the temperature profiles taken downstream the boundary layer of methanol-air diffusion flame, u_∞ = 0.5 m/s. 60
Figure 3-7 Cross-sectional longitudinal normalized velocity $(UUref)$ at (a) *X*/*D*=-3, (b) *X*/*D*=3, (c) *X*/*D*=6, (d) *X*/*D*=10, (e) *X*/*D*=13 and (f) *X*/*D*=16, for *Q*=580 kW case. 62
Figure 3-8 Distributions of normalized longitudinal (a) velocity, (b) total acceleration along the domain center plane at various distances and (c) components of acceleration at *X/D*=6, downstream of the fire source for *Q*=580 kW case. The cross-from reference velocity for all cases are 3 m/s. 64
Figure 3-9 Distribution of normalized longitudinal velocity $(UUref)$at different horizontal plane: (a) *Z/D*=0.3, (b) *Z/D*=1, (c) *Z/D* =2, (d) *Z/D* =3 and (e) *Z* /*D* =4 for the case *Q*=580 kW. The cross-from reference velocity for all cases are 3 m/s. 65
Figure 3-10 Distribution of normalized (a) longitudinal pressure gradient (b) density at different distances downstream of the fire source centreline for *Q*=580KW case**.** The cross-from reference velocity for all cases are 3 m/s. 66
Figure 3-11 Normalised Longitudinal velocity profile at *X*/*D*=6 for different heat release rates. The cross-from reference velocity for all cases are 3 m/s. 67
Figure 3-12 Distribution of normalized (a) longitudinal pressure gradient (b) density and (c) total acceleration along a vertical line at *X/D*=6 and free stream for different heat release rates. The cross-from reference velocity for all cases are 3 m/s. 68
Figure 3-13 Normalised longitudinal (a) pressure gradient $(dp/dx)/(\rho\infty g)$, (b) viscous acceleration a_{v1}/g and (c) pressure acceleration a_{p1}/g, planar distribution at *Y*=0 for different heat release rates. The cross-from reference velocity for all cases are 3 m/s. 68
Figure 3-14 Distribution of (a) CO_2 mass fraction and (b) normalized longitudinal velocity $(UUref)$ at *Y/D*=0.2, *Y/D*=0.5 and *Y/D*=0.7 respectively for *Q*=58 kW, *Q*=580 kW and *Q*=1.16 MW. The cross-from reference velocity for all cases are 3 m/s. 70
Figure 4-1 Schematic views of the computational domain for the cross-wind and fire simulations. 77

Figure 4-2 Comparison of vertical distribution of normalized time-averaged (a) longitudinal velocity and (b) density at $X^*=3$ for different grid sizes. 79

Figure 4-3 Fraction of resolved turbulent kinetic energy $k_{res}/(k_{res}+k_{sgs})$ along domain center plane ($Y=0$) for S#1. (a) vertical distribution at different distances downstream of the fire and (b) planar distribution.. 80

Figure 4-4 Normalised power spectra density of longitudinal velocity on a horizontal line (Y^*, Z^*) = (0, 1.6) at $X^*=-7$ (upstream of the fire source) and $X^*=6$ (downstream of the fire source within the plume region) for S#1. 81

Figure 4-5 Comparison of longitudinal time-averaged normalized velocity profiles at (a) $X^*=-3$ and (b) $X^*=6$ for different simulation scenarios 83

Figure 4-6 Normalized distribution of time-averaged (a) longitudinal velocity (first column), (b) density (second column) and (c) pressure gradient (third column) for different simulation scenarios at $Y=0$.Vertical and horizontal axis indicates normalized vertical and longitudinal distance. Plume tilt angle (γ) is the angle between the dash lines. 85

Figure 4-7 variation of tilt angle (γ) with Richardson number and (b) plume axis for different simulation scenarios 87

Figure 4-8 Comparison of different normalized fire-induced time-averaged longitudinal forces, including (a) pressure force (first column), (b) viscous force (second column) and (c) total force (third column) in different simulation scenarios. Vertical and horizontal axis indicates normalized vertical and longitudinal distances. 89

Figure 4-9 normalized cross-sectional distribution of fire-induced time-averaged longitudinal (a) velocity (first column), (b) pressure force (second column) and (c) viscous force (third column) for different upstream wind velocities at $X^*=12$. The vertical and horizontal axis indicates normalized vertical and spanwise distance. 91

Figure 4-10 Vertical distribution of normalized time averaged longitudinal velocity in different distances downstream of the fire source for (a) simulation scenario #1 ($U_{ref}=3$ m/s) and (b) simulation scenario #2 ($U_{ref}=4.5$ m/s), (c) simulation scenario #3 ($U_{ref}=6$ m/s), (d) simulation scenario #4 ($U_{ref}=7.5$ m/s), (e) simulation scenario #5 ($U_{ref}=9$ m/s). The arrows in the figure indicate the location corresponding to the maximum level of enhancement at each simulation scenario. 93

Figure 4-11 Comparison of the level of enhancement for different upstream wind velocities (simulation scenarios) at different distances downstream of the fire. S#1, S#2, and S#3 are respectively corresponding to the simulation scenarios with free-stream reference velocity of 3m/s, 4.5 m/s and 6m/s 94

Figure 4-12 Comparison of Ri_x and Eu_x number at different distances downstream of the fire source for different simulation scenarios. The green dash line is corresponding to the location at which maximum velocity enhancement happens in the specified scenario. 95

Figure 5-1 Schematic view of the (a) computational domain, (b) comparison of normalized centreline velocity profile of the current study with numerical and experimental data available in the literature. 104

Figure 5-2 Schematic views of the computational domain (a) pool fire and (b) line fire source (all dimensions are in meter). 106

Figure 5-3 Comparison of normalized longitudinal velocity ($U1^*$) for (a) line source and (b) point source case at $Y=0$. 108

Figure 5-4 Comparison of normalised longitudinal mean velocity planar distributions for line (S#1) and point (S#2) fire sources at various longitudinal locations: (a) $X=-3D$, (b) $X=6D$, (c) $X=9D$, (d) $X=12D$, (e) $X=24D$ and (f) $X=48D$. 110

Figure 5 5 Cross-sectional distributions of (a) normalized longitudinal pressure force (b) normalized density (c) normalized longitudinal pressure acceleration and (d) normalized longitudinal velocity at $X=9D$ for line fire case (left column) and point source case (right column). 112

Figure 5-6 Distribution of fire-induced longitudinal (a) pressure force (b) viscous force and (c) total force at $X=9D$ for the line (left column) and pool fire (right column) source. 113

Figure 5-7 Distribution of normalized vertical (a) velocity (b) fire-induced total force (c) fire-induced pressure force, (d) gravitational force and (e) fire-induced viscous force for line fire case (left column) and point source case (right column). 115

Figure 5-8 Comparison of the normalized vertical distribution of longitudinal, spanwise, vertical and mean velocity profile at different distances downstream of the fire on the plane Y=D for line fire (left column) and point source (right column). 117

Figure 5-9 Air flow path-lines generated froma cross-cut of near ground inlet surface (-1≤Y≤1 and 0≤Z≤2) for (a) line source and (b) point source fire cases…………………………… 118

Figure 5-10 Iso-contour of mixture fraction coloured by normalised longitudinal velocity for (a) line fire source (S#1) and point source case (S#2). 119

Figure 6-1 Schematic view of the computational domain. 129

Figure 6-2 Comparison of the vertical distribution of (a) normalized longitudinal velocity and (b) density at X^* =12 for different grid sizes in S#5. 131

Figure 6-3. Ratio of the resolved turbulent kinetic energy to total turbulent kinetic energy for S#2 at different distances downstream of the fire source. 131

Figure 6-4 Distribution of normalized longitudinal velocity for different simulation scenarios at a vertical plane passing the centreline (Y=0). 134

Figure 6-5 Planar distribution of normalized longitudinal pressure gradient for different simulation scenarios at a vertical plane passing the domain centreline (Y=0). 135

Figure 6-6 Distribution of normalized density for different simulation scenarios at a vertical plane passing the domain centreline (Y=0). 136

Figure 6-7. Cross-sectional distribution of normalized longitudinal velocity (U/U_{ref}) at different distances downstream of the fire source for S#1, S#2. 138

Figure 6-8 Comparison of the maximum wind enhancement by between the results of Eq. (6-9) and CFD data of the first 20 simulation scenarios. 141

Figure 6-9 Comparison of Eq. (6-10) with all CFD data. 142

Figure 6-10 vertical distribution of normalized longitudinal velocity at different distances downstream of the fire source for three different simulation scenarios. (The line and position corresponding to $U^*_{e\_max}$ is shown by an arrow for each simulation scenario). 144

Figure 6-11. Comparison of wind enhancement plume line in different simulation scenarios: (a) the effects of I^* under constant Fr, (b) the effects of Fr under constant I^*. 145

Figure 6-12 Comparison of wind enhancement plume line between CFD data and that of correlation [Eq.(6-13)] for different simulation scenarios 146

Figure 6-13 comparison of $\boldsymbol{Xe\_max} *$ values by CFD and by correlation Eq. (6-15) 147

Figure 6-14 variations of normalized plume velocity along the wind enhancement plume line. .. 149

Figure 6-15 Comparison of normalized plume velocity ($Up *$ for $X *> Xe\_max *$) between CFD data and the developed correlation [Eq. (6-16)] 150

Figure 7-1. A schematic view of the computational domain at a slope angle θ from Earth horizontal direction (θ>0: upslope; θ=0: no slope; and θ<0: downslope). Dimensions are in meter. 158

Figure 7-2 Comparison of normalized streamwise velocity $\left(\frac{U}{U_{ref}}\right)$, normalized streamwise pressure gradient$\left(\frac{\frac{dp}{dx}}{\rho_\infty g}\right)$, normalised streamwise acceleration axg and normalised streamwise component of buoyancy force Fbx at Y=0 for three inclination angles. 160

Figure 7-3 Cross-sectional normalized streamwise velocity $\left(\frac{U}{U_\infty}\right)$ at different distances (X/D) from the fire source subjected to different slope conditions. 162

Figure 7-4. Comparison of normalized streamwise velocity $\left(\frac{U}{U_\infty}\right)$, normalized streamwise pressure gradient$\left(\frac{\frac{dp}{dx}}{\rho_\infty g}\right)$, normalized streamwise acceleration $\left(\frac{a_x}{g}\right)$ and normalized streamwise component of buoyancy force Fbx for (a) without slope (θ = 0°), (b) middle downslope (θ = -10°), high downslope (θ = -20°). 163

Figure 7-5 Cross-sectional normalized streamwise velocity $\left(\frac{U}{U_\infty}\right)$ at different distances (X/D) from the fire source for the case without slope (θ=0°) and downslope (θ= -10°, θ= -20°) scenarios. 164

Figure 7-6 Left column (a): the trend of (a_1) maximum velocity enhancement and (a_2) its corresponding location with slope angle for all simulation cases; right column (b): Contour of plume region (the domain region where the density is less than half of the freestream density ($0.5\rho\infty$)

coloured by normalised streamwise velocity $\left(\frac{U}{U_\infty}\right)$ for downslope (b_1), no-slope (b_2) and upslope (b_3) conditions. 166

NOMENCLATURE

A	area of the fire source (m^2)
A_f	Fuel surface area (m^2)
a	Fluid acceleration (m/s^2)
a'	constant coefficient
a_i	acceleration in direction i (m/s^2)
a_p	pressure acceleration (m/s^2)
a_v	viscous acceleration (m/s^2)
a_t	total acceleration (m/s^2)
$b_{\Delta T}$	Plume in a point at which temperature rise drops to $0.5\Delta T_0$
b_u	Plume radius in a point at which velocity drops to $0.5u_0$
b'	constant coefficient
C_p	Specific heat capacity of ambient air
C_v	Constant for plume centreline velocity equation
C_T	Constant for plume centreline temperature equation
C_k	sub-grid scale coefficient
C_ϵ	sub-grid scale coefficient
C_{EDC}	time scale coefficient
C_{diff}	molecular diffusion coefficient in Eddy Dissipation Model
d'	constant coefficient
D	Fire source characteristic length (m) (fuel bed depth)
D_h	characteristic dimension of the burner (m)
$D_{h'}$	equivalent hydraulic diameter for the line source (m)
D_m	diffusion coefficient
exp	exponential function
E_r	unit energy release rate of the fire (W/m^2)
Eu	Euler number
Eu_x	modified local Euler number
f_p	fire-induced pressure force per unit volume (N/m^3)
f_v	fire-induced viscous force per unit volume (N/m^3)
f_T	fire-induced total force per unit volume (N/m^3)
f'	function
F	force (N)
F_p	pressure force (N)
F_v	viscous force (N)
F_T	total force (N)
F_0	Buoyancy flux (N/m^2)
$\mathrm{Fr_j}$	Froude number based on fuel jet velocity
$\mathrm{Fr_w/Fr}$	Froude number based on wind velocity
g	Gravitational acceleration (m/s^2)
g'	constant coefficient
H	domain height (m)
H_f	flame height in presence of wind
H_{f0}	flame height in absence of wind
h	specific enthalpy per unit volume (kJ/m^3)
h'	constant coefficient
h_0	Height of virtual origin above the fire source (m)
I	Fire intensity (kW/m, MW/m)
I^*	normalized fire intensity

I_B	bushfire intensity, line source fire intensity (MW/m)
I_r	radiation intensity (W/m^2)
K_G	Flame geometry factor
k_{res}	resolved turbulent kinetic energy
k_{sgs}	sub-grid scale turbulent kinetic energy (m^2/s^2)
k'	constant coefficient
l'	constant coefficient
L	domain length (m)
LE	level of enhancement
L_f	Flame length (m)
L_v	Latent heat of gasification (kJ/kg)
m	mass (kg)
m'	constant coefficient
$\dot{m}_{fu}''$	Burning intensity (burning rate) (kg/s.m^2)
$\dot{m}''^{*}_{fu}$	non-dimensional burning rate per unit area
M_0	Momentum flux (N/m^2)
n	Frequency (1/s)
n'	constant coefficient
p	static pressure (pa)
p_d	dynamic pressure of the ambient wind
P	perimeter of the fire source (m)
Pr	Prandtl number
Pr_t	turbulent Prandtl number
$\dot{q}_{fl}''$	Heat transfer rate (kW/m^2)
$\dot{q}_l''$	Heat loss rate (kW/m^2)
$\dot{q}_r''$	radiation flux (W/m^2)
$\dot{q}'''$	fuel heat release rate per unit volume (W/m^3)
$\dot{q}_l'''$	local heat release rate per unit volume (W/m^3)
$\dot{q}_r'''$	radiative heat transfer per unit volume (W/m^3)
$Q*$	None-dimensional heat release rate
Q_0	Source volume flux (m^3/s.m^2)
$\dot{Q}_c$	Convective heat transfer rate (kW)
$\dot{Q}$	Heat release rate (kW)
Q	Heat release rate (kW)
$\dot{Q}_l'$	Heat release rate per unit length of the line source (kW/m)
r^2	correlation coefficient
r'	coefficient of correlation
R	gas constant (J/kgK)
R_m	momentum flux ratio
Ri	Richardson number
S_{uu}	Power spectrum density (W/Hz)
s_r	distance along a special ray (m)
s_a	amount of air required to burn a unit mass of fuel (kg)
s'	constant coefficient
S#	scenario number
t	time (s)
t'	coefficient of correlation
T	temperature (K)
T_f	flame temperature (K)
T_∞	Ambient temperature (K)
U	longitudinal velocity

U_w	Free-stream wind velocity in the same elevation where maximum velocity of the bulge happens. (m/s)
U_f	maximum velocity of the bulge in the wind velocity profile (m/s)
U_{ref}	reference velocity (m/s)
U_{enh}^*	normalized wind enhancement
U_{e_max}	maximum wind enhancement (global value)
$U_{e\_max}^*$	normalized maximum wind enhancement (global value)
$U^*_{max\_l}$	normalized maximum wind enhancement (local value)
X, Y, Z	coordinates of computational domain (m)
Y	mass fraction of mixture
u^*	Normalized velocity
u_c	Flame characteristic velocity (m/s)
u_f	Fuel injection velocity (m/s)
u_m	Velocity profile (m/s)
u_w	Wind velocity (m/s)
u_0	Fuel exit velocity (m/s)
u_∞	Free-stream wind velocity (m/s)
U_p	wind enhancement plume line velocity
U_p^*	normalized wind enhancement plume line velocity
u_f	fuel injection velocity
u_R	Radial velocity of plume (m/s)
W	Fire source width (m)
X, Y, Z	coordinates of computational domain
x	Downstream longitudinal distance from the fire source ($x=X-D/2$) (m)
X^*	normalized X position
$X_{e\_max}^*$	normalized location corresponding to the maximum wind enhancement
x_i	coordinate in i direction
x_j	coordinate in j direction
X^*	normalised longitudinal distance (X/D)
Y_m	mass fraction of mixture
Y^*	normalized spanwise distance (Y/D)
$\forall$	Volume (m^3)
Z^*	normalized vertical distance (Z/D)
z_c	Characteristic length for the fire line source (m)
Z_{st}	Stoichiometric mixture fraction
Z^*_m	Z^*corresponding to $U^*_{max\ l}$
Greek Symbols	
α	terrain coefficient
α_c	Efficiency of combustion [Eq.(2-2)]
α_e	Entrainment coefficient [Eq.(2-4)]
α_{th}	thermal diffusivity (m^2/s)
β	Thermal expansion coefficient (1/K)
Γ	Dimensionless force balance in plume mechanism
δ	Kronecker delta
Δ	grid spacing
ΔH_c	Heat of combustion (kj/kg)
ΔT	Temperature difference (K)
ΔT_0	Temperature difference between plume centreline and ambient (K)
ΔT_f	Change of flame temperature (K)

ΔT_R	Radial temperature difference of plume (K)
ϵ	Dissipation rate of turbulent kinetic energy
η	Constant in velocity profile
η_k	Kolmogorov length scale
θ	Flame tilt angle
κ	Constant temperature profile
κ_{ab}	absorption coefficient
κ_p	Plank mean absorption coefficient
λ	Constant varies for different temperature regions
μ	kinematic viscosity (m^2/s)
v	kinematic viscosity
ρ	Gas density (kg/m^3)
ρ_∞	Ambient density (kg/m^3)
ρ_a	Air density (kg/m^3)
ρ_f	Fuel injection density (kg/m^3)
σ	stress (Pa)
σ_r	Stefan-Boltzmann constant (W/m^2K^4)
χ	radiation fraction
Φ	viscous stress tensor (kg/m^2s^2)
ω	mass rate of production of species (kg/m^3s)
Ω	mass rate of production of species

Symbols

<>	Mean (time-averaged)

Super-script

*	Normalized
–	spatial filtering
~	favre filtering
→	vector variable

Subscript

0	at fuel surface
1, 2, 3	in *X*, *Y* and *Z* direction respectively
ref	reference value
res	resolved
∞	free-stream
g	gravitational
t	turbulent
T	total
N	normalized
p	pressure
i, j, k	direction or component indices
T	total
sgs	sub grid scale
v	viscous

List of acronyms and abbreviations

ACT	Australian Capital Territory's
CFD	Computational Fluid Dynamics
CVP	Counter-rotating vortex pair
DNS	Direct Numerical Simulation
LES	Large Eddy Simulation
PIV	Particle image velocimetry
RANS	Reynolds-averaged Navier–Stokes

CHAPTER 1. INTRODUCTION

1.1. Background

1.1.1 The problem of bushfires

Bushfires (forest fires or wildland fires) are a well-known, potentially dangerous natural phenomenon in the world, particularly in Australia. The high-frequency and the erratic nature of bushfire occurrences make it difficult to implement effective control and management measures. Bushfire stands at 5th in the ranking of social and environmental effects of natural hazards (or more specifically, the integrated costs incurred) in Australia, following flood, storm, tropical cyclone and earthquake (Gentle, Kierce & Nitze 2001). Between 1900 and 2008, bushfires claimed 552 lives in Australia and in 1967 and 1983, 64 and 60 civilians were killed by bushfires, respectively. The most fatal bushfire occurred in 2009, claiming 173 lives in Victoria and destroying 2039 houses (BoM 2009). The 54 most house-destructive bushfires occurred between 1957 and 2009, destroying 8256 houses (Blanchi et al. 2010) and, on average, 83 houses per year have been lost due to bushfires in the last century (Ashe, McAneney & Pitman 2009). In Europe, on average 50000 bushfires occur, destroying approximately 0.5 million hectares of jungles annually (European & Commission 2014; European & Commission. 2013). In 2015, bushfires in Siberia, Russia, killed more than 30 people, injured 800 civilians and demolished approximately 1300 houses (Liesowska 2015). During 10 months between January and October 2015, over 50000 bushfires occurred in North America which destroyed 38000 km^2 of land (NIFC 2015a; USDoA 2015).

The unpredictable and inevitable nature of bushfires make it necessary to take effective measures well in advance to mitigate the associated hazards intertwined with this natural calamity. Proactively conducting sufficient scientific research on different aspects of bushfire-wind interaction will facilitate mitigating the hazardous consequences of bushfire events. Bushfire-wind enhancement, referred to as the increase of wind velocity due to interaction with bushfires, is believed to be one of the dire phenomena associated with bushfires (He et al. 2011b; Lambert 2010) that is under-represented in the literature. Bushfire-wind enhancement can tremendously affect buildings prone to bushfire events. Lambert (2010) and McRae et al. (2013) used evidence to prove that the wind velocity in the bushfire near-ground downstream region is higher than that reported by weather forecasters. This hot and powerful enhanced wind may cause significant damage to buildings in the bushfire downstream region.

1.1.2 Bushfire attack mechanism

Bushfires mostly occur when a high amount of fuel or dried vegetation and favorable weather conditions are available (Blanchi et al. 2010). The potential places for bushfire occurrence are grasslands and forests; the latter has more potential for major bushfires with high intensities. Generally, deficiency in rainfall in the forests, strong and hot winds, a low level of humidity in vegetation and preexisting fire are factors contributing to severe bush-fire occurrences (Sullivan, 2004). Pre-fire data collection achieved from full investigation of environmental conditions connected to fire intensity, can be used to analyze bushfire attack mechanisms.

Bushfire attack mechanisms have been conventionally classified into direct flame contact, radiant heat exposure and ember attack (Blanchi & Leonard 2005; Mell et al. 2010; NSWRFS 2006). Figure 1-1 schematically shows how these bushfire mechanisms attack buildings. Direct flame contact and radiant heat contribute to the ignition of houses when the bushfire is sufficiently close. The proximity of houses to bushfire allows direct fire impingement and also sets houses on fire through radiation. Embers, however, can ignite buildings through either combustible debris that is carried by wind over considerable distances or adjacent burning structures (Blanchi & Leonard 2005). The ignition of vegetation or buildings over distances from a bushfire front is referred to as spotting. Accumulated embers can maintain glowing combustion for a long period of time. This is why many properties that survive from an initial direct bushfire front attack may be ignited by embers a few hours later (Blanchi & Leonard 2005). Burning buildings are also able to ignite adjacent structures through direct flame or radiation effects.

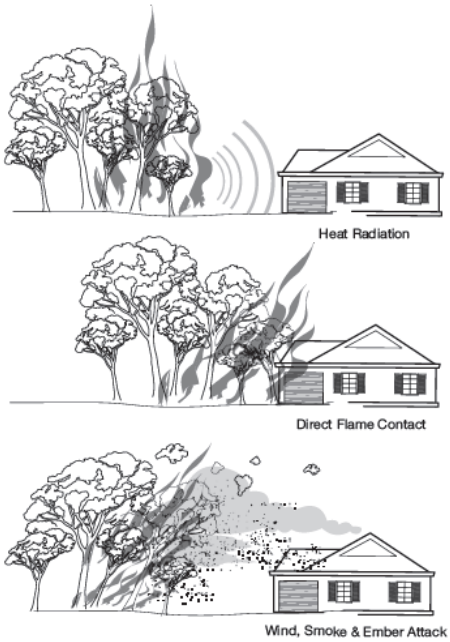

Figure 1-1 Bushfire attack mechanisms (NSWRFS 2006)

The role that wind plays in increasing fire intensity, fire spread (Mills 2009) and flame characteristics is generally accepted (Gould, McCaw & Cheney 2007). However, the destructive role of wind had not been taken seriously before Ash Wednesday in 1983, when wind caused serious damage to houses through breaking windows, lifting roofs from buildings, moving the fire fronts to unaffected buildings and igniting structures (Ramsay, Mcarthur & Dowling 1987). The damages caused by the wind were considered even greater than fire (Ramsay, Mcarthur & Dowling 1987). Wind can carry burning embers, preheating and igniting vulnerable parts of buildings before the bushfire front reaches them (NSWRFS 2006). Strong winds also fell trees in forests (see Figure 1-2). Some anecdotal evidence in the literature proves that local wind is not the only responsible factor for wind-attributed destruction. ACT (Australian Capital Territory) fire (Wang 2006) is a telling example. During this bushfire, the local weather forecast failed to report on a wind velocity beyond 50km/h, while a higher wind velocity (possibly more than 100km/h) was required to cause destructive damages on buildings (Wang 2006). Also, much higher wind velocities than what had been reported by the weather forecast had been felt by firefighters working at the bushfire site (Kwok, He & Douglas 2012). It can be postulated from the aforementioned evidence that there should be a force strengthening the local wind velocity.

It is generally accepted that wind plays a critical role in intensifying bushfire spread rate, which is referred to as the advance of a fire front in the direction perpendicular to the fire front (Mills 2009). However, as reported by Lambert (2010) and McRae et al. (2013), bushfire can also intensify the local near ground wind velocity, something which has not been fully recognized or understood. Reporting the house losses in the 1983 Ash Wednesday bushfire, Ramsay, Mcarthur, and Dowling (1987) suggested the dominant destructive effects of wind in some cases.

Figure 1-2 Trees fallen due to strong wind after bushfire attack (Lambert 2010)

1.2. Research problem

Bushfire enhanced wind and the corresponding impacts have been numerically investigated by He et al. (2011) and Kwok, He and Douglas (2012) using Fire Dynamic Simulator (FDS) software. Their work has demonstrated that bushfires can interact with and intensify the local wind flow near the ground. This increases the wind near ground level up to 50% compared to the free-stream wind speed (Figure 1-3). $z*$ and $u*$ are respectively, the height and longitudinal velocity (Figure 1-4) normalised with the reference height and reference velocity, respectively. In Figure 1-3, x is the longitudinal distance from the fire source to the point of interest. Longitudinal direction is shown in Figure 1-4. As a rule of thumb 50 % of increase in velocity corresponds to 125% increase in pressure load on a building (according to $P = \frac{1}{2}\rho U_{\infty}^{2}$), which depicts how big can be the impacts of wind enhancement on buildings. Moreover, they showed the corresponding increase of the pressure coefficient or pressure load over a simplified building block located downstream of the fire front. Although their studies had a new perspective in the domain of bushfire-wind enhancement, the nature of mechanisms involved in the interaction between horizontal (longitudinal) momentum flow and vertical buoyant flow resulting in enhancement of horizontal flow remains unknown.

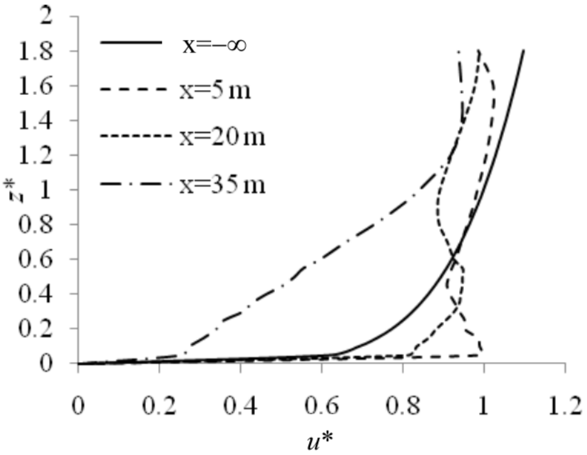

Figure **1-3** Longitudinal velocity profiles downstream of the fire. $z*$ and $u*$ are respectively, non-dimensional height and longitudinal velocity. Fire source is located at *x*=0. (He et al. 2011a)

The experimental study of Hirano and Kinoshita (1975) in laboratory scales confirms the increase of free-stream flow velocity due to interaction with flame. Employing experimental data analysis, Volchkov, Terekhov & Terekhov (2004) speculated that thermal expansion and low-density in the flame zone are responsible for velocity profile distortion. Recently, Fang et al. (2016), using the Lagrangian approach, presented an analytical solution for longitudinal acceleration and velocity along the axis of flame from a round surface fuel source subjected to cross-wind. However, they did not investigate whether and how the downstream wind velocity profile undergoes changes.

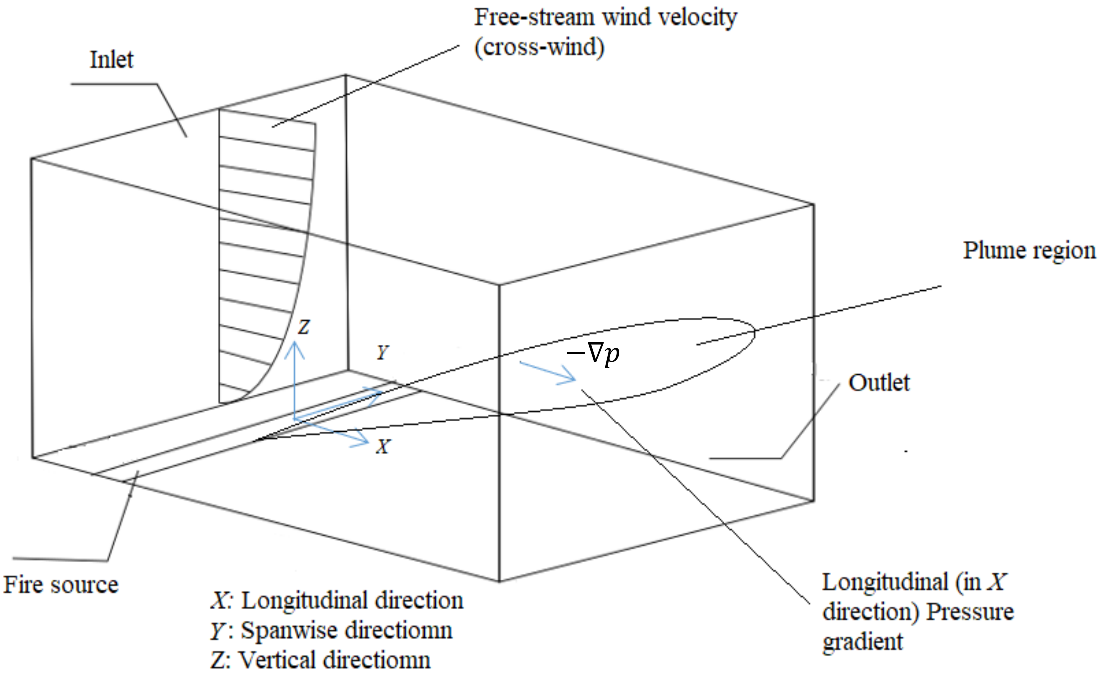

Figure **1-4** Schematic view of fire in cross-flow showing the common terminologies used in this research studies

Recently, Hu (2017) carried out a comprehensive study on reviewing geometrical features of a pool fire in cross-wind conditions. According to Hu (2017), there are some correlations for pool fire geometrical features under wind conditions. Many research studies have been devoted to characterize correlations for flame geometries such as flame length, flame height, and flame tilt angle under cross-flow conditions (Hu et al. 2011; Lin et al. 2019; Liu & Hu 2019; Lu et al. 2019; Ping et al. 2018; Wang et al. 2019). Nmira et al (2010) utilized numerical simulation and developed correlations for flame geometrical features such as flame length, height and tilt angle in fire-wind interaction scenarios as a function of dominant non-dimensional groups such as Froude and non-dimensional fire intensity. However, no correlations have been reported in the literature for aerodynamic characteristics of the flame.

Despite the significance of this issue, a comprehensive understanding of the mechanisms through which bushfire enhances wind has remained elusive and consequently, neither qualitative nor quantitative studies have been reported to determine the factors contributing to this phenomenon. Hence, wind-blown fire turbulent structures and the interaction of wind with buoyant plumes requires more fundamental studies.

1.3. Objectives of the research project

The main aim of this research is to fundamentally investigate mechanisms involved in fire-wind interactions that cause enhancement of wind by fire.

The objectives of this research project are to:

(1) Identify how the interaction of horizontal wind velocity and vertical buoyant plume leads to the enhancement of wind in a horizontal direction.

(2) Quantify the effects of factors that enhance wind (i.e. fire intensity, wind velocity, terrain slope, and fire source configuration).

(3) Develop correlations for enhanced wind as a function of the dominant non-dimensional groups, representing the main contributing factors to wind enhancement by fire.

1.4. Overview of research methodology

The research starts with a comprehensive review of the literature in fundamentals of fire dynamics with an emphasis on fire-wind interaction. Flow and flame characteristics features during fire-wind interactions are reviewed with the aim to find the knowledge gap on the effects of fire flame in flow aerodynamic characteristics.

Theoretical analysis is conducted by examining the governing Navier–Stokes equations in order to answer the key question as to why during fire-wind interaction, wind velocity increases downstream of the fire source. It is speculated that variation in the flow velocity profile caused by fire is because of the changes in one or more force terms in the right-hand side of the momentum equation. These forces include pressure force, viscous force and gravity force.

Computational Fluid Dynamic (CFD) based on the Large-Eddy simulation approach is employed to quantify the contribution of each of these individual forces to unravel the mechanisms involved in the enhancement of wind by fire. Additional modules are developed and incorporated into FireFOAM solver to quantitatively extract the impacts of individual forces in each simulation scenario.

Once the mechanisms involved in the enhancement of wind by fire are determined, a parametric study is initiated to identify the effects of external contributing factors such as wind velocity, fire intensity, fire source configuration and terrain slope on wind enhancement.

Dimensional and regression analyses are conducted to develop correlations for fire-induced enhanced wind flow characteristics as a function of dominant non-dimensional groups (Froude number and normalized fire intensity).

1.5. Significance of the research

This research will contribute to the literature by explaining the fundamental mechanisms involved in fire-wind enhancement.

It will employ numerical simulations to discover the underlying mechanisms involved in enhancement of wind and fire with the aim to boost the current knowledge of bushfire-wind enhancement phenomena. In doing so, the factors contributing to fire-wind enhancement phenomena are recognized based on which correlations are developed to predict the extent to which wind is enhanced in different environmental conditions.

Practical contributions to industrial applications are as follows:

AS3959 (2018) is an Australian standard providing guidelines for the construction of buildings in bushfire-prone areas. Similarly, standards like AS/NZS1170.2 (2011) and AS4055 (2012) supply information about wind action for use in structural design.

The effects of bushfire wind enhancement phenomena have not been considered in these standards. They only provide guidelines for bushfire and wind separately and the integrated actions imposed upon buildings have been completely overlooked. For example, Australian standard, AS3959 (2018) contains building standards based on the extent to which buildings are close to the bushfire prone area. This standard provides guidelines for protection measures based on Bushfire Attack Level (BAL). BAL categorizes buildings according to the level of heat-flux exposure and does not take into account the effects wind loading (Blanchi & Leonard 2005). Australia/ New Zealand Standards 1170.2 (2011) determines the site wind speed and consequently pressure distribution and wind force, from which the wind action is determined. This standard does not take into account the combined effects of fire and wind. Similarly, Australia Standard 4055 (2012) contains guidelines only about wind load on some specific building geometries and do not consider the effects of fire.

This research aims to boost the current knowledge about the enhancement of wind by fire in an attempt to discover and formulate the mechanisms contributing to this phenomenon. This study will provide a solid foundation for future research in this domain to modify the current Australian wind/building standards.

As well as the promising contribution of this research as a basis for future studies aiming to modify the relevant standards, the outcomes of this research can be used to develop guidelines for engineering design practice, safeguarding lives and properties against unprecedented and destructive bushfire attacks. It also provides a basis for the future studies aiming to modify the relevant standards

1.6. Thesis contents

Chapter 1. Introduction: This chapter describes a background on the enhancement of wind by fire and the mechanisms involved in the phenomenon, provides a research problem, aims, and the contributions of this research, as well as an overview of research methodology, the research's significance, and thesis content.

Chapter 2. Fundamentals of Fire Dynamics: This chapter presents a basic literature review of fundamental concepts and mechanisms involved in fire-wind interaction with the aim to identify the research gap.

Chapter 3. Investigation of fire-driven cross-wind velocity enhancement: This chapter provides detailed expansion and explanations of the research methodology. A theoretical framework based on Navier-Stokes equations is presented. Further analysis is carried out to identify various force components that may help to explain the mechanisms of fire-wind interactions and the enhancement of wind by fire. A module is developed and implemented to the FireFOAM solver to evaluate flow acceleration due to the pressure gradient, gravity, and viscous effects. The developed numerical model is validated against two sets of experimental data, namely, a buoyant diffusion fire plume in still air and the other in cross-wind conditions. The strategy for numerical simulations to achieve the three objectives is delineated. The effects of the heat release rate of point source fires on wind enhancement are also investigated in this chapter.

Chapter 4. Numerical analysis of wind velocity effects on fire-wind enhancement: Based on the developed theoretical framework in Chapter 3, the effects of upstream wind velocity under constant fire intensity are developed for a point source of fire. In this study, the Euler number is modified to take into account the fire-induced pressure force. Moreover, the Richardson number and the modified Euler number are employed to determine the influence of free-stream wind velocity and longitudinal distance from the fire source on wind velocity enhancement. This study also provides the details of an LES uncertainty analysis including the resolved fraction of the kinetic energy of turbulence, the ratio of the grid spacing to the Kolmogorov scale as well as presenting turbulent spectra at characteristic locations.

Chapter 5. Numerical analysis of the effect of fire source configuration on fire-wind enhancement: Given that bushfire starts with a point source of fire and then evolves to a line source, comparison of the physics of fire-wind enhancement between the point source and line source is worth investigating. Based on the developed theoretical framework in Chapters 3 and 4, a comparison is made between the wind enhanced by a line source and point source of fire under the same fire intensity. Fire-induced vertical velocity is also compared for the point and line source of the fire. In this study also a new parameter as an equivalent hydraulic diameter of line fire sources is introduced to represent the non-dimensional bushfire intensity.

Chapter 6. Correlations for fire-wind enhancement flow characteristics based on LES Simulations: This chapter presents a range of simulation scenarios defined for different combinations of upstream wind velocity and fire intensity of a line source fire which resembles the evolved bushfire source. The combined effects of upstream wind velocity and fire intensity on wind enhancement are investigated. A correlation is developed to determine the maximum wind enhancement as a function of the Froude number and normalized line fire intensity representing free-stream wind velocity and fire source heat release rate, respectively. A correlation is also developed for the longitudinal location at which maximum wind enhancement occurs as a function of the Froude number and normalized fire intensity. Furthermore, the concept of a wind enhancement plume line is defined as a line along which the local wind enhancement occurs at a given longitudinal location downstream of the fire source, for which a correlation is also developed. Moreover, a gradual decaying trend is observed in wind enhancement after reaching a peak along the wind enhancement plume line in all simulation scenarios for which a correlation is also developed as a function of normalized longitudinal direction.

Chapter 7. Investigation of terrain slope effects on wind enhancement by a line source fire: This chapter investigates the effects of terrain slope on wind enhancement by a line fire source based on the theoretical framework developed in Chapter 2. Four different terrain upslope angles and four terrain downslope angles are investigated, and maximum wind enhancement is quantified. Also, a trend for variation of maximum wind enhancement with slope angle is developed.

Chapter 8. Conclusion: A summary is presented of the findings of this thesis.

Chapter 9. References: Inclusion of all the references used in the thesis.

1.7. Publications generated from the thesis

1. Investigation of fire-driven cross-wind velocity enhancement, **Esmaeel Eftekharian**, Yaping He, Robert H. Ong, Kenny C. S. Kwok, Jianping Yuan, International Journal of Thermal Sciences. 2019; Volume 141, Pages 84-95. https://doi.org/10.1016/j.ijthermalsci.2019.03.033.

2. Numerical analysis of wind velocity effects on fire-wind enhancement, **Esmaeel Eftekharian**, Maryam Ghodrat, Yaping He, Robert H. Ong, Kenny C. S. Kwok, Ming Zhao, International Journal of Heat and Fluid Flow. 2019; Vol 80, Article No, 108471.
https://doi.org/10.1016/j.ijheatfluidflow.2019.108471

3. Numerical analysis of the effect of fire source configuration on fire-wind enhancement, **Esmaeel Eftekharian**, Maryam Ghodrat , Yaping He, Robert H. Ong, Kenny C. S. Kwok, Ming Zhao, Heat Transfer Engineering. 2019, Volume 42, issue 1, Pages 1-20,

https://doi.org/10.1080/01457632.2019.1685249

4. Correlations for fire-wind enhancement flow characteristics based on LES simulations, **Esmaeel Eftekharian**, Maryam Ghodrat, Yaping He, Robert H. Ong, Kenny C. S. Kwok, Ming Zhao, International Journal of Heat and Fluid Flow. 2020; Volume 82, Article number: 108558.

https://doi.org/10.1016/j.ijheatfluidflow.2020.108558

5. Investigation of terrain slope effects on wind enhancement by a line source fire, **Esmaeel Eftekharian**, Maryam Ghodrat, Yaping He, Robert H. Ong, Kenny C. S. Kwok, Ming Zhao, Bijan Samali, Case Studies in Thermal Engineering. 2019; Volume 14, Article No 100467. https://doi.org/10.1016/j.csite.2019.100467.

CHAPTER 2. LITERATURE REVIEW ON FUNDAMENTALS OF FIRE DYNAMICS

2.1. Heat of combustion and heat release rate

Fires are generally diffusion flames burning solid mostly solid fuels which undergo a range of processes including volatilization and subsequent mixing with air before ignition. The burning intensity $\dot{m}''_{fu}$ (kg/s.m^2) is linked to the amount of heat transferred to the fuel by (Drysdale 2011) :

$$\dot{m}_{fu}{}'' = \frac{\dot{q}_{fl}{}'' - \dot{q}_l{}''}{L_v} \tag{2-1}$$

in which, $\dot{m}_{fu}{}''$ is the mass release rate per area unit, $\dot{q}_{fl}{}''$ is the heat transfer rate from the flame and/or other heat sources to a unit fuel surface area (kW/m^2) and $\dot{q}_l{}''$ is the heat loss rate per unit fuel surface area (kW/m^2) to the surrounding area. L_v is the amount of heat required for volatilization (kJ/kg), or latent heat of gasification. In solid fuel fires, the fuel surface temperature is quite high and there will be considerable heat loss. Hence $\dot{q}_l{}''$ becomes important. In many investigations, it has been shown that the dominant mechanism of transferring heat from the flame to the fuel burner is radiation, especially for large scale fire events and where oxygen concentration is high (Tewarson 1972). Also, for round fuel bed fires, it has been proven that the higher fuel bed diameter, the greater contribution of radiation mechanisms in flame heat transfer (Iqbal & Quintiere 1994; Modak & Croce 1977).

Having calculated the mass release rate ($\dot{m}_{fu}{}''$) in Eq. (2-1), and the heat of combustion, $\Delta \mathrm{H_c}(\frac{\mathrm{kJ}}{\mathrm{kg}})$, one can express heat release rate of the fire ($\dot{Q}$) as:

$$\dot{Q} = \alpha_c\, \dot{m}_{fu}{}'' A_f \Delta H_c \text{ (kW)} \tag{2-2}$$

where α_c and $\mathrm{A_f}$ are, respectively, efficiency of combustion (Tewarson 1982) and fuel surface area (m^2).

$\dot{Q}$ in Eq. (2-2) can be represented as a non-dimensional parameter (Q*) which can be defined as below (Heskestad 2016):

$$Q^* = \frac{\dot{Q}}{\rho_\infty C_p T_\infty \sqrt{gD} D^2} \tag{2-3}$$

in which, $\rho_\infty, T_\infty, C_p, D$ and g are respectively, ambient density (kg/m^3) and ambient temperature (K), specific heat of ambient air (kj/kg.K), fire source characteristic length (m) and gravitational acceleration (m/s^2).

2.2. Plume structure and orientation

2.2.1. Flame and buoyancy

Buoyant plume generally is referred to as the vertical flow movement caused by density gradient. In other words, because of the density gradient, buoyancy force pushes the low-density fluid in opposite direction of gravitational acceleration, while the flow viscous force counteracts this movement.

Generally, buoyant plumes can be classified in weak and strong plumes. The former is generated from weak sources of heat causing low-density gradient, while the latter stems from strong heat sources making large density gradients (Morton 1965). Yet, flow entrainment, involved in buoyant plume phenomena, tends to counteract and decelerate buoyancy effects with increasing distance from the heat source. That is why after a certain height level, a strong buoyant plume starts to turn to a weak one (Morton 1965).

Plumes forming as a result of the fire are strong buoyant plumes in which the temperature is high and the density gradient is considerably strong. Radiation effects are evident in strong buoyant plumes arising from combustion and a remarkable amount of heat can be transferred to the surrounding area via radiation, differentiating between strong fire buoyant plumes and strong buoyant plumes without combustion effects.

Weak fire plumes were investigated by Morton, Taylor, and Turner (1956). Their research was continued by Morton (1959) in which he investigated the momentum dominated plume regime with a relatively high velocity at the source of heat. Investigation of fire buoyant plumes entrainment dates back to 1965 when Morton (1965) extended the existence theory for weak buoyant plumes by exercising some modifications on the existence entrainment rate correlation for weak plumes to be applicable for strong fire plumes whose sources are in high temperatures and density gradients. He characterized fire flame into three regions:

1- The region near the fire source where the temperature is high, buoyancy and radiation effects are dominant. (continuous flame region shown in Figure 2-1)

2- The middle region where there are also high temperatures and buoyancy and radiation effects still play an important role, while negligible combustion reactions occur. (intermittent flame region in Figure 2-1)

3- The region relatively far from the combustion source in which the temperature has decreased and buoyancy tends to get close to weak buoyant plumes. (buoyant plume region shown in Figure 2-1)

According to Ganji and Sawyer (1980), the entrainment rate in a non-reacting mixing layer region is about 30% higher than a reacting mixing layer (flame) and this is mainly because of acceleration of flow due to dilation. They developed an analytical explanation for the entrainment rate of strong buoyant plumes and indicated that it considerably reduces in strong buoyant plumes. This is mainly because it depends on the ratio of the local plume density to the ambient density. They also investigated the radiation behaviors of such huge fire plumes. It should be noted that in turbulent plumes, entrainment is caused by shear turbulence force applied to the surrounding air resulting in the suction of the surrounding air and rising within the plume. In the same vein, Thomas (1963b) showed that there is a relationship between the amount of air entrained into the fire plume and the stoichiometric air volume it needs to burn the fuels. Following that, Morton and Middleton (1973) developed a dimensionless diagram against a parameter indicative of force balance involved in the plume mechanism in which Γ, a parameter characterizing local balance of momentum, volume flux, and buoyant flux, is defined as a function of source volume flux (Q_0), momentum flux (M_0) and buoyancy flux (F_0):

$$\Gamma = \frac{5Q_0^2F_0}{4\alpha_e M_0^{5/2}} \tag{2-4}$$

where α is the constant entrainment coefficient. This way, plumes can be classified as fully-buoyant plumes ($\Gamma > 1$), balanced plumes ($\Gamma = 1$) and momentum dominated plumes ($\Gamma < 1$). Briggs (1975b) and Briggs (1984) investigated plume rise in different atmospheric and environmental conditions and proposed correlations for plume growth in different conditions, based on experimental data. Cetegen, Zukoski, and Kubota (1984) presented relations for fire plume centreline velocity and temperature rise from ambient:

$$u_0 = C_v(gh)^{\frac{1}{2}}{Q^*}_h^{\frac{1}{3}} \tag{2-5}$$

$$\Delta T_0 = C_T {Q^*}_h^{\frac{2}{3}} T_\infty \tag{2-6}$$

in which, h (m) is the flame height, u_0 is the flame centreline velocity, and C_v and C_T are dimensionless constants. Q^* is non-dimensional heat release rate respect to *h:*

$$(Q_h^* = \frac{\dot{Q}}{\rho_\infty C_p T_\infty h^2\sqrt{gh}}) \tag{2-7}$$

Using the basic theory presented in (Morton, Taylor & Turner 1956), Caulfield and Woods (1995) developed a model to be applicable for plumes with non-linear density variation. After that, Sreenivas and Prasad (2000) investigated the other contributing factors affecting the entrainment rate of buoyant plumes as well as plumes caused by a vertical jet flow and demonstrated that using the constant entrainment factor, presented in (Morton, Taylor & Turner 1956), may cause some errors in calculating entrainment rate. These factors include adverse pressure gradient or other body forces that may be applied to some plume regimes. However, Hunt and Kaye (2005) used the constant entrainment coefficient model suggested by Morton, Taylor and Turner (1956) and reshaped their presented conservation equation through introducing three non-dimensional parameters, namely: plume radius, force balance parameter, Γ in Eq.(2-4), and the rate of achieved buoyancy flux with height for plumes with momentum deficiency (lazy plumes) ($\Gamma > 1$). Liu and de Ris (2013) used Kelvin's theorem that vorticity is responsible for pushing the air and oxidant into the flame. Vorticity cascade and kinetic energy translation in buoyant flames have also been investigated.

As noted before, natural fires generally are categorized as buoyancy-driven and diffusion controlled combustion in which air and fuels are mixed, chemical reactions happen and flame appears. In fact, fuel vapor momentum force to buoyancy force ratio determines the type of fire. This ratio is defined as the Froude number (Fr):

$$\mathrm{Fr}_j = \frac{{u_f}^2}{gD} \tag{2-8}$$

in which u_f is fuel injection velocity (m/s). $\mathrm{Fr_j}$ means that the Froude number is determined based on the fuel injection velocity, while $\mathrm{Fr_w}$ is called the modified Froude number (Nmira et al. 2010) which indicates Froude number calculation based on the ambient wind velocity (u_∞):

$$\mathrm{Fr}_w = \frac{u_\infty^2}{gD} \tag{2-9}$$

In natural fires, gas velocity cannot be measured directly, however, if the fuel heat release rate is determined using Eqs. [(2-2) and (2-8)] and assuming that α=1; considering $\dot{m}''_{fu}A_f = \dot{m}_{fu}$ ($\dot{m}_{fu}$ is fuel mass flow rate (kg/s)), it can be expressed as a function of heat release rate [Eq. (2-10)].

$$u_f = \frac{\dot{Q}}{\rho_f A_f . \Delta H_c} \tag{2-10}$$

where ρ_f , is the fuel density (kg/m^3). Thus, Fr can be represented as a function of heat release rate, instead of velocity.

The Richardson number is also an important non-dimensional group representing the effects of thermal expansion, defined as:

$$Ri_x = \frac{g\beta(T_f - T_\infty)x}{U_\infty^2} \tag{2-11}$$

where β is gravitational acceleration, x is the longitudinal distance from the fire surface (m), and T_f is the flame temperature (K) at x.

Combusted flow regimes can be classified in laminar or turbulent flames. When gaseous fuels enter the still atmosphere, the Re number at the proximity of the fuel bed can be used to determine flow regime. According to (Drysdale 2011), source Re number below 2000 provides laminar flow. According to Eq. (2-10), u_f is directly proportional to the rate of heat release rate ($\dot{Q}$) hence, the heat release rate can be considered as an element for specifying the type of flow regime. Moreover, it was depicted that turbulent transition starts from the flame tip where the local Re number gets high enough (Hottel & Hawthorne 1948).

2.2.2. *Flame characteristics of free-standing fires*

2.2.2.1. *Point source fire*

When it comes to characterizing flame geometry, flame length is one of the most important factors to be taken into account. Generally, the area of the plume in which the air is entrained from the surrounding area and makes a combustion reaction with the fuel vapor is considered a flame zone. Thomas and Bowes (1961b) were pioneers in analyzing flame length, which is defined as the length of the zone at which fuel is burning (Thomas, 1963b). Applying an analytical analysis, they presented key factors affecting flame length. Walton and Thomas (2008) made an attempt to present a relationship for flame length in terms of thermo-flow and geometrical characteristics of the flame:

$$\frac{L_f}{D} = f(\frac{\dot{m}_{fu}^2}{\rho^2 g D^5 \beta \Delta T}) \tag{2-12}$$

where L_f and D are respectively flame length (m) and fuel bed diameter. ΔT is the temperature difference of flame and ambient air. Equation (2-12) contains similar parameters existing in the Fr number, as $\dot{m}$ is directly proportional to the flame gas velocity which can also be represented in terms of Q^*, according to Eqs. (2-3) and (2-8).

Heskestad (2016) also presented correlations for fire flame length (*L_f*) for pool fire in still conditions based on experimental data:

$$\frac{L_f}{D} = -1.02 + 3.7\dot{Q}^{*2/5} \tag{2-13}$$

Heskestad (2016) also presented correlations for fire Diffussion flame centreline velocity and temperature profile:

$$u_c = 3.4\left(\frac{g}{c_p \rho_\infty T_\infty}\right)^{\frac{1}{3}} \dot{Q}_c^{\frac{1}{3}} (h - h_0)^{-\frac{1}{3}} \tag{2-14}$$

$$\Delta T_c = 9.1\left(\frac{T_\infty}{g {c_p}^2 {\rho_\infty}^2}\right)^{\frac{1}{3}} \dot{Q}_c^{\frac{2}{3}} (h - h_0)^{-\frac{5}{3}} \tag{2-15}$$

$$b_{\Delta T} = 0.12\left(\frac{T_c}{T_\infty}\right)^{\frac{1}{2}} (h - h_0) \tag{2-16}$$

where u_c is the flame centreline velocity (m/s), $\dot{Q}_c$ is the convective heat transfer rate ($\dot{Q}_c \sim 0.7\dot{Q}$), ΔT_c is the temperature difference between the flame centreline and ambient temperature, h is the height above the fire source (m) and h_0 is the height of virtual origin above the fire source (m). $b_{\Delta T}$ (m) is the plume in a point at which the temperature rise drops to $0.5\Delta T_c$. Beside the radius of the plume, velocity radius b_u can also be defined as the plume radius in a point at which velocity drops to $0.5u_c$. According to Heskestad (2016), there is a relationship between plume radius and velocity radius:

$$b_u \sim 1.1 b_{\Delta T} \tag{2-17}$$

There exist correlations for flame radial velocity and temperature (Heskestad 2016):

$$u_R = u_c \exp\left[-\left(\frac{R}{1.2 b_u}\right)^2\right] \tag{2-18}$$

$$\Delta T_R = \Delta T_c \exp\left[-\left(\frac{R}{1.2 b_{\Delta T}}\right)^2\right] \tag{2-19}$$

2.2.2.2. *Line source fire*

Compared to the investigation of plumes with axisymmetric fuel source, fewer studies have concentrated on plumes arising from fires of line fuel sources. For line source fires, Hasemi and Nishihata (1989) proposed a correlation for flame height (L_f) of the line source:

$$L_f = 0.035\,\dot{Q}'^{\frac{2}{3}}_l \tag{2-20}$$

where,$\dot{Q}'_l$ is the heat release rate per unit length of the line source (kW/m), which in bushfire studies is referred to as bushfire intensity.

Yuana and Cox (1996) presented correlations for temperature rise (ΔT) and velocity profile (u_m) as:

$$\Delta T = \kappa\left(\frac{h}{\dot{Q}'^{\frac{2}{3}}_l}\right)^{2\xi-1} \tag{2-21}$$

$$\frac{u_m}{\dot{Q}'^{\frac{1}{3}}_l} = \eta\left(\frac{h}{\dot{Q}'^{\frac{2}{3}}_l}\right)^{\xi} \tag{2-22}$$

where κ and η are constants, h is the height from the source surface (m) and ξ is 0 for both intermittent ($\frac{1}{2} < \frac{h}{L_f} < 1$) and thermal plume region ($1 < \frac{h}{L_f} < 6$), or $\frac{1}{2}$ for continuous flame ($\frac{h}{L_f} < \frac{1}{2}$).

Eqs. (2-21) and (2-22) were derived for pure buoyant plumes of pool fire of line configuration where there is no forced injection of fuel. Zang et al. (2014) considered the effects of jet fuel momentum and presented correlations for flame length and temperature profile for line source fires. They experimentally developed three separate correlations for continuous, intermittent and buoyant regions of flame length:

$$L_{f-continuous} = 0.0114\,\dot{Q}'^{\frac{2}{3}}_l \tag{2-23}$$

$$L_{f-thermal\,plume} = 0.021\,\dot{Q}'^{\frac{2}{3}}_l \tag{2-24}$$

$$L_{f-intermittent} = 0.0287\,\dot{Q}'^{\frac{2}{3}}_l \tag{2-25}$$

In addition, according to the temperature behavior of the flame, apart from continuous, intermittent and buoyant regions, they added a non-linear region into the category, following the buoyant region (the non-linear region in Figure 2-1). Following that, they developed a correlation for the temperature rise profile of a jet fuel line source:

$$\frac{\Delta T}{T_\infty} = \kappa\left(\frac{z}{z_c}\right)^{\lambda} \tag{2-26}$$

where z_c is the characteristic length for the fire line source and κ and λ are coefficients and vary for

$$z_c = \left(\frac{\dot{Q}'_l}{\rho_\infty C_p T_\infty \sqrt{g}}\right)^{\frac{2}{3}} \tag{2-27}$$

different temperature regions. The corresponding values can be found as below:

Table 2-1 values of κ and λ coefficients for temperature and velocity profile (Zang et al. 2014)

Temperature region	κ	λ
Continuous	3.17	0
Intermittent	5.52	-1.8
Buoyant region (Linear plume)	2.25	-1
Axi-symmetric region	22.8	-5/3

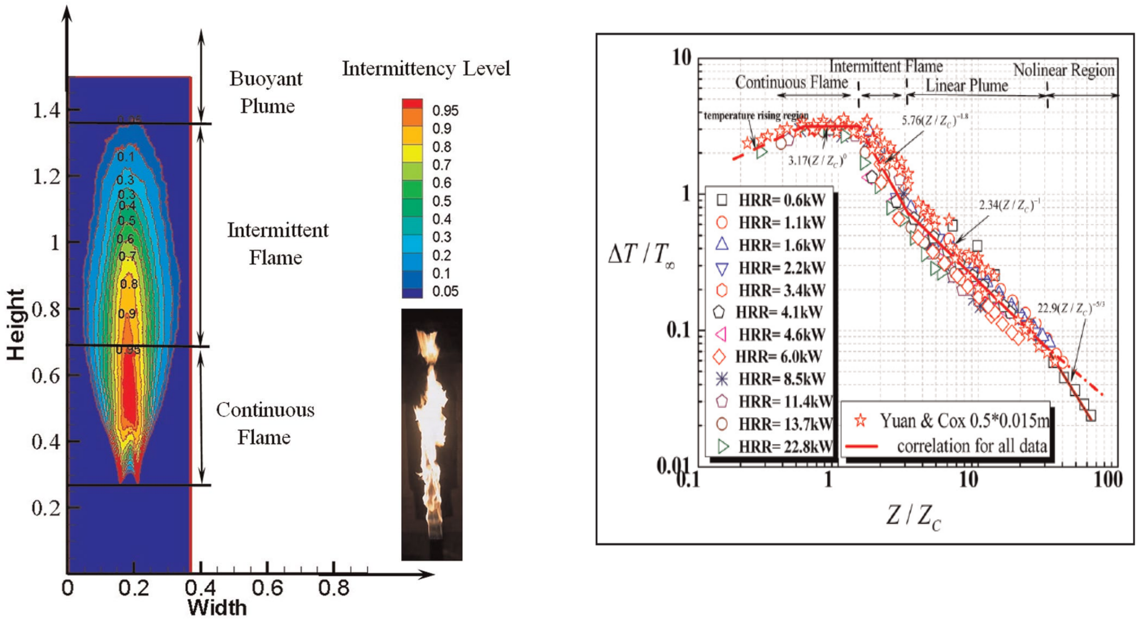

Figure 2-1 Introducing different regions for (a) flame length and (b) flame temperature profile for line source of fire (Zang et al. 2014)

2.2.3. *The effects of wind*

2.2.3.1. *Cross-flow buoyant plume of point source fire*

Wind is one of the main factors significantly affecting the fire tilt angle in fire events in open spaces like bushfire. The level of flame deflection mostly depends on the fire heat release rate as well as wind speed. Wind can tremendously magnify the fire effects on the objects in fire downstream via both an increase in flame's direct contact with objects and growth in the level of radiation effects

(Beyler 2008; Pipkin & Sliepcevich 1964). Several attempts have been made to experimentally investigate the correlation of flame characteristics, fuel-burning rate, and crosswind. Hu et al. (2011) developed a correlation for the burning rate of gasoline in terms of the cross-wind velocity and pool size. In the same vein, Tang et al. (2015) developed a correlation for burning rate and flame tilt characteristics for a cross-wind acetone pool fire. In another study, Hu, Liu and Wu (2013) investigated the impacts of radiation on the burning rate of heptane and ethanol in different cross-wind velocities. In the same domain, a correlation for flame length has been developed correlating flame length to the Froude Number as well as other reactants' properties (Hu, Wu & Liu 2013; Lam & Weckman 2015). In cross-wind fire interaction, the Froude Number is usually defined based on wind velocity (u_w) (Nmira et al. 2010):

$$Fr_w = \frac{{u_w}^2}{gD} \tag{2-28}$$

Recently, Jiang and Lu (2016) demonstrated that the fuel-burning rate of pool fire has a non-linear relationship with cross-wind velocity. They classified the trend of fuel-burning rate in three stages, based on the increase of cross-wind velocity. In low wind velocities (low Fr_w numbers), the burning rate increases with the increase of wind velocities, this is the radiation dominant stage. In the middle stage, both convection and radiation play a role and the burning rate reduces with the increase of cross-wind velocity. For high values of Fr_w , convective heat transfer becomes dominant and the fuel rate starts to increase as cross-wind velocity increases. Drysdale (2011) addressed the flame tilt angle [θ, see (Figure 2-2)] induced by wind. He summarized the flame tilt angle as a general form of

$$\cos\theta = d'(u^*)^{e'} \qquad \text{For } u^* \geq 1 \tag{2-29}$$

$$\cos\theta = 1 \qquad \text{For } u^* < 1 \tag{2-30}$$

in which

$$u^* = {}^{u_w}\!/_{u_c} \text{ if } u_w \geq u_c$$

$$u^* = 1 \text{ if } u_w < u_c$$

in which u_w is the wind velocity and

$$u_c = \left(\frac{g\dot{m}''_{fu}D}{\rho_a}\right)^{\frac{1}{3}}$$

where ρ_a is air density (kg/m^3). d' and e' are constants that have different values for different pool fire fuels. In the same vein, Nmira et al. (2010) used CFD data to develop a correlation for the flame tilt angle of a point source fire under cross-wind conditions.

Hu, Liu, et al. (2013) showed the shortcomings of Eq. (2-29) for some ranges of $u*$. They presented a new mathematical model with the aim to develop a more accurate correlation for the flame tilt angle in wind conditions. They formulated vertical velocity affected by buoyancy based on a non-dimensional analysis. Then they presented a correlation for the tilt angle as the ratio of wind and vertical velocity [Eq. (2-31)]. This takes into account the type of fuel by considering ΔH in the presented formula.

$$tan(\theta) = 9.1\left[\frac{\rho_\infty C_p \Delta T_f u^5}{\dot{m}''_{fu} d^2 \Delta H_c}\cdot\left(\frac{T_0}{g\Delta T_f}\right)^2\right]^{1.5} \tag{2-31}$$

where θ, $\dot{m}''_{fu}$, ΔT_f and ΔH_c are respectively tilt angle, fuel-burning rate, change of flame temperature and heat of combustion. Tang et al. (2016) investigated the effects of cross-wind on the near-wall flame. They proved that flame length and the burning rate will increase in near-wall conditions, compared to the free flame condition. It was also shown that flame length first decreases, then increases and again reduces with the increase in cross-wind velocity.

Experimental studies on large-scale pool fires have been carried out to investigate the effects of cross-wind on flame geometry (Lam & Weckman 2015). It was shown that as wind velocity increases beyond 7m/s, flame length increases significantly. For a wind velocity of 10m/s, the flame becomes almost horizontal.

There have been recent studies unfolding new physics in the interaction of pool fire and wind. A comprehensive review of pool fire-wind interaction has been performed by Hu (2017) in which the pool fire behavior in cross-flow is also reviewed. It reveals that when an external flow with ambient temperature is imposed over a fire, both natural convection from buoyancy and forced convection from the wind play a role in altering the flame shape (Tang, Miller & Gollner 2017). Moreover, a new mathematical model for the flame trajectory under cross-wind has been developed (Zhang et al. 2016). It has shown that in contrast to the previous reports (Hu et al. 2013), the flame trajectory is curved rather than a straight line and more importantly, with their validated numerical model, they prove that when cross-wind velocity is extremely high, the flame trajectory will be completely horizontal.

Using the control volume approach under the forces of buoyancy and viscous wind, Fang et al. (2016) formulated axial acceleration and velocity within flame axis (Figure 2-2). They showed that the axial flow acceleration (a) (m/s^2) and axial flame velocity $[v_f(z)]$ (m/s), can be presented as:

$$a = \left\{\left[\frac{(\rho_\infty - \rho_f)g}{\rho_f}\right]^2 + \left[\frac{(4\rho_w {u_w}^2)}{\pi\rho_f K_G L_f}\right]^2\right\}^{\frac{1}{2}} \tag{2-32}$$

$$v_f(z) = \left\{2\left(\left[\frac{(\rho_\infty - \rho_f)g}{\rho_f}\right]^2 + \left[\frac{(4\rho_w {u_w}^2)}{\pi\rho_f K_G L_f}\right]^2\right)^{\frac{1}{2}} z + {u_0}^2\right\}^{\frac{1}{2}} \tag{2-33}$$

where, K_G is the flame geometry factor, and L_f is the flame length. Their findings showed that when the flame is exposed to cross-wind, there would be an axial flow in the flame region. However, the effects of buoyant plume acceleration on the downstream wind velocity profile were not investigated.

Moreover, their investigation was limited to round fuel sources, rather than a line source which would be closer to a bushfire fuel source.

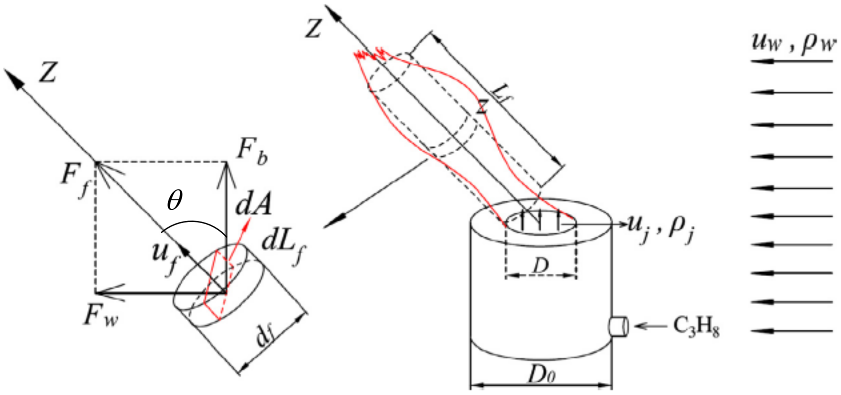

Figure 2-2 Schematic view of the control volume and the acting force, considered by (Fang et al. 2016)

Apart from experimental studies, Nmira et al. (2010) performed a range of numerical simulations to develop correlations for geometrical futures of point source fires under wind conditions.

Using the Froude Number based free-stream wind velocity [Eq. (2-28)] and non-dimensional point source fire heat release rate [Eq. (2-7)], Nmira et al. (2010) developed correlations for flame length [Eqs. (2-34), (2-35)], flame height [(2-36), (2-37)] and flame tilt angle (2-38):
where L_f^* and H_f^* are the flame length and flame height normalized by square point source

$$L_f^* = 2.4\mathrm{Fr}_D^{-0.11} I^{*0.53} \text{ for } 0.024<\mathrm{Fr_D}<0.38 \qquad (2\text{-}34)$$

$$L_f^* = 2.84\mathrm{Fr}_D^{-0.16} I^{*0.85} \text{ for } 0.38<\mathrm{Fr_D}<4.66 \qquad (2\text{-}35)$$

$$H_f^* = 2.04\mathrm{Fr}_D^{-0.20} I^{*0.71} \text{ for } 0.024<\mathrm{Fr_D}<0.38 \qquad (2\text{-}36)$$

$$H_f^* = 1.16\mathrm{Fr}_D^{-0.08} I^{*1.13} \text{ for } 0.38<\mathrm{Fr_D}<4.66 \qquad (2\text{-}37)$$

$$\tan\theta = 2.2 Fr_{z_c}^{0.71} \qquad (2\text{-}38)$$

characteristic length (D), respectively. θ is the flame tilt angle and z_c is the characteristic length for line fire sources [Eq. (2-27)]. All other variables have been defined previously.

Investigation of wind and pool fire interaction is highly applicable to the safety of industrial oil tank fires as well (Lautkaski 1992; Lois & Swithenbank 1979). A theoretical model was developed to characterize temperature and air entrainment in pool fire scenarios in windy conditions (Lois & Swithenbank 1979). The effects of wind on the burning rate of methanol pool fires were investigated and it was shown that flow characteristics are determined by the ratio of momentum to buoyancy force (Richardson number) (Woods, Fleck & Kostiuk 2006). The interaction of a pool fire source with free-stream velocity was also investigated to simulate burning vehicles in tunnels (Gannouni, Zinoubi & Maad 2019; Zhou et al. 2018). However, the majority of these studies are focused on temperature distribution, rather than velocity profile. Moreover, much fewer numbers of studies have been carried out to investigate the opposite effect, that of fire on the wind, or the changes in flow aerodynamics caused by the interaction of cross-flow with diffusion flame. It was experimentally shown that the velocity profile immediately after the fire source is distorted and there is an increase in velocity near the flame zone because of the interaction of free-stream velocity and buoyant diffusion flame (Hirano & Kinoshita 1975). Based on the analysis of experimental data, thermal expansion and low-density in the flame zone were speculated to be responsible for distortion in the velocity profile (Volchkov, Terekhov, & Terekhov 2004).

2.2.3.2. Cross-flow buoyant plume of line source fire

In spite of the significance of the line fire source in bushfire modeling, limited numbers of studies have been performed in line-source fire-wind interaction. Nmira et al. (2010) are among the main contributors in this regard. Nmira et al. (2010) used CFD and pyrolysis modeling to investigate flame geometry features arising from a line fire source subjected to free-stream wind velocity conditions. They considered the Froude Number based free-stream wind velocity [Eq. (2-28)] and normalized fire intensity [Eq. (2-39)] as dominant non-dimensional groups in fire-wind interaction scenarios.

$$I^{*} = \frac{I}{\rho_{\infty} c_{p} T_{\infty} \sqrt{g} D^{(3/2)}} \tag{2-39}$$

in which, U_{ref} (m/s) is reference velocity, I (kW/m) is fire intensity, C_p (kJ/kg.K) is the specific heat of air, D (m) is the fire source depth, υ (m^2/s) is the kinematic viscosity, ρ_{∞} (kg/m^3) is the ambient density, T_{∞} (K) is the ambient temperature and g is the gravitational acceleration (m/s^2).

Using the above-mentioned non-dimensional groups, Nmira et al. (2010) proposed correlations for flame length [Eqs. (2-40), (2-41)], flame height [Eqs. (2-42), (2-43)] and flame tilt angle [Eq. (2-44)] for line fire-wind interaction.

$$L_f^{*} = 2.54 \mathrm{Fr}_D^{-0.14} I^{*0.66} \text{ for } 0.024<\mathrm{Fr}_D<0.38 \tag{2-40}$$

$$L_f^{*} = 3.64 \mathrm{Fr}_D^{-0.16} I^{*0.87} \text{ for } 0.38<\mathrm{Fr}_D<4.66 \tag{2-41}$$

$$H_f^{*} = 1.81 \mathrm{Fr}_D^{-0.20} I^{*0.57} \text{ for } 0.024<\mathrm{Fr}_D<0.38 \tag{2-42}$$

$$H_f^{*} = 1.53 \mathrm{Fr}_D^{-0.31} I^{*1.06} \text{ for } 0.38<\mathrm{Fr}_D<4.66 \tag{2-43}$$

$$\tan \beta = 2.8 Fr_{z_c}^{0.71} \tag{2-44}$$

The implication of enhancement of free-stream velocity with a line fire source can be found in the phenomenon of wind enhancement by bushfire (forest fire or wildfire). That is the increase of local wind velocity by bushfire. Bushfire enhanced wind is believed to be one of the destructive forces in bushfire events. It is generally accepted that the wind can enhance bushfire spread rate as well as flame characteristics (Gould, McCaw & Cheney 2007). In contrast, there is only some anecdotal evidence in the literature to indicate the contribution of bushfire to wind enhancement (Wang 2006). The role of bushfire in wind enhancement has been preliminarily investigated using CFD (Computational Fluid Dynamics) techniques (He et al. 2011a). It has been shown that bushfires can significantly increase near-ground wind as well as pressure load on buildings located downstream of a bushfire front. Coanda or trench effects have been postulated to contribute into enhancement of wind by fire. Coanda effect is the phenomenon of fluid jet attachment to the solid object when the jet enters to a quiescent environment. This happens due to unbalanced flow entrainment near solid surface (Gallacher, Ripa & Butler 2018). This phenomena is postulated to account for the attachment of a plume to the ground immediately downstream of a bushfire front, while further downstream, buoyancy force dominates and eventually lifts the plume above the ground. However, the results presented in (He et al. 2011a) are crude and no information has been reported regarding mechanisms that explain the phenomenon.

2.2.3.3. Cross-flow jet-flow

Fuel injection into cross-flow is an integrated part of many fire scenarios. Therefore, investigating jet in cross-flow structures can fundamentally provide insight into flow characteristics of the injection process. Early fundamental studies in jet in cross-flow shed light on the general dynamics of such flow regimes. Fric and Roshko (1994) classified the vortical structure of vertical jet and cross-flow interaction into four categories (Figure 2-3): (1) Horseshoe vortices which appear upstream of the jet flow and circulate around the jet flow. (2) Wake structures that form in the jet nozzle downstream in the jet wake region. It was shown that the cross-flow boundary layer is responsible for the wake structure. (3) The jet shear layer has ring-shaped structures and appears in the boundary between cross-flow and jet. (4) The vortex structure is a counter-rotating vortex pair (CVP) which is generated in the near field of the jet and then prevails downstream of the jet flow trajectory as shown in Figure 2-3. The more jet to cross-wind velocity ratio, the longer it takes for CVP to form (Mahesh 2013).

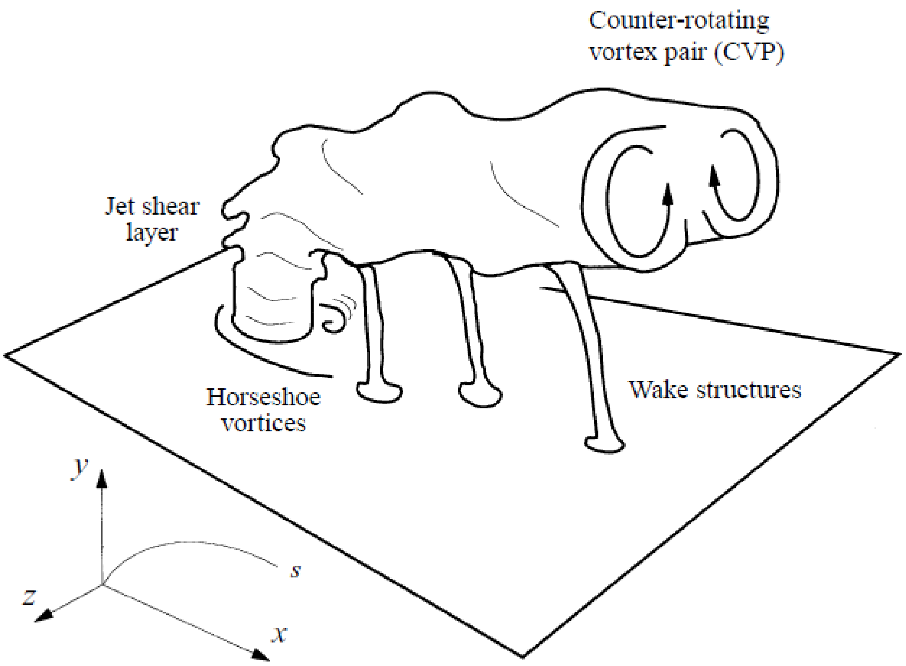

Figure 2-3 Four vertical structures of jet in cross-flow suggested by (Fric & Roshko 1994)

Much research has been conducted to formulate the centerline of jet trajectory. Some researchers quantified jet trajectory based on only the jet diameter (*d*) (Margason 1993), while some others believed that *rd* should be considered as the length scale in the domain (Broadwell & Breidenthal 1984), where *r* is the jet flow velocity normalized with jet cross-wind velocity. Smith and Mungal (1998) experimentally investigated vortical structure and centerline decay concentration in both the near and far regions. Their results showed that jet trajectory suggests *rd* scaling. In another study, Su and Mungal (2004) applied PIV measurement to visualize and determine velocity field for jet in cross-flow velocity fields. They also measured flow turbulent features and showed that while initially the mixing rate is higher in jet windward than the leeward side, eventually the wake front gets a higher value. Muppidi and Mahesh (2007) applied Direct Numerical Simulation (DNS) to investigate turbulence and aerodynamic structures of jet in cross-wind flow. They showed that the flow is devoid of turbulent equilibrium. That is, the ratio of production of turbulent kinetic energy to the kinetic energy dissipation rate along the jet edge is more than 1, while this fraction is less than 1 for the jet centerline. They considered the non-equilibrium nature of jet in cross-flow as the reason for failure of RANS turbulence models in simulating such flow regimes. Concerning the entrainment rate, Mahesh (2013) indicated that the entrainment rate of jet in cross-flow is considerably higher than free shear jet and this is mainly because of the formation of CVP structures in jet in cross-flow regimes.

Shear-layer vortices have an impact on CVP (Cortelezzi & Karagozian 2001). Hence, apart from the dynamic structure of jet in cross-flow, analysis of shear-layer instabilities in jet upstream is worth investigating. Some researchers have reached a consensus that Kelvin–Helmholtz instability close to a jet exit is responsible for the formation of shear-layer vortices (Kelso, Lim & Perry 1996). It was also shown that as cross-wind velocity increases, shear-layer vortices change from low to high frequency as vortices displace across the shear jet downstream (Megerian et al. 2007). The Strouhal Number, $St = \frac{fD}{U_j}$, is used to quantitatively describe shear-layer instabilities, where f is the frequency. Some researchers presented a dominant St number for jet in cross-flow instabilities for an array of conditions (Fric & Roshko 1994; Kelso, Lim & Perry 1996).

2.3. Other characteristics of flame and effect of wind

Apart from flame geometric features such as flame length, flame tilt angle in still air and cross-wind conditions, other parameters such as flame characteristic features under sloped conditions are worth investigating due to the potential significance of terrain slope on aerodynamic flow field.

2.3.1. Flame spread on solid fuel surface

2.3.1.1. Flame spread on horizontal surface

Surface flame spread is referred to as the process of flame movement in the pyrolysis region on surface fuel source (Heskestad 2016). Generally, flame spread on a surface is governed by the heat transfer process at the flame front. Heat transfer processes are contingent upon fuel type and configuration as well as environmental conditions (Heskestad 2016). Hence, material data for a specific case is required to conduct analysis and estimate the flame spread. Fire spread in wind presence has been measured over a horizontal surface (Apt et al 1991). The modes of fire propagation were studied and correlations were developed for flame length in each mode.

2.3.1.2. Effects of slope and wind on flame spread

When it comes to the spread of wildfire, terrain topographic conditions (or site terrain) play an important role. The effect of the slope is one of the key factors controlling the rate of fire spread as well as shaping the flame geometry. Weise and Biging (1996) experimentally investigated the effects of slope on flame length and angle in wind presence and observed the difference of flame orientation and length for different slopes. Viegas (2004) presented a mathematical approach for investigating the effects of slope and wind on the fire front. Dupuy et al. (2011) studied fire behavior in different slope ranges ($0° - 30°$) and different fuel bed widths (1m-3m). They examined the rate of fire spread, fuel consumption, flame residence time, flame geometry and temperatures. It was found that the greater the slope angle and fuel bed width, the higher the rate of fire-induced wind which was considered as the reason behind the increase of fire spread with slope angle. In addition, restricting air entrainment by placing vertical walls on the lateral sides of the upslope fire, they concluded that the presence of lateral walls will significantly increase the fire spread rate. Dupuy and Maréchal (2011), in another study, compared the contribution of different heat transfer mechanisms, radiation, and convection, in up-slope fires. This study showed that in the whole fire region except very close to the fuel bed, radiation is the prevailing mechanism when the slope angle is below 20°. However, when the slope angle increases to somewhat between 20° and 30°, the convective heat transfer mechanism remarkably increases, leading to a growth in fire spread rate. Silvani, Morandini and Dupuy (2012) confirmed that for steep slopes, eventually, convection becomes dominant heat transfer. It was also shown that at a slope angle near 30°, curvature of the fire front shape increases, resulting in changing the fire front from U-shape to V-shape (Figure 2-4). This is mainly because of a growth in formation of whirls rolling the fire front in steep slopes.

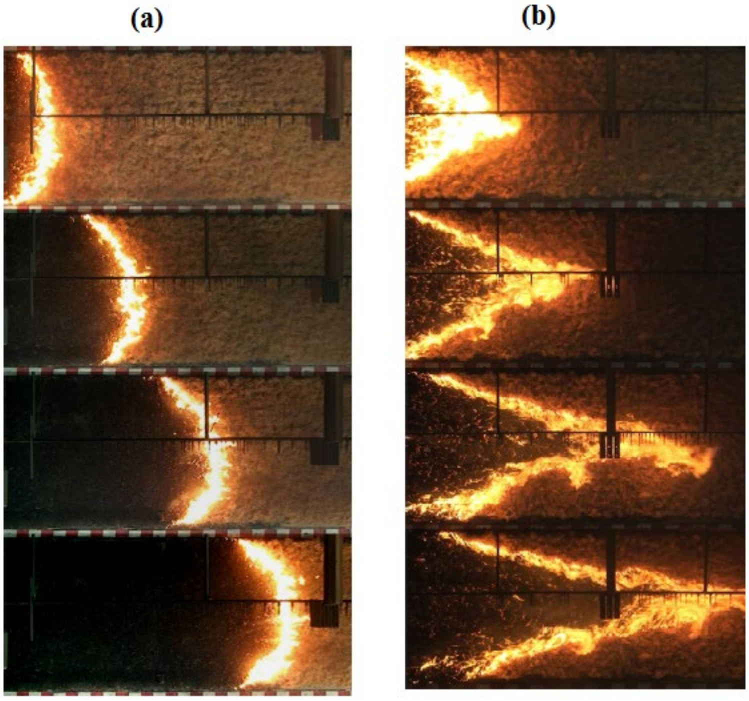

Figure 2-4 Fire front shape under (a) no slope condition with 120s interval (b) slope degree of 30°with 15s interval (Silvani, Morandini & Dupuy 2012)

Using PIV measurement, Morandini et al. (2014) investigated the aerodynamics of upslope fire. The fuel bed is a line source of excelsior with a length of 0.85m and a width of 0.45m. Comparing the fire-induced flow of horizontal fire surface with the 30° sloped surface, they showed that at the center of the flame, the instantaneous velocity of the former fluctuates between 1.3-2.2 m/s, while this value is 1.4-4.1m/s for the latter. Also, it was demonstrated that the fire-induced flow and the flow entrainment for the inclined surface are much higher than the horizontal surface. The higher upward velocity of upslope fire in comparison with the horizontal flame can be clearly seen in Figure 2-5. Note that the *x*-coordinate in Figure 2-5 is the coordinate along the surface.

The effects of slope on fire spread rate under pine needle fuel conditions were also experimentally investigated by (Liu et al. 2014). Flow velocity characteristics near the flame front as well as flame heat flux were measured and investigated. Two flow streams were observed in their experiment. The first stream is weak reverse inflow that appears close to the flame front and the second one is fire-induced upslope wind. The significant difference between these two flow streams was considered as the mechanism for additional flame front forward tilting.

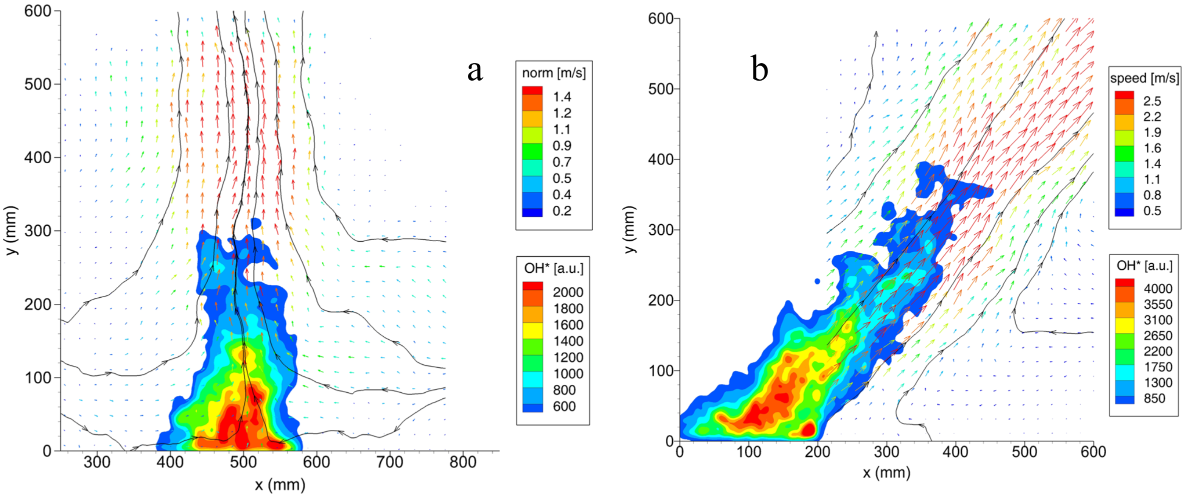

Figure 2-5 time-averaged velocity vector for five consecutive instantaneous velocities for (a) horizontal fire and (b) up-slope fire.

2.3.2. *Flame oscillation*

Oscillatory behavior of buoyant plumes of reacting and non-reacting flows has attracted lots of attention. In early studies, Chamberlin and Rose (1928) fundamentally investigated buoyant plume oscillation phenomena and stated that this is basically because of the time interval taken for air to remove products of the previous reaction and diffuse into the fuel jet to make a new reaction. They also showed that this frequency is independent of burner size and fuel flow rate. Following that, Grant and Jones (1975) moved their research toward higher fuel flow rates and showed that low-frequency flame oscillatory behavior and high-frequency boundary layer instability can occur independently. Cetegen and Kasper (1996) conducted an experimental study to analyze oscillatory behavior of non-reacting helium plumes. Using non-dimensional groups like the Strouhal (St) and Richardson (Ri) numbers, they developed a correlation for the oscillatory frequency of helium plume for laminar and turbulent plume regimes.

In an experimental investigation, Hamins, Yang and Kashiwagi (1992) presented the minimum required velocity for the initiation of pulsation for propane flame. It was also reported that puffing frequency is proportional to the inverse square root of fire source diameter (Hamins, Yang & Kashiwagi 1992; Malalasekera, Versteeg & Gilchrist 1996). Classifying fire flame instability into three categories (short life RT instability, extended RT instability and puffing instability, Hu, Hu and de Ris (2015) quantified the frequency of each category. They showed that compared to puffing instability, extended RT instability frequency possesses a greater value and that the frequency of short life RT instability is higher than that of RT extended instability. Moreover, they demonstrated that extended RT instability is the dominant factor responsible for entrainment phenomena. Recently, Fang et al. (2016) established an analytical analysis for the explanation of the oscillation behavior of diffusion flame with cross-wind. They analytically achieved a correlation for flame puffing frequency in the presence of cross-wind and then validated their derivation with experimental data. The formula they presented takes into account buoyancy, entrainment deceleration, as well as the effects of cross-wind derived for inertial force (cross-wind), and dominated flow regimes ($6\times10^{-5}<Fr< 2\times10^{-2}$). Although their study sheds light on the oscillation features of fire-wind interaction, it is limited to round geometrical fire sources and may not be used for wildfire model application concerns.

2.4. Summary

The presented literature review shows that there are many invaluable experimental and numerical studies in the domain of fire-wind interaction. Most of the previous studies have focused on the effects of wind on fire flame geometric features such as flame length, flame tilt angle and flame height for which correlations were developed based on both experimental and numerical simulations. The effects of fire on flow aerodynamic characteristics, however, have been considerably overlooked in previous studies. The application of the effects of fire on flow characteristics can be observed in fire-wind enhancement phenomena whose fundamental mechanism has neither been investigated nor understood. This thesis study aims at filling the gap in understanding wind enhancement by fire. The objective of this study is to conduct numerical simulations to unravel the mechanisms involved in the enhancement of wind by fire as well as being intended to investigate the effects of potential contributing factors such as wind velocity, fire intensity, fire source configuration and terrain slope on fire-wind enhancement. Moreover, it aims to develop correlations for fire-wind enhancement flow characteristics based on the dominant non-dimensional characteristics. The scope of this study includes numerical simulations of stationary fire sources and no flame spread is concerned.

CHAPTER 3. INVESTIGATION OF FIRE-DRIVEN CROSS-WIND VELOCITY ENHANCEMENT

This chapter provides detailed explanations of the research methodology. A theoretical framework based on Navier-Stokes equations is presented. Further analysis is carried out to identify various force components that help to explain the mechanisms of fire-wind interactions and the enhancement of wind by fire. A module is developed and implemented to the FireFOAM solver to evaluate flow acceleration due to the pressure gradient, gravity, and viscous effects. The developed numerical model is validated against two sets of experimental data, namely, a buoyant diffusion fire plume in still air and another in cross-wind conditions. The strategy for numerical simulations to achieve the three objectives is delineated. The effects of heat release rate of a point source fire on wind enhancement are also investigated in this chapter.

A reprint of this study entitled 'Investigation of fire-driven cross-wind velocity enhancement', **Esmaeel Eftekharian**, Yaping He, Robert H. Ong, Kenny C. S. Kwok, Jianping Yuan, published by the *International Journal of Thermal Sciences*, 2019; Volume 141, Pages 84-95 (https://doi.org/10.1016/j.ijthermalsci.2019.03.033) is appended in Appendix A1.

3.1. Abstract

Understanding the aerodynamics associated with the interaction of fire and cross-wind flow is of great importance because the consequence may have major implications in building design against bushfire (or wildland fire) attacks. However, a fundamental understanding of how the interaction of fire and wind can alter free stream flow aerodynamic properties has remained elusive. The scope of this study is to examine the pool fire and wind interaction under fixed wind velocity condition. This study dissects the fundamental mechanisms of how the interaction of horizontal momentum flow with a vertical buoyant plume leads to enhancement of wind velocity in the horizontal direction at a certain elevation from the base case. Changes in flow aerodynamics caused by the interaction of fire and wind were analyzed using the computational fluid dynamics approach. The mechanisms causing the changes were explained. A module was developed and added to the FireFOAM solver to evaluate flow acceleration due to the pressure gradient, gravity, and viscous effects. The chosen computational model was validated against two sets of experimental data, namely, a buoyant diffusion fire plume in still air and the other in cross-wind condition. The numerical simulation revealed that due to the interaction of fire and wind, there is a negative longitudinal pressure gradient across the plume axis, causing the flow to accelerate and the velocity profile to alter. It was also shown that the distortion in velocity profile depends on the location downstream of the fire plume. The height of the distortion increases whilst the magnitude of the distortion diminishes as the longitudinal distance from the fire source increases. Investigation of the effects of heat release rate on wind enhancement further showed that fire with a higher heat release rate causes a greater pressure gradient and a lower density, culminating in higher flow acceleration and consequently increase of wind enhancement.

KEYWORDS: flow aerodynamics, fire-wind enhancement, flow acceleration, pressure gradient, fire plume.

3.2. Introduction

The interaction of fire and wind has long been a subject of interest. The effects of fire-wind interaction on the spread rate of fire-front were investigated in (Beer 1991; Li et al. 2018; Porterie et al. 2000) and it was demonstrated that wind can significantly increase the spread rate of fire-front in unstable conditions (Beer 1991). The role of convective and radiative heat transfer mechanism in fire spread rate has been experimentally investigated (Orloff, De Ris & Markstein 1975; Quintiere, Harkleroad & Hasemi 1986). Details of flame heat flux characteristics in the flame region have also been experimentally determined (Singh & Gollner 2016). In addition to experimental investigations, computational fluid dynamics have also been used to model fire spread rate (Consalvi, Pizzo & Porterie 2008; Xie & DesJardin 2009). Numerical studies based on Large Eddy Simulation (LES) was used to simulate smoke plumes from the interaction of large pool fires and cross-wind (Baum, McGrattan & Rehm 1994; Wang, Wen & Chen 2014). Extensive numerical works have also been done to effectively modify the combustion model (Chen et al. 2014a) as well as radiative heat transfer and soot modeling in pyrolysis calculation (Fukumoto, Wang & Wen 2018) used in FireFOAM solver.

Direct Numerical Simulation (DNS) was also employed to investigate puffing instability and vortical structure generated during interaction of buoyant plume with free-stream cross-flow (Hattori et al. 2013). A critical Reynolds and Froude number were used to determine thresholds for formation of these structures. Fire-induced flow in enclosures has also been numerically investigated (Tlili, Mhiri & Bournot 2015; Zhou, Sobiesiak & Quan 2006).

Many other studies also have concentrated on the effects of wind on flame characteristics such as geometry including length and tilt angle (Hu 2017; Hu, Wu & Liu 2013; Tang et al. 2016; Tang et al. 2015; Thomas 1963b). Air entrainment mechanism for different fire-wind flow regimes was investigated in (Nelson, Butler & Weise 2012) and an approximation for entrainment velocity in different wind-fire conditions was developed based on the convection number. However, much fewer numbers of studies have been carried out to investigate the opposite effect, i.e., the effect of fire on the wind, or the changes in flow aerodynamics caused by the interaction of cross-flow with diffusion flame. It was experimentally shown that velocity profile immediately after the fire source is distorted and there is an increase in velocity near the flame zone because of the interaction of free-stream velocity and buoyant diffusion flame (Hirano & Kinoshita 1975). Based on analysis of experimental data, thermal expansion and low-density in the flame zone were speculated to be responsible for distortion in velocity profile (Volchkov, Terekhov & Terekhov 2004). It was shown recently, based on an analytical solution for flame acceleration and velocity, that buoyancy force plays a role in flow acceleration of cross-wind (Fang et al. 2016).

Investigation of wind and pool fire interaction is highly applicable to fire safety of scenarios associated with burning industrial oil tank (Lautkaski 1992; Lois & Swithenbank 1979). A theoretical model was developed to characterize temperature and air entrainment in pool fire scenarios in windy conditions (Lois & Swithenbank 1979). It was shown that when multiple fire tanks are subjected to cross-wind, strong fire whirs can be generated causing huge influences on the flow field (Satoh et al. 2011). The effects of wind on burning rate of methanol pool fire were investigated and also it was shown that the flow characteristics are determined by ratio of momentum to buoyancy force (Richardson number) (Woods, Fleck & Kostiuk 2006). The interaction of pool fire source with free stream velocity was also investigated to simulate burning vehicles in tunnels (Gannouni, Zinoubi & Maad 2019; Zhou et al. 2018). However, the majority of these studies focused on temperature distribution, rather than velocity profile. Hence, little information is discernible as to how pool fires affect free stream wind velocity profiles.

The implication of enhancement of free-stream velocity with fire can be found in the phenomenon of wind enhancement by bushfire (forest fire or wildfire). That is the increase of local wind velocity by bushfire. Bushfire enhanced wind is believed to be one of the destructive forces in bushfire events. It is generally accepted that the wind can enhance bushfire spread rate as well as flame characteristics (Gould, McCaw & Cheney 2007). In contrast, there is only some anecdotal evidence in the literature to indicate the contribution of bushfire to wind enhancement (Wang 2006). The role of bushfire in wind enhancement has been preliminarily investigated using CFD (Computational Fluid Dynamics) technique (He et al. 2011a). It was shown that bushfire can significantly increase near-ground wind as well as pressure load on buildings located downstream of bushfire front. Coanda or trench effects were postulated to account for the attachment of plume to the ground immediately downstream of bushfire front, while further downstream, buoyancy force dominates and eventually lifts the plume above the ground. However, the results presented in (He et al. 2011a) are crude and no information was reported regarding mechanisms that explain the phenomenon.

The presented literature review indicates that in spite of a number of studies performed in the domain of wind-fire interaction, the basic understanding of aerodynamic effects of fire on wind requires further investigation, particularly in respect to the enhancement of near-ground wind by fire. Previous works provide invaluable experimental and numerical data into the impacts of buoyant diffusion flame on flow aerodynamics. However, the fundamental reasons as to how the interaction of fire and wind lead to enhancement of wind are unclear. This work aims to fill the gap by providing quantitative and systematic analysis into the factors contributing to distortion of the velocity profile in the interaction of wind and fire scenarios. The main objectives of this study are to provide an insight of flow acceleration during fire-wind interactions and to fundamentally explain how the interaction of horizontal wind and vertical buoyant plume leads to increase of wind horizontal velocity. For this purpose, the flow acceleration is explicitly expressed in terms of contributions from the pressure gradient, body force, and shear stress. The computational fluid dynamics method is used to quantitatively delineate each contribution term.

Bushfire almost always starts with a small ignition source that closely resembles a pool fire and then evolves into a line source of fire. Hence, the first step is to understand pool fire behavior for a given dimension. The fundamental mechanisms governing pool fire-wind interaction are applicable to better understand the mechanisms involved in bushfire wind enhancement phenomenon. Therefore, the interaction between pool fire and wind is the focus of the current study.

3.3. The numerical modeling approach

3.3.1. The modeling software and the governing equations

FireFOAM was used as a CFD solver in this study. This solver is a derivative of OpenFOAM (Greenshields 2015) platform, specifically designed for fire dynamics simulations. OpenFOAM is an object-oriented open-source platform that allows the users to add self-developed modules to the main code. It has been validated with many experimental results including methane diffusion flames (Almeida, Lage & Silva 2015; Wang, Chatterjee & de Ris 2011), methanol pool fire (Sedano et al. 2017) and hydrogen-methane jet fire (Wang et al. 2014). FireFOAM is a transient solver that uses the LES (Large Eddy Simulation) scheme to solve Favre-filtered continuity, momentum, energy, species and state equations for compressible-flow (Wang, Chatterjee & de Ris 2011):

$$\frac{\partial\bar{\rho}}{\partial t}+\frac{\partial(\bar{\rho}\tilde{u}_i)}{\partial x_i}=0 \tag{3-1}$$

$$\frac{\partial(\bar{\rho}\tilde{u}_i)}{\partial t}+\frac{\partial(\bar{\rho}\tilde{u}_i\tilde{u}_j)}{\partial x_j}=\frac{\partial}{\partial x_j}\left[\bar{\rho}(\nu+\nu_t)\left(\frac{\partial(\tilde{u}_i)}{\partial x_j}+\frac{\partial(\tilde{u}_j)}{\partial x_i}-\frac{2}{3}\frac{\partial\tilde{u}_k}{\partial x_k}\delta_{ij}\right)\right]-\frac{\partial\bar{p}}{\partial x_i}+\bar{\rho}g_i \tag{3-2}$$

$$\frac{\partial(\bar{\rho}\tilde{h})}{\partial t}+\frac{\partial(\bar{\rho}\tilde{u}_j\tilde{h})}{\partial x_j}=\frac{D\bar{p}}{Dt}+\frac{\partial}{\partial x_j}\left[\bar{\rho}\left(\alpha_t+\frac{\nu_t}{\mathrm{Pr}_t}\right)\left(\frac{\partial\tilde{h}}{\partial x_j}\right)\right]+\dot{q}'''-\nabla\cdot\dot{q}_r'' \tag{3-3}$$

$$\frac{\partial\bar{\rho}\tilde{Y}_m}{\partial t}+\frac{\partial(\bar{\rho}\tilde{u}_j\tilde{Y}_m)}{\partial x_j}=\frac{\partial}{\partial x_j}\left[\bar{\rho}\left(D_m+\frac{\nu_t}{\mathrm{Pr}_t}\right)\frac{\partial\tilde{Y}_m}{\partial x_j}\right]+\omega_m \tag{3-4}$$

$$\bar{p}=\bar{\rho}R\tilde{T} \tag{3-5}$$

where the superscripts "–" and "~" indicates spatial and Favre filtering. Also, ρ, p, h, Y_m, g, ν, ν_t, D_m, α_t, R, Pr_t, δ and ω_m are respectively, density, static pressure, specific enthalpy, mass fraction of species m in the gas mixture, gravitational acceleration, laminar viscosity, turbulent viscosity, laminar diffusion coefficient, thermal diffusion coefficient, gas constant, Prandtl number, Kronecker delta and production/sink rate of species m due to chemical reaction. The heat release rate per unit volume (W/m^3) from a chemical reaction and the radiation emission intensity (W/m^2) of the gas mixture are represented by $\dot{q}'''$ and $\dot{q}_r''$ respectively.

For ease of explanation, the momentum equation, i.e., (3-2), can be simply expressed in terms of acceleration vector:

$$\vec{a} = \frac{D\vec{u}}{Dt} = \frac{-\nabla p}{\rho} + \vec{g} + \frac{\Phi}{\rho} = \vec{a}_p + \vec{g} + \vec{a}_v \qquad (3\text{-}6)$$

where $\vec{a}$ is flow acceleration, $\vec{u}$ is velocity vector, $\vec{g}$ is the gravitational acceleration vector, and Φ is the viscous shear stress tensor $(\Phi_\mathrm{i}) = \frac{\partial(\sigma_{ji})}{\partial x_j}$ in which σ is the components of stress. The first, second and third term on the RHS (Right Hand Side) of Eq.(3-6) account for the accelerations due to respectively, pressure gradient, gravity, and viscous forces. For simplicity, the three components are referred to as pressure acceleration, gravitational acceleration, and viscous acceleration respectively in the remaining discussions of this paper. The directional components of $\vec{a}$ is presented individually as:

$$a_{ti} = a_{pi} + g_i + a_{vi} \qquad (3\text{-}7)$$

where index i=1, 2, 3 correspond to acceleration in *X*, *Y* and *Z* directions. In the current discussion, we are mainly concerned with velocity and acceleration in the longitudinal direction i.e., i=1.

FireFOAM iteratively solves Eqs. (3-1)-(3-5) to determine the flow prime variables. In order to conduct a quantitative analysis of flow acceleration, a module has been prepared and added to the FireFOAM platform to sort and output individual components of the total acceleration [see Eq.(3-6)] at the end of each iteration cycle.

The kEq model (Yoshizawa 1986) was used to treat sub-grid scale turbulence structures. This model solves a transport equation for sub-grid scale turbulent kinetic energy to model sub-grid turbulent structures.

The combustion simulation is based on the eddy dissipation concept (Magnussen 2005). Simulations of the current study uses Eddy Dissipation Model (EDM) model which assumes that the combustion process is infinitely fast and chemical reaction time scale is negligible compared to the turbulent time-scale. Therefore, turbulent mixing time-scale is controlling the combustion rate. The infinitely fast chemistry and single-step global reaction model was selected to model the combustion process.

Radiation is one of the most challenging parts of fire-related numerical simulations (Viskanta 2008). FireFOAM solves radiative heat transfer equation based on grey gas assumption [Eq.(3-8)], (Vilfayeau 2015).

$$\frac{d\overline{I_r}}{ds} = \overline{\kappa_{ab} I_b} - \overline{\kappa I_r} \qquad (3\text{-}8)$$

in which I_r is the radiation intensity, I_b is the black body radiation intensity ($I_{\mathrm{b}} = \sigma_{\mathrm{r}} T^4/\pi$) and κ is absorption coefficient of the grey gas, s_r is the distance along a special ray and σ_r is Stefan-Boltzmann constant (W/m^2K^4). Grey model assumes that radiation does not change with the wavelength and therefore, κ is replaced by Plank mean absorption coefficient (κ_p).

FireFoam uses finite volume discrete ordinates model (fvDOM) (Chai & Rath 2006) to solve radiation heat transfer equation [Eq. (3-8)]. This model solves radiative heat transfer equation for a discrete number of finite solid angles. Also, it was assumed that the grey model is non-absorbing and non-scattering thin medium. This assumption makes the second term on the right-hand side of Eq. (3-8) zero ($\overline{\kappa_{ab} I} = 0$). Assuming isotropic radiation emission for the flame ($\overline{\kappa_{ab} I_b} = \frac{\dot{q}_r'''}{4\pi}$), Eq.(3-8) will be simplified to Eq. (3-9), (Vilfayeau 2015):

$$\frac{d\bar{I}_r}{ds} = \frac{\chi_{rad}\dot{q}_l'''}{4\pi} \tag{3-9}$$

in which, $\dot{q}_l'''$is the local heat release rate per unit volume and χ_{rad} is the radiant fraction. In this study, radiant fraction of 0.2 was considered as used in previous studies for simulation of methane-diffusion flame (Wang, Chatterjee & de Ris 2011). Finally, the radiant heat transfer source term ($\nabla \cdot \dot{q}_r''$) in the energy equation [Eq. (3-3)] can be calculated by integrating from the right-hand side of Eq. (3-9) in the polar coordinates [Eq.(3-10)], (Vilfayeau 2015):

$$\nabla \cdot \dot{q}_r'' = \dot{q}_r''' = \int \left(\frac{\chi_{rad}\dot{q}_l'''}{4\pi} \right) d\Omega = \chi_{rad}\dot{q}_l''' \tag{3-10}$$

PIMPLE (combined PISO and SIMPLE) algorithm was used to couple velocity and pressure field. Adjustable time step approach was used to keep Courant-Friedrichs-Lewy (CFL) number below 0.6. As for the temporal discretization, the first-order Euler was used. Central differences were used to discretize gradients and diffusive terms, while unbounded Linear-Upwind Stabilised Transport (LUST) scheme was used for the advective terms. Pre-conditioned Bi-Conjugate Gradient (PBiCG) algorithm was used to solve momentum, energy and species and SGS turbulent kinetic energy equations.

3.3.2. *Geometrical model and simulation conditions*

Two computational domains have been separately prepared for a buoyant diffusion (for validating the model) and a cross-wind fire scenario. In the context of this paper, cross-wind means the flow in longitudinal direction that makes the right-angle with vertical buoyant plume. Figure 3-1 displays schematic views of the domains.

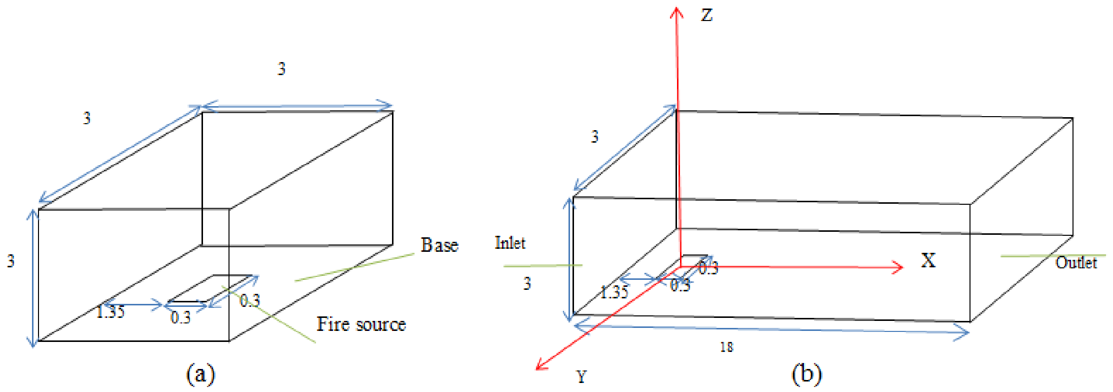

Figure 3-1 Schematic views of the computational domain for (a) validation (b) cross-wind fire scenarios.

For the simulation of the buoyancy diffusion flame experiment by McCaffrey (1979), the domain size in all directions was set at 3 m [see Figure 3-1(a)] and the number of cells in horizontal, spanwise and vertical direction are, 154, 154 and 100, respectively. A non-uniform grid was used to keep the smallest cell size the same as that suggested in (Wang, Chatterjee & de Ris 2011). Similar to (Wang, Chatterjee & de Ris 2011), the burner was simulated by a 0.3×0.3m square placed at the center of the domain. The surface of the burner abutted the base of the domain. The domain boundary conditions for the buoyant diffusion geometry were similar to those suggested by Wang et al. (Wang, Chatterjee & de Ris 2011).

For the simulation of the cross-wind fire interaction scenarios, the domain dimension in *X* direction was extended to 18 m, while other geometrical dimensions, including the fuel bed size, were the same as the computational domain prepared for buoyant diffusion scenarios [see Figure 3-1(b)]. The origin of the *XYZ* coordinate system was set at the center of the fuel bed. Methane was chosen to be injected from the fire source to generate heat release rate (HRR) of 58 kW, 580 kW and 1.16 MW for different scenarios (see Table 3-1). As for the other domain boundaries, outflow and open boundary conditions were prescribed for the domain outlet on the right and the ceiling, respectively. Slip and no-slip boundary conditions were applied respectively to the domain sides and base. To treat the near-wall flow region, the wall function approach (Spalding 1961) was applied. A power law velocity profile was used at the inlet on the left of the domain:

$$U(Z) = U_{ref}\left(\frac{Z}{Z_{ref}}\right)^{\alpha} \tag{3-11}$$

where, U_{ref} and Z_{ref} are, respectively, the reference velocity (6 m/s) and height (3 m), α is determined based on terrain category (here 0.16) (Tominaga et al. 2008). TurbulentInlet boundary condition was prescribed in the domain inlet to consider inflow turbulent fluctuations. This boundary condition uses Vortex method (Mathey et al. 2006) for generating synthetic turbulent fluctuations at the inlet of the computational domain in LES simulations which can be found in previous studies (Montorfano, Piscaglia & Ferrari 2013; Penttinen & Nilsson 2015; Xie et al. 2018).

In the current work, the turbulent intensity of about 11% was implemented at the inlet which produces turbulent intensity of 5% at the target location. We have performed simulations with lower turbulent intensity and no significant changes (less than 7% difference) were observed in wind enhancement which is the main focused parameter in the current study.

The initial temperature was considered to be 300 K, while adiabatic boundary was suggested for the domain base.

Table 3-1. Input parameters for different simulation scenarios.

Simulation Scenario #	Q (kW)	U_{ref} (m/s)	Fire source dimension (m×m)
1	58	3	0.3×0.3
2	580	3	0.3×0.3
3	1160	3	0.3×0.3

3.4. Results and discussion

3.4.1. Grid Sensitivity analysis

For the 3-D simulation of the tunnel fire flow depicted in Figure 3-1 (b), a grid sensitivity study with three different cell numbers of 400 k (coarse), 800k (medium) and 1200 k (fine) was conducted for the Q=580 kW case. In all cases, non-uniform grid was used to generate smaller cells near the burner, resulting in the near-burner cell sizes of 1×10^{-5}m^3, 5×10^{-6}m^3 and 2.5×10^{-6}m^3 for the coarse, medium and fine grid, respectively. Velocity and density profile for different grid sizes were compared as shown in Figure 3-2. The relative mean velocity difference between fine and medium grids was 1.5% while this was 10.5% between medium and coarse grids. The corresponding relative air density difference was 0.78% and 1.69%, respectively. Hence, the medium grid was chosen for this study.

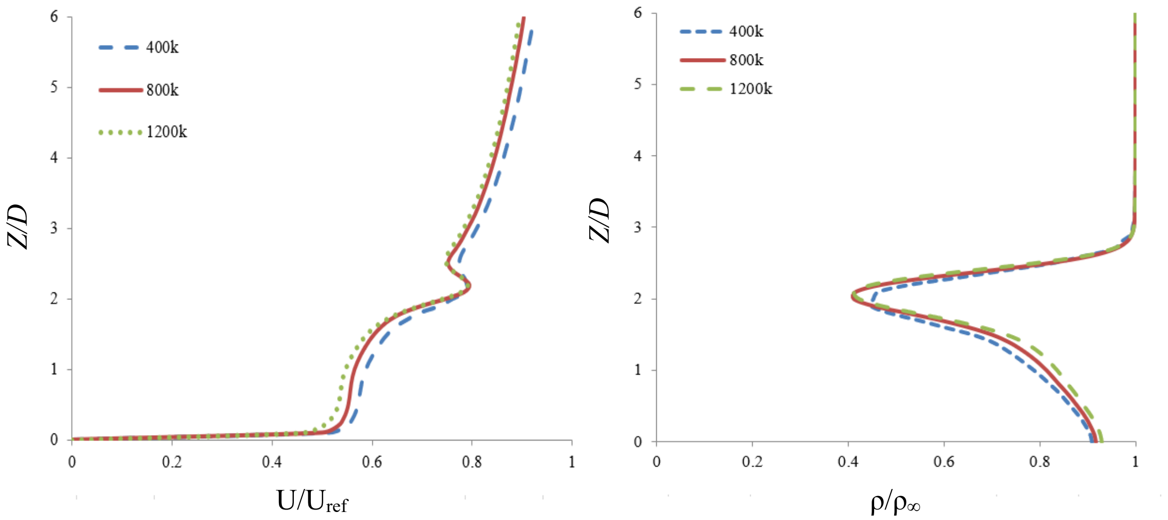

Figure 3-2 vertical distribution of normalized (a) horizontal velocity (b) density for different grid sizes at *X*=6*D* when *Q*=580 kW.

3.4.2. Results of validation

Two sets of experimental data were used to validate the numerical model of the current study. The first experiment involved a buoyant diffusion flame of methane in still air and was performed by McCaffery (McCaffrey 1979). The second experiment was the case of buoyant diffusion flame interacting with free-stream cross-flow reported by Hirano and Kinoshita (Hirano & Kinoshita 1975). In the first benchmarking case, a simulation with a constant HRR of 58 kW was performed and then compared with numerical results of Wang, Chatterjee & de Ris (2011) and experimental data of McCaffrey (1979).

McCaffery's (McCaffrey 1979) experiment was also simulated by Wang, Chatterjee and de Ris (2011) using an early version of FireFOAM. Their total simulation time was 20 s and it took 7 s for the simulation to reach the quasi-steady conditions. They also collected and averaged data during the remaining part of their simulation (13 s). The 13 s includes almost 40 puffing cycles, long enough for at least the convergence of the first order turbulent statistics. The same simulation and average times were used in the current study. The predicted fire plume centreline velocity is plotted in a log-log coordinate in Figure 3-3. which compares the results predicted in (Wang, Chatterjee & de Ris 2011) and measured in (McCaffrey 1979).

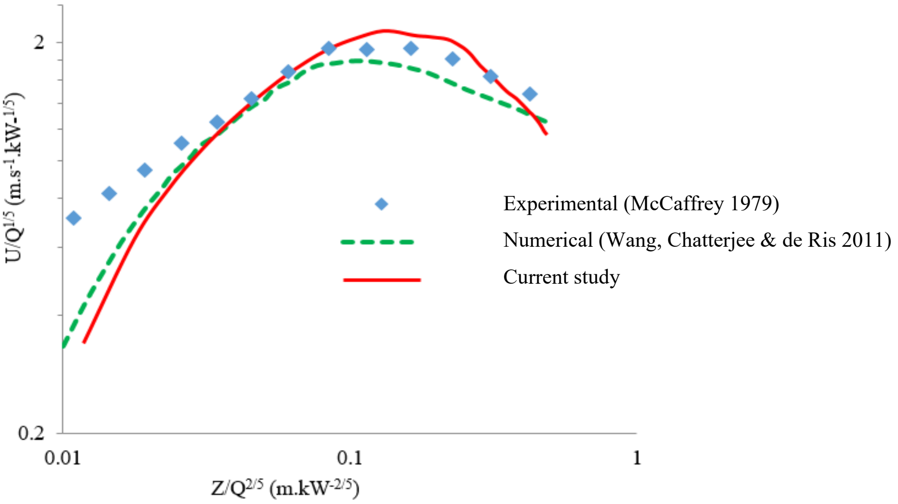

Figure 3-3 Comparison of the normalized centreline velocity profile of the current study with numerical and experimental data available in the literature.

The mean absolute error (MAE) associated with the current study and numerical results reported in (Wang, Chatterjee & de Ris 2011) are 0.156 and 0.179, respectively. MAE is calculated based on the average of absolute difference between experimental data and the corresponding numerical data (MAE= $\frac{\sum_{i=1}^{n}|Uexp_i - Unum_i|}{n}$, $Uexp$ and $Unum$ are respectively the experimental and corresponding numerical velocity and n is the number of experimental data). where These statistics show that in spite of similarities in the geometrical model, boundary conditions and simulation time in the two studies, the current study shows slightly better agreement with the experimental data than the previous study (Wang, Chatterjee & de Ris 2011). The reason might be rooted in the version difference of FireFOAM in the two studies. The older versions of FireFOAM (based on OpenFOAM V.1.7) was used in (Wang, Chatterjee & de Ris 2011). This version of FireFOAM employed the mixture fraction combustion model, whereas, the version used in the current study is based on OpenFOAM V.4.1 which uses eddy dissipation combustion model.

The second numerical model validation was against the experimental data of a steady burning of a liquid-fuel methanol pool in a forced convective environment (Hirano & Kinoshita 1975). The flow velocity and temperature profiles across the laminar boundary layer with a methanol-air diffusion flame were measured in a combustion chamber with 3×9.8 cm (width×height) cross-section and 13.5 cm in length. Figure 3-4. shows the 2-D schematic of experimental setup of Hirano and Kinoshita (Hirano & Kinoshita 1975).

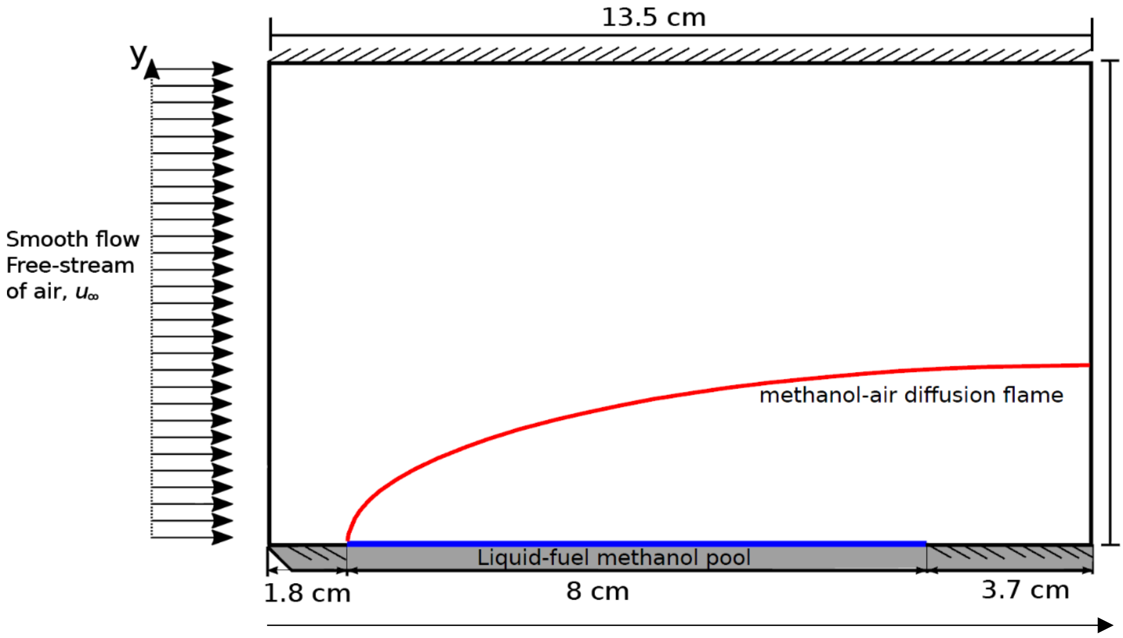

Figure 3-4 Schematic of Hirano and Kinoshita's experimental configuration (Hirano & Kinoshita 1975).

Considering the symmetry in the spanwise direction, a 2-D model was used for validation of cross-wind fire in the current study to solve the mass, momentum, energy, and species equations in Cartesian coordinates as was outlined earlier. Ali, Raghavan, and Tiwari (2010) also used a 2-D approach to validate their numerical model with the experimental data of Hirano and Kinoshita (1975). The computation domain coincides with the chamber boundary. A smooth and uniform fixed velocity of air was imposed at the inlet, while the flow of diffusion flame leaves to the atmosphere at the exit boundary of the domain. Methanol, the same fuel as used by (Hirano & Kinoshita 1975) was injected at the fuel pan for the numerical simulation. A constant temperature of 300 K was set for the initial condition. The pressure outlet boundary conditions utilize the initialization of the pressure field and density. The top and bottom walls were fixed with no-slip velocity conditions and adiabatic conditions for the temperature. The uniform grid of 550×400 cells in streamwise (X) and spanwise (Y) directions was considered to balance the solution accuracy and computational cost.

In Figure 3-5, both the measured and the CFD simulated velocity profiles downstream of the leading flame edge across the boundary layer over the burning liquid methanol revealed the result of flow acceleration or flow enhancement due to the local pressure gradient generated by the local temperature gradient and distortion of the streamline due to the chemical reaction (Hirano & Kinoshita 1975). Furthermore, the aerodynamic structure of the region near the trailing flame edge showing a shift in its shape change and the maximum velocity in this higher velocity region increases with the downstream distance (Hirano & Kinoshita 1975).

Figure 3-6 also compares the measured temperature profile (Hirano & Kinoshita 1975) with the current numerical results at different distances downstream of the fire. Both Figure 3-5 and Figure 3-6 show reasonably good agreements between the current numerical results and experimental data (Hirano & Kinoshita 1975).

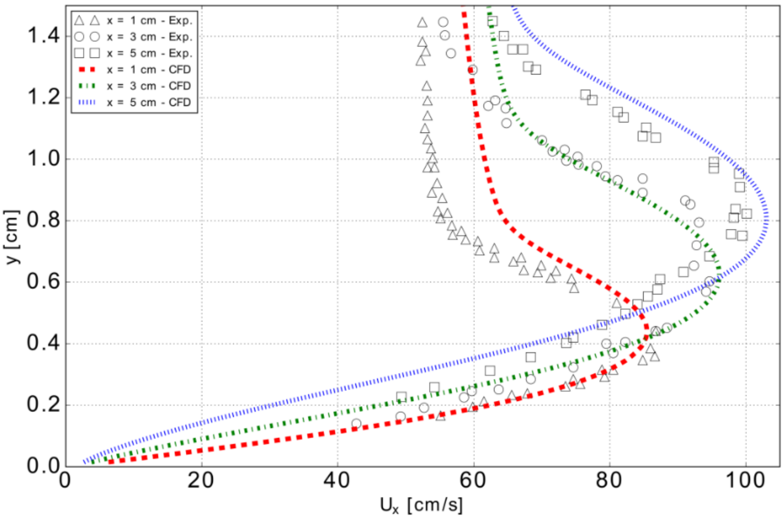

Figure 3-5 Comparison between experiment (Hirano & Kinoshita 1975) and CFD of the velocity profiles taken downstream the boundary layer of methanol-air diffusion flame, $u_\infty = 0.5$ m/s.

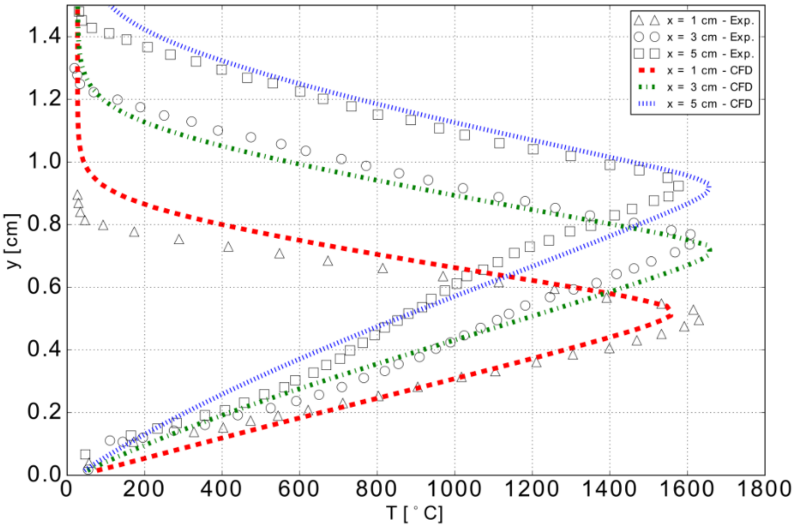

Figure 3-6 Comparison between experiment (Hirano & Kinoshita 1975) and CFD of the temperature profiles taken downstream the boundary layer of methanol-air diffusion flame, $u_\infty = 0.5$ m/s.

3.4.3. *Results of fire-wind interaction*

3.4.3.1. *General description and observation*

Numerical simulations were performed for three heat release rates (58 kW, 580 kW, and 1.16 MW) under the constant free stream velocity of 6 m/s. Tang, Miller, and Gollner (2017) suggest that fire wind interaction scenarios can be divided into three major categories based on the dominant contributing force (i.e, inertia or buoyancy). Richardson number $\left[\mathrm{Ri}_x = \frac{g\beta(T_f - T_\infty)x}{U_\infty^2}\right]$ was used to show that whether the flow is controlled by force convection (Ri< 0.1), mixed convection (0.1<Ri<10), or natural convection (Ri>10). Based on the suggested boundaries for heat and velocity, the results showed that flow regime of all fire-wind simulation scenarios in this study can be considered as mixed convection in which both the effects of buoyancy and inertia are important.

The simulated time period for all flow scenarios was 20s. It took about 7 seconds of the simulated time period for the flow to reach quasi-steady state. Hence, all the presented results in this section are the time-averaged values over the last 13s of the simulated period.

In the presentation of the results, all length dimensions are normalized over the characteristic dimension *D* which is defined as the dimension of the fire source (0.3m).

3.4.3.2. *Velocity and acceleration profile*

Planar distributions of normalized longitudinal velocity at different longitudinal distances are depicted in Figure 3-7. By comparing the free-stream, or ambient, velocity distribution [Figure 3-7 (a)] with that downstream of the fire source [Figure 3-7 (b), (c), (d), (e) and (f)], it is seen that velocity is significantly enhanced at different regions downstream of the fire source. For example, at *X*/*D*=10 the longitudinal velocity has increased by almost 40% in the neighborhood of the plume center [Figure 3-7 (d)], compared to the velocity upstream of the fire source at the same height. It is believed that the mushroom structure being formed initially in the near ground region at each side of the fire source [Figure 3-7 (b)] is due to the Rayleigh–Taylor instability. This mushroom structure grows along the central column further downstream of the fire source and form vortical structures [Figure 3-7 (d), (e) and (f)]. This observation is consistent with those reported in (Hattori et al. 2013; Plourde et al. 2008).

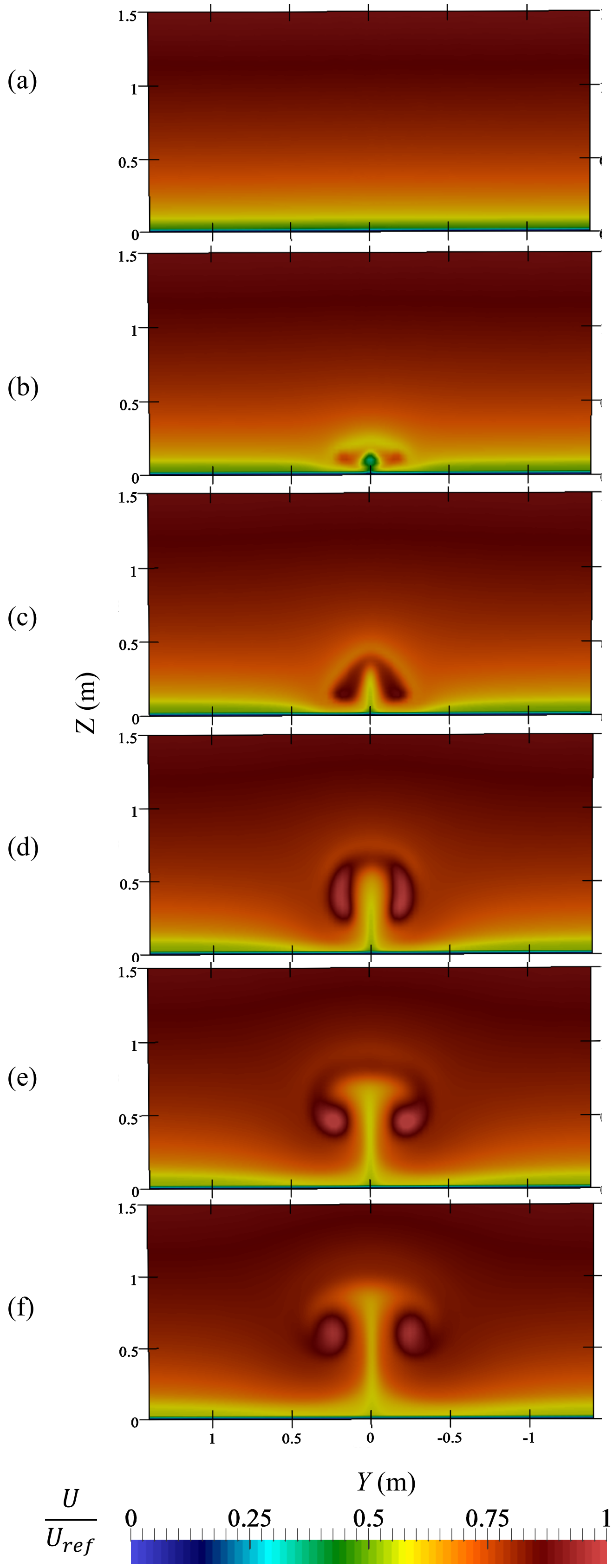

Figure 3-7 Cross-sectional longitudinal normalized velocity ($\frac{U}{U_{ref}}$) at (a) $X/D=-3$, (b) $X/D=3$, (c) $X/D=6$, (d) $X/D=10$, (e) $X/D=13$ and (f) $X/D=16$, for $Q=580$ kW case.

For a detailed investigation of the phenomenon, normalized longitudinal velocity and total acceleration profiles along the domain center plane at various distances from the fire source under the cross-wind condition are plotted in Figure 3-8. Note that the profiles corresponding to $X/D = -3$ are the free-stream profiles. The distortions of the longitudinal velocity vertical profiles downstream of the fire can be clearly seen in Figure 3-8 (a). At $X/D=6$, the velocity profile exhibits a bulge which is encircled at the height of $Z/D \approx 1.2$. This bulge represents the center of the tilted plume and also reveals that the local velocity there exceeds that of the free stream as a result of the enhancement due to the interaction of the cross-wind and the buoyant plume. At the near ground level ($0<Z/D<0.2$), the longitudinal velocity downstream of the fire is also seen to exceed that of the free-stream. As X/D increases, the plume rises from the ground and the location of the bulge in the velocity profile, though becoming weaker, is lifted further.

Under the influence of buoyancy, the fire plume accelerates upwards. The longitudinal wind flow, on the other hand, interacts with the plume, bending it by pressure and viscous force towards downstream. This is indicated by the longitudinal acceleration presented in Figure 3-8 (b) and (c). As observed in Figure 3-8 (b), at all distances downstream of the fire, wind accelerates at two regions: (1) very close to the ground ($Z/D \approx 0.2$) and (2) above the ground at the plume region. At further downstream when $X/D>6$, near ground ($Z/D \approx 0.2$) longitudinal acceleration is dominant, resulting in an increase of wind velocity in that region. All these confirm the observations previously reported in (He et al. 2011a), (Kwok, He & Douglas 2012) and (Hirano & Kinoshita 1975), though the extents of the velocity enhancement are different due to the differences in the simulated fire source configurations. Further downstream of the fire source ($X/D>10$), the longitudinal velocity profiles appear to be lower than that of free-stream for the elevation within the range $0.3<Z/D<4.5$.

During fire-wind interaction, fire buoyant plume acts as a jet blockage against wind and causes formation of wake and low-velocity regions around the domain centreline downstream of the fire source. As shown in Figure 3-9, when wind velocity impinges the buoyant plume, the longitudinal velocity is significantly reduced at the point of impact as well as downstream of the fire align with the domain centreline. The formation of counter-rotating vortex pair (CVP), generated due to interaction of cross-flow with buoyant plume (Hattori et al. 2013; Lin, Zhang & Hu 2018), can be clearly observed in Figure 3-9. Formation of CVP creates a wake region through flow entrainment, reducing the longitudinal velocity along the domain centreline downstream of the fire source. Similar phenomena have also been observed in cross-wind-jet interaction studies (Margason 1993). However, just below and above the plume region [before and after the bulge in Figure 3-8 (a)], flow entrainment is the main cause of flow deceleration and reduction of longitudinal velocity.

The variations in velocity profiles are consistent with variations in the normalized total horizontal acceleration a_{t1} profiles shown in Figure 3-8 (b). For example, at $Z/D=1.2$ for $X/D=6$, the increase in velocity is accompanied by the large acceleration at the same elevation around $Z/D=1$.

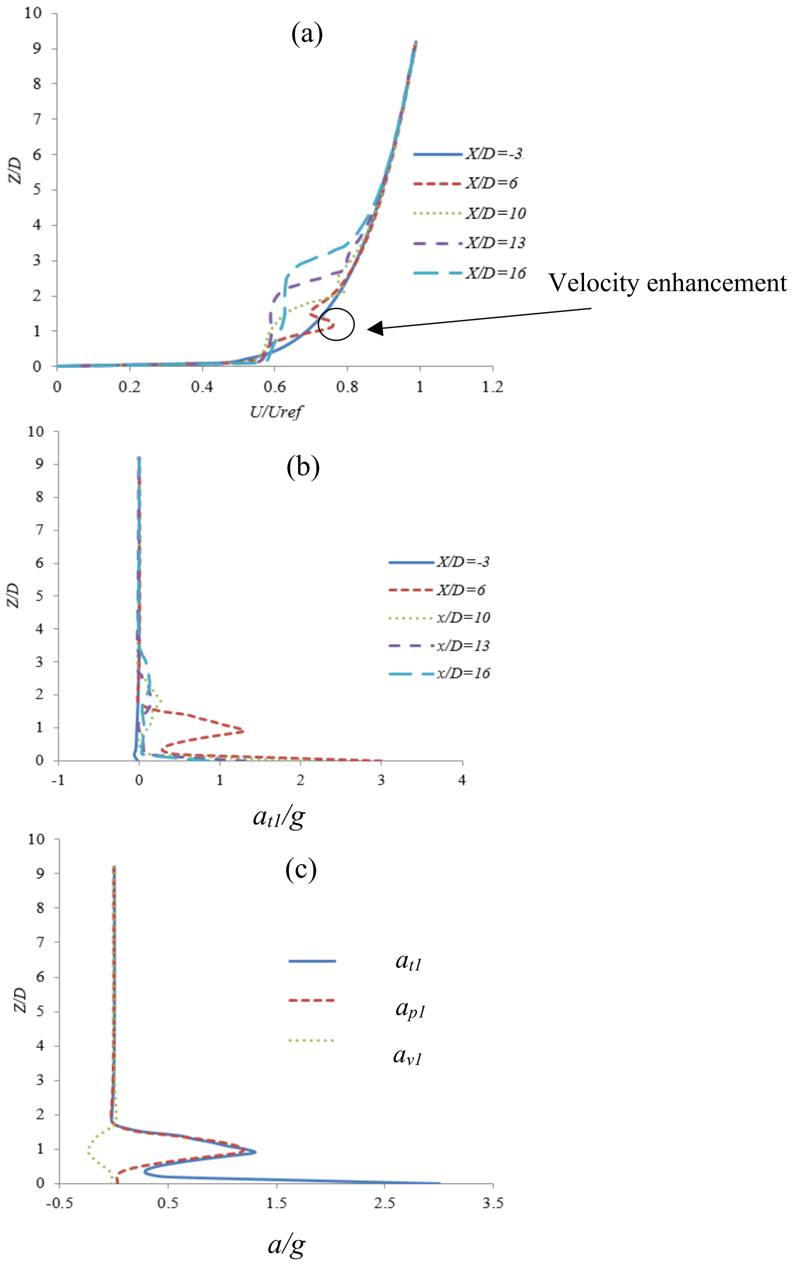

Figure 3-8 Distributions of normalized longitudinal (a) velocity, (b) total acceleration along the domain center plane at various distances and (c) components of acceleration at *X/D*=6, downstream of the fire source for *Q*=580 kW case. The cross-flow reference velocity for all cases is 3 m/s.

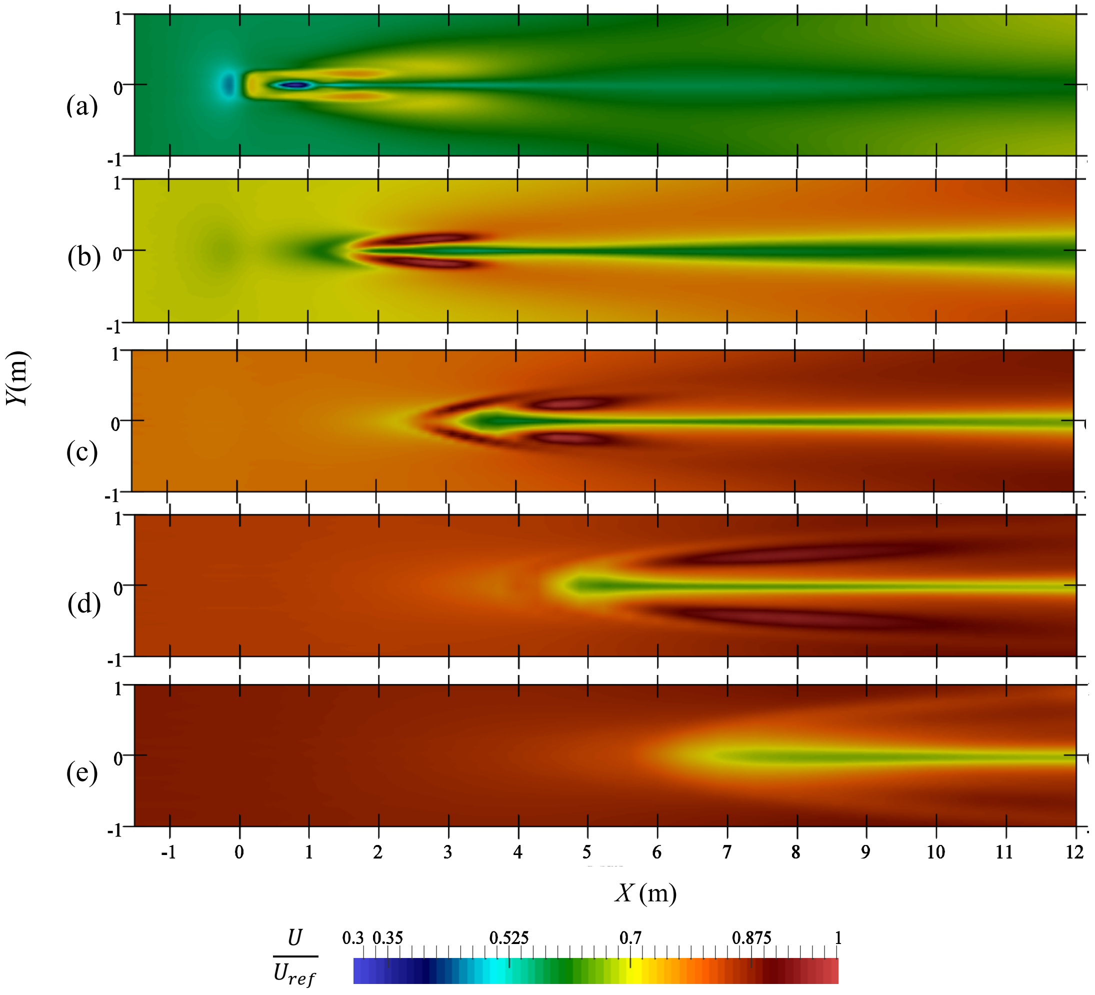

Figure 3-9 Distribution of normalized longitudinal velocity ($\frac{U}{U_{ref}}$)at different horizontal plane: (a) *Z/D*=0.3, (b) *Z/D*=1, (c) *Z/D* =2, (d) *Z/D* =3 and (e) *Z /D* =4 for the case *Q*=580 kW. The cross-flow reference velocity for all cases is 3 m/s.

According to Eq. (3-6), acceleration vector field can be decomposed into three different components, namely, pressure acceleration ($\frac{-\nabla p}{\rho}$), gravitational acceleration (g) and viscous acceleration ($\frac{\Phi}{\rho}$). The vertical distribution of the longitudinal total acceleration and each of the components at the 6*D* distance downstream of the fire source for the *Q*=580 kW case is plotted in Figure 3-8 (c). Gravitational acceleration is non-existent in the longitudinal direction, i.e., g_1=0 and therefore is not shown in Figure 3-8 (c). In the region up to the height of *Z/D*=0.5, because of the dominance of viscous effects in the boundary layer, flow acceleration is only limited to viscous forces. Flow acceleration gradually declined in this region as velocity gradient and correspondingly viscous acceleration reduces with height. This is followed by the dominance of pressure acceleration which experiences a sharp increase, reaching its maximum value at *Z/D*≈1 and then drops to zero at

Z/D≈1.8. In the region above *Z/D*=1.8, total acceleration almost remains zero as there is neither buoyant plume to create pressure acceleration nor shear stress gradient to create viscous acceleration.

Pressure acceleration term is the dominant acceleration component in velocity enhancement region 0.3< *Z/D*<1.5 for *X/D*=6. Immediately downstream of the fire source, because of thermal expansion, the magnitude of longitudinal pressure gradient is high, while density has the lowest value because of high temperature and its value increases further downstream as shown in Figure 3-10 (b). Accompanied by density changes is a gradual reduction in the magnitude of longitudinal pressure gradient as shown in Figure 3-10 (a). Hence, immediately downstream of the fire source, the combined effects of large magnitude of longitudinal pressure gradient and low density create a large acceleration which causes significant distortion of velocity profile as shown in Figure 3-8 (a).

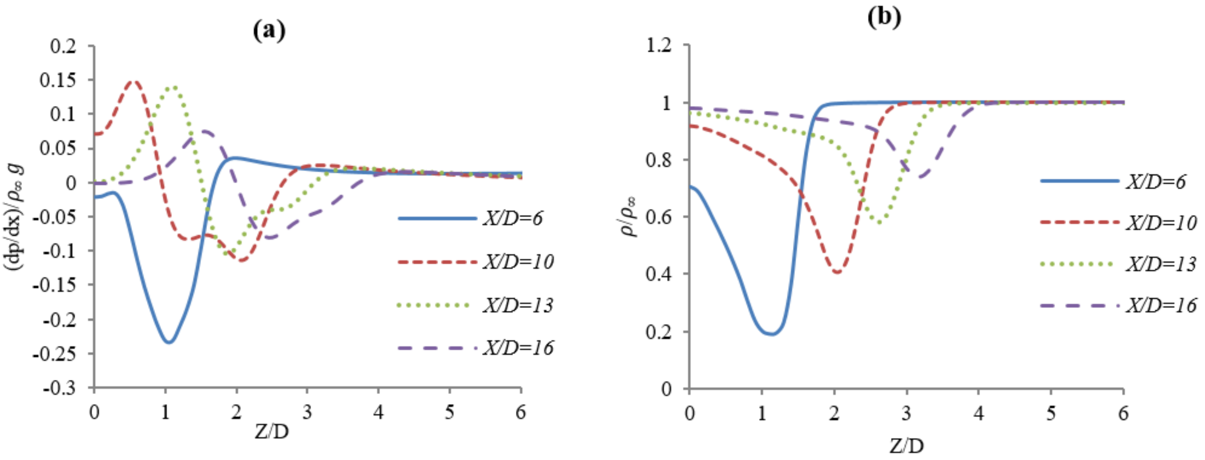

Figure 3-10 Distribution of normalized (a) longitudinal pressure gradient (b) density at different distances downstream of the fire source centreline for *Q*=580KW case**.** The cross-flow reference velocity for all cases is 3 m/s.

3.4.3.3. Sensitivity to heat release rate

Higher heat release rates create greater distortion in the velocity profile as revealed in Figure 3-11. The peak of velocity enhancement or the bulge in the velocity profile also shifts upwards in *Z* direction as the heat release rate increases. Different heat release rates generate different longitudinal pressure acceleration, density, and total acceleration profiles, as shown in Figure 3-12 (a), (b) and (c). Lower density means greater thermal expansion which is associated with velocity increase as shown in Figure 3-11.

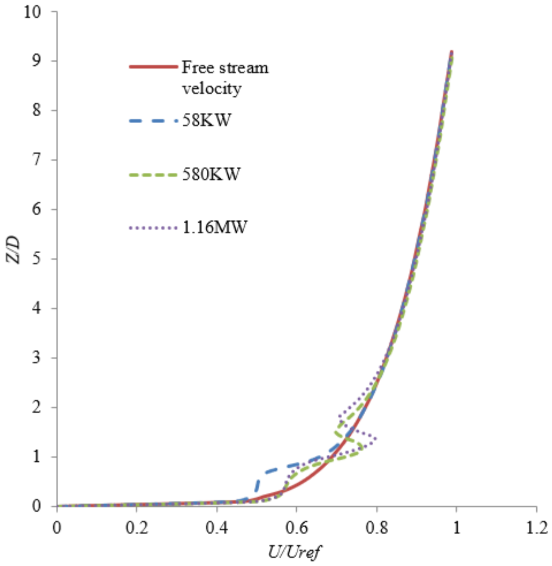

Figure 3-11 Normalised Longitudinal velocity profile at *X/D*=6 for different heat release rates. The cross-flow reference velocity for all cases is 3 m/s.

Figure 3-12 also shows that as heat release rate increases, the peaks in the horizontal pressure gradient, density and consequently acceleration profile move upwards in the *Z* direction. Such shifts are driven by the increased buoyancy force associated with the increased heat release rate.

Negative values of near ground (*Z/D*<2) longitudinal pressure gradient not far downstream of fire source are due to the attachment of the plume to the ground, which prevents or hinders flow entrainment from the region below the plume. However, further downstream of the fire plume, where the plume starts to lift from the ground, it can entrain flow from either side. Hence, in the near ground region, the plume imposes a positive pressure gradient to the surrounded air. This positive pressure gradient increases along with vertical direction up to just underneath the plume region where there exists negative pressure gradient as shown in Figure 3-13 (a).

Figure 3-13 (a) also reveals that the maximum value for the magnitude of the positive longitudinal pressure gradient at the up side of the plume (vertically above the plume) happens immediately after the fire source, while the corresponding maximum value at the downside of the plume (vertically underneath the plume) occurs in further downstream of the fire source where the plume is detached from the ground. This is because initially, plume imposes a positive pressure gradient to the surrounding flow only in the up side of the plume to complete the flow entrainment process. In this region, because plume is attached to the ground, the flow is not entrained from the downside of the plume and therefore all the flow entrainment is only supplied from the plume up side. Hence, the maximum positive pressure gradient for the up side of the plume is observed immediately downstream of the fire. Further downstream, as the plume is detached from the ground, because of the low-velocity in the downside region of the plume, the plume is inclined to entrain flow from this region rather than the up side. Thus, the magnitude of the positive pressure gradient in the region downside of the plume exceeds that in the region above the plume.

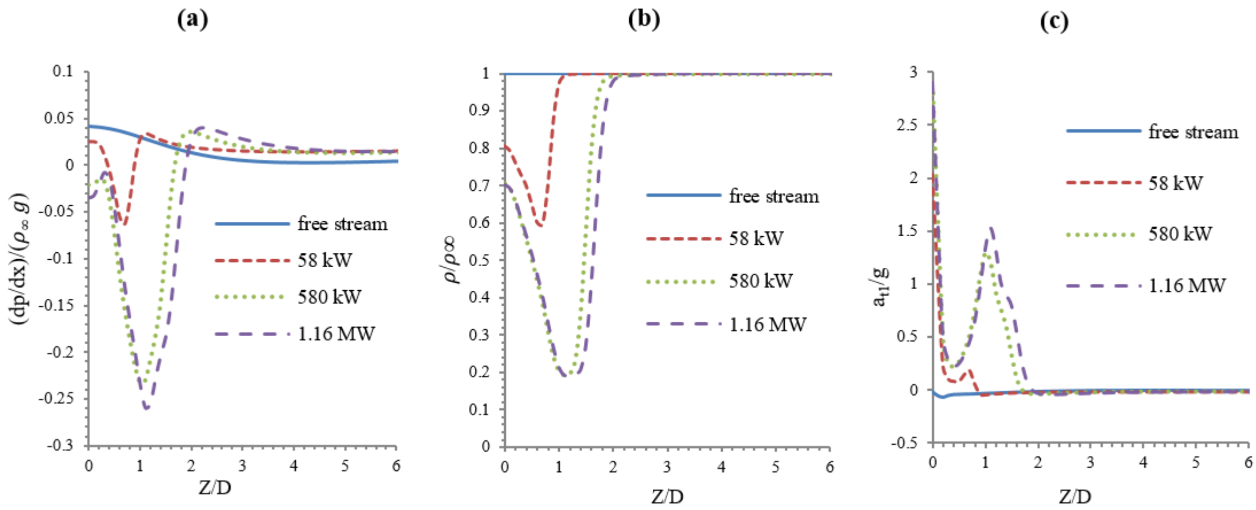

Figure 3-12 Distribution of normalized (a) longitudinal pressure gradient (b) density and (c) total acceleration along a vertical line at *X/D*=6 and free stream for different heat release rates. The cross-flow reference velocity for all cases is 3 m/s.

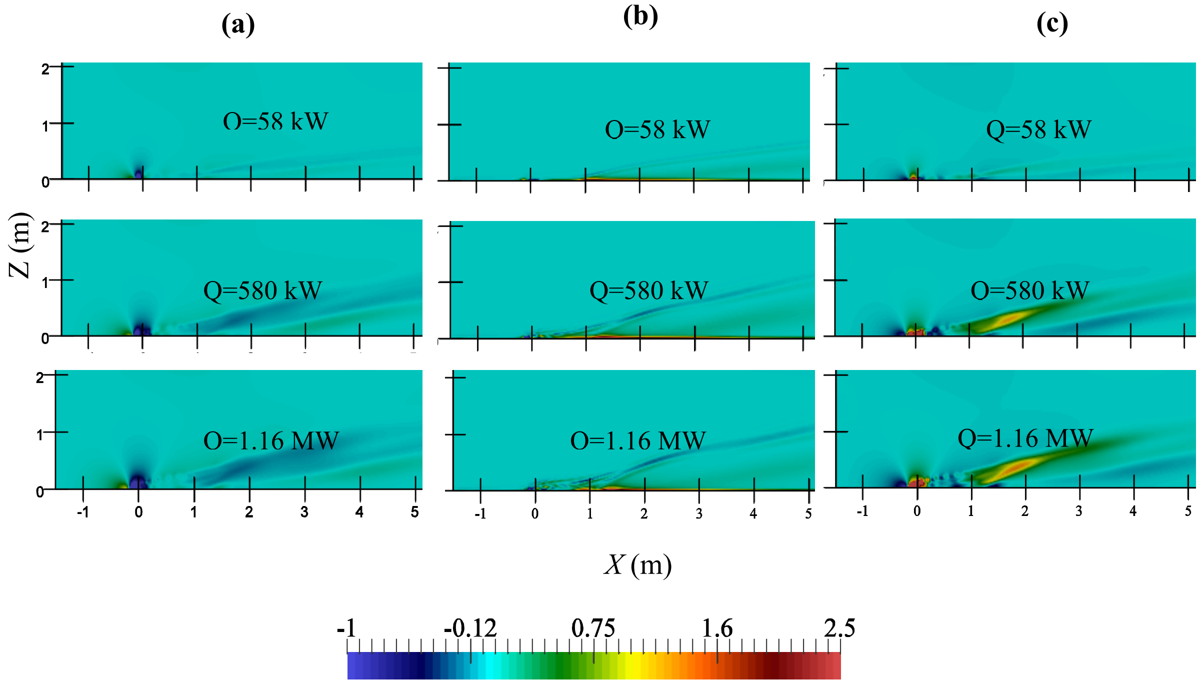

Figure 3-13 Normalised longitudinal (a) pressure gradient $(dp/dx)/(\rho_\infty g)$, (b) viscous acceleration a_{v1}/g and (c) pressure acceleration a_{p1}/g, planar distribution at Y=0 for different heat release rates. The cross-flow reference velocity for all cases is 3 m/s.

During the interaction of cross-wind with fire, viscous forces also undergo changes. As viscous forces in the longitudinal direction increases, correspondingly the longitudinal viscous acceleration increases, as shown in Figure 3-13 (b). Furthermore, the magnitude of longitudinal viscous acceleration increases as the heat release rate increases. This is because the fire changes the turbulent mixing process and increases the turbulent shear stress of the free stream airflow. Along the plume region for all heat release rates, as longitudinal pressure acceleration increases [Figure 3-13 (c)], the magnitude of viscous acceleration also increases [Figure 3-13(b)]. The main reason is that the flow viscous acceleration is correlated with velocity gradient [according to Eq. (3-2)]. Velocity gradient itself is generated due to the pressure acceleration. Consequently, when pressure acceleration increases, viscous forces and correspondingly viscous acceleration increase.

3.4.3.4. Heat release rate effects on flame length

One of the ways to recognize the flame region and length is to plot the distribution of combustion products (e.g CO_2) where the point corresponding to the maximum (threshold) value of CO_2 can determine the flame length (Sedano et al. 2017). The value of CO_2 in different planes was reviewed and it was found that the maximum value of CO_2 occurs at the plane Y/D=0.2, Y/D=0.5 and Y/D=0.7, respectively for the cases Q=58 kW, Q=580 kW and Q=1.16 MW in this study. Hence, the distribution of CO_2 and the normalized longitudinal velocity were plotted in these planes in Figure 3-14. Figure 3-14 (a) shows that the highest value of CO_2 happens at around X=1 m, X=3 m and X=4 m which approximate the flame length for Q=58 kW Q=580 kW and Q=1.16 MW, respectively.

Heskestad (Heskestad 2016) presented a correlation for flame length for pool fire in still condition based on experimental data:

$$\frac{L_f}{D} = -1.02 + 3.7\dot{Q}^{*2/5} \tag{3-12}$$

where L_f is the flame length, D is the characteristic length of square pool (here 0.3). Parameter Q^* is the normalized heat release rate.

$$Q^* = \frac{Q}{T_\infty \rho_\infty c_p \sqrt{g} D^{5/2}} \tag{3-13}$$

where c_p is specific heat at constant pressure.

The flame lengths estimated from the current study are compared with the values determined by Eq. (3-12) and presented in Table 3-2.

Table 3-2. Comparison of estimated flame length

Method	Q (kW)		
	58	580	1160
Without wind, Eq. (3-12)	0.83	2.55	3.46
With wind, CO_2 mapping	0.95	3.04	4.03

As can be seen in Table 3-2, flame length in the presence of wind is slightly higher than that in still condition. This trend is in agreement with the observation reported in (Tang et al. 2016) for a range of strong cross-wind flame interaction.

Figure 3-14 reveals that the flame is attached to the ground and horizontally extended immediately downstream of the fire source. This phenomenon is referred as the flame base drag and has been observed in many previous studies (He et al. 2011a; Hu et al. 2017; Kwok, He & Douglas 2012; Lin, Zhang & Hu 2018; Tang, He & Wen 2019; Tang et al. 2015). Figure 3-14 (b) shows that accompanied by the horizontal flame extension, the enhanced longitudinal velocity region is also horizontally extended immediately downstream of the fire source and then lifts from the ground further downstream.

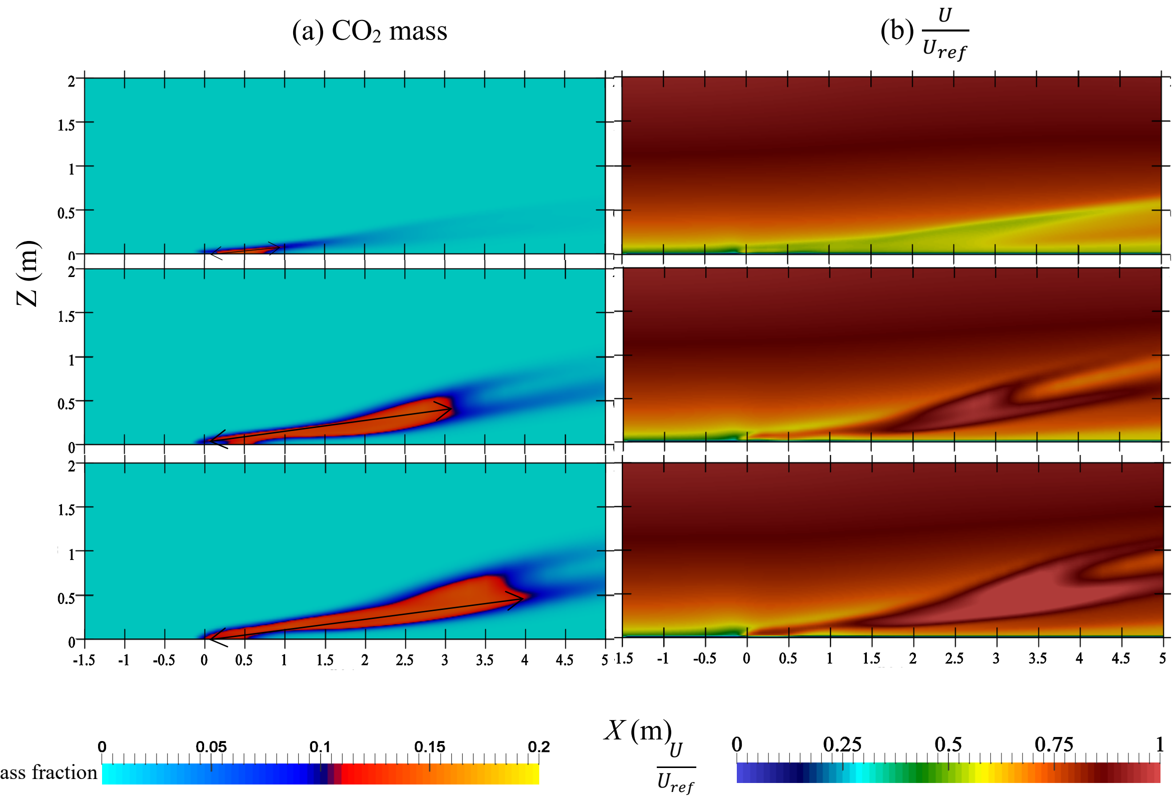

Figure 3-14 Distribution of (a) CO_2 mass fraction and (b) normalized longitudinal velocity ($\frac{U}{U_{ref}}$) at *Y/D*=0.2, *Y/D*=0.5 and *Y/D*=0.7 respectively for *Q*=58 kW, *Q*=580 kW and *Q*=1.16 MW. The cross-flow reference velocity for all cases is 3 m/s.

The flame base drag phenomenon was attributed by some researchers (Welker & Sliepcevich 1966) to the fuel gas density being greater than air. It is noted that in the present study, the fuel gas is methane of which the density is less than air. Therefore, the possible explanation of the flame base drag phenomenon is the Coanda-effect as speculated in (Gould, McCaw & Cheney 2007).

3.5. Conclusions

This paper presents a numerical investigation of the phenomenon of wind enhancement by fire and provides a fundamental explanation of longitudinal wind flow acceleration as a result of actions induced by a buoyant plume. The changes in flow characteristics by the interaction of cross-wind and fire are revealed by examining flow accelerations due to the pressure gradient, gravity and shear stress. Negative longitudinal pressure gradient and low-density values within the plume region are found to act as a driving force to accelerate the flow and cause the wind enhancement downstream of the fire source. It was also revealed that interaction between pool fire and wind in a mixed convection flow regime can increase the horizontal velocity by up to 40%. It is also found that in the near ground region downstream of the fire source, the magnitude of longitudinal acceleration, as well as density difference, increases with increasing heat release rate, leading to a higher flow enhancement. Also, the results reveal that elevation of the peak of enhanced wind velocity increases with the increasing heat release rate of the fire.

The results of the current study support the findings of some previous studies in the sense that interaction of wind and fire can lead to enhancement of wind. However, this study fundamentally investigated the mechanisms involved in the phenomenon.

Although the current study focuses on the pool fires with the finite burning surface area, the outcomes have the implications to the understanding of bushfire wind enhancement phenomenon in the larger scales. Experiments are being prepared in a wind tunnel using a line-source fire to simulate a bushfire front. The results will be used to validate the FireFOAM model and verify the findings of the numerical studies.

CHAPTER 4. NUMERICAL ANALYSIS OF WIND VELOCITY EFFECTS ON FIRE-WIND ENHANCEMENT

In the previous chapter, the mechanisms involved in enhancement of wind with fire were fundamentally studied. The effects of fire heat release rate on enhancement of wind with fire was also investigated. Another important factor contributing to fire-wind enhancement is free-stream wind velocity. Based on the developed theoretical framework in Chapter 3, the effects of upstream wind velocity under constant fire intensity are developed for a point source of the fire. In this study, the Euler number is modified to take into account the fire-induced pressure force. Moreover, the Richardson number and the modified Euler number are employed to determine the influence of free-stream wind velocity and longitudinal distance from the fire source on wind velocity enhancement. This study will also present the details of an LES uncertainty analysis including the resolved fraction of the kinetic energy of turbulence, the ratio of the grid spacing to the Kolmogorov scale and turbulent spectra at characteristic locations.

A reprint of this study entitled ‘Numerical analysis of wind velocity effects on fire-wind enhancement’, **Esmaeel Eftekharian**, Maryam Ghodrat, Yaping He, Robert H. Ong, Kenny C. S. Kwok, Ming Zhao, published by the *International Journal of Heat and Fluid Flow*, 2019; Volume 80, Article number 108471 (https://doi.org/10.1016/j.ijheatfluidflow.2019.108471) is appended in Appendix A2.

4.1. Abstract

Variation in flow characteristics triggered through the fire-wind interface can potentially damage the buildings during bushfires. Fire-wind enhancement which is referred to as the increase of wind velocity, caused by the fire-wind interaction, is one of the destructive phenomena in this regard. In spite of the significance, the underlying mechanism contributing to this phenomenon is still not well understood. This study employs computational fluid dynamic (CFD) simulation to fundamentally investigate the effects of free-stream wind velocity on fire-wind enhancement through analyzing the momentum and buoyancy of fluid. Fire-wind interaction is shown to cause the generation of fire-induced longitudinal negative pressure gradient which results in fire-induced pressure and viscous forces in longitudinal direction. These forces are further found as the prime reason for the distortion of the wind velocity profile. A module is implemented to the FireFOAM solver to calculate and extract these forces quantitatively. The results reveal that under a constant fire intensity, the level of distortion and/or enhancement in the wind velocity profile comparatively reduces with the increase of free-stream wind velocity. A new non-dimensional group (modified Euler number) is introduced to take into account dominant fire-induced forces causing fire-wind enhancement. Richardson number and the modified Euler number are employed to determine the influence of free-stream wind velocity and longitudinal distance from the fire source on wind velocity enhancement. Large-eddy simulation (LES) results indicate that while the level of enhancement generally depends on both Richardson and the modified Euler number, the location of the maximum level of enhancement along the plume centreline coincides with the maximum value of modified Euler number under a constant free-stream wind velocity scenario.

KEYWORDS: Fire-induced forces, Fire-wind enhancement, wind velocity distortion, wind effects, buoyant plume.

4.2. Introduction

Understanding the interaction between fire and wind has always been a significant challenge (Scesa, 1957b; Scesa & Sauer 1954). Several studies have been devoted to the burning behavior of pool fires in wind condition and the effects of wind on flame features (Hirano & Kinoshita 1975; Hu et al. 2011; Hu, Wu & Liu 2013; Kwok, He & Douglas 2010; Meroney 2011; Tang et al. 2015; Thomas, 1963a; Yeoh & Yuen 2009). However, the studies investigating the changes in flow aerodynamics caused by the interaction of wind and fire are very limited. Hirano and Kinoshita (1975) studied the interaction of fire and wind and revealed that the wind velocity profile is deformed immediately after the fire source and the interaction of free-stream velocity and buoyant diffusion flame led to an increase in velocity close to the flame zone. Entrainment regimes and flame characteristics of wildland fires were studied by Nelson, Butler, and Weise (2012). Their research revealed that buoyancy and convection-controlled regimes for line source of fire can be divided into three categories based on the convection number that is defined as the ratio of fire buoyancy force to the free-stream wind momentum force. This number can be used to determine the extent to which flow regime is buoyant or wind dominant. They also presented a correlation between plume tilt angle and the convection number. Detailed analysis by Volchkov, Terekhov & Terekhov (2004) and the experimental results of (Hirano & Kanno 1973) indicate the association of thermal expansion with low-density value in the flame zone accountable for deformation of the free-stream velocity profile.

Wind has been observed to increase the burning rate of pool fires (Tang et al. 2015). A correlation was developed in (Tang et al. 2015) to describe the burning behavior of pool fire within a specific range of cross-wind and it was shown that with the increase of the cross-air flow speed, the enhancement rate of the mass burning rate (The difference between mass burning rate in wind and still condition divided by the cross-wind velocity) was higher for smaller pool fires.

A numerical model was used by Ali, Raghavan, and Tiwari (2010) to investigate the influence of free-stream air velocity on the burning behavior of pool fires. After a 2-D numerical model was validated with experimental data of Hirano and Kinoshita (1975), Ali, Raghavan and Tiwari (2010) focused on fuel mass burning rate, flame stand-off distance, temperature and flow fields behind the fire source. In their study, the flame stand-off distance was considered as a distance from the pool surface to the flame zone center where the temperature has the highest value. Ali, Raghavan and Tiwari's (2010) results showed that with the increase in air velocity, the average fuel mass burning rate increases but the flame stand-off distance decreases. However, the flame stand-off distance and the velocity profile remain almost invariant once the free-stream velocity increases beyond a threshold.

In another study, the effects of fuel exit velocity and cross-flow variation on the radiant fraction of a high-momentum jet flame were investigated numerically (Lawal et al. 2010). The results indicated a good agreement with experimental measurement for the jet-to-cross-flow momentum flux ratio of 100 to 800. Majeski, Wilson, and Kostiuk (2004) developed a theoretical method to relate the length of the flame to the diameter and velocity of the jet as well as cross-flow velocity.

Most recently, analytical studies for flow acceleration and velocity showed that buoyancy force has a significant effect on the flow acceleration of cross-wind (Fang et al. 2016).

Bushfire-wind enhancement phenomenon is one of the most destructive consequences of bushfire attacks. It is well understood that bushfires can be regarded as energy sources which inject thermal energy into the atmosphere and wind can increase bushfire spread rate as well as influencing other flame characteristics (Gould et al. 2007). Field data analysis also indicates that the enhanced wind by bushfire can play a significant role in ember attack mechanism (Wang 2006).

Application of Computational Fluid Dynamics (CFD) models has gained popularity due to the rapid advancement of numerical methods and computational power. For example, large-scale pool fires in the presence of wind have been modeled using computational fluid dynamics approach by many researchers (Sikanen & Hostikka 2016; Sun, Guo & Pareek 2014; Vasanth et al. 2013; Vasanth, et al. 2015, 2017; Wang et al. 2016).

The influence of bushfire on wind enhancement has been studied by Kwok, He and Douglas (2010) using CFD. The outcome of their studies indicated that bushfire significantly intensifies the wind velocity at the near-ground region and considerably escalates pressure load on buildings situated at a certain distance downstream of the bushfire front. Coanda effect was claimed to be responsible for the attachment of plume to the ground immediately downstream of bushfire front, while further downstream, buoyancy force is in control and ultimately lifts up the plume.

Recently, Eftekharian et al. (2019) performed large eddy simulation analysis to fundamentally investigate the enhancement of wind caused by fire wind interaction. It was found that as a result of the interaction of wind with fire, a longitudinal negative pressure gradient is generated in the fire plume region which accelerates the wind and causes wind enhancement. They also revealed that enhancement of wind is intensified with the increase of fire heat release rate. In another study, Eftekharian et al. (2019) investigated the effects of terrain slope on the enhancement of wind by line source of fire and showed that while upslope terrain intensifies wind enhancement, the existence of downslope reduces the effects of fire-induced negative pressure gradient and causes mitigation of fire wind enhancement effects.

A detailed survey of the existing literature reveals that how variation of free-stream wind velocity affects fire wind enhancement still requires further study. This study aims to investigate the effects of free-stream wind velocity on fire wind enhancement by conducting a systematic analysis. The objective of this study is, therefore, to investigate how the distortion in the wind velocity profile, caused by fire, is affected by the upstream wind velocity. For this purpose, the longitudinal forces generated due to the interaction of fire and wind are explicitly expressed in terms of fire-induced pressure and viscous forces.

4.3. Numerical modeling

4.3.1. Simulation method

In the current study, FireFOAM was employed to simulate a series of small-scale buoyant fire plumes with a heat release rate of 580kW. Governing equations (Eq.s 3-1 to 3-5) including continuity, momentum, energy, species and state equations were solved by fireFOAM solver using LES model. More details about governing equations and numerical schemes were provided in Section 3.3.

According to the momentum equation, the force imposed on the infinitesimal fluid parcel is equal to the fluid parcel mass multiplied by the acceleration. Generally:

$$d\vec{F} = \vec{a}dm = \rho\vec{a}d\forall = \rho\left(\vec{a}_p + \vec{g} + \vec{a}_v\right)d\forall \tag{4-1}$$

$$= \vec{f}_p d\forall + \vec{f}_g d\forall + \vec{f}_v d\forall = \overrightarrow{dF_p} + \overrightarrow{dF_g} + \overrightarrow{dF_v}$$

where ρ is density, $\forall$ is volume, $\vec{a}$ is flow acceleration, $\vec{g}$ is gravitational acceleration and f is the force per unit volume.

The flow acceleration in the Eulerian system can be expressed as (based on momentum equation):

$$\vec{a} = \frac{D\vec{u}}{Dt} = \frac{-\nabla p}{\rho} + \vec{g} + \frac{\Phi}{\rho} = \vec{a}_p + \vec{g} + \vec{a}_v \tag{4-2}$$

where $\vec{u}$ is velocity vector, $\vec{g}$ is the gravitational acceleration vector, and Φ is the viscous shear stress vector $(\Phi_i) = \frac{\partial(\sigma_{ji})}{\partial x_j}$ in which σji is the components of stress. The first, second and third terms on the right-hand side of Eq. (4-2) represents the accelerations due to the pressure gradient, gravity, and viscous forces, respectively. The three components are referred to as pressure acceleration, gravitational acceleration, and viscous acceleration respectively hereafter in this paper. Similarly, $\vec{f}_p$, $\vec{f}_g$ and $\vec{f}_v$ are referred to as fire-induced pressure force, gravitational force and fire-induced viscous force. The directional components of $\vec{f}$ and $\vec{a}$ are presented separately:

$$a_{Ti} = a_{pi} + g_i + a_{vi} \tag{4-3}$$

$$\vec{f}_{Ti} = \vec{f}_{pi} + \vec{f}_{gi} + \vec{f}_{vi} \tag{4-4}$$

where index *i*=1, 2, 3 accounts for forces and acceleration in *X*, *Y* and *Z* directions. In the current discussion, the focus is on velocity, force, and acceleration in the longitudinal direction, i.e., *i*=1.

A module has been developed and attached to the FireFOAM platform in the current study to generate individual output components of the total fire-induced forces and acceleration [Eq. (4-2)] at the end of each computational time step.

4.3.2. Geometrical model and simulation conditions

A computational domain with the dimension of 34 m, 9 m, and 15 m has been generated for simulation of cross-wind fire scenarios as shown in Figure 4-1. A square burner with the dimension of 0.3m was placed on the bottom surface 3m downstream of the domain inlet.

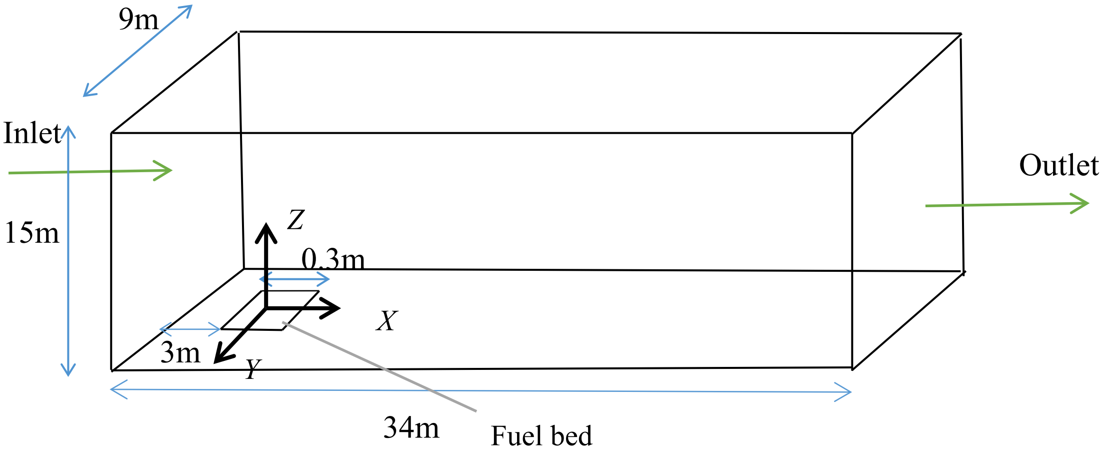

Figure 4-1 Schematic views of the computational domain for the cross-wind and fire simulations.

Cross-wind was specified as the flow entering the domain at the inlet. See Figure 4-1. Methane was selected as the fuel injected from the fire source to produce heat release rate (HRR) of 580 kW for different reference wind velocities (3, 4.5, 6, 7.5 and 9 m/s). A fixed fuel mass flow rate was suggested for the burner in all simulation scenarios to achieve a constant HRR of 580 kW. A summary of different simulation scenarios was shown in Table 4-1.

Table 4-1 Demonstration of different simulation scenarios

Scenario ID (S#)	U_{ref} **(m/s)**	**Ri$_D$**
1	3	1.81
2	4.5	0.84
3	6	0.48
4	7.5	0.33
5	9	0.22

For simplicity, non-dimensional distances are introduced as *X*=X/D*, *Y*=Y/D*, and *Z*=Z/D*, where *X*, *Y*, and *Z* are distances respectively in longitudinal, transverse (spanwise) and vertical directions and *D* is the fire source dimension (*D*=0.3m).

In the study of momentum and buoyancy flow interactions, Richardson number is used to characterize flow regimes as to whether it is a buoyancy or momentum dominant. Richardson number is the ratio of buoyancy and inertial forces (Boirlaud, Couton & Plourde 2012; Fuaad, Baig & Khan 2016) and is used in fire wind flow regimes (Tang, Miller & Gollner 2017):

$$\mathrm{Ri}_x = \frac{g\beta(T_f - T_\infty)x}{{U_{ref}}^2} \tag{4-5}$$

where Ri_x is the local Richardson number, *g* is gravitational acceleration, β is thermal expansion coefficient, T_f is the flame temperature, T_∞ is the ambient temperature, *x* is the downstream distance from the fire source (*x*=*X*-*D*/2) and U_{ref} is the ambient wind reference velocity.

Outflow and open boundary (total pressure) conditions were set for domain outlet on the right and the domain ceiling, respectively. Therefore, the flow can freely get in and out of the domain top surface. The slip and no-slip boundary conditions were applied respectively to the domain sides and base. The adiabatic condition was assumed for the domain base. As for the initial condition for temperature, a constant temperature of 298 K was applied. A power law velocity profile was employed at the inlet on the left of the domain:

$$U(Z) = U_{ref}\left(\frac{Z}{Z_{ref}}\right)^{\alpha} \tag{4-6}$$

where, U_{ref} and Z_{ref} are the reference velocity and reference height (3 m) respectively, the value of power α depends on terrain category (here 0.16). In order to consider turbulent fluctuations in the domain inlet, the “2D vortex method” (Mathey et al. 2006) was utilized.

4.4. Validation and numerical setting

4.4.1. Validation

Validation and the corresponding numerical modelling have been presented in Section 3.4.2 and will not be presented here.

4.4.2. Grid sensitivity analysis

A grid sensitivity analysis with three grid sizes of course, medium and fine was carried out for the simulation scenario #1. The grid sizes were defined as 360 k (50×80×90) for coarse, 2.4 million (127×149×130) for medium and 7 million (197×163×220) for fine. The non-uniform structured grid was used to generate smaller computational cells near the fire source so that the smallest cell takes the volume of 0.000013 m^3 (1.7×2.9×2.5 cm) for the medium case. Figure 4-2 compares the normalized longitudinal velocity and density of simulation #1 for the three grid sizes at $X^*=3$. There is negligible difference between the medium and fine grid for both velocity and density profiles. The average difference ratio of the corresponding velocity between fine and medium cases is 0.32% while this value for the medium and fine case is 7.24%. For the density parameter, the abovementioned values are 0.36% and 7.4%, respectively. Therefore, the medium grid size is chosen for this study.

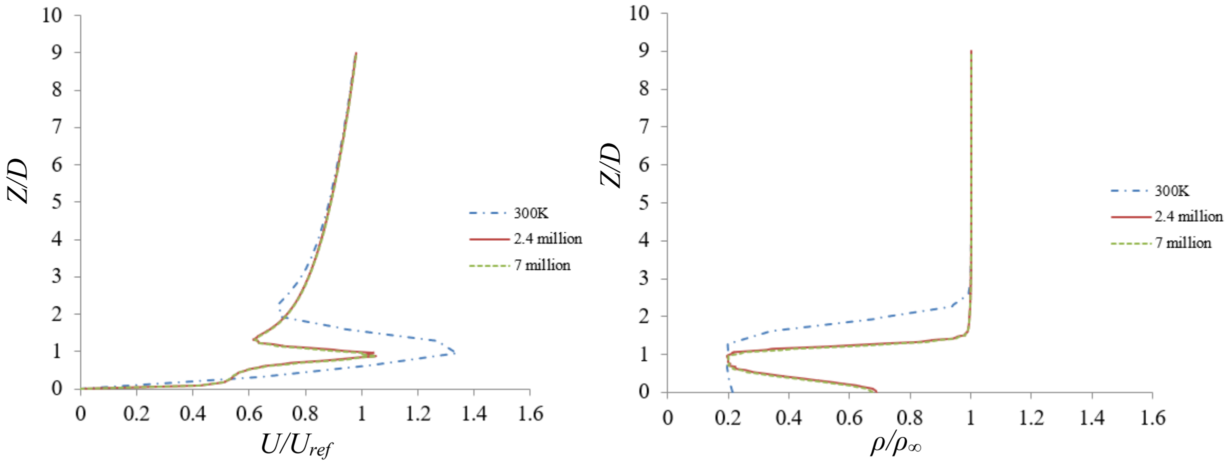

Figure 4-2 Comparison of vertical distribution of normalized time-averaged (a) longitudinal velocity and (b) density at $X^*=3$ for different grid sizes.

4.4.3. Details of LES analysis and uncertainties

In order to check if the chosen (i.e., the medium) grid is fine enough to appropriately resolve a high fraction of turbulent kinetic energy, it is necessary to define turbulent length scale and the corresponding wave number for the flow largest eddies, Kolmogorov length scale and the smallest eddies captured by the grid. The flow largest eddies are limited by the domain physical boundary (Vilfayeau, 2015), here we consider the fire bed width as the characteristic length (0.3m). The corresponding wave number for the physical domain boundary length scale is 20.93 (m^{-1}). Kolmogorov length scale can be calculated by $\eta_k = \left(\frac{\nu^3}{\epsilon}\right)^{(1/4)}$ (Landahl & Mollo-Christensen 1992). The Kolmogorov length scale and the corresponding wave number would be respectively 7 $\times 10^{-4}$m and 8971.42 m^{-1}. The grid spacing is calculated based on the grid size in the plume region: $\Delta = \left(\Delta_x \Delta_y \Delta_z\right)^{(1/3)}$. The corresponding wave number for this grid spacing is 314 m^{-1}. The credibility of LES model for a computational grid depends on the extent to which turbulent structures of large eddies is resolved. In other words, the grid spacing should be fine enough to resolve the dominant eddy structures in the model. The sizes of large eddies are determined based on integral of turbulent length scale. For buoyant diffusion of methane flame in a finite fire source, integral length scale can be approximated based on the fire source width. In Vilfayeau et al. (2016), it was shown that for buoyant turbulent diffusion flames of methane, the results can be considered to be independent of the grid size for $\frac{W}{\Delta} > 12$, where W is the fire source width and Δ is the grid spacing. In our case, this ratio is 15 in the plume region for the chosen grid structure.

Another method to verify the functionality of the LES for a given computational model is to check if 80 % of total turbulent kinetic energy is resolved by the chosen grid for the LES simulation (Pope and Pope, 2000). Figure 4-3 presents the plots of the ratio of resolved turbulent kinetic energy (k_{res}) to the total turbulent kinetic energy ($k_{res} + k_{sgs}$), in which the latter is the summation of resolved turbulent kinetic energy (k_{res}) and sub-grid turbulent kinetic energy (k_{sgs}). Figure 4-3 shows that within the plume region, at almost all distances downstream of the fire source, more than 70 % of turbulent kinetic energy is resolved, except very close to the wall. This is because we used a wall function for near-ground turbulent shear stresses. However, if one focuses on the plume region, the turbulent kinetic energy is satisfactorily (more than 90 %) resolved. This trend is consistent with that reported in Vilfayeau et al. (2016).

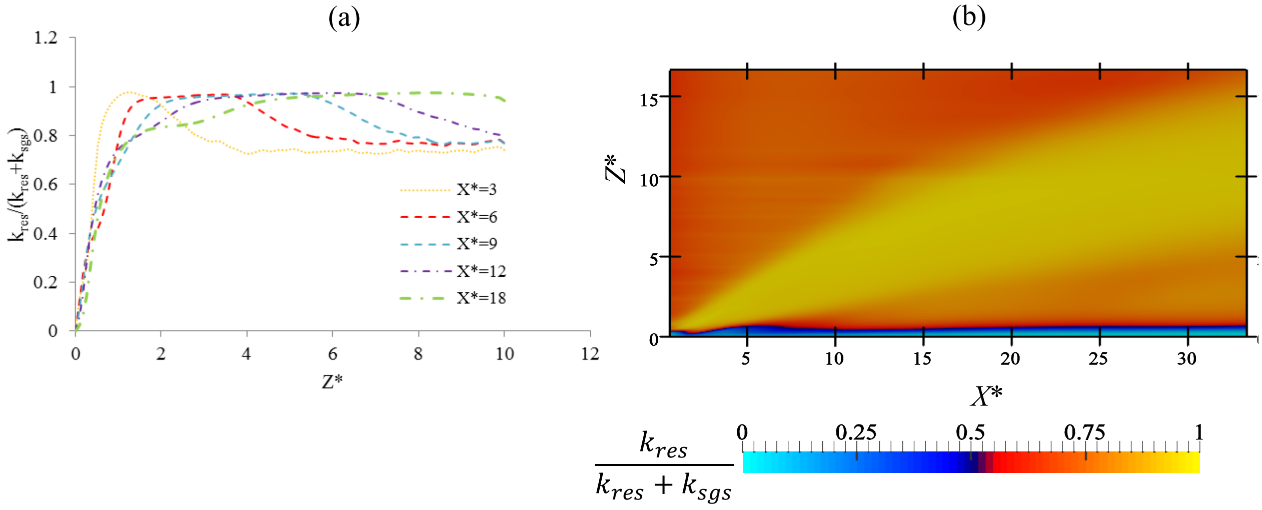

Figure 4-3 Fraction of resolved turbulent kinetic energy $k_{res}/(k_{res}+k_{sgs})$ along domain center plane (Y=0) for S#1. (a) vertical distribution at different distances downstream of the fire and (b) planar distribution.

Power spectra is another important flow characteristic in turbulent flows. Normalized power spectra density of the longitudinal velocity ($nS_{uu}/<U>^2$) along a horizontal line (Y^*, Z^*) = (0, 1.6) at upstream (X^*=-7) and downstream of the fire source (X^*=6) are plotted in Figure 4-4. Here n is the frequency, S_{uu} is the power spectra density. The power spectra and frequency plotted in Figure 4-4 are normalized with the mean velocity (time-averaged velocity) ($<U>$) which is the mean velocity of the point where the data is collected. It is worth mentioning that the chosen point downstream of the fire source ($6D$, 0, $1.6D$) falls within the plume region which is affected by fire. Figure 4-4 shows that the chosen grid size is fine enough to capture the large eddy structures up to the normalized frequency of 10^{-2}. Figure 4-4 also demonstrates the effects of fire on energy content of the spectrum. It is believed that fire increases the velocity fluctuations which lead to the increase of power spectra amplitude by almost two orders of magnitude as shown in Figure 4-4. The highest domain travel time in the simulations is 12s. It should be noted that the first 115 s of the simulation time (which corresponds to at least 10 domain travel cycle) was considered as the transition period and the data were collected in the following 160 s (which corresponds to 14 domain travel cycle) for statistical analysis.

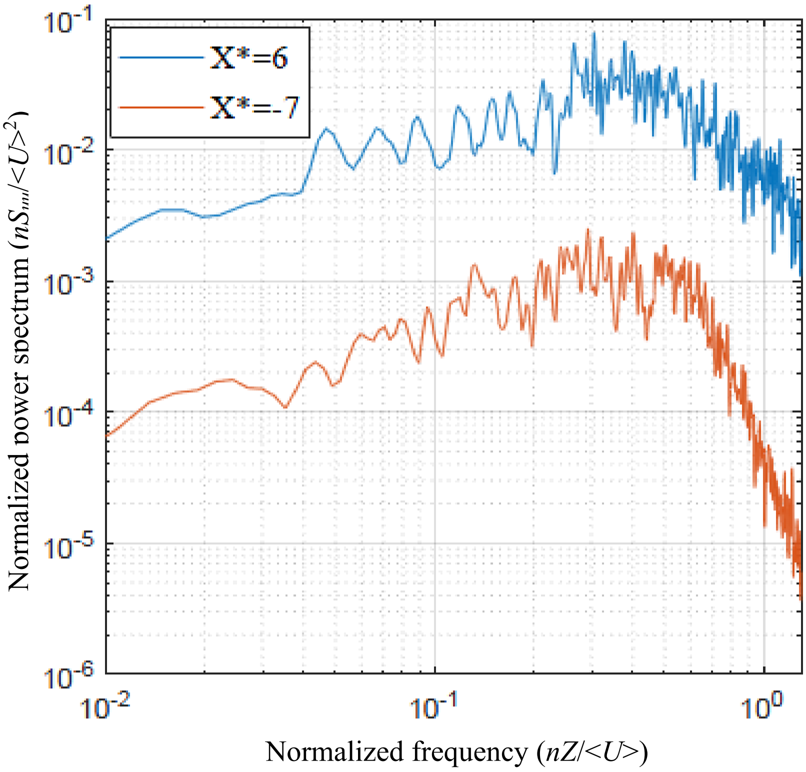

Figure 4-4 Normalised power spectra density of longitudinal velocity on a horizontal line (Y^*, Z^*) = (0, 1.6) at X^*=-7 (upstream of the fire source) and X^*=6 (downstream of the fire source within the plume region) for S#1.

4.4.4. Vortex method and turbulent intensity

Vortex method (Mathey et al. 2006) is shown to be an effective method for generating synthetic turbulent fluctuations at the inlet of the computational domain in LES simulations which can be found in the work of (Montorfano, Piscaglia & Ferrari 2013; Penttinen & Nilsson 2015; Xie et al. 2018).

In the current work, the turbulent intensity is about 11% at the inlet at the height of $Z^*=10$. This, in turn, produces approximately 5% turbulent intensity at the target height location (1*D* upstream of the fire source).

4.5. Fire-wind interaction simulation results and discussion

The findings of this research are presented into two parts. The first part is a fundamental analysis of how fire wind interaction leads to distortion of the wind velocity profile. Furthermore, the effect of wind velocity variation on velocity distortion downstream of the fire is explained. Simulation scenarios with different free-stream wind velocities were performed to investigate the issue. Table. 4-1 contains a summary of the considered simulation scenarios.

The second part of the research investigates how distortion in the wind velocity profile varies in different longitudinal distances downstream of the fire.

All the presented results are based on the time averaging data in the quasi-steady condition.

4.5.1. The effects of fire-induced forces

A comparison between the normalized longitudinal velocities for different wind reference velocities (described in Table 4-1) at $X^*= -3$ and $X^*= 6$ are respectively shown in Figure 4-5 (a) and Figure 4-5 (b). Figure 4-5 (a) includes free-stream ($X^*= -3$) wind velocity profiles for different simulation scenarios. As observed in Figure 4-5 (a), normalized free-stream wind velocity profile for all simulation scenarios are almost identical and therefore, one of these profiles (S#1) is selected for comparison with the longitudinal velocity profile downstream of the fire, as shown in Figure 4-5 (b). Local Richardson number [Eq. (4-5)] has been calculated for all the simulation scenarios as shown in Figure 4-5 (b). The distance x at Eq. (4-5) is $x= X-D/2$. T_f in Eq. (4-5) is the maximum flame temperature at distance the x. Therefore, because of the absence of flame, $Ri= 0$ for all $x^*\leq -1$, or $X^*\leq -0.5$. Figure 4-5 (b) shows that longitudinal velocity is enhanced for the simulation scenarios with the higher Richardson number at the specified x distance. The effects of fire on wind velocity distortion can be vividly observed in Figure 4-5 (b). Figure 4-5 (b) shows that the longitudinal wind velocity decreases in the region very close to the ground before it is subjected to a significant enhancement. Wind velocity undergoes an enhancement in a comparatively thin region above the ground and then experiences a reduction, possessing a lower velocity than the condition where the fire is non-existent (the upstream velocity profile), as shown in Figure 4-5 (b). The wind velocity profile undergoes a distortion due to the presence of the fire. The distorted profile possesses a local peak whose magnitude and vertical location are seen to vary with the local Richardson number. Figure 4-5 (b) also demonstrates that the higher level of velocity enhancement happens in simulation scenarios with a higher Richardson number. The level of enhancement (*LE*) is defined as:

$$LE = \frac{U_f - U_w}{U_w} \tag{4-7}$$

where, U_f is the enhanced velocity at the specific height Z^* and U_w is the corresponding upstream wind velocity. Note that LE is a function of U_∞, Q, X^* and Z^*. $U_f - U_w$ for S#1 is shown in Figure 4-5 (b).

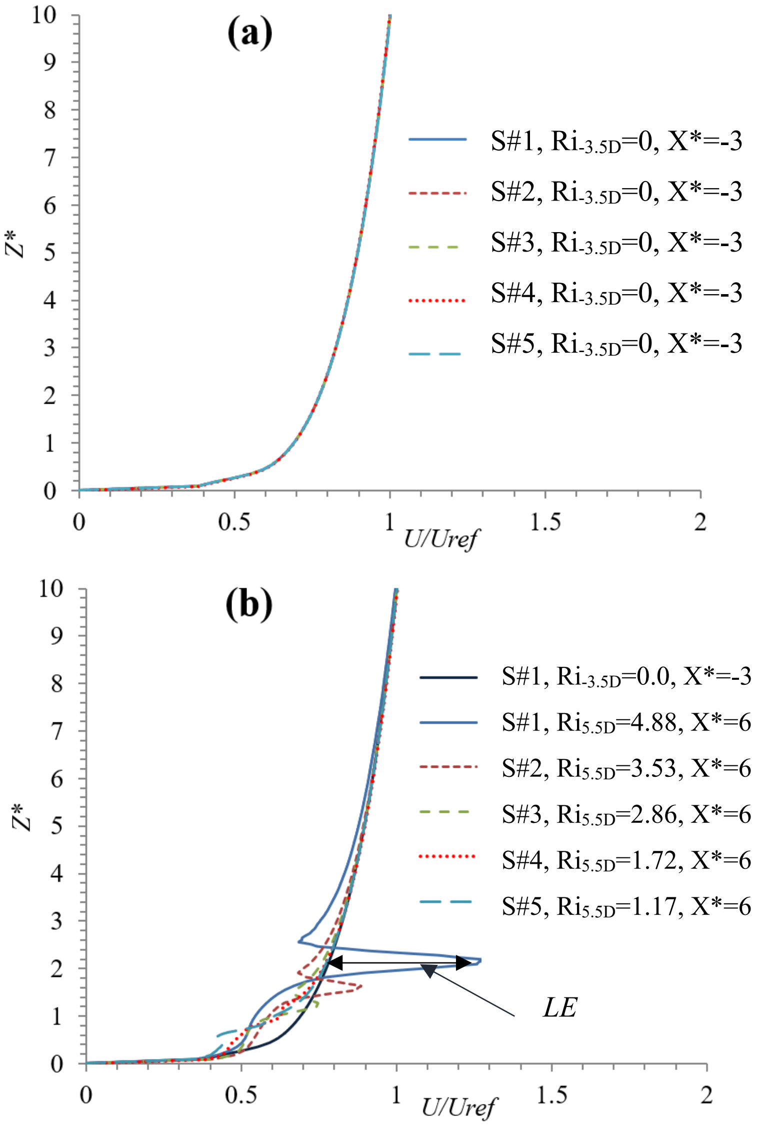

Figure 4-5 Comparison of longitudinal time-averaged normalized velocity profiles at (a) X^*=-3 and (b) X^*=6 for different simulation scenarios.

To explain the observed trend that lower wind velocities undergo a higher variation in the velocity profile subjected to the same fire intensity, it is necessary first to explain the mechanism through which wind is enhanced by fire. Comparison of Figure 4-6 (a) and (b) shows that wind enhancement happens within the plume region where density is comparatively low. This is because due to the effects of buoyancy and thermal expansion, a negative longitudinal pressure gradient is generated along the fire plume, accelerating the flow. Since the interaction between wind and fire causes the fire plume to be tilted towards the downstream direction (as shown in Figure 4-6) a longitudinal component of the pressure gradient is generated, driving the flow in the longitudinal direction. The tilt angle, γ, is defined as the angle between the plume centreline and vertical axis. Plume region can be defined based on the density distribution (Eftekharian et al. (2019)) which includes the area of the domain where the density is comparatively lower than the free-stream density ($\rho \leq 0.5\rho_\infty$ according to Eftekharian et al. 2019). Figure 4-6 shows that although fire-induced pressure force is asymmetry, density distribution shows almost a symmetrical trend. Thus, the plume axis can be defined as an axis passing the plume region centreline as shown in Figure 4-6 (b). This way, the angle between the plume axis and vertical direction can be considered as the plume tilt angle. This longitudinal force imposed on the flow due to the longitudinal fire-induced pressure gradient is referred to as “fire-induced longitudinal pressure force” in the reminder of this chapter. In other words, as a result of the fire wind interaction, flow accelerates within the plume region and causes an increase of flow momentum in the longitudinal direction that culminates in wind velocity enhancement, as shown in Figure 4-6 (a), (b) and (c). Fire or a heat source induces the buoyancy force in the vertical direction only. Fire-induced force in the longitudinal direction is the ensemble effect of the rise of the fire plume and the deflection of it due to the wind. This component appears in the form of pressure and viscous force. The fire-induced pressure force happens due to the pressure gradient generated in the fire plume as shown in Figure 4-6 (c). The pressure gradient along the longitudinal direction accelerates the flow longitudinally. Based on Eq.(4-2), this longitudinal acceleration is also reciprocally proportional to flow density. Therefore, since in the plume region density is low and fire-induced pressure force is high, in all considered scenarios, the highest distortion in the velocity profile appears within the plume region.

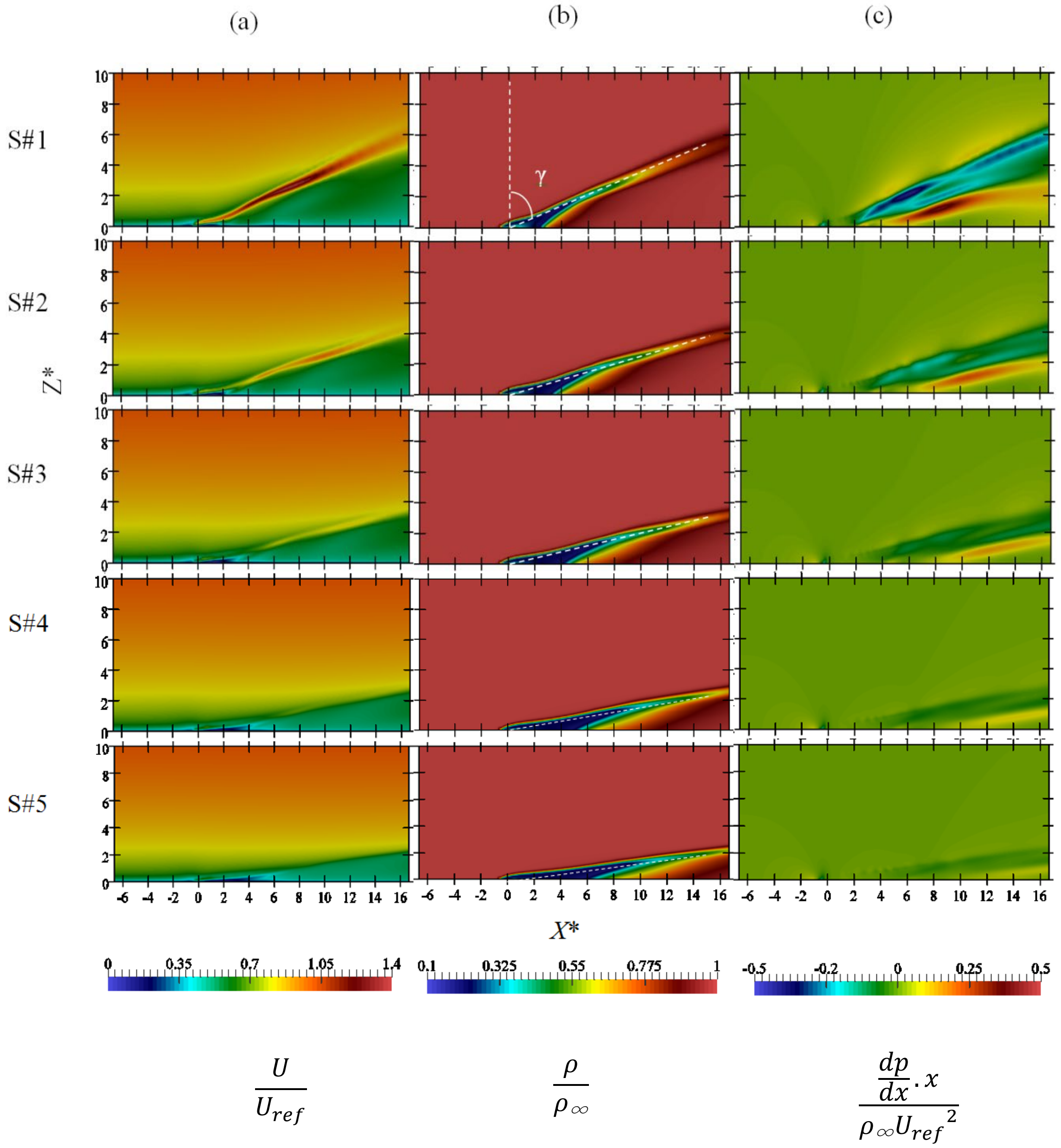

Figure 4-6 Normalized distribution of time-averaged (a) longitudinal velocity (first column), (b) density (second column) and (c) pressure gradient (third column) for different simulation scenarios at *Y*=0.Vertical and horizontal axis indicates normalized vertical and longitudinal distance. Plume tilt angle (γ) is the angle between the dash lines.

Figure 4-6(b) also depicts that immediately downstream of the fire source, the fire plume is attached to the ground due to the entrainment restriction which is a manifestation of Coanda effects. When the wind interacts with fire, the fire plume is tilted toward the ground surface and restricts flow entrainment in the near-ground region. Therefore, flow accelerates to balance the momentum transfer which eventually results in the plume attachment to the ground. However, in further downstream of the fire source where the buoyancy force becomes dominant, the flow starts to lift up from the ground and create a near-ground low-velocity region downstream of the fire source as observed in Figure 4-6. This effect has been observed and reported in previous studies (Eftekharian et al. 2019; He et al. 2011; Hu et al. 2017).

Figure 4-6 (b) also illustrates that the plume tilt angle increases with the increase of upstream wind velocity profile. Figure 4-6 for each simulation scenario shows that in contrast to the density distribution, the U-velocity and longitudinal pressure gradient distributions are not symmetrical about the plume axis. The main reason why U-velocity and longitudinal pressure gradient distributions are not symmetrical is because of unbalanced flow entrainment at each side of the plume axis caused by Coanda effects. In further downstream of the fire plume, flow velocity gradient on the down-side region of the plume axis is higher than that of its up-side region. Consequently, the flow is more inclined to be entrained and decelerated from down-side of the plume axis than the up-side, causing the asymmetrical distribution of longitudinal velocity and pressure gradient at each side of the plume axis. However, as density is a thermodynamic property of the flow and is less affected by the entrainment process, it preserves its symmetrical configuration about the plume axis.

Figure 4-6(a) and (b) for each simulation scenario also shows that in contrast to the normalized density distribution which does not change significantly with the increase of inertia force (wind velocity), the normalized pressure gradient decreases with the increase of upstream wind momentum. Thus, wind velocity distortion decreases with the increase of wind velocity profile as shown in Figure 4-5 (b).

In order to quantify the variation of plume tilt angle with the increase of free-stream wind velocity, changes of tilt angle with free-stream wind velocity were plotted in Figure 4-7. Figure 4-7 (a) and (b) show how plume tilt angle changes with variation of the incoming flow momentum. Figure 4-7 (a) demonstrates that as the incoming flow increases, Ri number which implies the ratio of vertical buoyancy force to the horizontal inertia force decreases; consequently tilt angle increases and plume axis becomes closer to ground as shown in Figure 4-7 (b). As enhancement of wind by fire happens in the fire plume region (Eftekharian et al. 2019) it is expected that wind enhancement in the scenarios with higher momentum happens in the relatively closer area to the ground as confirmed in Figure 4-6 (a). Figure 4-7 shows that for the $\mathrm{Ri}(D) \geq 0.5$, tilt angle almost linearly decreases with the increase of Ri number. This reduction in tilt angle is approximately equivalent to 3° for each 1 m/s reduction of free-stream wind velocity, under a constant fire intensity.

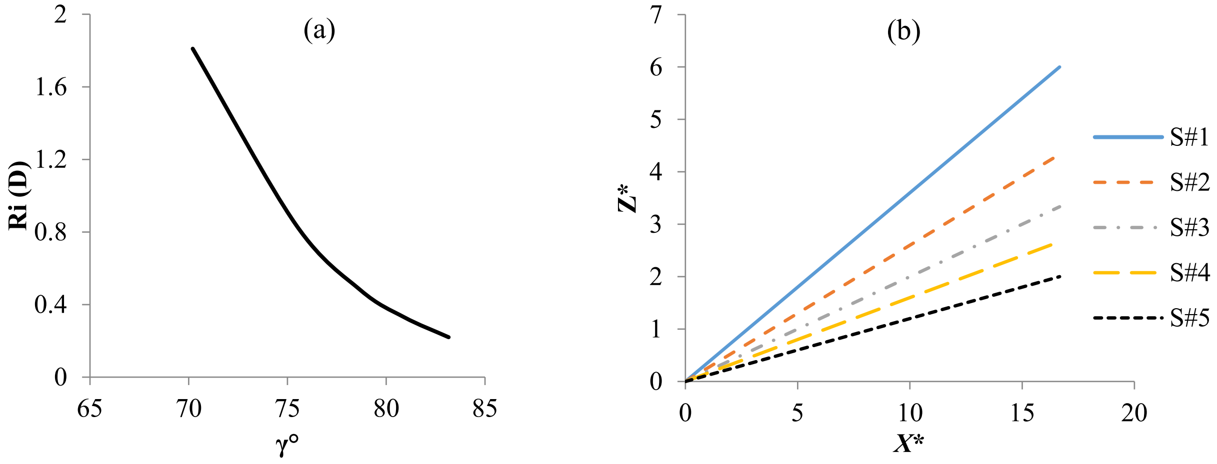

Figure 4-7 (a) variation of tilt angle (γ) with Richardson number and (b) plume axis for different simulation scenarios.

In fluid dynamics and wind engineering, pressure is conventionally normalized by dynamic pressure (i.e. $\frac{1}{2}\rho_\infty {U_{ref}}^2$). Hence, here, the fire-induced pressure force $(\overrightarrow{f_p})$ in Eq.(4-4) can be normalized with dynamic pressure as below:

Normalized fire-induced pressure force (stress):

$$\left(\overrightarrow{f_p}\right)_N = \frac{\rho \overrightarrow{a_p} D}{\frac{1}{2}\rho_\infty {U_{ref}}^2} = \frac{-\frac{dp}{dx} D}{\frac{1}{2}\rho_\infty {U_{ref}}^2} \tag{4-8}$$

Similarly, other forces can be normalized by the same factor:

Normalized viscous force (stress):

$$\left(\overrightarrow{f_v}\right)_N = \frac{\rho \overrightarrow{a_v} D}{\frac{1}{2}\rho_\infty {U_{ref}}^2} \tag{4-9}$$

Normalized total force (stress):

$$\left(\overrightarrow{f_T}\right)_N = \frac{\rho \overrightarrow{a_T} D}{\frac{1}{2}\rho_\infty {U_{ref}}^2} \tag{4-10}$$

While Eq.(4-8) physically represents the extent to which the interaction of wind and fire can increase the incoming flow momentum, Eq. (4-9) shows how viscous forces can decelerate and counteract fire wind enhancement. Eq. (4-10) takes into account the combined effects of fire-induced pressure and viscous forces.

Eq.(4-8) is highly similar to the Euler number which represents the ratio of pressure force to the inertia force (Batchelor 2000):

$$Eu = \frac{\Delta P}{\rho U^2} \tag{4-11}$$

where ρ is fluid density, ΔP is the pressure difference and U is the characteristic velocity of the flow. Here instead of ΔP, we use $\frac{-dp}{dx}x$, where $\frac{-dp}{dx}$ takes into account the induced longitudinal pressure force due to the fire wind interaction and x is the downstream distance from fire source:

$$Eu_x = \frac{-\frac{dp}{dx}x}{\rho_\infty {U_{ref}}^2} \tag{4-12}$$

where Eu_x is the modified local Euler number. The replacement of ΔP with $\frac{-dp}{dx}x$ is on the basis of dimensional analysis and also an analogy between the Richardson number [Eq.(4-5)] and Euler number [Eq.(4-11)].

As shown in Figure 4-6, longitudinal fire-induced pressure force in the form of Euler number plays a significant role in the enhancement of wind velocity. However, it should be noted that although buoyancy force applies in the vertical direction, it is prerequisite for generation of fire-induced pressure force. Therefore, indirectly, buoyancy force affects the longitudinal fire wind enhancement phenomenon. In the following discussion of this study, it will be shown that fire-induced viscous forces play a minor role in wind enhancement phenomenon. Hence, the modified Euler number [Eq. (4-12)] and Richardson number [Eq.(4-5)] are incorporating all the important forces (buoyancy, fire-induced pressure, and wind inertia force) that contribute to the fire wind enhancement phenomenon. It is then considered that modified Euler number and Richardson number are appropriate non-dimensional groups to study the mechanisms involved in fire wind enhancement phenomenon.

The distribution contours of the longitudinal components of the normalized fire-induced pressure, viscous and total forces along the surface passing through the domain centreline (*Y*=0, Figure 4-1) for all simulation scenarios are plotted in Figure 4-8.

Figure 4-8 shows that fire-induced pressure forces are dominant within the plume region while fire-induced viscous forces prevail in near-ground (boundary layer) region. A comparison between Figure 4-8 (a), (b) and (c) reveals that fire-induced pressure force is the dominant force which causes wind enhancement within the plume region.

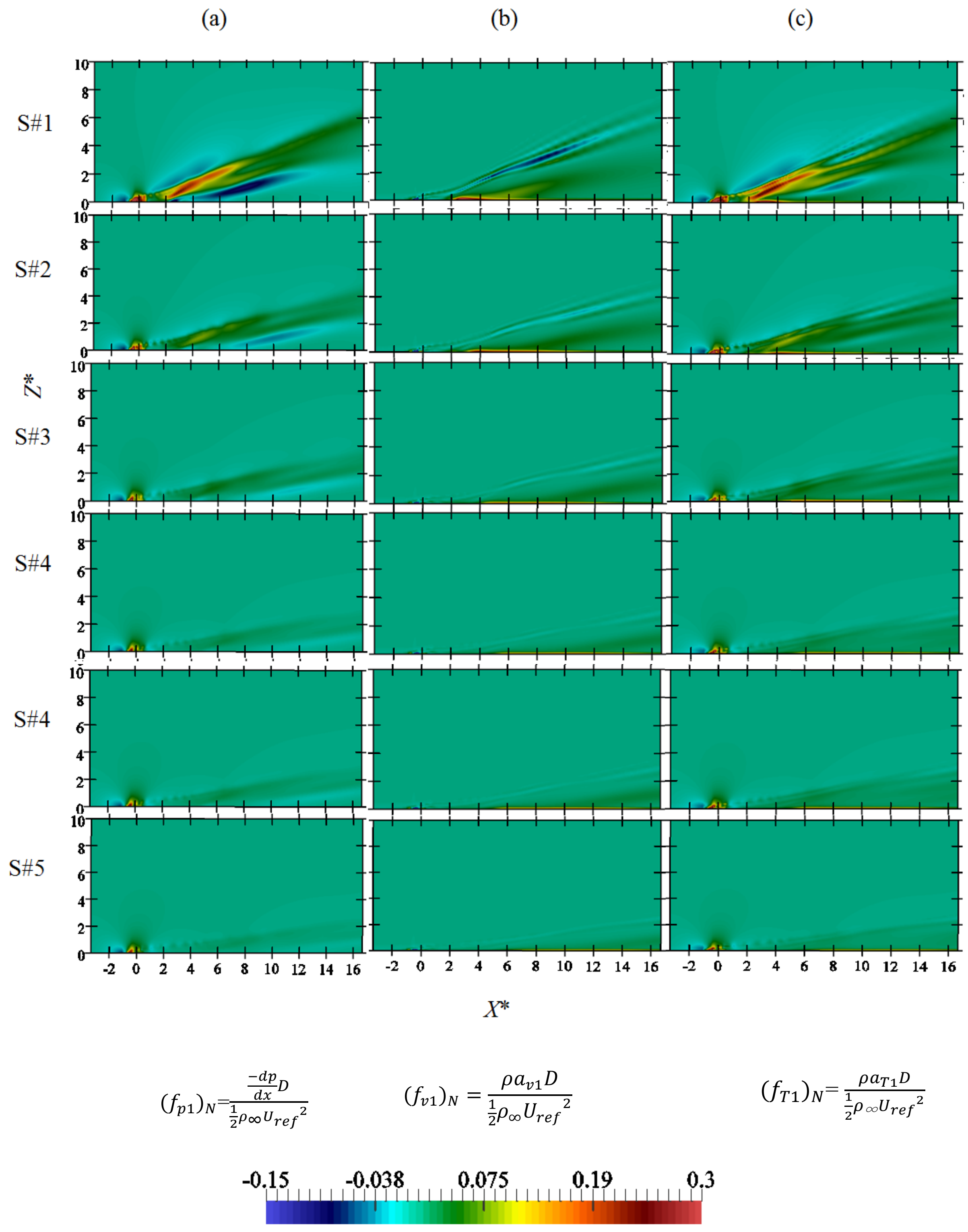

Figure 4-8 Comparison of different normalized fire-induced time-averaged longitudinal forces, including (a) pressure force (first column), (b) viscous force (second column) and (c) total force (third column) in different simulation scenarios. Vertical and horizontal axis indicates normalized vertical and longitudinal distances.

Figure 4-8 (a) also indicates that the normalized fire-induced longitudinal pressure force decreases with the increase of free-stream wind velocity. It means that under constant fire intensity, the free-stream wind velocity is less influenced by the fire when the wind velocity increases, or Ri_D decreases. Under a constant fire intensity, fire-induced pressure force value does not change significantly with the increase of upstream wind velocity. However, the flow momentum upstream of the fire source increases when wind velocity increases. Therefore, $(\vec{f}_p)_N$, or the ratio of fire-induced pressure force to free-stream momentum force diminishes. Consequently, an upstream flow with higher momentum is less affected by the fire-induced pressure force.

As can be seen in Figure 4-8 (b), fire-induced viscous forces appear in two regions: in boundary layer region near the ground and within the plume region. It was shown that fire-induced pressure forces distort the velocity profile within the plume region. This distortion creates a velocity gradient in the flow field. According to the Eq.(3-2), this velocity gradient generates viscous forces within the plume region as shown in Figure 4-8 (b). Accordingly, fire-induced viscous forces within the plume region are indirectly generated due to fire-induced pressure forces. In other words, pressure force controls the generation of velocity enhancement, and velocity enhancement controls viscous force. Therefore, both normalized longitudinal fire-induced pressure and viscous forces follow the same trend of reduction when free-stream wind velocity increases.

Figure 4-9 shows a cross-sectional view (at X^*=12) of normalized longitudinal velocity, fire-induced pressure, and viscous forces for different simulation scenarios. For all simulation scenarios, longitudinal velocity enhancement distribution has a horse-saddle shape which is due to the counter-rotating vortices generated as a result of the interaction of longitudinal wind velocity and vertical buoyant plume. A similar trend can be seen in the previous studies (Eftekharian, et al. 2019; Fric & Roshko 1994; Margason 1993). Moreover, Figure 4-9 explicitly shows the role of fire-induced pressure force on the longitudinal wind enhancement which confirms the trend observed in Figure 4-5 and Figure 4-8. Figure 4-9 also demonstrates that a negative fire-induced pressure force is generated just below the region of enhancement where positive fire-induced pressure force exists. This is due to the flow entrainment process which causes flow deceleration just below the fire plume.

Figure 4-9 confirms the trend of fire wind enhancement reduction with the increase in free-stream wind velocity, as observed in Figure 4-6. As discussed earlier, this is because as wind velocity increases, the flow becomes more dominant by inertial force and the buoyant plume which causes the generation of fire-induced pressure forces does not play a significant role in forming the flow field. Therefore, as wind velocity increases under constant fire intensity, the corresponding Euler number becomes smaller and therefore the effective fire-induced pressure forces decreases and consequently, the level of wind enhancement reduces.

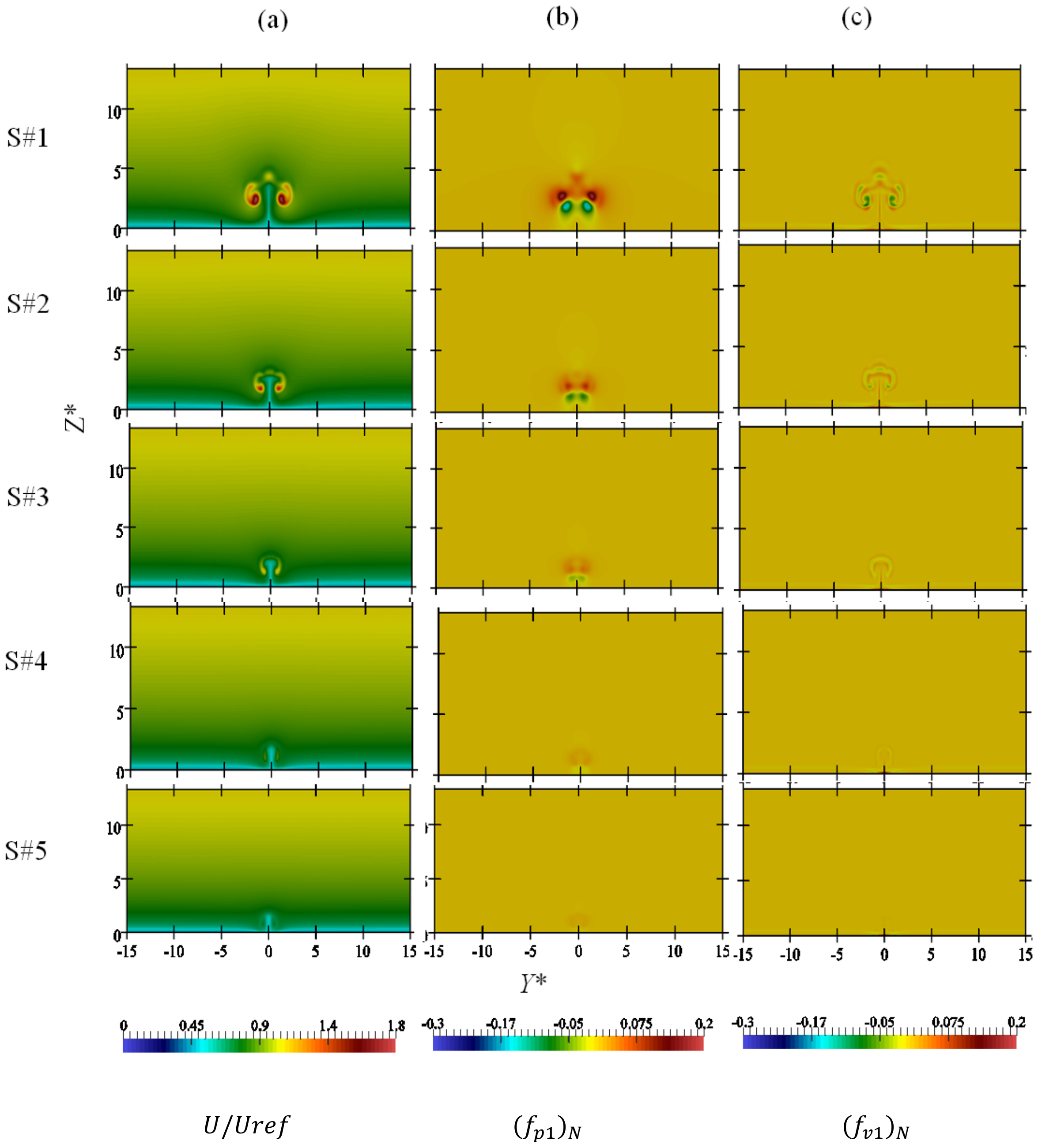

Figure 4-9 normalized cross-sectional distribution of fire-induced time-averaged longitudinal (a) velocity (first column), (b) pressure force (second column) and (c) viscous force (third column) for different upstream wind velocities at $X^*=12$. The vertical and horizontal axis indicates normalized vertical and spanwise distance.

4.5.2. Longitudinal changes in longitudinal velocity profile

In Figure 4-5, the variation in U profile is due to the variation in U_{ref}. In contrast, the variation in U profile in each plot of Figure 4-10 is due to the variation in X, or in x. The results shown in Figure 4-5 confirm the trend observed in Figure 4-6. It is seen that longitudinal velocity in the region just above and below the plume is weakened in comparison to the free-stream profile at the same elevation. The amount of reduction seems proportional to U_{ref}, or reversely proportional to Ri_D. This is mainly because the flow entrainment process happens around the plume region and decelerates the flow surrounding the plume region. In other words, as shown in Figure 4-6 (c) and Figure 4-6 (b), flow entrainment around the plume region causes the generation of an adverse (positive) pressure gradient and decelerates the flow surrounding the plume region which eventually leads to the reduction of longitudinal velocity in those regions. As can be observed in Figure 4-6 and Figure 4-10, in far enough vertical distance from the plume region (e.g., $Z^{*}\approx 10$) where the effects of entrainment disappear, wind velocity downstream of the fire source converges to the corresponding velocity at the upstream of fire source.

Variation of the level of enhancement for different wind reference velocities at different distances downstream of the fire source is plotted in Figure 4-11. Figure 4-11 confirms that the level of enhancement is highly affected by the upstream wind velocity and experiences a considerable reduction as free-stream wind velocity increases, as shown in Figure 4-11. Figure 4-11 also highlights that the level of enhancement also highly depends on the distance from the fire source, as depicted in Figure 4-10. Figure 4-11 indicates that for all simulation scenarios, the level of enhancement first increases longitudinally reaching a peak value and then undergoes a reduction further downstream of the fire source.

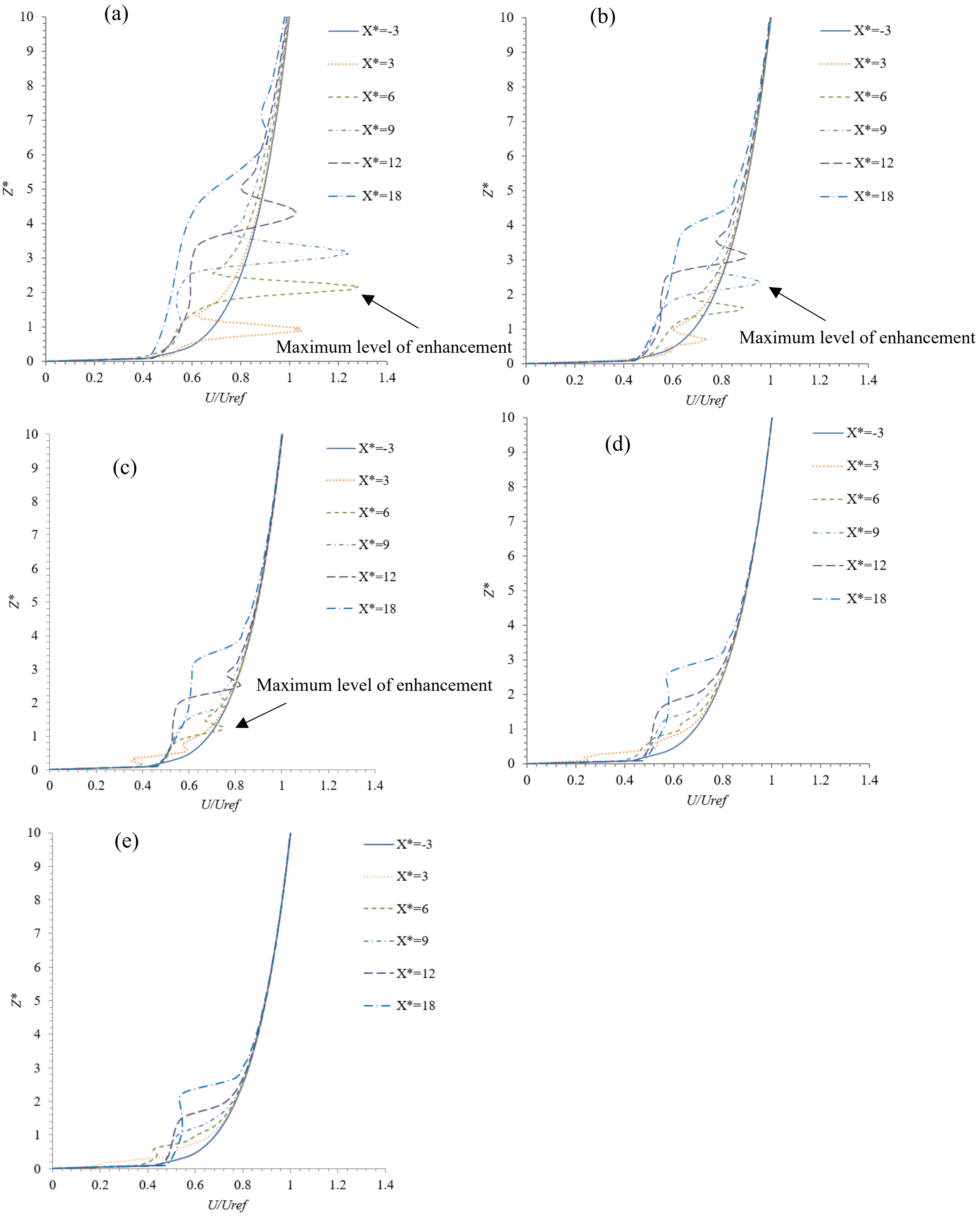

Figure 4-10 Vertical distribution of normalized time averaged longitudinal velocity in different distances downstream of the fire source for (a) simulation scenario #1 (U_{ref}=3 m/s) and (b) simulation scenario #2 (U_{ref}=4.5 m/s), (c) simulation scenario #3 (U_{ref}=6 m/s), (d) simulation scenario #4 (U_{ref}=7.5 m/s), (e) simulation scenario #5 (U_{ref}=9 m/s). The arrows in the figure indicate the location corresponding to the maximum level of enhancement at each simulation scenario.

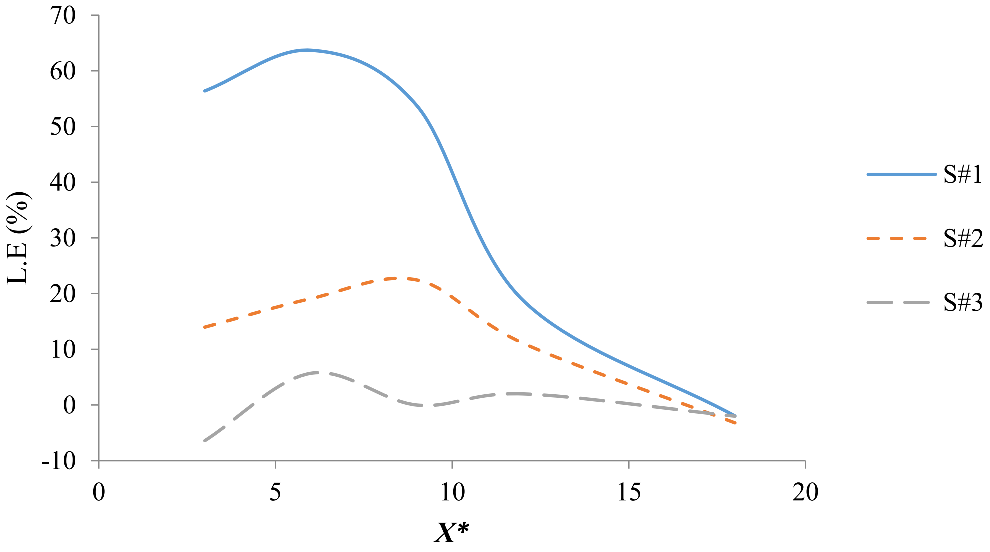

Figure 4-11 Comparison of the level of enhancement for different upstream wind velocities (simulation scenarios) at different distances downstream of the fire. S#1, S#2, and S#3 are respectively corresponding to the simulation scenarios with free-stream reference velocity of 3m/s, 4.5 m/s and 6m/s.

The corresponding Ri_x and Eu_x number for each simulation scenario at different distances downstream of the fire source are plotted in Figure 4-12. Comparison of Figure 4-12 with Figure 4-10 shows that in each simulation scenario, the longitudinal distance corresponding to the maximum level of enhancement and maximum Eu_x number are the same, at about X^*=6, X^*=9, and X^*=6 for simulation scenarios # 1, #2 and #3, respectively.

Figure 4-12 also reveals that with the increase of free-stream wind velocity, both Ri_x and Eu_x number decreases for a given X^*, and consequently the level of enhancement decreases significantly. Figure 4-12 also shows that with the increase of wind momentum, generally, the ratio of Eu_x number to Ri_x number reduces. For example, for free-stream wind velocity of 3 m/s, the graph corresponding to the Eu_x number is entirely above the Ri_x number and gradually with the increase of wind velocity, the graph related to Eu_x number falls behind that of Ri_x number and for reference velocity of 9 m/s, Eu_x number graph entirely falls behind the corresponding Ri_x number graph.

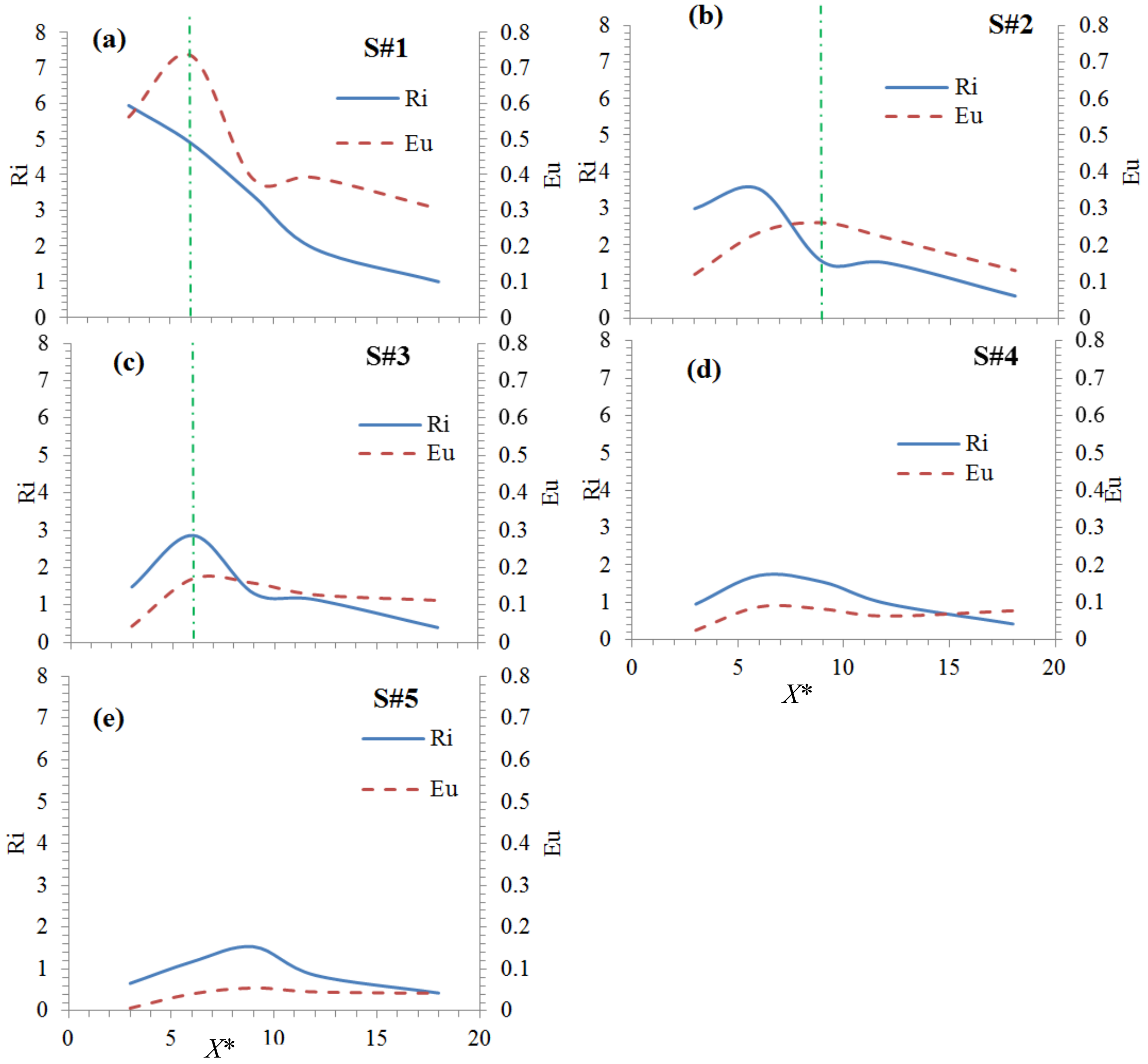

Figure 4-12 Comparison of Ri_x and Eu_x number at different distances downstream of the fire source for different simulation scenarios. The green dash line is corresponding to the location at which maximum velocity enhancement happens in the specified scenario.

4.6. Conclusion

This study employed LES results to fundamentally investigate the mechanisms involved in fire wind enhancement phenomenon, caused by the interaction between the fire-induced buoyancy flow and momentum wind flow. The effects of change in Richardson number due to variation in free-stream wind velocity on fire wind enhancement were investigated for pool fire wind scenarios. A module was implemented to the Fire-FOAM solver to explicitly calculate the fire-induced force components under different free-stream wind velocity conditions. Below are the main conclusions of this study.

(1) It was shown that the interaction of wind and fire causes the generation of longitudinal fire-induced pressure and viscous forces. Longitudinal fire-induced pressure forces accelerate the flow and create distortion/enhancement in the velocity profile.

(2) LES results also indicated that with the increase of wind velocity, the normalized fire-induced pressure force decreases, resulting in a reduction in the level of wind enhancement.

(3) Richardson number and the modified Euler number were utilized in the analysis to predict the patterns for the level of enhancement at different distances from the fire in different free-stream wind velocity conditions. It was revealed that although the level of wind enhancement depends on both Richardson and the modified Euler number, the maximum level of enhancement in each simulation scenario (free-stream wind velocity) happens in the longitudinal location where the modified Euler number has the highest value.

(4) Plume tilt angle which represents the region of wind enhancement was also investigated and it was shown that for the $\mathrm{Ri}(D) \geq 0.5$, an increase of 1 m/s of the incoming wind velocity corresponds to 3° increase in plume tilt angle under a constant fire intensity.

CHAPTER 5. NUMERICAL ANALYSIS OF THE EFFECTS OF FIRE SOURCE CONFIGURATION ON FIRE-WIND ENHANCEMENT

In previous chapters, the effects of free-stream wind velocity and fire heat release rate of point source fire on fire-wind enhancement were studied. Another important factors affecting wind enhancement by fire is fire source configuration. Given that a bushfire starts with a point source of fire and then evolves to a line source, comparison of the physics of fire-wind enhancement between point source and line source fires is worth investigating. Based on the developed theoretical framework in Chapters 3 and 4, a comparison is made between wind enhanced by a line source and point source of fire under the same fire intensity. Fire-induced vertical velocity is also compared for the point and line sources of fire. This study further introduces a new parameter as an equivalent hydraulic diameter of line fire sources to represent non-dimensional bushfire intensity.

A reprint of this study 'Numerical analysis of the effect of fire source configuration on fire-wind enhancement', **Esmaeel Eftekharian**, , Maryam Ghodrat, Yaping He, Robert H. Ong, Kenny C. S. Kwok, Ming Zhao, published by "*Heat Transfer Engineering*" 2019, Volume 42, Pages 1-20 (https://doi.org/10.1080/01457632.2019.1685249) is appended in Appendix A3.

5. 1. Abstract

Detailed investigation of fire-wind interaction is highly instrumental in understanding the cause of the devastating consequences of major fire events in windy weather conditions. Enhancement of wind downstream of the fire source is a phenomenon caused by fire-wind interaction. The main objective of this study is to compare the behavior of wind enhancement for fire of either line or point sources under similar wind and heat release rate conditions. This paper uses the OpenFOAM platform as a numerical simulation tool to fundamentally investigate fire-wind enhancement phenomenon in both point and line source of the fire. A module has been developed and implemented in the FireFOAM solver to extract different components of fire-induced longitudinal and vertical forces. A new parameter expressed as an equivalent hydraulic diameter of line fire sources was introduced to represent the non-dimensional bushfire intensity. The results indicate that under the same intensity of heat release rate per unit area, enhancement of longitudinal wind in line fire is significantly higher than that of the point fire source. On the other hand, the fire-induced vertical velocity of point source fire is higher than that of the line source case.

5. 2. Introduction

Wind-driven line fires are becoming increasingly important to understand wildland fire to minimize the danger of wildfires and to enhance our ability to anticipate its behavior (Hu 2017). The dominant feature and behavior of wind-driven fire and its effects are a result of various compound processes. A profound understanding of the science behind these phenomena helps us to better manage fire-induced changes in flow aerodynamics which is a significant factor in assessing potential fire hazard.

Several studies have been carried out on flame spread over liquid fuels. Most of those are focused on flame propagation in a cross-flow environment. For example, flame spreading behaviors in a system with forced air flow is investigated by Li et al. (2018) using a series of flame spread tests on sub-flash temperature diesel fuel. The results of their study showed that the flame spread rate decreases monotonically with an increase in the opposed air flow velocity. They further suggested that the subsurface flow length increases with opposed air flow velocity, while it becomes irregular under concurrent air flows. For actual fire problems (bushfire wind enhancement), the development of fire is usually accompanied by the environmental winds, which highlight the importance of studying the interaction of wind with fire (Tang et al 2017). Bushfire wind enhancement phenomenon is the enhancement of freestream velocity and can be described as the increase of local wind velocity by bushfire. There are only some subjective proofs in the literature on the contribution of bushfire in wind enhancement (Wang 2006).

Computational fluid dynamics (CFD) models have been utilised widely to model complex physical phenomena such as large-scale pool/line fires in the presence of wind (He et al. 2011a; Sikanen & Hostikka 2016; Sun, Guo & Pareek 2014; Vasanth et al. 2015, 2017; Vasanth et al. 2013) and wildfire modelling (Mell et al. 2013; Morvan & Dupuy 2004). It has been identified that bushfire causes an increase in near-ground wind velocity and increases downstream pressure load on building structures considerably. The Coanda effect was assumed to account for the attachment of the plume to the ground downstream of the bushfire front, whereas further downstream, buoyancy force governs and finally raises the plume above the ground (Kwok, He & Douglas 2012).

Nelson, Butler and Weise (2012) studied the flame characteristic and fire behavior of wind-aided pine litter and grass fires and compared them with some simple theoretical flame models. The aim of their study was to determine whether the data support their derived models. It was concluded that both the models and the experimental data are aligned with recently reported results of CFD simulations (Nelson, Ralph M., Butler & Weise 2012). Their results also suggested that the existence of buoyancy- and convection-controlled regimes of fire behavior is defined by a critical Byram's convection number (Byram1959).

Many researchers including (Fang et al. 2016; Kazemipour, Afshin & Farhanieh 2017; Tang, et al. 2016); Fang et al. (2016); Zhang et al. (2016); de Ris (2013) and Kazemipour et al. (2017) analysed the buoyant diffusion flame in cross-wind or still condition and it was concluded that buoyancy forces play a major role in air entrainment, axial velocity, and tilt angle. Albini (1981) developed a one-dimensional model for the wind-blown, turbulent flame from a line fire in which buoyancy is the main source of vertical momentum. His research results showed that the flow angle of the flame fluid is nearly independent of the flame height Albini (1981). Other researchers also showed that when an external flow with ambient temperature is imposed over a fire, both natural convection from buoyancy and forced convection from the wind play a role in altering the flame shape (Hu, Wu & Liu 2013). Hu et al. (2013) proposed a generalized model to describe the flame length elongation behavior of pool fires due to cross air flow and revealed that the flame length and the mass burning rate of the pool fire increase with the cross airflow speed.

In addition to the flame length, the flame tilt angle is another parameter that assists the determination of flame shape. Early experimental studies for the determination of flame tilt in cross-flow can be found in (Thomas, Pickard & Wraight 1963; Thomas, 1963a). Other researchers (Pipkin & Sliepcevich 1964; Welker & Sliepcevich 1966) found that the flame tilt behavior under wind conditions is mainly dominated by the balance between momentum wind flow and flame buoyant flow. In more recent work, Yoshihara et al. investigated flame characteristics of small pool fires under downslope and upslope angled winds and claimed that the difference between horizontal and angled wind flow is the existence of two momentum component (horizontal and vertical). They proposed a set of modified semi-empirical correlations for calculating flame length and flame tilt angle for lower wind speeds. Meanwhile, a new mathematical modeling based on experimental data was developed by Hu et al. to present a correlation for the flame tilt angle of small pool fires. Flame tilt angle in large scale pool fire source was also investigated in (Ferrero, Munoz & Arnaldos 2007). A comprehensive review of flame tilt angle developments can be found in (Hu 2017).

The flame base drag phenomenon is referred to as flame trailing downstream of the fire source (Welker & Sliepcevich 1966) caused by fire-wind interaction. This phenomenon is expected to happen when fuel gas with a density higher than air is dragged by wind beyond the downwind edge, causing the fire plume to be stretched downstream of the fire source (Raj 2010). The effects of cross-wind on flame drag base length were experimentally investigated (Lam & Weckman 2015; Lin, Zhang & Hu 2018; Tang He & Wen 2019) and correlations for this parameter were developed (Johnson 1993; Moorhouse 1982; Raj 2010; Welker 1965). Cross-wind effects on flame base drag length in sub-atmospheric conditions were also investigated (Hu et al. 2017).

Flame sag is another phenomenon involved in the fire-wind interaction when pool fire source is above the ground (Zhang et al. 2019). This phenomenon refers to the fire flame sink below the leeward edge of the pool fire source in the presence of cross-wind (Zhang et al. 2019). Early observations of this phenomenon have been reported in (Lautkaski 1992; Rew, Hulbert & Deaves 1997). However, recently an experimental study was performed to determine the correlations for flame sag length and the associated critical cross-wind velocity (Zhang et al. 2019).

Many common fire scenarios can be classified as pool fires (Hamins, Kashiwagi & Buch 1996). In pool fire modeling, wind Froude number (Hamins Kashiwagi & Buch 1996) which is the ratio of inertia to buoyant forces, is the key parameter for estimating flame height and mass entrainment rate (Bouhafid et al. 1989). Large scale vortices roll into the fire, entrain air, and define the boundaries of the fuel-rich core (Forthofer & Goodrick 2011). In line source fires, however, vertical vortices are often the most dramatic. These vorticities are generated by wind shear (Forthofer & Goodrick 2011) and can result in sudden increases in fire intensity (Forthofer & Goodrick 2011).

A global correlation was developed for acetone burning rate and flame length in pool fire-cross wind condition by Tang et al. (2015). The burning characteristics of controlled rectangular pool fires in a reduced pressure atmosphere were also investigated by Hu et al. (2013). They found that the corner effect of the square/rectangular pools produces vortex and increase the convection to the surface of the fuel. The air entrainment of ring pool fires was investigated experimentally by Tao et al. (2018). They found that air entrainment rate of the ring pool fire is a function of non-dimensional parameters and a correlation has been proposed to describe the variation of flame height.

Albini (1981) developed a one-dimensional model for the structure of the wind-blown, turbulent flame from a line fire and showed that buoyancy is the principal source of vertical momentum and his model can calculate the time-average and mass-averaged flow properties within the flame zone.

Limited theoretical and numerical efforts have been carried out in building models applicable to wind-driven line fire. Flames from line (Steward 1964) and point (Becker & Liang 1978; Becker & Yamazaki 1978) sources in still air and also the wind deflected fuel jet with buoyancy (Botros & Brzustowski 1979; Gollahalli, Brzustowski & Sullivan 1975) have been investigated and some semi-empirical flame-size correlations (Byram 1959; Nelson 1980) have been developed. Smoke plumes from large pool fire cross-flow interaction were simulated using large eddy simulation (LES) approach (Baum, McGrattan & Rehm 1994; Wang, Wen & Chen 2014). Modifications have been performed to effectively enhance combustion model (Chen et al. 2014a) and radiative heat transfer and soot modeling in pyrolysis calculation (Fukumoto, Wang & Wen 2018) applied in FireFOAM solver.

Most recently, Eftekharian et al. (2019) investigated the enhancement of wind by pool fire and explained fundamentally how the interaction of buoyant plume with wind leads to enhancement of wind downstream of the fire. They showed that enhancement of wind by fire is caused by the generation of a negative longitudinal pressure gradient in the low-density region (plume region) due to fire-wind interaction. They also examined the effects of pool fire heat release rate on wind enhancement. In another study, Eftekharian et al. (2018) investigated the effects of wind velocity on the line fire-wind interaction and showed that under a constant fire intensity, wind velocity is comparatively less influenced by fire when the upstream wind velocity increases. The effects of terrain slope on fire-wind enhancement was also investigated by Eftekharian, et al. (2019). However, no comparison has been made between fire-wind enhancement for line and point source of the fire.

The presented literature review reveals that even though a number of investigations have been conducted in the domain of wind-fire interaction, a fundamental understanding of the flow aerodynamics is still in its early observation and empirical modeling stages. More attention was devoted to pool fires (which are approximated by point source fires) than to line source fires. There are only limited experimental and numerical data for the comparison of line and pool fire source in terms of the impacts of buoyant diffusion flame on flow aerodynamics.

This work is aimed to fill the gap by providing quantitative and systematic analysis into the factors contributing to the change of the velocity, acceleration and density profile in the interaction of wind and fire scenarios and makes a detailed comparison between pool fire and line fire sources. The main objective of this study hence is to provide a comprehensive analysis of flow characteristics in pool fire and line fire sources during fire-wind interactions. Using fire-induced force and analysis, it is aimed to provide a better understanding of how fire-wind enhancement phenomenon is affected by the type of fire source. For this purpose, the fire-induced forces and acceleration components are explicitly expressed in terms of contributions from pressure force, body force, and shear stress. Then the computational fluid dynamics method is used to quantitatively delineate the contribution of each term.

5. 3. Numerical modeling

The CFD solver used in this study was FireFOAM which is a derivative of OpenFOAM 4.1 platform (Greenshields 2015). Continuity, momentum, energy, species and state equation are solved by fireFOAM using LES model. A module was added to the fireFOAM solver to extract fire-induced forces and acceleration for further analysis of the effects of fire source configuration on fire-wind enhancement. More details of this module as well as governing equations were fully elaborated in Section 3.3 and 4.3.

5. 4. Validation

In this study, two sets of experimental data were used to validate FireFOAM numerical model: McCaffrey's (1979) experiment and the experimental results of Hirano and Kinoshita (1975).

McCaffrey' (1979) experiment includes experimental data of buoyant diffusion flame in the still environment. To validate the numerical model employed in this study, a simulation with constant heat release rate of 58 kW was carried out. The simulation results were then assessed against the numerical results of (Eftekharian et al. 2019; Wang, Chatterjee & de Ris 2011) and experimental data of McCaffrey (1979). McCaffrey (1979) utilized a natural gas burner and measured the centreline of flow velocity for various heat release rates including 58 kW. Wang, Chatterjee and de Ris (2011) used FireFOAM to simulate this experiment. A bi-directional pressure probe was used in McCaffrey (1979) to measure velocity. The diameter of the probe is 0.016m and the spatial averaging was performed to get the flame structure. Apart from spatial averaging, time-averaging approach was also used to obtain quasi-steady centreline velocity reading. Velocity measurement based on pressure probe is a challenging task in flame-related experiments. Due to the high temperature of the flame, the Reynolds number around the pressure probe can significantly drop to 200. Therefore, the maximum error in the velocity measurement was considered to be 15% closer to the burner. However, the error is reduced at the greater heights where the velocity is increased. Wang, Chatterjee and de Ris (2011) and Eftekharian et al. (2019) conducted the simulation of 20 second burning time and showed that it takes 7 seconds of the simulated period for the buoyancy diffusion flame to reach a quasi-steady condition. They also gathered data and averaged them during the last 13 second of the analysis and compared with the experimental results. The 13 s includes almost 40 puffing cycles, long enough for at least the convergence of the first order turbulent statistics. A schematic view of the computational domain is presented in Figure 5-1(a). In order to model the buoyancy diffusion flame experiment done by McCaffrey (1979), the domain size in all directions is set at 3 m and the grid size of 0.019 m×0.019 m×0.03 m was used to keep the smallest cell size the same as that suggested in Wang, Chatterjee and de Ris (2011). Similar to Wang, Chatterjee and de Ris (2011), the burner is simulated by a 0.3×0.3m square placed at the center of the domain. The domain boundary conditions for the buoyant diffusion geometry were similar to those suggested by Wang, Chatterjee and de Ris (2011). It is noted that in previous studies (Eftekharian et al. 2019; Wang, Chatterjee & de Ris 2011), the surface of the burner was set to about the base of the domain. An attempt is made in the current study to replicate precisely McCaffrey's (1979) experimental setup by setting the burner surface at 75 cm above the floor.

Figure 5-1 (b) presents the predicted velocity profile of fire plume centreline in a log-log coordinate and compares it with the results predicted in (Eftekharian et al. 2019; Wang, Chatterjee & de Ris 2011) and measured in (McCaffrey 1979). It is revealed that moving the burner above the ground does not significantly affect the predicted velocity profile.

The second set of experimental data for model validation was that by Hirano and Kinoshita (1975). The details of this validation are provided in the Section 3.4.2.

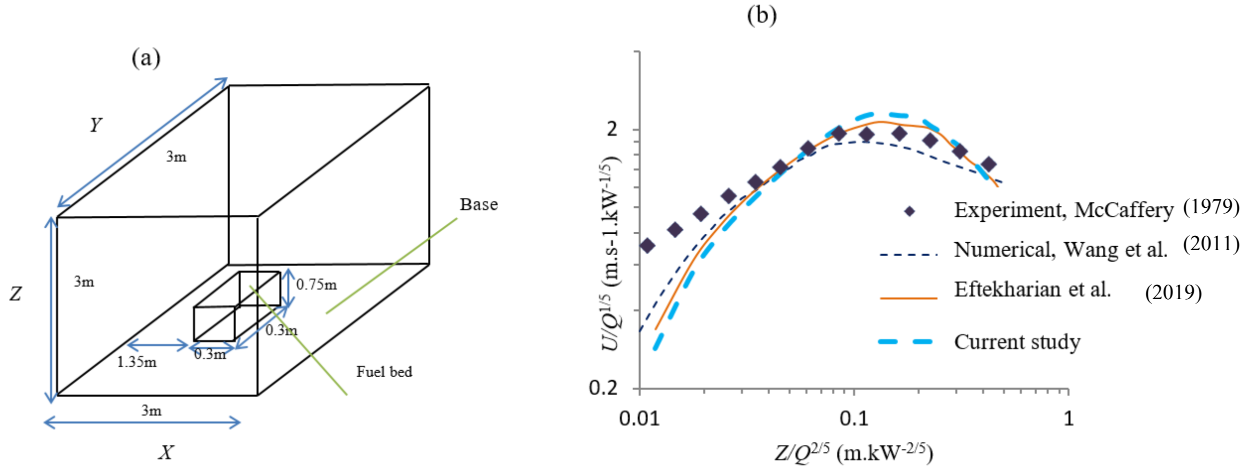

Figure 5-1 Schematic view of the (a) computational domain, (b) comparison of normalized centreline velocity profile of the current study with numerical and experimental data available in the literature.

5. 5. Geometric model and simulation condition

The computational domain consists of a rectangular box with the dimension of 9×15×34 m as shown in Figure 5-2. Two separate domains have been prepared in this study. The first one is for pool fire with a square burner (0.3×0.3m) [Figure 5-2 (a)] and the second for line fire source [Figure 5-2 (b)]. The depth of both line and pool fire sources are considered to be 0.3m (D=0.3) and they are introduced 3m downstream of the domain inlet. The width of the fire source, however, is 0.3m and 9m in the point source and line source cases, respectively. Although the two fire sources have finite dimensions: the first having finite width and depth and the second representing a truncated infinitely long line source with finite depth, they are referred in the current paper as the point source and line source for short without ambiguity, or pool fire and line fire.

Cross-wind in this paper means the wind which is in the longitudinal direction and makes the right-angle with vertical buoyant plume. Methane was chosen to be injected from the fire source to generate heat release rate intensity of 6.44 MW/m^2 for different scenarios. Bushfire intensity (I_B) is usually described as the heat release rate per unit width of bushfire front (Byram 1959), which in this study is 1.93 MW/m for the line source case. The rational behind choosing these fire heat release rates for point source and line source is that both cases have an identical heat release rate per unit area of fire. A review of the boundary condition for CFD modeling of turbulent diffusion flame can be found in (Kumar & Dewan 2014). As for the boundary condition, outflow and open boundary conditions were prescribed for domain outlet on the right and ceiling, respectively. Open boundary condition allows the flow to freely get in and out of the domain. Slip and no-slip boundary conditions were applied respectively to the domain sides and base. A power law velocity profile was used at the inlet on the left side of the domain:

$$U(Z) = U_{ref}\left(\frac{Z}{Z_{ref}}\right)^{\alpha} \tag{5-1}$$

where, U_{ref} and Z_{ref} are, respectively, the reference velocity (3 m/s) and height (3 m), α is determined based on terrain category (here 0.16). In order to consider turbulent fluctuations in the domain inlet, the "Two-dimensional vortex method" (Sergent 2002) was used. The initial temperature was considered to be 300 K, while the adiabatic boundary was suggested for the domain base.

In this study, two simulation scenarios have been considered to identify the difference in flow aerodynamics of line and pool fire sources, as shown in Table 5-1.

To compare the initial momentum strengths of the fuel injection flow and of the wind, a ratio of momentum flux R_m can be defined as:

$$R_m = \frac{\rho_0 u_0^2}{\rho_\infty U_\infty^2} \tag{5-2}$$

where u_0 and ρ_0 are the fuel injection velocity and density at the surface of the fuel bed respectively, U_∞ and ρ_∞ are that of ambient air and U_∞=U_{ref}=3m/s. In the current study, u_0=0.1977 for both line and pool fire cases.

Some parameters are introduced to describe the strength of the two fire types. For the pool fire, it is the non-dimensional heat release rate (Heskestad 2016).

$$Q^* = \frac{Q}{\rho_\infty c_p T_\infty \sqrt{g} D_h^{5/2}} \tag{5-3}$$

where c_p is the specific heat of air, D_h is the characteristic dimension of the burner (Herwig, Gloss & Wenterodt 2010) which can be considered as the hydraulic diameter of the pool fire source. For a fire with finite dimensions of width, W, and depth, D, the hydraulic diameter is defined as (Blocken & Gualtieri 2012):

$$D_h = \frac{4A}{P} = \frac{4WD}{2(W+D)} = \frac{2D}{1+D/W} \tag{5-4}$$

where A and P are the area and perimeter of the fire source respectively.

In the study of bushfires or line source fires, the intensity of the fires is characterized by the heat release rate per unit length of bushfire front (Byram 1959). Based on dimensional analysis, it is postulated that the non-dimensional parameter to describe the strength of the line fires can be defined as:

$$I_B^* = \frac{I_B}{\rho_\infty c_p T_\infty \sqrt{g} D_{h\prime}^{3/2}} \tag{5-5}$$

where $D_{h'}$ is the equivalent hydraulic diameter for the line source cases. In the current study, we will use the basic definition of hydraulic diameter [Eq. (5-4)] as well as valid assumptions for the underlying bushfire source configuration to present an equivalent hydraulic diameter for line fire sources.

Unlike a mathematical line in theoretical studies, the bushfire front (or fire bed) in the physical reality always has a finite depth while its width (length) may stretch very long. The depth may be approximated as a constant and the width be treated as infinitely long. Therefore, the equivalent hydraulic diameter for the line source bushfire can be regarded as the limiting case of D_h when the width W is approaching infinity:

$$D_{h'} = \lim_{W\to\infty}(D_h) = \lim_{W\to\infty}\frac{2D}{1 + D/W} = 2D \tag{5-6}$$

In the current study, the D/W value is 0.033 and Eq. (5-6) gives a good approximation of the $D_{h'}$ value.

Table 1 shows that the value of I_B* for the line source case is almost one-third of Q* in the point source case, although the heat release rate per unit area of the two simulations is the same.

Table 5-1. Description of simulation scenarios

Simulation Scenario Number (S#)	Source type	D (m)	W (m)	Q (MW)	I_B (MW/m)	Reference velocity (m/s)	R_m	I_B* or Q*
1	Line fire	0.3	9	17.4	1.93	3	0.0024	0.0035
2	Pool fire	0.3	0.3	0.580	–	3	0.0024	0.0106

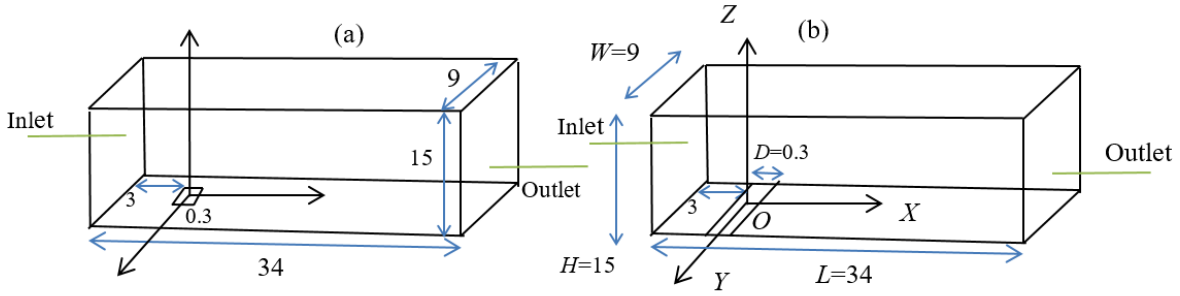

Figure 5-2 Schematic views of the computational domain (a) pool fire and (b) line fire source (all dimensions are in meter).

5. 6. Results and discussion

5.6.1. Grid sensitivity analysis

Grid sentivity analysis have been performed in section 4.5.2. The mesh used in this chapter is generated based on the grid sensitivity study.

5.6.2. Fire-wind interaction simulation results and discussion

The results presented in this section can be divided into two parts. The first part fundamentally explains why the interaction of longitudinal wind velocity and vertical buoyant plume leads to enhancement of wind velocity and how it is affected by the type of fire source (i.e. pool fire and line fire source).

The second part focuses on flow aerodynamic properties in the vertical direction and discusses how they vary between pool fire and line fire source. Domain travel time in the simulations is 12s. The simulation time for all simulation scenarios is 24s, which corresponds to the two domain travel cycle. The first travel cycle (12s) was considered as the transition period and therefore the data are averaged during the second cycle (last 12s). All the presented data in this section are based on the quantity of the time-averaged variable between t=12s and t=24s (second domain travel cycle).

5.6.3. Enhancement of wind by fire in longitudinal direction

Figure 5-3 compares the distribution of longitudinal velocity at the centreline plane (Y=0) for line source and point source cases. Dash-lines shown in Figure 5-3 (a) and (b) represent the characteristic longitudinal locations at which cross-sectional normalized longitudinal velocity distribution is plotted in Figure 5-4. In Figure 5-3, it is seen that velocity is enhanced in both cases. However, the enhancement in the line source case is much stronger than in the point source case even though heat release rate per unit fuel surface area and wind velocity are the same. Figure 5-3 also demonstrates that in the line source case, the plume is attached to the ground for comparatively a long distance before it is lifted off the ground by buoyancy. This is a manifestation of the Coanda effect that was also observed in a previous study (He et al. 2011a). In the point source case, the Coanda effect is much weaker and almost unobservable. Hence, the plume lifts immediately downstream of the fire source. Moreover, in the line source case, the wind is enhanced in a larger region, compared to the point source case. It is observed that in both Figure 5-3 (a) and (b), wind velocity is significantly reduced downstream of the plume region once the plume lifts from the ground. The buoyancy force creates the upward motion of the fluid and by continuity, the surrounding air needs to move in to replenish the plume region. For the line source fire, in the upstream entrainment, the replenishment is accomplished by wind flow. For the downstream region of the plume, a low-pressure region is created to draw in and replenish the flow. Formation of the low-velocity region downstream of the plume was observed in previous studies investigating jet-cross-flow (Margason 1993) and buoyant plume-crossflow interactions (Eftekharian, et al. 2019; Hattori et al. 2013; Wang, Chenglong et al. 2019).

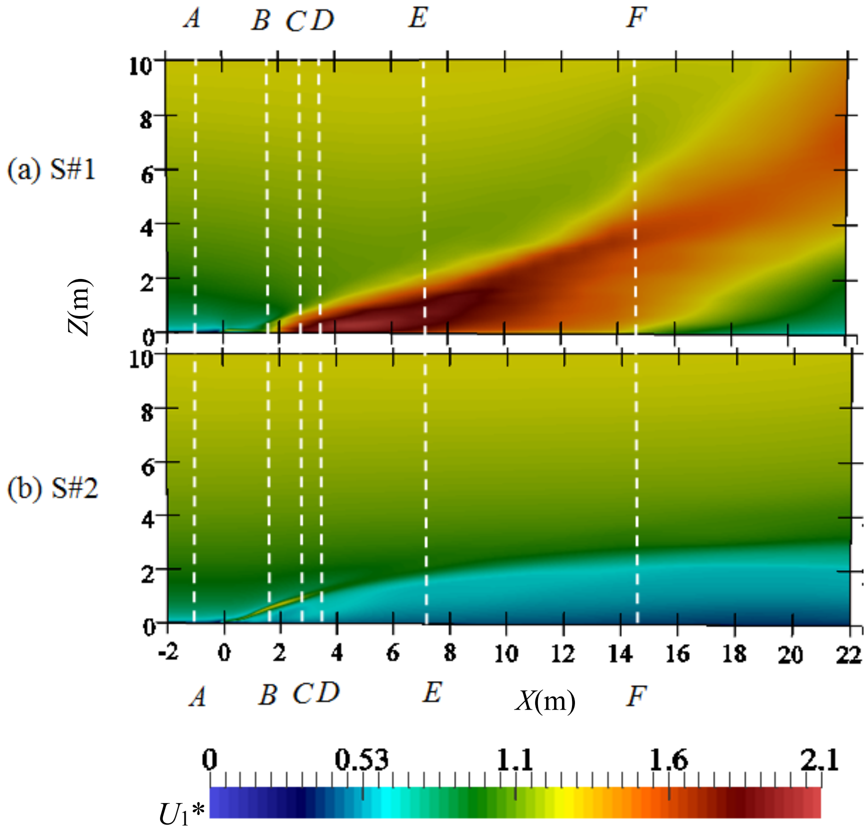

Figure 5-3 Comparison of normalized longitudinal velocity (U_1*) for (a) line source and (b) point source case at *Y*=0

To highlight the differences in the wind enhancement by the two fire sources, the normalized longitudinal velocity planar distributions at different cross-sections downstream of the fire source (which are indicated by dash-lines in Figure 5-3) for both line and point sources (S#1 and S#2) are presented in Figure 5-4. For point source fire, normalized plume longitudinal velocity ($U1^*=\frac{U_1}{U_\infty}$) first increases immediately downstream of the fire source [Figure 5-4(b); S#2] and then undergoes a reduction further downstream [Figure 5-4 (c), (d), (e) and (f); S#2]. For line source fire, the increase in the normalized plume longitudinal velocity downstream of the fire source is slower than that for the point source [Figure 5-4 (b), (c) and (d); S#1]. The slighter reduction occurs further downstream [Figure 5-4 (e) and (f); S#1]. Meanwhile, the region of velocity enhancement is expanded. Apart from the dissimilarity in the fire-wind enhancement trend, there are fundamental differences in the flow field structures of the two cases. The enhancement region appears quasi-homogeneous along the transverse direction (*Y* direction) in the line source fire case. On the other hand, a horse-saddle shape of the enhanced region is observed for pool fire case, indicating the three-dimensional effect and the formation of vortices in X direction. This observation is in agreement with the similar findings reported in the literature (Margason 1993) for the case of the vertical jet in cross-flow. The horse-saddle shape of the enhanced region in S#2 also indicates that the strongest enhancement is not along the center plane (Y=0) of the pool fire plume. Plume entrainment and formation of counter-rotating vortices at each side of the plume centreline are believed to be responsible for the higher velocity at each side than along the plume centreline in the pool fire case. It is believed that Rayleigh–Taylor instability causes the formation of the mushroom structure at a near ground region immediately downstream of pool fire source [Figure 5-4 (b) S#2]. Gradually, these mushroom structures grow and are shifted upward and form vortical structures as observed in Figure 5-4 (d), (e) and (f). These results are in agreement with those observed in Eftekharian et al. (2019).

In order to explain the trends observed in Figure 5-4, it is required to understand the factors and mechanisms that result in the wind velocity enhancement downstream of the fire. Due to the interaction of fire and wind, a longitudinal pressure gradient is induced by the fire to its surrounding region within which the density is comparatively low. This favorable pressure gradient represents a fire-induced force which according to the Eq. (3-6) accelerates the flow and causes enhancement of free-stream wind velocity in the longitudinal direction (Eftekharian et al. 2019).

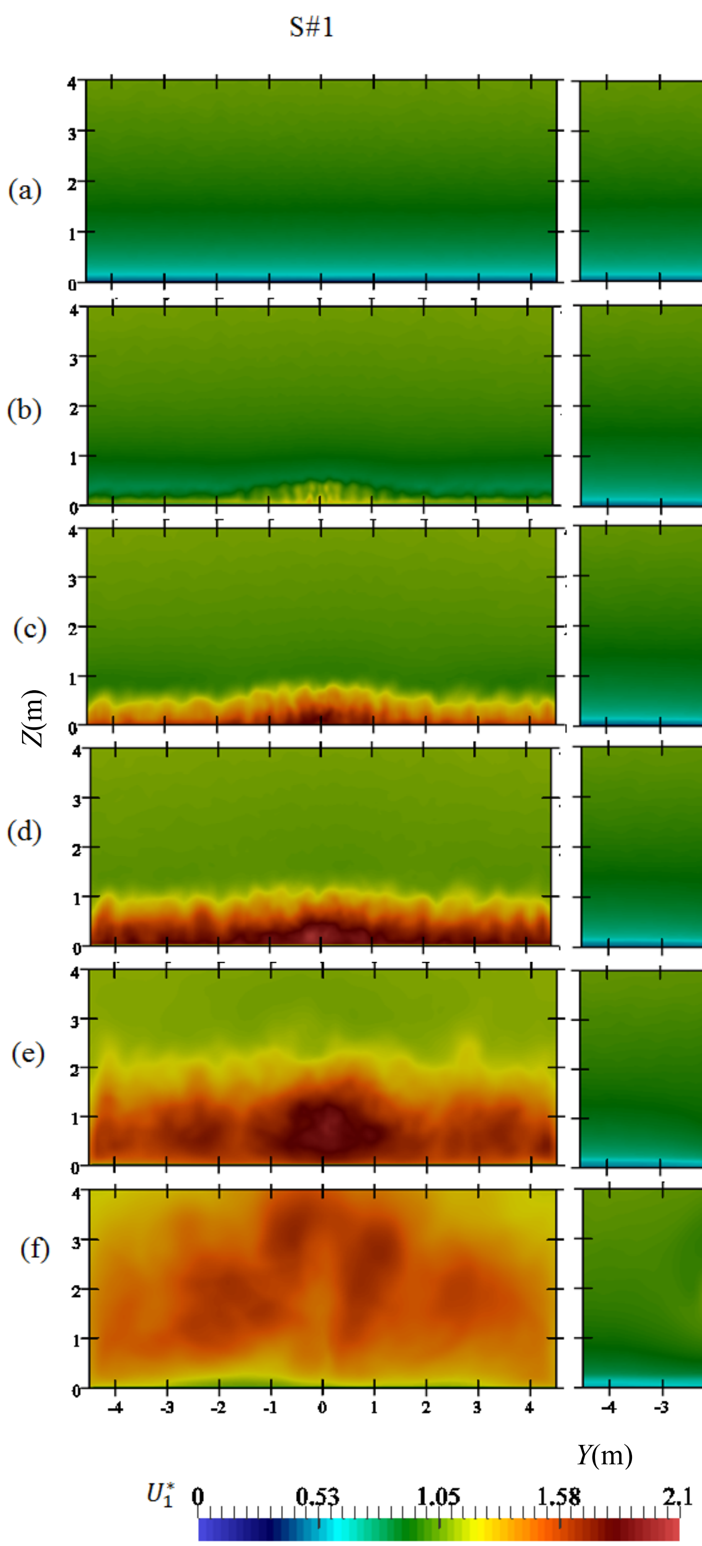

Figure 5-4. Comparison of normalised longitudinal mean velocity planar distributions for line (S#1) and point (S#2) fire sources at various longitudinal locations: (a) *X*=-3*D*, (b) *X*=6*D*, (c) *X*=9*D*, (d) *X*=12*D*, (e) *X*=24*D* and (f) *X*=48*D*

Figure 5-5 shows the cross-sectional distribution of normalized longitudinal pressure force, normalized density, normalized longitudinal pressure acceleration and normalized longitudinal velocity at X=9D downstream of the fire source. As shown in Figure 5-4 and Figure 5-5, wind velocity enhancement is significant for both line and a point source of fire at X=9D.

According to Eq. (3-6), the maximum acceleration and correspondingly velocity enhancement happen where the density is relatively low and the value of pressure gradient is relatively high. This happens within the plume region as can be seen in Figure 5-5 (a) and (b). Normalized parameters used in Figure 5-5 are as below:

Normalized density:$\frac{\rho}{\rho_\infty}$

Normalized fire-induced force:$\frac{\rho\vec{a}}{\rho_\infty U_\infty^2/D}$

Normalized fire-induced acceleration: $\frac{\vec{a}}{U_\infty^2/D}$

Figure 5-5 (a) and (b) show that in both line and pool fire sources, a longitudinal pressure force is generated within the plume region (low-density area) which culminates in the generation of longitudinal acceleration and enhances the wind velocity. However, in the case of line fire, the more intense pressure gradient is generated in a comparatively lower density region which results in a higher wind enhancement, compared to the point source case.

Apart from the quantitative difference of wind enhancement in the line and pool source fires, the enhancement region is also different in the two cases. In the case of pool fire, there is a horse-saddle shape region where the wind is enhanced, while in line fire source, wind enhancement happens along a line parallel to the fire source. The reason is that the two factors (high-pressure force and low density) that cause wind enhancement are generated within the plume region. Hence, the plume region shape determines the region where velocity enhancement has the potential to happen. When the flow is accelerated, the displaced air within the plume region is replenished by the surrounding air through the entrainment process. Therefore, when the flow within the plume region is accelerated in the positive X direction, the entrainment process necessitates the surrounding flow to be negatively decelerated in the X direction, as shown in Figure 5-5 (c). The entrainment process plays an important role in shaping the plume region (where velocity enhancement happens). In the pool fire case, entrainment from around the perimeter of the plume happens by the generation of vortices (Margason 1993) which results in the horse-saddle shape of the plume. In the line fire source case, flow is only entrained from the fire source top region which causes the plume to be formed homogeneously along a line parallel to fire line source. Figure 5-5 also confirms that in the point source case, a low-velocity region is formed below the plume region along the domain centreline. This low-velocity region is formed because of the formation of a wake region as a result of the interaction of wind with pillar-jet-like fire buoyant plume which was observed in previous studies (Eftekharian et al. 2019). In this case, buoyant plume acts as a jet blockage against wind and creates a low velocity behind the plume once it lifts from the ground further downstream of the fire source. Formation of the low-velocity region downstream of the plume was observed in previous studies investigating jet-cross-flow (Margason 1993) and buoyant plume-cross-flow interaction (Eftekharian et al. 2019; Wang et al. 2019).

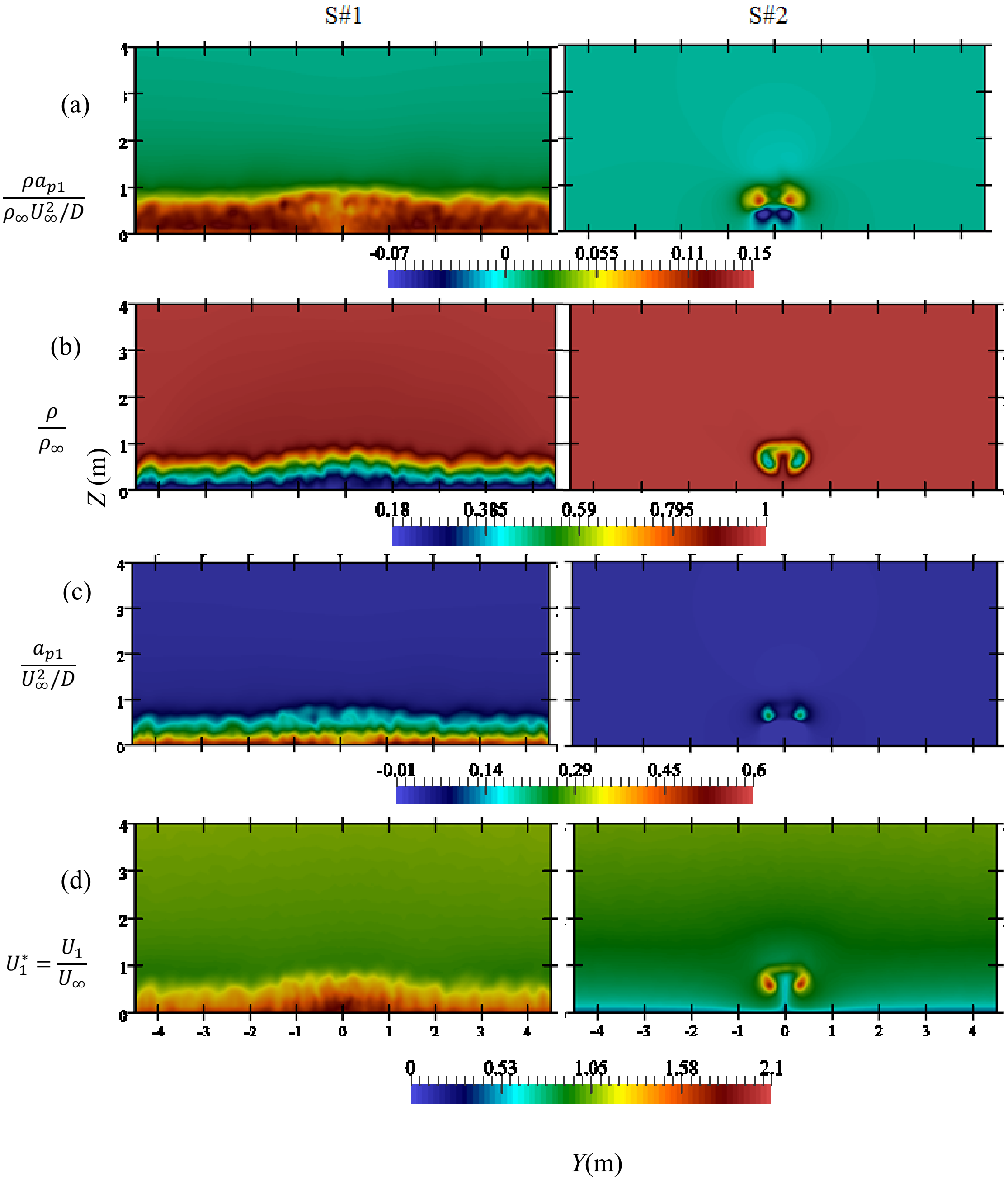

Figure 5-5 Cross-sectional distributions of (a) normalized longitudinal pressure force (b) normalized density (c) normalized longitudinal pressure acceleration and (d) normalized longitudinal velocity at X=9D for line fire case (left column) and point source case (right column).

According to Eq.(4-1), the total longitudinal force induced by the fire consists of two components: pressure force and viscous force. These longitudinal components of fire-induced longitudinal forces are plotted in Figure 5-6. High level of similarity between the distribution of longitudinal fire-induced total and pressure force indicate that pressure force plays a dominant role in fire wind enhancement, while, fire-induced viscous forces have a marginal impact on the phenomenon.

Figure 5-6 (b) shows that fire-induced viscous forces are concentrated on the plume region where fire-induced pressure forces are dominant. This is because the fire-induced pressure force enhances the longitudinal wind velocity which creates velocity gradient. According to the Eq. (3-2), the generation of viscous forces are dependent upon the existence of the velocity gradient. Therefore, fire-induced viscous forces are indirectly caused by fire-induced pressure force.

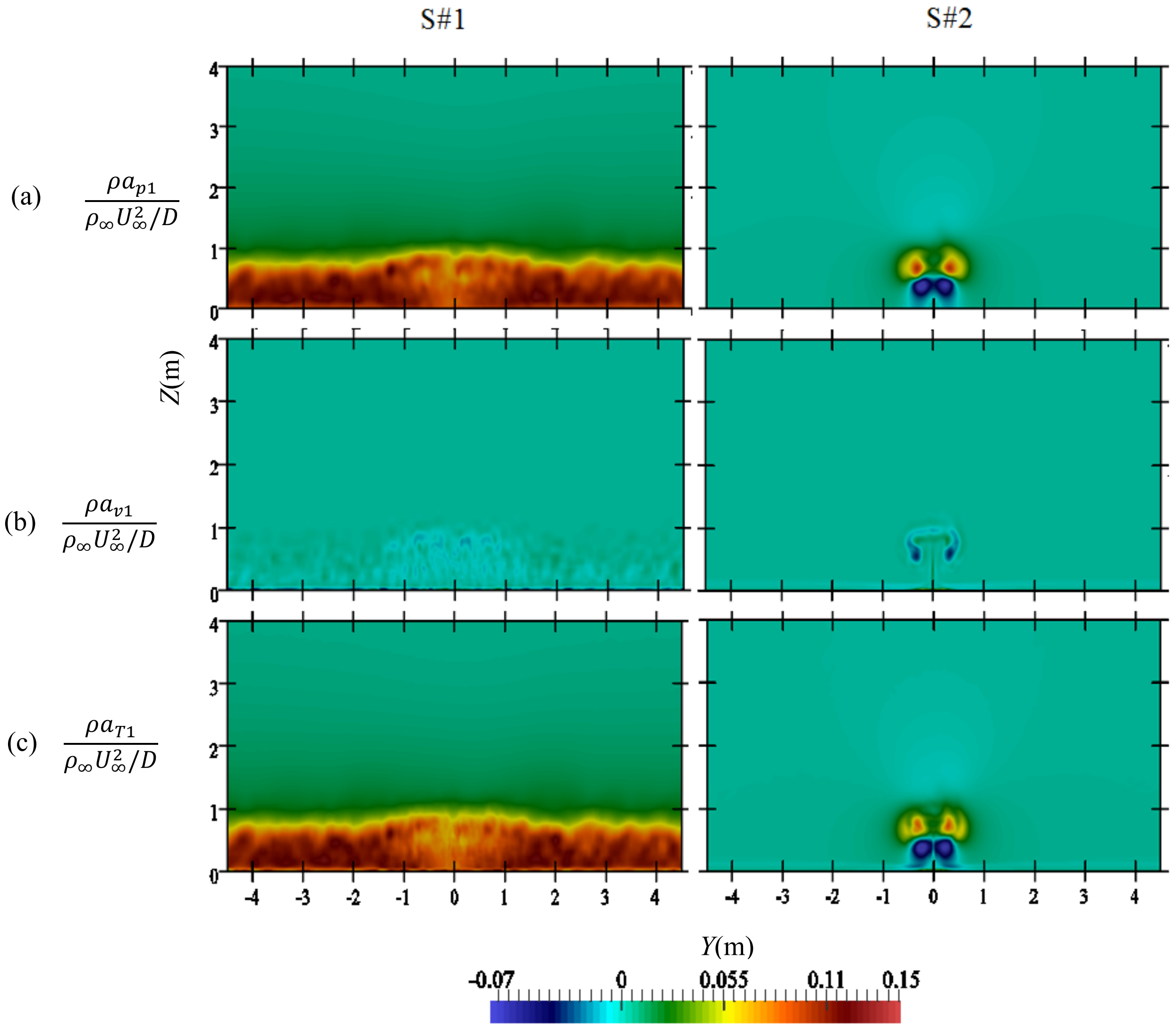

Figure 5-6 Distribution of fire-induced longitudinal (a) pressure force (b) viscous force and (c) total force at X=9D for the line (left column) and pool fire (right column) source.

Figure 5-6 also shows that in contrast to the line fire case in which only viscous acceleration causes deceleration, in the point fire scenario, pressure acceleration also takes negative values below the plume region. The main reason can be traced to the entrainment process. In the line source case, the entrained flow to replenish the upward motion is sourced by wind, while in the point fire scenario, flow is entrained from the plume surrounding region as well.

5.6.4. Vertical velocity distribution

Vertical velocity follows a different trend. Figure 5-7 (a) compares normalized cross-sectional vertical velocity at 9*D* downstream of the two fire sources. As can be observed, in contrast to the longitudinal velocity distribution in Figure 5-5 (d), the fire-induced vertical velocity of point source fire is significantly higher than that of the line fire source. This is mainly because, in the point source case, fire-induced total vertical force [Figure 5-7 (b)] is more intense than that of line source in the plume region. Figure 5-7 (a) provides further evidence of the existence of longitudinal vortices in the point fire source (S#2 cases). The central region of the plume has upward movement whilst that outer region of the plume displays downward movement. According to Eq. (4-1), fire-induced total vertical force is a summation of fire-induced pressure force, fire-induced viscous force, and gravity force. The magnitude of the total fire-induced vertical force in the plume region for the point source case is significantly higher than the line source scenario [Figure 5-7 (b)] which results in a higher fire-induced vertical velocity for the point source than the line source case [Figure 5-7 (a)]. This is mainly because out of the three contributing fire-induced vertical forces (pressure force, gravitational force and viscous force), the fire-induced pressure force is more dominant in point source fire. Besides, Figure 5-7 shows that in contrast to the longitudinal acceleration in which gravitational acceleration is non-existence (Figure 5-5), gravitational acceleration noticeably affects the total vertical acceleration. Figure 5-7 also shows that although vertical pressure acceleration is positive in all domains including the plume region, total acceleration takes negative values in near plume region due to the combined effects of gravitational acceleration and viscous acceleration.

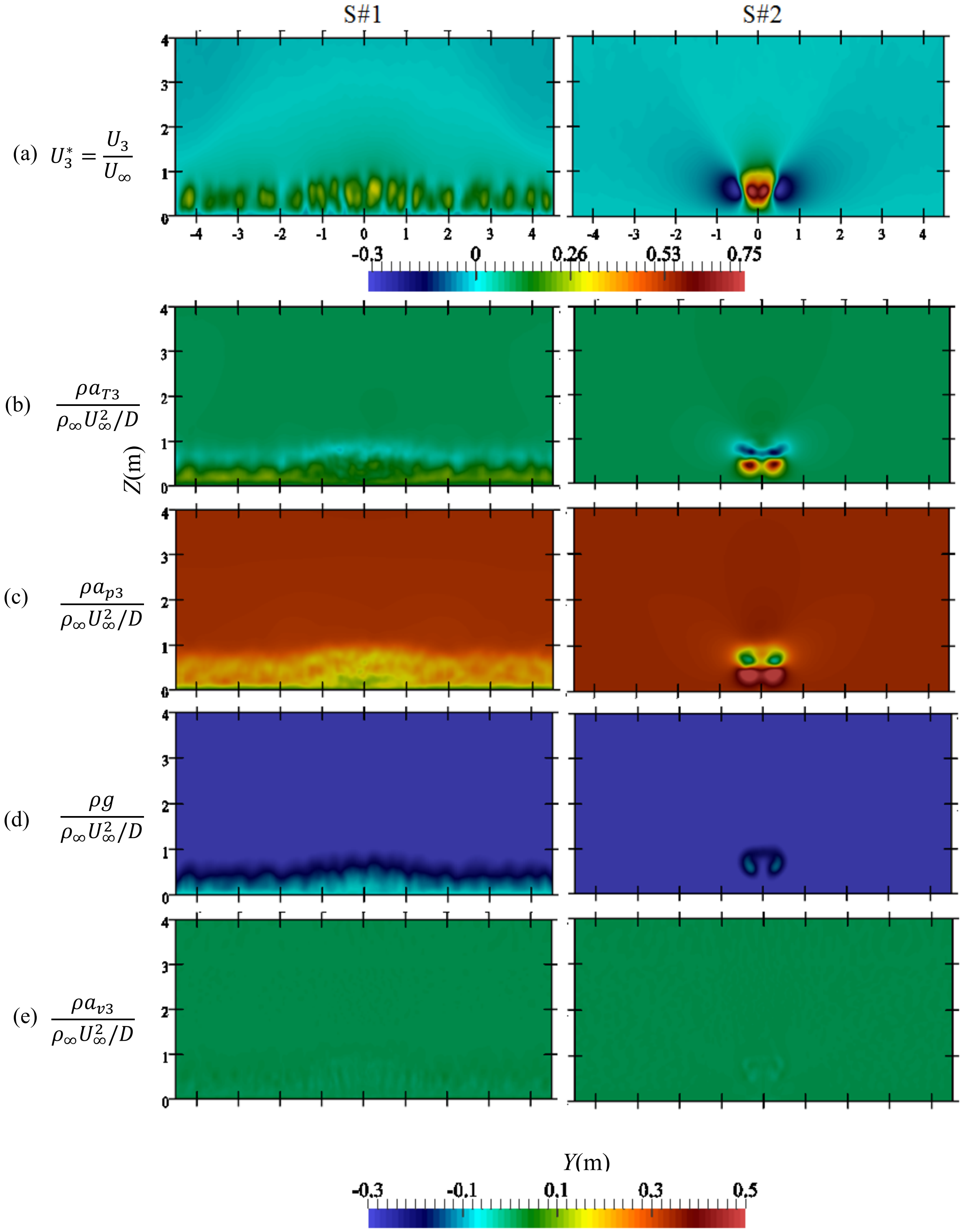

Figure 5-7 Distribution of normalized vertical (a) velocity (b) fire-induced total force (c) fire-induced pressure force, (d) gravitational force and (e) fire-induced viscous force for line fire case (left column) and point source case (right column).

Figure 5-8 demonstrates the vertical distributions of normalized longitudinal (U_1*), spanwise (U_2*), vertical (U_3*) and total velocity [= $(U_1^{*2} + U_2^{*2} + U_3^{*2})^{1/2}$] profiles at different distances downstream of the fire source on the plane Y=0 for both line and point source cases. Figure 5-8 shows that longitudinal velocity is dominant at almost all distances downstream of the fire source, whereas velocity in spanwise direction takes the lowest velocity component value. Figure 5-8 confirms the trend observed in Figure 5-3 and Figure 5-4 and shows that in both line and point source cases, enhancement in longitudinal and vertical velocity happens in the plume region, as shown in Figure 5-5 and Figure 5-7. Flow in the plume region (low-density region) is enhanced by fire-induced pressure force. This region is more expanded as the longitudinal distance from the fire increases, as shown in Figure 5-8. Figure 5-8 also shows that for the line source simulation scenario, the enhancement region attaches to the ground downstream of the fire source and then starts to shift vertically. This is mainly because the plume region for line fire is attached to the ground downstream of the fire. This trend is also observed in previous studies (He et al. 2011a; Kwok, He & Douglas 2012).

Moreover, in both line and point source cases, vertical velocity starts to increase once the plume lifts up from the ground and this is because plume detachment from the ground happens where the buoyancy force is strong enough to overcome the Coanda effects and lifts the plume up.

Air flow path-lines generated from near ground inlet surface ($-1 \leq Y \leq 1$ and $0 \leq Z \leq 2$) for the two fire sources are shown in Figure 5-9. Streamlines and surfaces are colored by velocity magnitude. Similar to the previous figures, the airflow path-lines and the velocity are averaged through the last 12 seconds of the simulation.

The effects of fire on the free-stream fluid particles can be vividly seen in Figure 5-9 which shows that under constant fire intensity, both line and point source affect air flow free-stream path-lines as well as velocity. However, the effects of line fire on the distortion of fluid path-lines as well as enhancement of free-stream velocity are much more significant than the point fire source. This is because the fire-induced total force in the line source is stronger than the point source resulting in the generation of a more intense fire-induced longitudinal pressure gradient. Figure 5-9 shows that in point and line fire source scenarios, fire-induced wind enhancement region starts from the near ground at immediately downstream of the fire source and gradually lifts up by the increase of distance from the fire source. Moreover, in the line-source case, homogeneity in flow and wind enhancement in span-wise (Y) direction can be observed, while the point-source of fire causes symmetrical wind enhancement configuration in the domain. In fact, the nature of flow in the point source case can be considered three- dimensional, whereas, the line source case creates a quasi-homogeneous two-dimensional flow. The twisted flow path-lines in Figure 5-9 (b) is another evidence of longitudinal vortex.

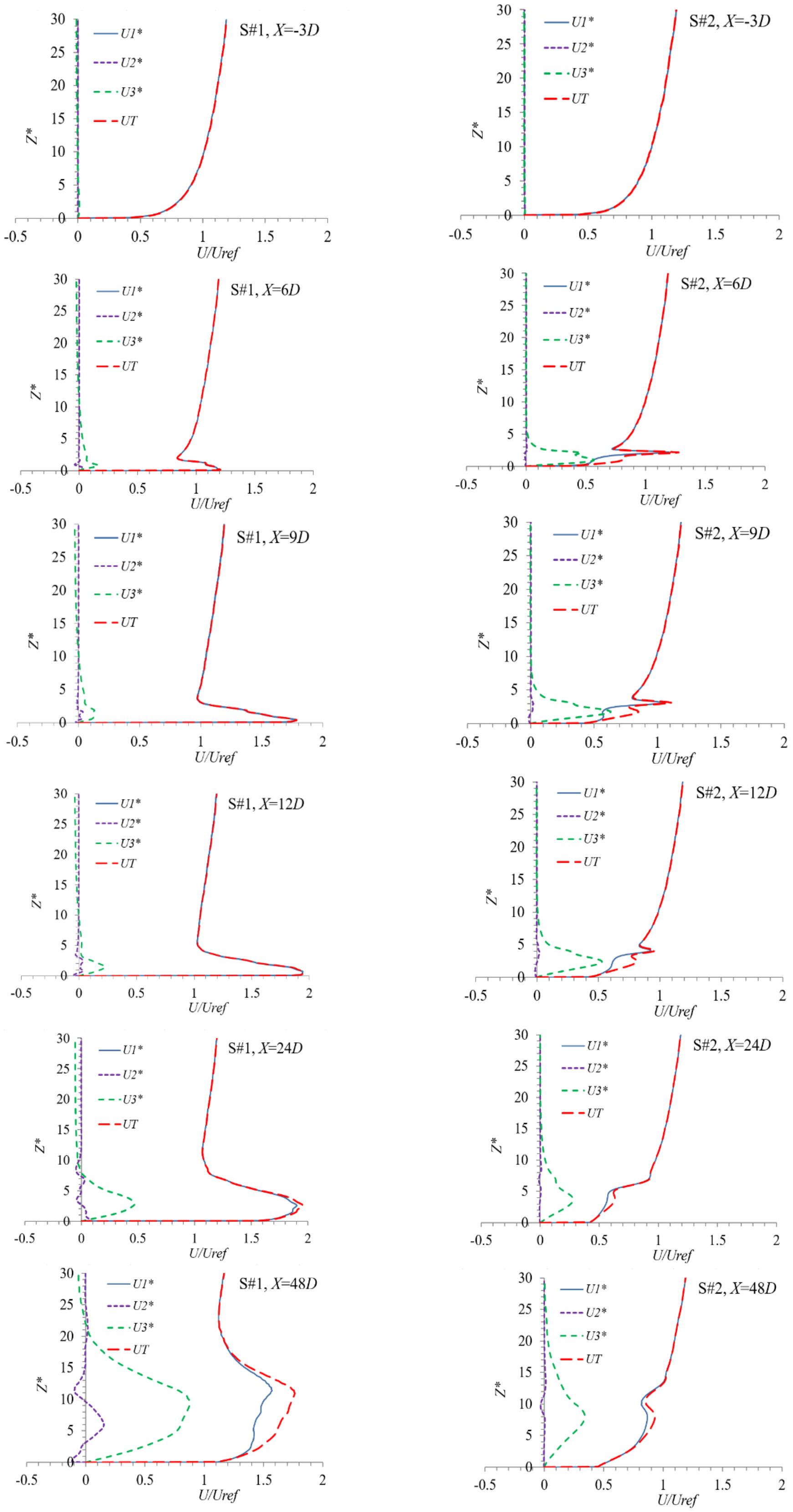

Figure 5-8 Comparison of the normalized vertical distribution of longitudinal, spanwise, vertical and mean velocity profile at different distances downstream of the fire on the plane *Y*=*D* for line fire (left column) and point source (right column).

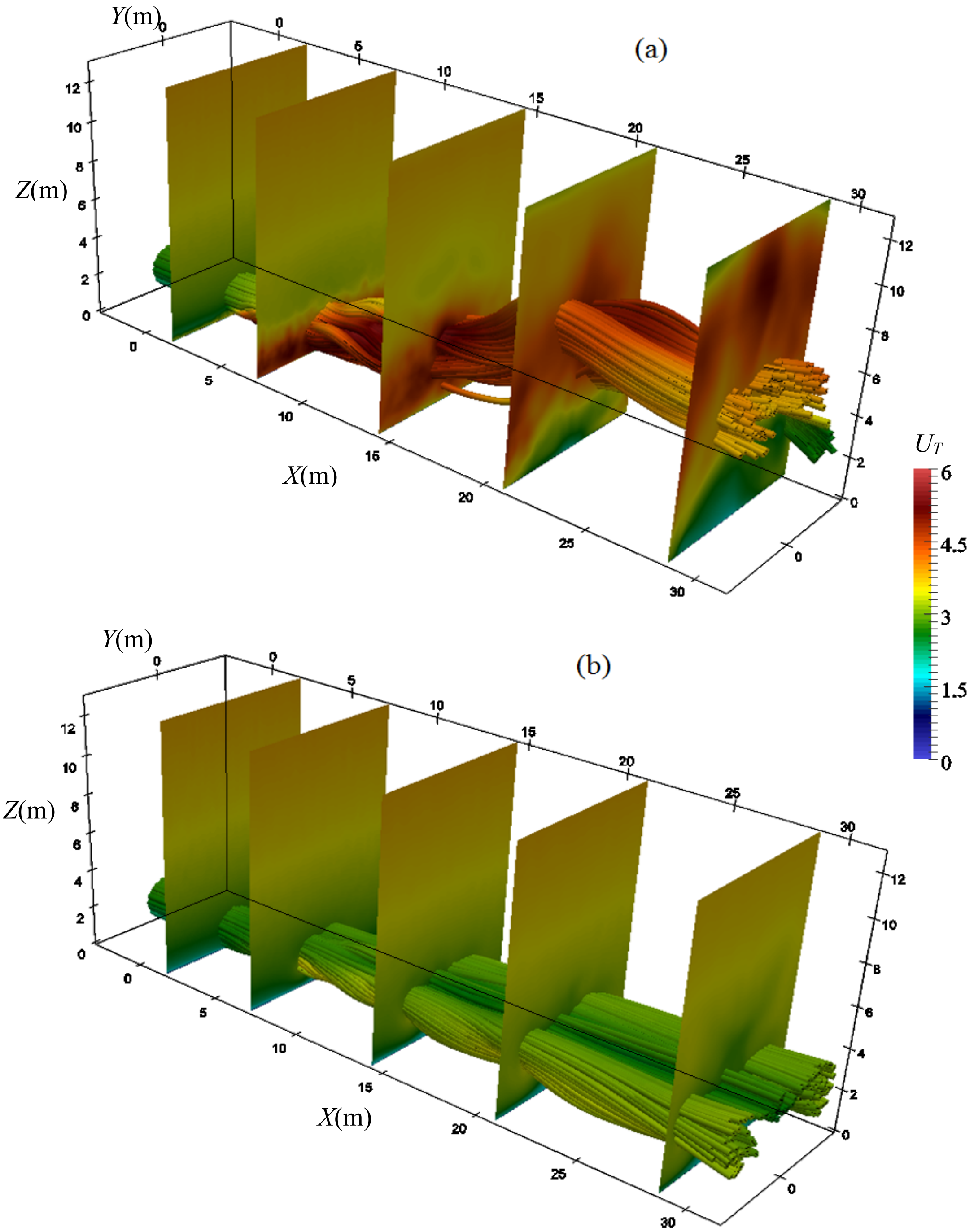

Figure 5-9 Air flow path-lines generated from a cross-cut of near ground inlet surface ($-1 \leq Y \leq 1$ and $0 \leq Z \leq 2$) for (a) line source and (b) point source fire cases.

To determine the flame contour, one approach is to plot iso-contour of mixture fraction at stoichiometric value. Stoichiometric mixture fraction (Z_{st}) can be defined as below (Mahalingam et al. 1999):

$$Z_{st} = \frac{1}{(1+\varphi)} \tag{5-7}$$

where φ is the equivalence ratio $s_a(\frac{\gamma_f}{\gamma_{air}})$ in which s is air required to burn a unit mass of fuel completely, γ_f and γ_{air} are respectively, mass fractions of fuel and air in the unmixed state (Heskestad 2016; Mahalingam et al. 1999). Figure 5-10 shows the iso-contour of the mixture fraction, colored by normalized longitudinal velocity for both line and point fire source cases. Hence, Figure 5-10 shows how longitudinal velocity varies in the fire flame region. Figure 5-10 shows that the enhanced wind velocity in line source case significantly exceeds that of point source case. Moreover, Figure 5-10 reveals that both wind enhancement and flame region are distributed homogeneously and symmetrically in line and point source cases, respectively. Also, Figure 5-10 confirms that the flame length in line source case is much higher than that of the point source case.

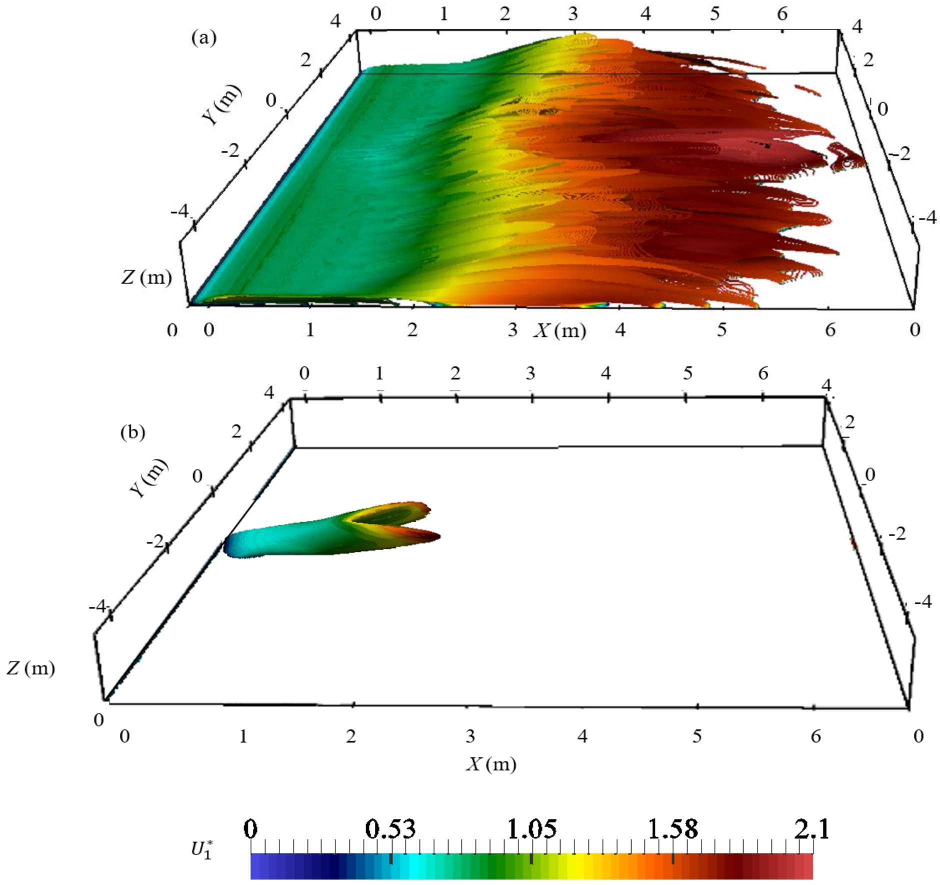

Figure 5-10 Iso-contour of mixture fraction coloured by normalised longitudinal velocity for (a) line fire source (S#1) and point source case (S#2).

5. 7. Conclusion

This study investigated the differences in fire-wind enhancement phenomena associated with two types of fire sources, namely line, and pool (point) fire sources. In an analogy to the non-dimensional description of the heat release rate of pool fires, a non-dimensional line source fire intensity is introduced based on an equivalent hydraulic diameter for the line source that has a finite depth. Because of the differences in the source configuration and the dimension of the burning surface area, the interactions between the two types of fires and wind yielded dramatically different results. The findings of this study can be summarized as below:

(1). Interaction of wind and fire generates a longitudinal fire-induced pressure force which results in wind enhancement within the plume region downstream of the fire.

(2). For constant heat release rate per unit area, the line source fire induces a higher longitudinal force which leads to a higher wind enhancement compared to the pool fire source.

(3). In contrast to the longitudinal (wind) velocity enhancement trend, fire-induced vertical velocity in point source case is considerably higher than the line source scenario under constant heat release rate per unit area. This is because vertical fire-induced total force in the pool fire case is higher than that in the line fire scenario.

(4). There is a fundamental difference in the wind enhancement region between line and pool fire cases. The pool fire enhancement region takes a horse-saddle shape, while in the line source case wind enhancement region happens in a belt parallel to the fire source. The reason was found to be rooted in the difference in the plume region shape as well as the entrainment process between line and pool fire cases. Moreover, in the line source case, homogeneity of wind enhancement is observed in the span-wise direction which is indicative of two-dimensional flow. However, in the point source case, the symmetrical behavior of wind enhancement against the domain centreline can be observed.

CHAPTER 6. CORRELATIONS FOR FIRE-WIND ENHANCEMENT FLOW CHARACTERISTICS BASED ON LES SIMULATIONS

In previous chapters, the effects of factors contributing in enhancement of wind with fire including, fire heat release rate, free-stream wind velocity and fire source configuration were studied separately. However, combined (simultaneous) effects of these parameters were not studied. This chapter presents a range of simulation scenarios defined for different combinations of upstream wind velocity and fire intensity of a line source fire which resembles an evolved bushfire source. The combined effects of upstream wind velocity and fire intensity on wind enhancement are investigated. A correlation is developed to determine the maximum wind enhancement as a function of the Froude number and normalized line fire intensity representing free-stream wind velocity and fire source heat release rate, respectively. A correlation is also developed for the longitudinal location at which maximum wind enhancement occurs as a function of the Froude number and normalized fire intensity. Furthermore, the concept of a wind enhancement plume line is defined as a line along which the local wind enhancement occurs at a given longitudinal location downstream of the fire source, for which a correlation is also developed. Moreover, a gradual decaying trend is observed in wind enhancement after reaching a peak along the wind enhancement plume line in all simulation scenarios and a correlation is developed as a function of normalized longitudinal direction.

A reprint of this study entitled “Correlations for fire-wind enhancement flow characteristics based on LES simulations”, **Esmaeel Eftekharian**, Maryam Ghodrat, Yaping He, Robert H. Ong, Kenny C.S. Kwok, Ming Zhao published by “*International Journal of Heat and Fluid Flow”* 2020, Volume 82, Article No. 108558 is appended in Appendix. 4.

https://doi.org/10.1016/j.ijheatfluidflow.2020.108558

6.1. Abstract

Unraveling the physics of fire-wind interaction has long been a subject of interest. Among all the physics involved, enhancement of wind by fire deserves great attention due to its potential effects on building structures downstream of the fire source in bushfire attack events. Predominantly, two contributing factors determine the extent to which wind is enhanced by fire: free-stream wind velocity and fire intensity. This study employs Large-Eddy Simulation (LES) to fundamentally investigate the combined effects of free-stream wind velocity and fire intensity on fire-wind enhancement. An added module was implemented to an open-source transient fire solver in order to analyze the effects of free-stream wind velocity and fire intensity based on the analysis of interactions between momentum and fire-induced buoyancy forces. Simulations are performed for parametric combinations of wind velocity and fire intensity. The LES results demonstrate that the maximum wind enhancement increases with a reduction of free-stream wind velocity and an increase in fire intensity. The non-dimensional Froude number, Fr, and normalized fire intensity, I^*, were employed to quantify the effects of free-stream wind velocity and fire intensity, respectively. A correlation was developed to determine the maximum wind enhancement as a function of Fr and I^*. The location corresponding to maximum wind enhancement occurs further downstream of the fire source as free-stream wind velocity or fire intensity increases. A correlation based on the Fr number and I^* was developed for the location at which maximum wind enhancement occurs. Furthermore, the concept of wind enhancement plume line was defined as a line along which the local wind enhancement occurs at a given longitudinal location downstream of the fire source, for which a correlation was also developed. Moreover, a gradual decaying trend is observed in wind enhancement after reaching a peak along the wind enhancement plume line in all simulation scenarios for which a correlation was also developed as a function normalized longitudinal direction.

6.2. Introduction

Wind-driven fires are complex phenomena as a result of various compound processes. On the other hand, the understanding of wildland fire is of great importance to lessen the risk of bushfire attacks and to increase our capability to predict their behavior (Hu 2017). A detailed understanding of the dominant feature and the behavior of wind-driven fire assists us to better manage fire-induced changes in flow aerodynamics which plays a pivotal role in measuring potential fire threats.

Theoretical investigation offers a decent comprehension of buoyant diffusion flames from axisymmetric, line and pool fire sources in no-wind condition (Quintiere & Grove 1998). However, the knowledge behind wind-blown diffusion flames requires more robust theoretical framework combining the semi-empirical flame-size correlations attained from the broad number of wind tunnel data (Hu et al. 2017; Lam & Weckman 2015; Lin et al. 2019; Lin, Zhang & Hu 2018; Nelson & Adkins 1986; Sun et al. 2019; Tang et al. 2015; Tang, Miller & Gollner 2017; Thomas, Pickard & Wraight 1963; Thomas 1963; Wang et al. 2019; Zhang et al. 2016).

The comprehensive numerical models (Mell et al. 2013; Morvan & Dupuy 2001; Morvan & Dupuy, 2004; Zhou, Mahalingam & Weise 2005) can be helpful to enhance the knowledge behind the mechanisms that are accountable for the fire-wind interaction and the geometric properties of the flame but these models are highly computationally demanding which make them not very attractive particularly for estimating large fire characteristics. Some simplified models have been proposed by other researchers (Balbi et al. 2007; Koo et al. 2005; Margerit & Séro-Guillaume 2002) in this regard. These models commonly need input parameters, which depends on fire profile itself such as the flame length and tilt angle. The value of these input parameters are generally identified from experimental measurements (Koo et al. 2005; Weise et al. 2016) and outputs of these models help to deliver detailed insight into fire behavior. These physics-based models have the potential to be used as a substitute method to regulate and generalize experimental model parameters.

In spite of the abundance of simplifies models/correlations for flame geometry, the literature lacks model development for flame flow characteristics. This study aims at filling the knowledge gap in this regard by presenting correlations for flow velocity affected by fire-wind interaction. The appropriate non-dimensional groups (Froude number and non-dimensional fire intensity) reflecting the contributing forces in fire-wind interaction scenarios are employed to develop these correlations. Bushfire-wind enhancement is one of the implications of the current study in which the wind enhancement by bushfire causes increase of pressure coefficient around the buildings and damaging building structures downstream of the bushfire source.

6.3. Fire-wind interaction

The spread rate of wildland fire escalates with growth in wind speed, which clarifies the great importance of wind-blown flames in the bushfire. Laboratory-scale (Mendes-Lopes, Ventura & Amaral 2003; Nelson & Adkins 1986) and field-scale (Butler et al. 2004; Gould et al. 2007) experiments showed that the fire spread rate intensifies with wind speed. It was also noted that even though the general behavior of the fire spread observed was consistent, the scattered data measured in the experiment make it hard for the case to case comparison with the numerical modeling (Mendes-Lopes, Ventura & Amaral 2003).

The pioneer studies by Thomas and his co-workers (Thomas, Pickard & Wraight 1963; Thomas 1963a) on the effect of wind on flame characteristics of finite burning surface area (natural fire) revealed that the dimensionless flame length is governed by the dimensionless burning intensity (or burning rate per unit area) and the modified Froude number as:

$$L_f^* = 70\dot{m}''^{*0.86} Fr_D^{-0.11} \qquad (6\text{-}1)$$

where $\dot{m}''^{*}$ is the non-dimensional burning rate per unit area; defined as $\dot{m}''^{*}_{fu} = \dot{m}''_{fu}/(\rho_\infty \sqrt{gD}\,)$ in which $\dot{m}''$ is the burning rate per unit area (kg.m^{-2}.s^{-1}), g is gravitational acceleration and D is flame depth (m). The modified Froude number ($\mathrm{Fr_D}$) is defined on the basis of freestream velocity and characteristic buoyancy force as: $\mathrm{Fr_D} = U_\infty^2/(\,gD\,)$.

The low value of the exponent of the modified Froude number (-0.11) in Eq.(6-1) suggests a small direct effect of wind velocity on flame length. However, the observed reduction in flame length with an increase in wind velocity is believed to stem from more effective plume entrainment (Thomas, Pickard & Wraight 1963). From fire experiments in pine needle fuel beds, Hilton and Miller (2015) suggested an exponent factor of 0.86 instead of 0.97 in Eq. (6-1). Furthermore, they proposed that the tangent of the flame tilt angle (hereafter called tilt coefficient of the flame) is proportional to p_dU_∞/E_r, where p_d is the dynamic pressure of the ambient wind and E_r the equivalent unit energy release rate of the fire.

Putnam (1965) derived formula for calculating flame heights and horizontal extensions of the flame for natural-gas line fires using experimental data. Normalizing the flame height in wind presence (H_f) with that in the absence of wind, H_{f0}, Putnam presented a correlation for flame height under wind condition:

$$\frac{H_f}{H_{f0}} = (\,1 + 4U_\infty^2\ /gH_{f0}\,)^{-1/2} \qquad (6\text{-}2)$$

while the tilt coefficient of the flame is found to be proportional to $(U^2_\infty/gH_{f0})^{-1/2}$, the tangent of the flame angle varied directly with the square root of the Froude number.

Using fuel beds of pine needles with different widths, Rossa and co-authors (Rossa, Davim & Viegas 2015) showed that flame width (corresponding to the width of the fuel bed) has a considerable effect on the total radiation emitted by the flame and then significantly influences the rate of spread.

By conducting experiments of fires propagating with wind through beds of pine needles, Nelson and Adkins (1986) found that the flame length and the tilt coefficient of the flame correlate roughly with the square root of the fire intensity and the Froude number. In the fire experiments concerning individual plant species of hummocks and eucalyptus, Bradstock and Gill (1993) focused on the flammability of individual plant species in relation to flame height or length. Flame length is defined as the distance from the base of the fire source to the tip of the flame and flame height is the vertical distance measured from the ground to the tip of the flame. They found in the case of no wind, flames are vertical and height equates to flame length; whereas with wind, flame height is less than flame length.

One of the primary numerical studies is that of Albini (1981), who developed a one dimensional model for the structure of wind-blown, turbulent flame from a line fire. The model was built based on some assumptions. One assumption is that wind speed was constant, homogeneous combustion happened only above the fuel bed, and combustion products were integrated as a pure gaseous fuel added to the top of the fuel bed with an insignificant speed compared to wind speed. Simulations were conducted for an extended range of Fr_D. Another assumption used in the simulation was that the flame tip was the height at which the mean temperature inclined below 500K and the air entrained up to this height is roughly 10 times as much as the stoichiometric air prerequisite (Albini 1981). Analyzing the numerical outcomes, Albini suggested that the square of tilt coefficient of the flame from vertical is equal to 1.5 of the Froude number defined based on flame height $\left(Fr_{Hf} = {U_\infty^2}/{gH_f}\right)$ where the numerical factor was found to be dependent on the flame tip temperature only (Albini 1981).

Other researchers such as Sinai and Owens (1995) utilized a commercial code, namely FLOW3D, to simulate large-scale unconstrained pool fires exposed to a cross-wind highlighting the flame geometry. Their model was founded on the buoyancy-modified k-ε turbulence model, the Eddy-Break-Up combustion model (Sinai & Owens 1995) and a grey medium estimate for thermal radiation. Morandini et al. (2005) numerically analyzed the impacts of wind on fire plumes by replacing the fuel bed with a 0.25 m×0.4 m propane burner. The combustion route was disregarded in their model with the assumption of uniform heat release within the flame. Morvan et al. (1998)

adopted a multicomponent k - ϵ turbulent reacting flow and numerically investigated the effect of a cross-wind upon the buoyant turbulent flow induced by a diffusion flame. Their outcomes revealed that the flow is characterized by oscillations which influences the flame behavior. These authors also concluded that as the cross-wind velocity escalates, a transition from buoyancy dominated flow to cross-wind dominated flow can be realized along with a cut in oscillation (Morvan 1998).

Of late, Snegirev (2004) used a Computational Fluid Dynamics (CFD) model and simulated the pool fire and crosswind interactions. In his model, Monte Carlo method combined with the Weighted Sum of Gray Gases model was utilized to capture the thermal radiation effects. Snegriev (2004) also concluded that the burning rate rises with wind velocity. These results were found to be in good agreement with experimental observations (Souil, Joulain & Gengembre 1984).

In more recent work, Yoshihara & Torikai (2013) examined flame characteristics of small pool fires in the downslope and upslope angled winds and stated that the alteration between horizontal and angled wind flow is due to the presence of both horizontal and vertical momentum components. Yoshihara and his co-authors suggested a set of reformed semi-empirical correlations for flame length and flame tilt angle calculation for low wind speeds. At the same time, Hu et al. 2013 developed a novel mathematical model based on experiments to establish a correlation for the flame tilt angle of small pool fires. A dimensionless global parameter, linking the wind speed by a characteristic rising velocity of the flame underpinned by the buoyancy strength of the pool fire sources, was suggested, that is shown to better converge and correlate the flame tilt angle data comparing to the previous models.

Tang et al. (2015) also developed a global relation to identify the burning behavior of acetone pool fire-cross-wind conditions. They showed that an increase in cross airflow speed, leads to a higher mass burning rate in relative smaller pool fires.

The influence of cross-wind on flame drag base length was also examined experimentally (Lam & Weckman 2015; Lin, Zhang & Hu 2018; Tang, He & Wen 2019). The flame drag length is associated with the unburnt fuel adjacent to the burner surface and dragged towards the downwind direction. Dimensionless correlations for the flame base drag length have been suggested by several researchers (Hu et al. 2017; Raj 2010; Tang, Miller & Gollner 2017). Flame sag is another phenomenon during fire-wind interaction that was studied in previous works (Lautkaski 1992; Rew, Hulbert & Deaves 1997; Zhang et al. 2019)

The previous studies presented correlations for flame geometries such as flame length, flame height, and flame tilt angle under cross-flow conditions (Hu et al. 2011; Lin et al. 2019; Liu & Hu 2019; Lu et al. 2019; Ping et al. 2018; Wang et al. 2019). However, no correlations have been reported in the literature for aerodynamic characteristics of the flame. Nmira et al (2010) showed that Froude number (which takes into account wind effects) and dimensionless heat release rate (for point source fire) and dimensionless fire intensity (for line source fire) are appropriate non-dimensional groups [Eq.(6-3) and (6-4)] to develop correlations for flame geometrical features such as flame length, height and tilt angle in fire-wind interaction scenarios:

$$Fr = \frac{{U_{ref}}^2}{gD} \tag{6-3}$$

$$I^* = \frac{I}{\rho_\infty c_p T_\infty \sqrt{g} D^{(3/2)}} \tag{6-4}$$

It is hypothesized that flame aerodynamic characteristics can also be correlated as a function of these non-dimensional groups as they take into account the important contributing forces (inertia and buoyancy and thermal expansion) during fire-wind interaction:

The interactions between wind and fire are not limited to changes in burning rate and flame geometry. Previous numerical simulation studies showed that interaction of wind and fire can also lead to the increases of wind velocities and pressure load on buildings downstream of a line fire source (He et al. 2011b; Kwok, He & Douglas 2012). Recently Eftekharian et al (2019) performed LES studies to fundamentally investigate the enhancement of wind by pool fire sources and expounded in details of how the interaction of buoyant plume with wind results in augmentation of wind downstream of the fire source. They revealed that the enhancement of wind by fire is triggered by the generation of a negative longitudinal pressure gradient in the low-density region due to fire-wind interaction. In other studies by the same group (Eftekharian et al. 2019; Eftekharian et al. 2018), the influence of freestream wind velocity on the alteration of velocity profile downstream of a point (Eftekharian et al. 2019) and line (Eftekharian et al. 2018) fire source was investigated. Eftekharian et al (2018 & 2019) showed that the effects wind velocity enhancement downstream of the fire source is reduced as free-stream wind velocity increases. Moreover, Eftekharian et al investigated the effects of fire source configuration of the wind enhanced by fire (Eftekharian et al. 2019). It was found that the wind enhanced by a line source of fire is considerably higher than that induced by a point source under the same fire intensity condition. The stronger fire-induced pressure force in line source fire scenario than the point source case was considered as the reason behind this trend (Eftekharian et al. 2019). Eftekharian et al (2019) also investigated the effects of terrain both in upslope and downslope conditions on fire-wind enhancement. They showed that in contrast to the downslope cases, in upslope scenarios an additional component of buoyancy force in wind direction is generated which assists fire-induced pressure force and causes stronger wind enhancement.

The presented literature review confirms that in spite of these recent studies performed in unraveling the physics of the fire-wind enhancement phenomenon, there is still a gap in formulating wind enhancement by fire based on the major contributing factors (wind velocity and fire intensity). This work aimed to fill the gap by developing correlations to determine fire-wind enhancement as a function the contributing non-dimensional groups (Froude number and normalized fire intensity).

The main objective of this study hence is to provide a comprehensive and fundamental understanding of fire-wind enhancement behavior under a range of free-stream wind velocity and line-fire intensity conditions. The final goal is to develop correlations to predict maximum fire-wind enhancement as well as the decay of wind enhancement velocity as a function of the contributing non-dimensional groups.

In summary, Flow characteristics can be correlated with the controlling non-dimensional groups (Fr, I^* and X^*). In other words, there exist correlations in the form of multi-variant functions:

$$U^* = f(\mathrm{Fr}, I^*, X^*) \tag{6-5}$$

where U^* represent generally a flow characteristic. Fr, I^* and X^* are respectively Froude number, normalized fire intensity and normalized longitudinal location from the fire source.

6.4. Numerical Modelling

6.4.1. Overall methodology and simulation strategy

In order to establish the correlations of the form given by Eq. (6-5), a data set (U_{enh}^*, Fr, I^*, X^*) of reasonable size needs to be obtained. A number of simulation scenarios with different free-stream wind velocity and fire intensity inputs were defined to generate sufficient data set of U_{enh}*, Fr, I^*, X^* with the aim to develop trends and correlations between fire-wind enhancement flow characteristics and the appropriate non-dimensional groups (Fr, I^*, X^*). These characteristics include maximum wind enhancement by fire, the corresponding location at which maximum wind enhancement occurs, wind enhancement plume line and the decay of wind enhancement velocity along the plume line. These concepts and parameters will be defined and explained in the following sections.

6.4.2. Modeling software and governing equation

The CFD solver utilized for numerical simulation in this chapter is FireFOAM which is a derivative of OpenFOAM 4.1 platform (Greenshields 2015). FireFOAM uses LES (Large Eddy Simulation) to model turbulent structures in buoyant plumes. FireFOAM solves the Favre filtered compressible Navier–Stokes equations (contunuity, momentum, energy, species, and state equations) to capture turbulent structures of the flow. A module was developed and added to the FireFOAM solver to extract the components of flow acceleration to be used for analysis of wind enhancement by fire.

Details of governing equations as well as implementation of the developed module have been fully discussed in Sections 3.3 and 4.3.

6.5. Computational domain and simulation condition

The computational domain consists of a rectangular box with the dimension of 9×15×34 m as shown in Figure 6-1. A line source of fire with the depth of 0.3m was placed 3m downstream of the inlet as shown in Figure 6-1. The origin of the x-y-z coordinate is set at 3.15 m downstream of the inlet along with domain centreline (at the middle of fire source) as shown in Figure 6-1.

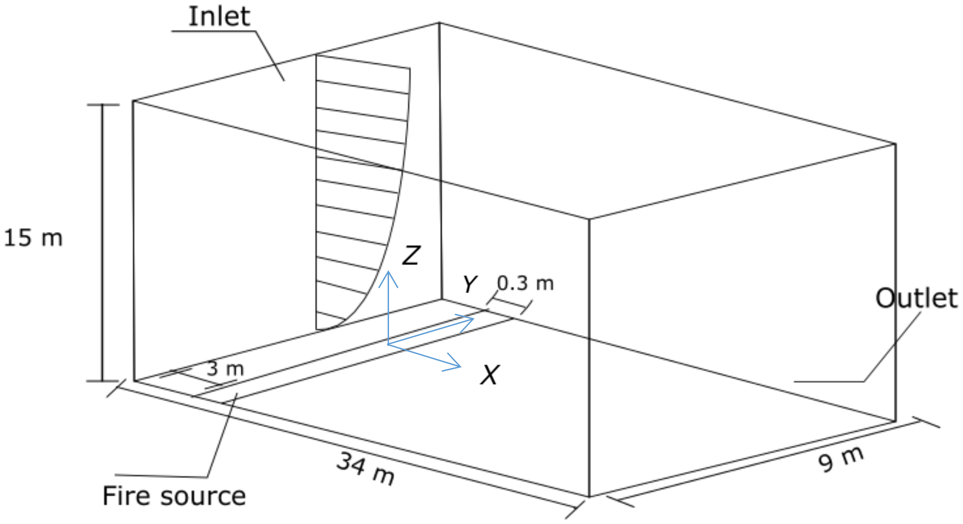

Figure 6-1 Schematic view of the computational domain.

Methane was chosen as the fuel source to be injected from the fire source. Bushfire intensity (*I*) is usually described as the heat release rate per unit width (here 9 m) of bushfire front (Byram 1959), which in this study is 2,3, 4 and 6 MW/m depending on the simulation scenario.

A power law velocity profile representing atmospheric boundary layer profile was used at the inlet on the left side of the domain:

$$U(Z) = U_{ref}\left(\frac{Z}{Z_{ref}}\right)^{\alpha} \tag{6-6}$$

where, U_{ref} and Z_{ref} are, respectively, the reference velocity (free-stream velocity at the height of Z_{ref}) and height (3m) and α is determined based on terrain category (here 0.16). In this study simulations with a range of different reference velocities including 3, 4.5, 6, 7.5 and 9 m/s were performed to investigate the effects of wind velocity on fire-wind enhancement. The injected fuel velocity (u_f) is negligible compared to the incoming cross-wind velocity as shown in Table 6-1. A summary of the simulation scenarios performed in this study can be found in Table 6-1.

Table 6-1. List of simulation scenarios based on free-stream wind velocity and fire line intensity.

Simulation number (S#)	**U_{ref} (m/s)**	**I (MW/m)**	**u_f (m/s)**	**Simulation number (S#)**	**U_{ref} (m/s)**	**I (MW/m)**	**u_f (m/s)**
1	3	2	0.18	**13**	7.5	2	0.18
2	3	3	0.27	**14**	7.5	3	0.27
3	3	4	0.36	**15**	7.5	4	0.36
4	3	6	0.55	**16**	7.5	6	0.55
5	4.5	2	0.18	**17**	9	2	0.18
6	4.5	3	0.27	**18**	9	3	0.27
7	4.5	4	0.36	**19**	9	4	0.36
8	4.5	6	0.55	**20**	9	6	0.55
9	6	2	0.18	**21**	3	1	0.09
10	6	3	0.27	**22**	4.5	0.66	0.06
11	6	4	0.36	**23**	6	0.66	0.06
12	6	6	0.55	**24**	2	1	0.09

The range of values used for wind velocity and fire intensity is consistent with those suggested in previous studies (Nmira et al. 2010) in which the vegetation fire characteristics under the wind condition were studied. In order to consider turbulent fluctuations in the domain inlet, the "2D vortex method" (Sergent 2002) was used so that the turbulent intensity of approximately 5% is obtained at the target location. As for the other domain boundaries, outflow and open boundary conditions were prescribed for domain outlet on the right and ceiling, respectively. Slip and no-slip boundary conditions were applied respectively to the domain sides and base. The initial and the incoming free-stream flow temperature was set to be 300 K, while the adiabatic boundary was suggested for the domain base.

6.6. Numerical uncertainty analysis

6.6.1. Grid sensitivity analysis

A grid sensitivity analysis was conducted using three grid sizes. The three grid sizes were 600 k (70×90×98), 8.7 million (127×527×130) and 23 million (197×550×220) for coarse, medium and fine grids, respectively. The non-uniform structured grid was used to create smaller computational cells close to the fire source so that the grid size of the fire source would be 1cm.

Figure 6-2 compares normalized velocity and density for the three grid sizes at *X**=12 for S#5, where *X**=*X/D*. The negligible difference (<1%) is observed between the medium and fine grid for both velocity and density profiles, whereas this value is about 1.7% of difference between the medium and coarse grid. Hence, the medium grid was chosen for all simulation scenarios in the current study.

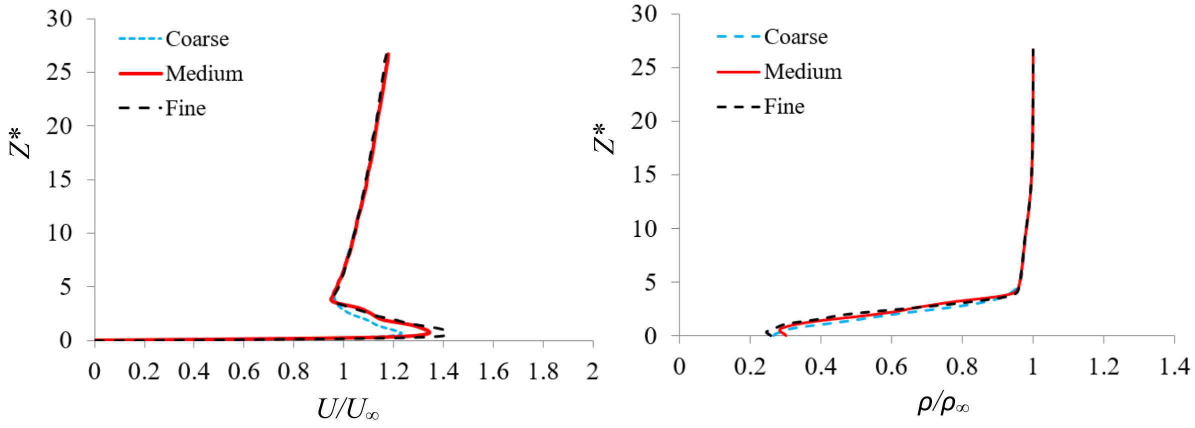

Figure 6-2 Comparison of the vertical distribution of (a) normalized longitudinal velocity and (b) density at *X** =12 for different grid sizes in S#5.

6.6.2. LES uncertainty analysis

Evaluating the ratio of resolved turbulent kinetic energy (k_{res}) to the total turbulent kinetic energy (k_{res}+k_{sgs}) is one of the criteria to assess the credibility of the applied LES model and appropriateness of the applied grid size in numerical simulations (Pope & Pope 2000). According to (Pope & Pope 2000), resolving 80% of turbulent kinetic energy shows the reliability of LES in a numerical model. Figure 6-3 (a) and (b) depicts this ratio for S#2 of the chosen (medium) grid along the plane *Y*=0. Figure 6-3 shows that more than 70% of turbulent kinetic energy is resolved for almost all distances downstream of the fire source. However, in the plume region, which is the region of focus in this study, turbulent kinetic energy is satisfactorily (more than 95%) resolved. This trend is consistent with that presented in previous studies (Vilfayeau et al. 2016).

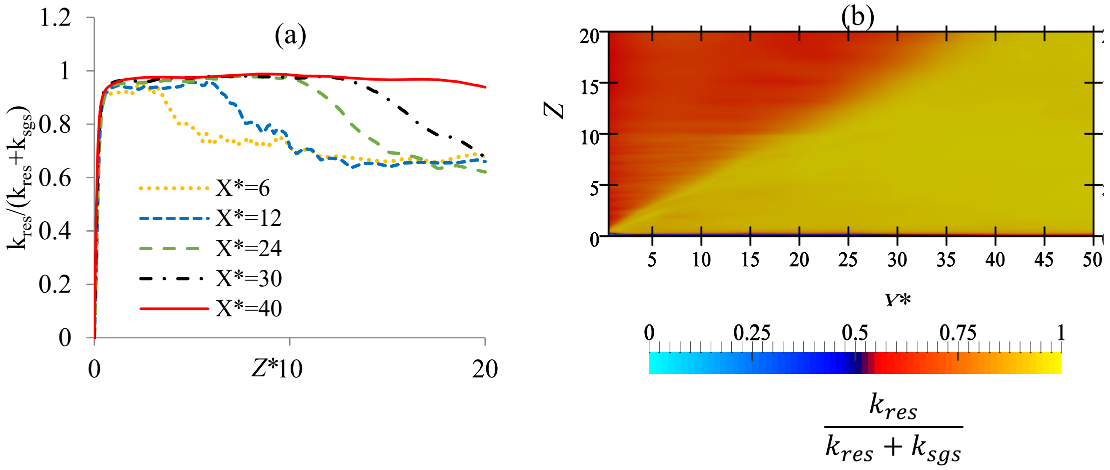

$$\frac{k_{res}}{k_{res}+k_{sgs}}$$

Figure 6-3. Ratio of the resolved turbulent kinetic energy to total turbulent kinetic energy for S#2 at different distances downstream of the fire source.

6.6.3. Validation

The developed numerical model has been validated against two sets of experimental data in our previous work (Eftekharian 2019). The first set includes experimental data of McCaffrey (1979) and the second set is associated with that of Hirano and Kinoshita (1975). McCaffrey experiment (1979) includes experimental data of buoyant diffusion flame in the still environment. McCaffrey (1979) utilized a natural gas burner and measured the centreline of flow velocity for various heat release rates. The simulation results were then assessed against the numerical results of (Wang, Chatterjee & de Ris 2011) and experimental data of (McCaffrey 1979). A reasonable agreement with experimental was obtained (Eftekharian 2019).

The second validation is associated with experimental data of Hirano and Kinoshita (1975) who measured velocity and temperature distribution at different distances downstream of the fire source. Their experiment involved a steady burning of a liquid-fuel methanol pool in a forced convective channel flow with a velocity of 0.5 m/s. The schematics of their experimental setup and the details of the validation of the model used in the current study can be found in our previous work (Eftekharian et al. 2019). A reasonable agreement between numerical and experimental data was reported in (Eftekharian et al. 2019) (with the overall error of approximately 7% and 8 % with experimental data respectively for velocity and temperature distribution in the plume region) (Eftekharian et al. 2019). More details of the validation set up can be found in our previous work (Eftekharian et al. 2019).

6.7. Results and discussion

The highest domain travel time in the simulations is 12s. All simulation scenarios were performed for 70 seconds which corresponds to at least five domain travel cycle. The first three travel cycles (35s) were considered as the transition period and the results were averaged over the last 35 seconds. Figure 6-4 shows the planar distribution of normalized longitudinal wind velocity for different combinations of free-stream wind velocity and fire intensity. This figure explains how the wind enhancement changes with variation of free-stream wind velocity and fire intensity. As can be observed in Figure 6-4, when wind interacts with fire, there would be an enhancement in wind velocity downstream of the fire. An explanation provided by Eftekharian et al. (2018 & 2019) is that when wind interacts with fire, a longitudinal negative pressure gradient is generated in the low-density region (plume area) which accelerates the flow and cause enhancement of wind by fire in the near ground region. This can be observed by comparison of Figure 6-4 with Figure 6-5 and Figure 6-6. When free-stream wind velocity increases and/or fire intensity decreases, the normalized longitudinal pressure gradient generated by fire-wind interaction undergoes a reduction, causing a reduction in flow enhancement by fire, as shown in Figure 6-4. As a consequence, wind enhancement is shown in Figure 6-4 to increase with an increase in fire intensity and/or a reduction in free-stream wind velocity.

Figure 6-6 shows the extent to which density distribution is affected by the variation of free-stream wind velocity and fire intensity at the domain centreline. Figure 6-6 shows that when fire intensity and/or wind velocity increases, the core of the plume region (where the minimum density happens) is extended to further downstream of the fire source. Also, when free-stream wind velocity increases under a constant fire intensity, it can be seen that the plume region becomes thinner and more inclined to attach to the ground. These results are consistent with the findings of (Nmira et al. 2010). Considerable reductions in the broadness of the plume region and flame height with the increase of wind velocity are observed in Figure 6-6. The fire intensity *I*, on the other hand, appears to have the opposite effect, i.e., the broadness of the flame region and the flame height tend to increase with increasing fire intensity. This is mainly because strong wind velocity causes great flow horizontal inertia forces which renders flame to bend significantly toward the ground, increasing flame tilt angle and reducing flame height. This trend of reduction of flame height with the increase of upstream wind velocity was also observed in previous experimental studies (Lin et al. 2019; Tang et al. 2015). High inclination of fire plume for ground attachment in strong freestream wind velocity is a manifestation of the increase of Froude number which indicates the ratio of freestream inertia to buoyancy effects (Nmira et al. 2010). High inclination of fire plume for ground attachment in strong free-stream wind velocity is the manifestation of increase of Froude number which indicates the ratio of inertia to buoyancy effects (Nmira et al. 2010).

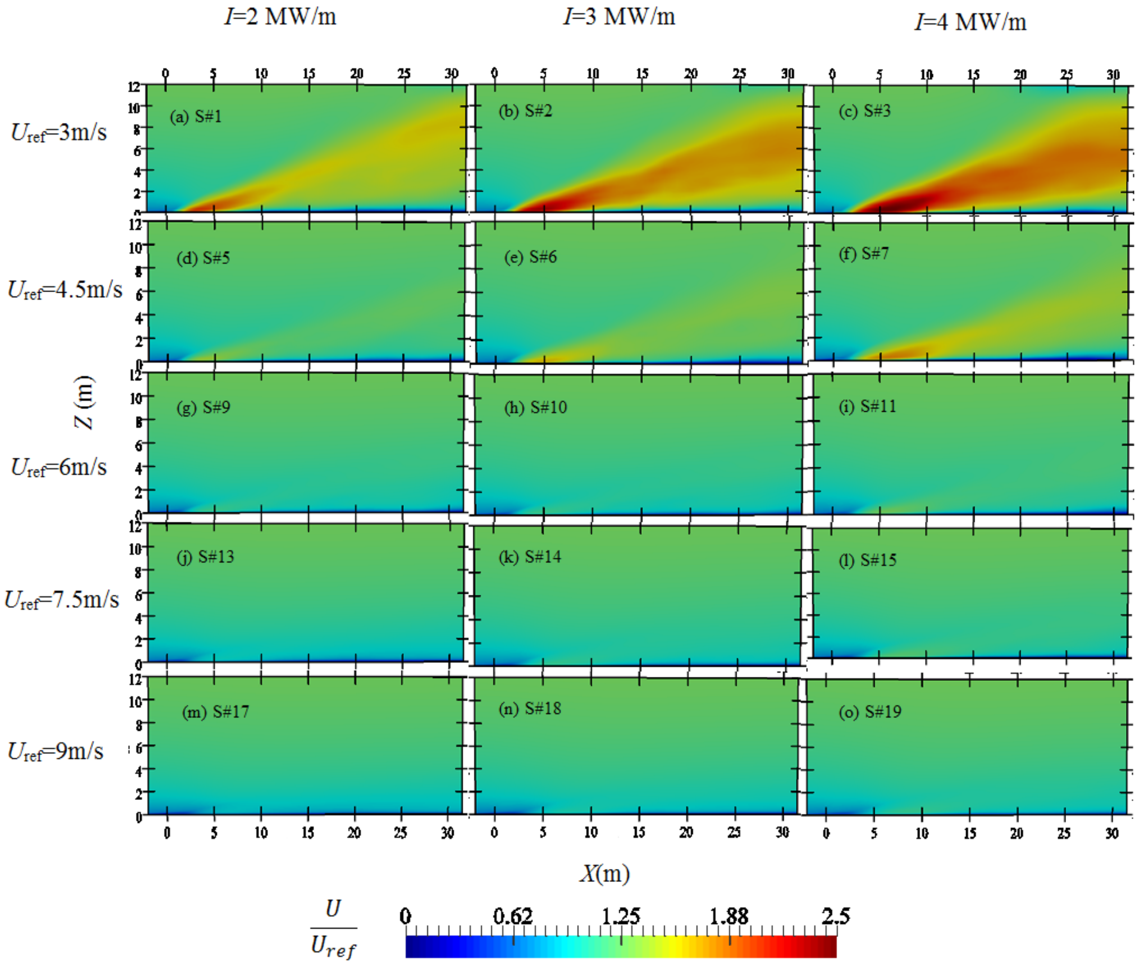

Figure 6-4 Distribution of normalized longitudinal velocity for different simulation scenarios at a vertical plane passing the centreline (Y=0).

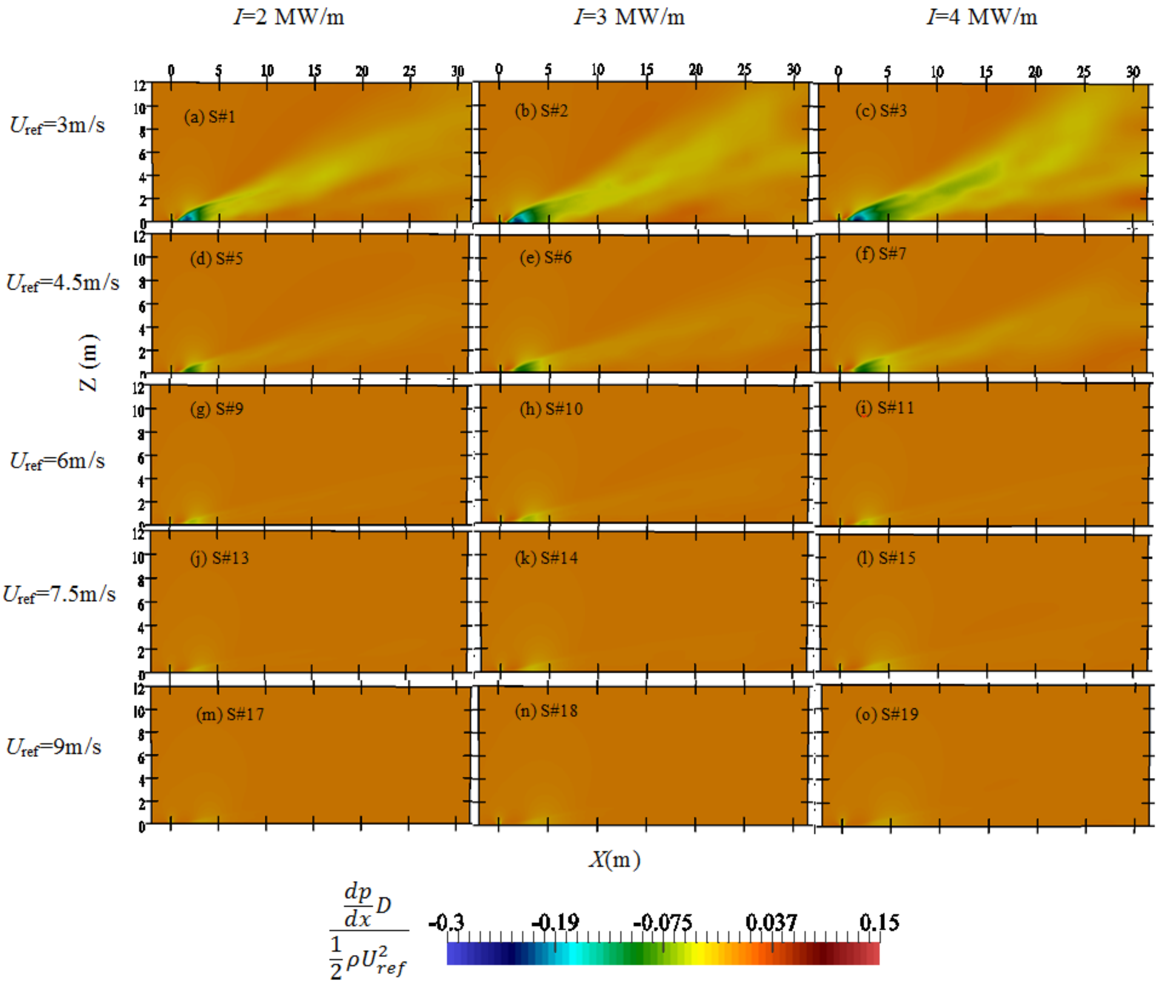

Figure 6-5 Planar distribution of normalized longitudinal pressure gradient for different simulation scenarios at a vertical plane passing the domain centreline (Y=0).

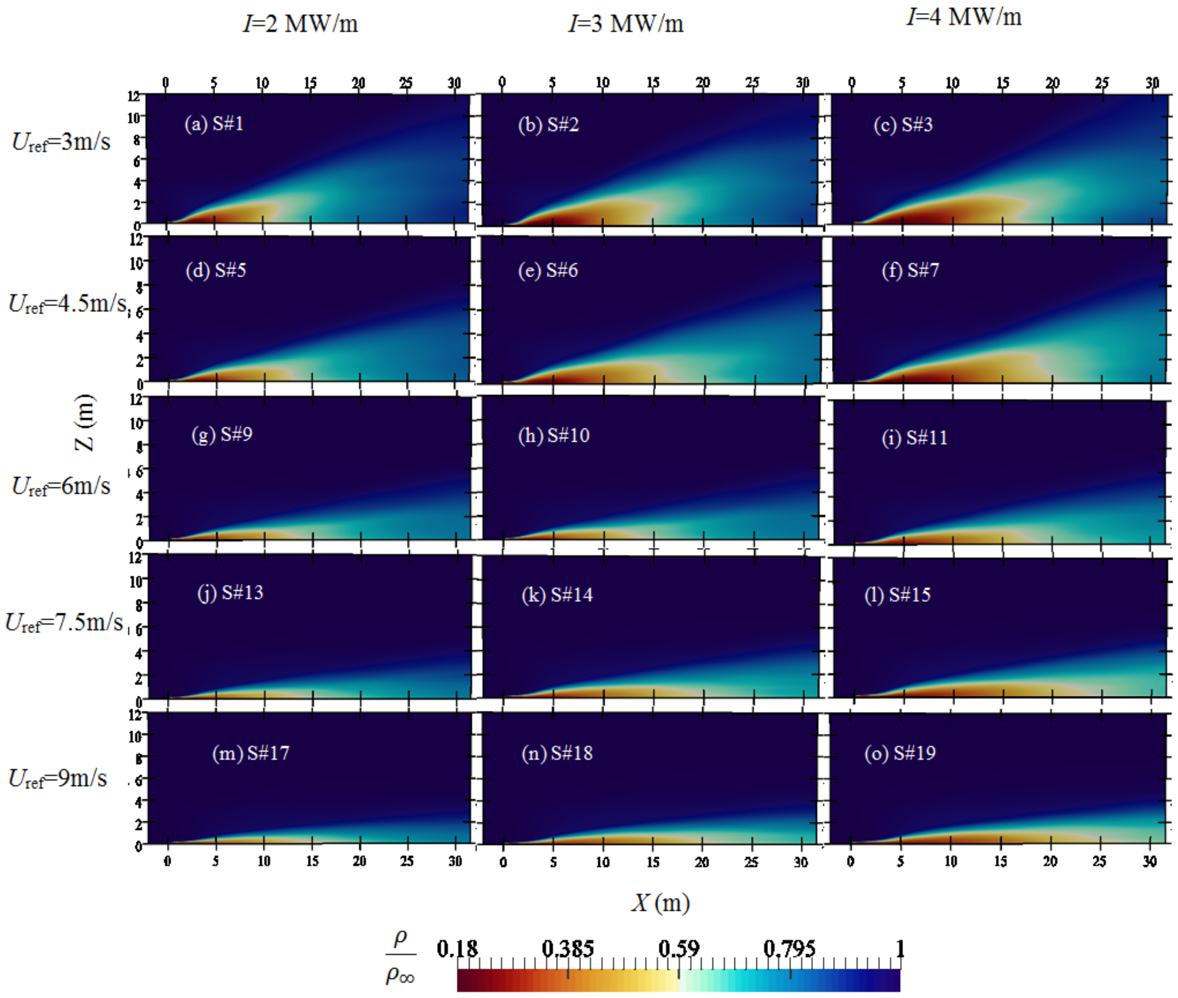

Figure 6-6 Distribution of normalized density for different simulation scenarios at a vertical plane passing the domain centreline (*Y*=0).

Figure 6-7 demonstrates the cross-sectional distribution of normalized longitudinal flow velocity at different distances downstream of the fire source for two simulation scenarios (S#1, S#2). It shows that the wind is enhanced along a belt-shaped region parallel to the fire source and the region of wind enhancement is shifted above the ground with the increase of distance from the fire source. Moreover, immediately downstream of the fire source, the wind enhancement starts to increase longitudinally, reaching to its maximum value and then undergoes a reduction in further downstream of the fire source which confirms the trend observed in Figure 6-4.

Figure 6-7 also indicates the homogenous distribution of wind enhancement along the spanwise (*Y*) direction. Hence the behavior of fire-wind enhancement along the domain centreline (*Y*=0) can be generalized to other spanwise locations.

Maximum wind enhancement is the most critical velocity information in fire-wind interaction scenarios as it can create the highest pressure load on buildings located downstream of the fire source. Figure 6-4 and Figure 6-7 confirm that the maximum wind enhancement by fire for each simulation scenario happens at near ground region somewhere downstream of the fire source. Therefore, the maximum wind enhancement normalized by the free-stream wind reference velocity, ($U^*_{e\_max} = \frac{U_{e\_max}}{U_{ref}}$), can be considered to be a function of free-stream wind velocity and fire intensity or the non-dimensional groups (Fr and I^*) reflecting these quantities.

In order to predict wind velocity enhancement in different combinations of free-stream wind velocity and fire intensity, corresponding data is tabulated in Table 6-2. Table 6-2 summarizes the maximum wind enhancement in different simulation scenarios.

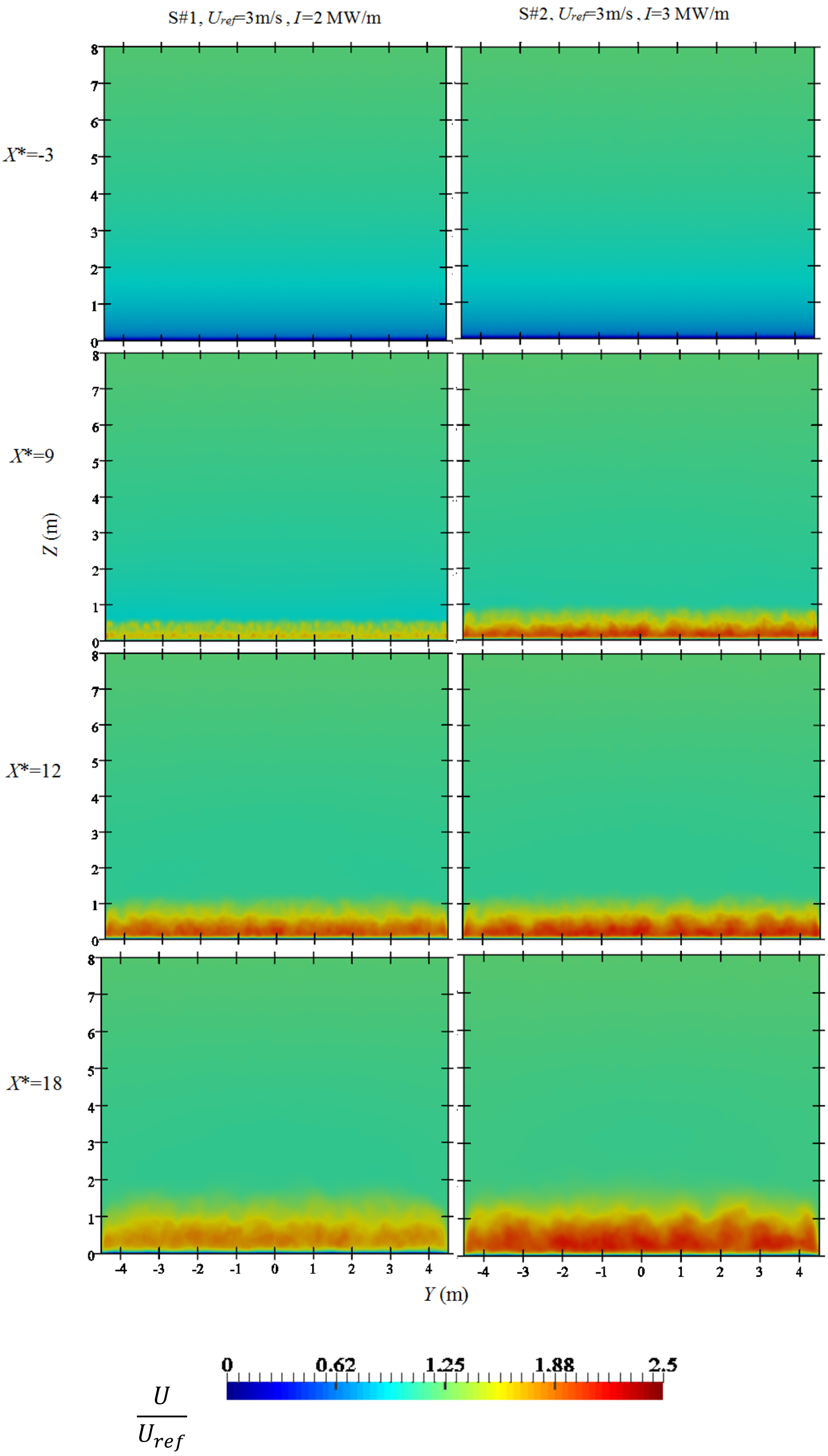

Figure 6-7. Cross-sectional distribution of normalized longitudinal velocity (U/U_{ref}) at different distances downstream of the fire source for S#1, S#2.

Table 6-2 Data related to the maximum wind enhancement predicted by CFD and the developed correlation for different simulation scenarios.

S#	U_{ref} (m/s)	I (MW/m)	Fr	I^*	$U^*_{e\_max}$		Error [Eq.(6-18)] (%)
					CFD	Eq. (6-18)	
1	3	2	3.058	11.0	2.03	2.05	0.99
2	3	3	3.058	16.5	2.37	2.34	1.1
3	3	4	3.058	22.1	2.51	2.57	2.67
4	3	6	3.058	33.1	3.01	2.94	2.12
5	4.5	2	6.88	11.0	1.38	1.44	4.82
6	4.5	3	6.88	16.5	1.64	1.65	0.83
7	4.5	4	6.88	22.1	1.8	1.81	1.02
8	4.5	6	6.88	33.1	2.05	2.07	3.93
9	6	2	12.23	11.0	1.08	1.12	4.58
10	6	3	12.23	16.5	1.25	1.29	3.3
11	6	4	12.23	22.1	1.36	1.41	4.4
12	6	6	12.23	33.1	1.59	1.62	1.57
13	7.5	2	19.11	11.0	0.93	0.93	0.24
14	7.5	3	19.11	16.5	1.06	1.06	0.54
15	7.5	4	19.11	22.1	1.12	1.17	0.16
16	7.5	6	19.11	33.1	1.3	1.33	3.05
17	9	2	27.52	11.0	0.88	0.79	9.42
18	9	3	27.52	16.5	0.98	0.91	7.02
19	9	4	27.52	22.1	1.06	1	5.48
20	9	6	27.52	33.1	1.19	1.14	3.75
			Testing Data				
21	3	1	3.058	5.53	1.62	1.63	0.67
22	4.5	0.66	6.88	3.68	0.93	1	8.24
23	6	0.66	12.23	3.68	0.76	0.78	3.42
24	2	1	1.35	5.53	2.56	2.31	9.7

On the one hand, Froude number (Fr) and normalized fire intensity (I^*) have been shown to be appropriate non-dimensional groups to characterize line fire flame features under cross-wind fire scenarios (Nmira et al. 2010). On the other, Froude number (Fr) and normalized fire intensity (I^*) take into account the effects of respectively free-stream wind velocity and fire intensity which are influential factors affecting fire-wind enhancement as shown Figure 6-4 and Figure 6-7. Another reason why Fr number was chosen in here rather than Ri number introduced in Chapter 4 is because of simplicity of application for engineers. Richardson number and Fr number both represent relation between inertia force and buoyant force. However, there is a subtle difference in the formulation: For calculation of Fr number one only needs to determine flow reference velocity, fire chsarachteristic dimension, and gravitational acceleration. This makes it more popular among the engineers. However, Richardson number includes more flow variables (flow temperature, and fluid expansion coefficient) (Eq 4-5) in the formulation, making it more appropriate for fundamental analysis of fire-wind enhancement mechanism as conducted in Chapter 4. Hence, it is postulated that the normalized maximum enhanced velocity ($U^*_{e\_max}$) correlates with the Fr and I^* in the following form:

$$U^*_{e\_max} = a'\mathrm{Fr}^{b'}I^{*c'} \tag{6-7}$$

where a', b' and c' are constants and

$$U^*_{e\_max} = U_{e\_max}/U_{ref}, \tag{6-8a}$$

$$Fr = \frac{U_{ref}{}^2}{gD} \tag{6-8b}$$

$$I^* = \frac{I}{\rho_\infty c_p T_\infty \sqrt{g} D^{3/2}} \tag{6-8c}$$

where c_p (kJ/kg.K) is the specific heat of air at constant pressure, D (m) is the fire source depth, ρ_∞ (kg/m^3) is the ambient density, T_∞ (K) is the ambient temperature and g is the gravitational acceleration (m/s^2). The Matlab (Inc 2016) regression method/software was used to determine the values of parameter a', b' and c' for the best fit to the simulation results. Equation (6-7) becomes:

$$U^*_{e\_max} = 1.5\mathrm{Fr}^{-0.43}I^{*0.33} \tag{6-9}$$

Equation (6-9) is plotted in Figure 6-8 together with the CFD simulation results. It is seen that the regression function of Eq. (6-9) produces a very good agreement with CFD data (with the average error of about 3%).

The developed correlation was based on the CFD simulation result within the parameter ranges of 3.05≤Fr≤27.72 and 11.06≤I^*≤33.18. In order to examine if the correlation is able to well predict wind velocity enhancement under a free-stream wind velocity and fire intensity for wider ranges of the input parameters, we performed four extra simulations whose results are shown as Testing Data in Table 6-2. It is seen that the errors related to the testing data are marginal and comparable with that associated with the original set of scenarios, confirming the capability of the presented correlation in predicting the extended range of the simulation conditions.

To check the agreement between the correlation function and the CFD simulation results, Eq. (6-9) is re-arranged into:

$$U^*_{e\_max}\mathrm{Fr}^{0.43} = 1.5I^{*0.33} \tag{6-10}$$

This equation is plotted in Figure 6-9 and compared with the CFD simulation results, including that of the additional simulations runs.

Comparison of Figure 6-8 (a) and (b) confirms the trend observed in Figure 6-4 which indicates that the maximum wind enhancement by fire has a direct and reverse relation with fire intensity and free-stream wind velocity, respectively.

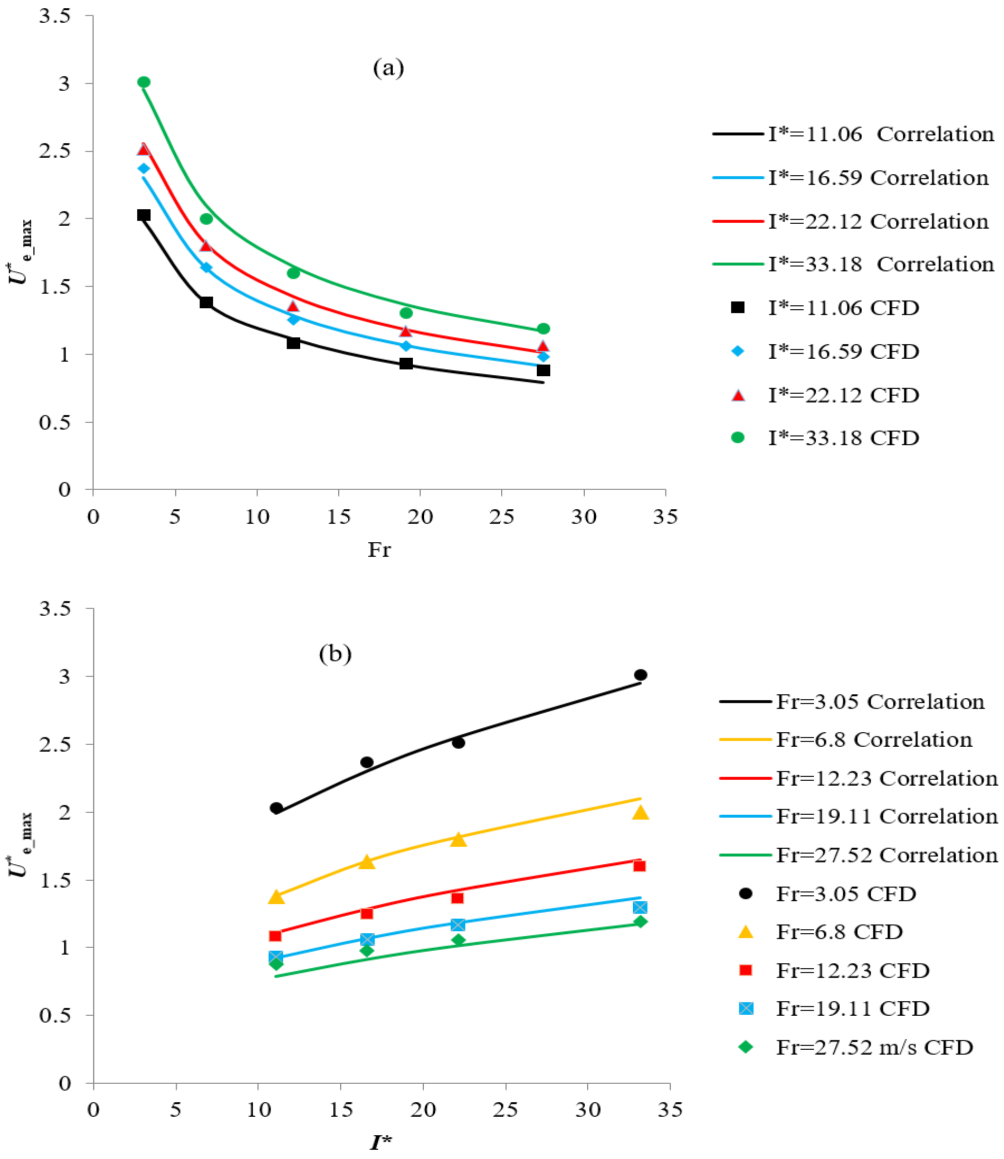

Figure 6-8 Comparison of the maximum wind enhancement by between the results of Eq. (6-9) and CFD data of the first 20 simulation scenarios.

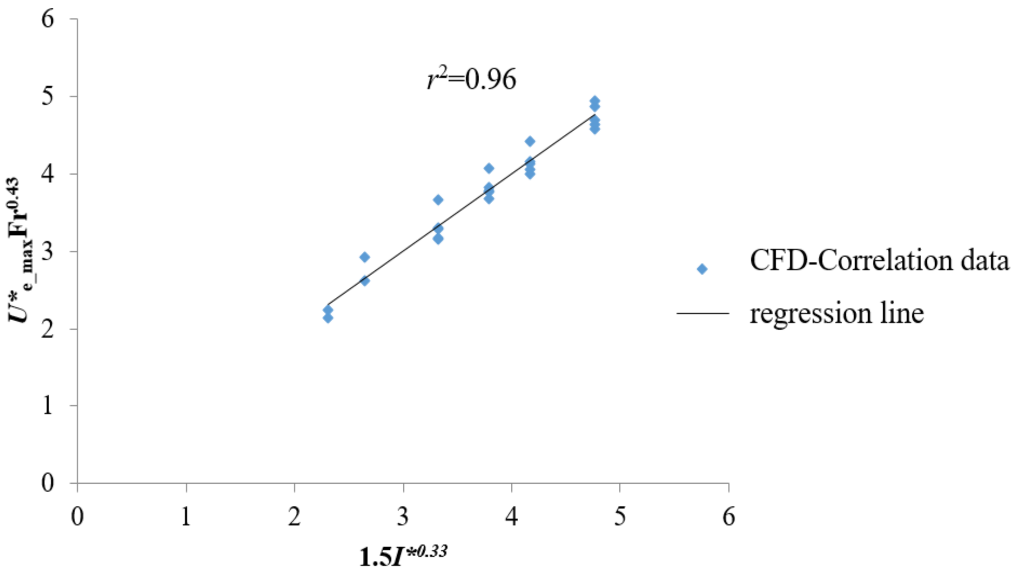

Figure 6-9 Comparison of Eq. (6-10) with all CFD data.

Figure 6-10 presents vertical distribution of normalized longitudinal velocity at different normalized distances ($X^*=\frac{X}{D}$) downstream of the fire source for three different simulation scenarios. Figure 6-10 shows that at a given X^*, there exists a local wind enhancement, $U^*_{max\_l}$ (X^*, Z^*_m), where Z^*_m represents the normalized z-coordinate ($Z^* = \frac{Z}{D}$) at which the local U_{max_l} occurs. Z^*_m is a function of X^*, or $Z^*_m=Z^*_m(X^*)$. This function in the x-z coordinate is called the wind enhancement plume line. Note that the parameter U_{e_max} refer to the global maximum wind enhancement. Figure 6-11 is the plot of wind enhancement plume line for different simulation scenarios. Figure 6-11 (a) and (b) show that in all simulation scenarios, immediately downstream of the fire source, wind enhancement plume line is horizontally extended at the near ground region and then is leveled up from the ground under a curved line in further downstream. This trend is consistent with previous observation of fire plume under cross-flow condition (He et al. 2011b). Figure 6-11 (a) and (b) also illustrates respectively the effects of I^* [Figure 6-11 (a)] and Fr number [Figure 6-11 (b)] on the wind enhancement plume line. Figure 6-11 (a) and (b) show that as Fr number and/or I^* increases, the wind enhancement plume line is more inclined to the ground. This is mainly due to the Coanda effects which necessitate the plume attachment to the ground immediately downstream of the fire source. With the increase of Fr number and/or I^*, the unbalanced flow entrainment downstream of the fire source at each side of the plume increases, strengthening the Coanda effects that consequently increases the plume inclination to the ground attachment. High inclination of plume line toward the ground in high cross-wind velocities observed in Figure 6-11 (b) also manifests the increase of flame tilt angle with the increase of wind inertia force. This trend is observed in the previous experimental (Hu, et al. 2017; Lam & Weckman 2015; Lin et al. 2019; Ping et al. 2018; Tang et al. 2015) and numerical (Eftekharian et al. 2019; Nmira et al. 2010) studies investigating flame tilt angle. On the other hand, Figure 6-11 (a) also indicates that under a constant cross-wind velocity, with the reduction of fire heat release rate (fire intensity), wind enhancement plume line becomes closer to the ground, or the tilt angle increases. This is mainly because vertical buoyancy reduces causing the increase of tilt angle. This trend is in agreement with that observed in (Lin et al. 2019). Figure 6-11 (b) also indicates the horizontal extension of plume line immediately downstream of the fire source. This phenomenon was referred to as flame base drag and has been observed in previous studies (Hu et al. 2017; Lin, Zhang & Hu 2018; Tang, He & Wen 2019). This horizontal extension increases with the increase of cross-wind velocity as observed in Figure 6-11 (b).

Another review of the entire Figure 6-11 also reveals that the wind enhancement plume lines could be approximated with functions of the parabolic form.

It is postulated that the wind enhancement plume line can be correlated in the following form:

$$Z_m^* = f'(\mathrm{Fr}, I^*)X^{*2} \tag{6-11}$$

where f' is a function of Fr number and I^* and can be written in the form of:

$$f' = d'\mathrm{F}r^{g'}I^{*h'} \tag{6-12}$$

in which d', g' and $h'$are constants which can be determined using Matlab (Inc 2016) regression method. Equation (6-11) becomes:

$$Z_m^* = 0.011\mathrm{F}r^{-0.31}I^{*-0.37}X^{*2} \tag{6-13}$$

To check the agreement between the correlation function Eq.(6-13) and the CFD simulation results, Figure 6-12 is plotted which compares the wind enhancement plume line predicted by CFD and the developed correlation [Eq. (6-13)]. Figure 6-12 shows that there is a reasonable agreement (with average regression coefficient of (r^2=0.95) between CFD results that those predicted by Eq.(6-13).

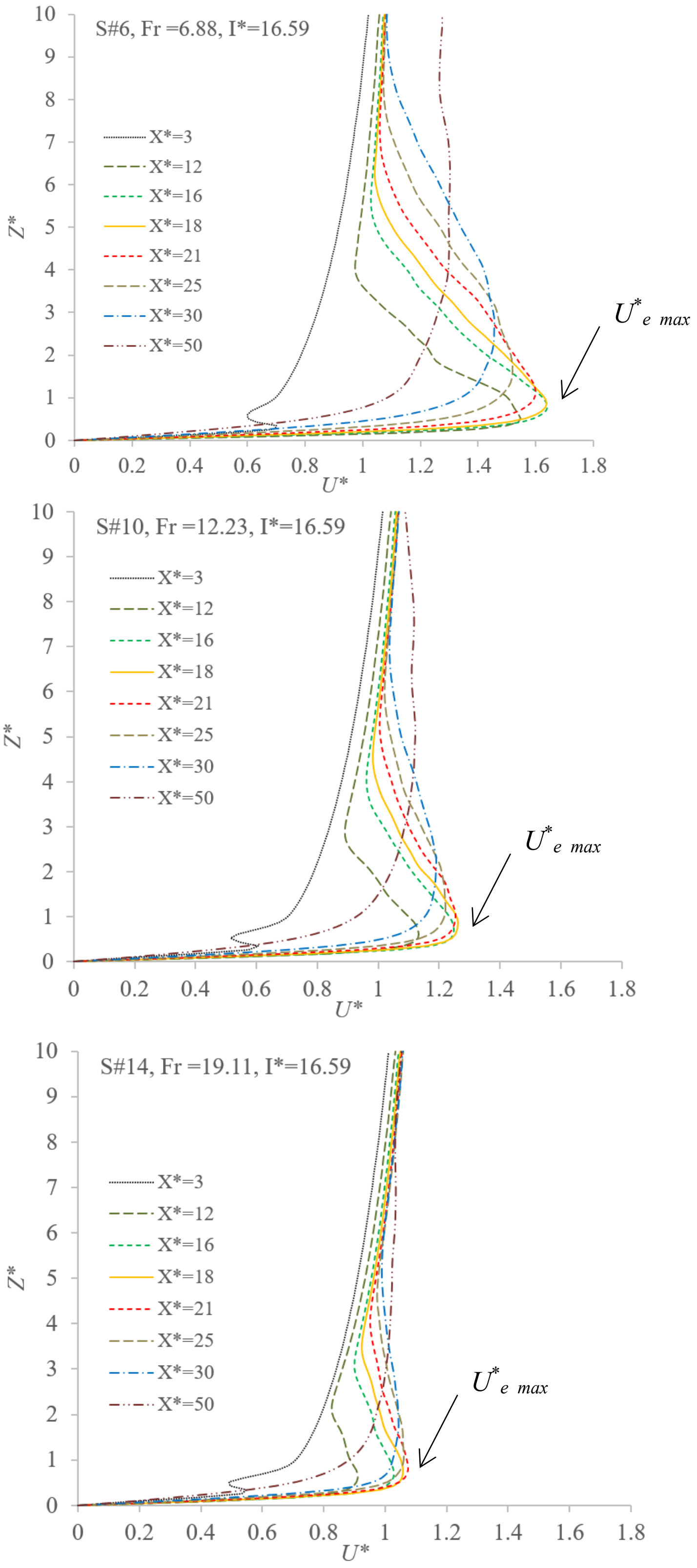

Figure 6-10 vertical distribution of normalized longitudinal velocity at different distances downstream of the fire source for three different simulation scenarios. (The line and position corresponding to $U^*_{e\_max}$ is shown by an arrow for each simulation scenario).

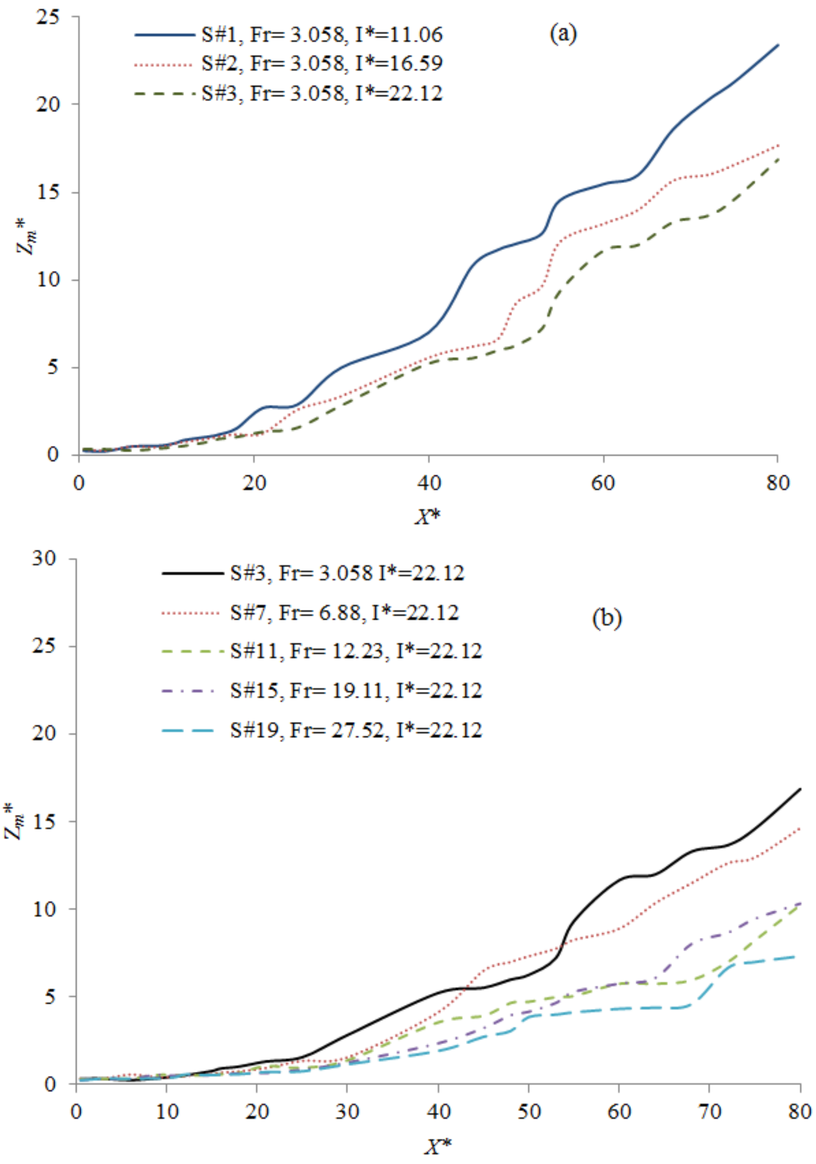

Figure 6-11. Comparison of wind enhancement plume line in different simulation scenarios: (a) the effects of *I** under constant Fr, (b) the effects of Fr under constant *I**.

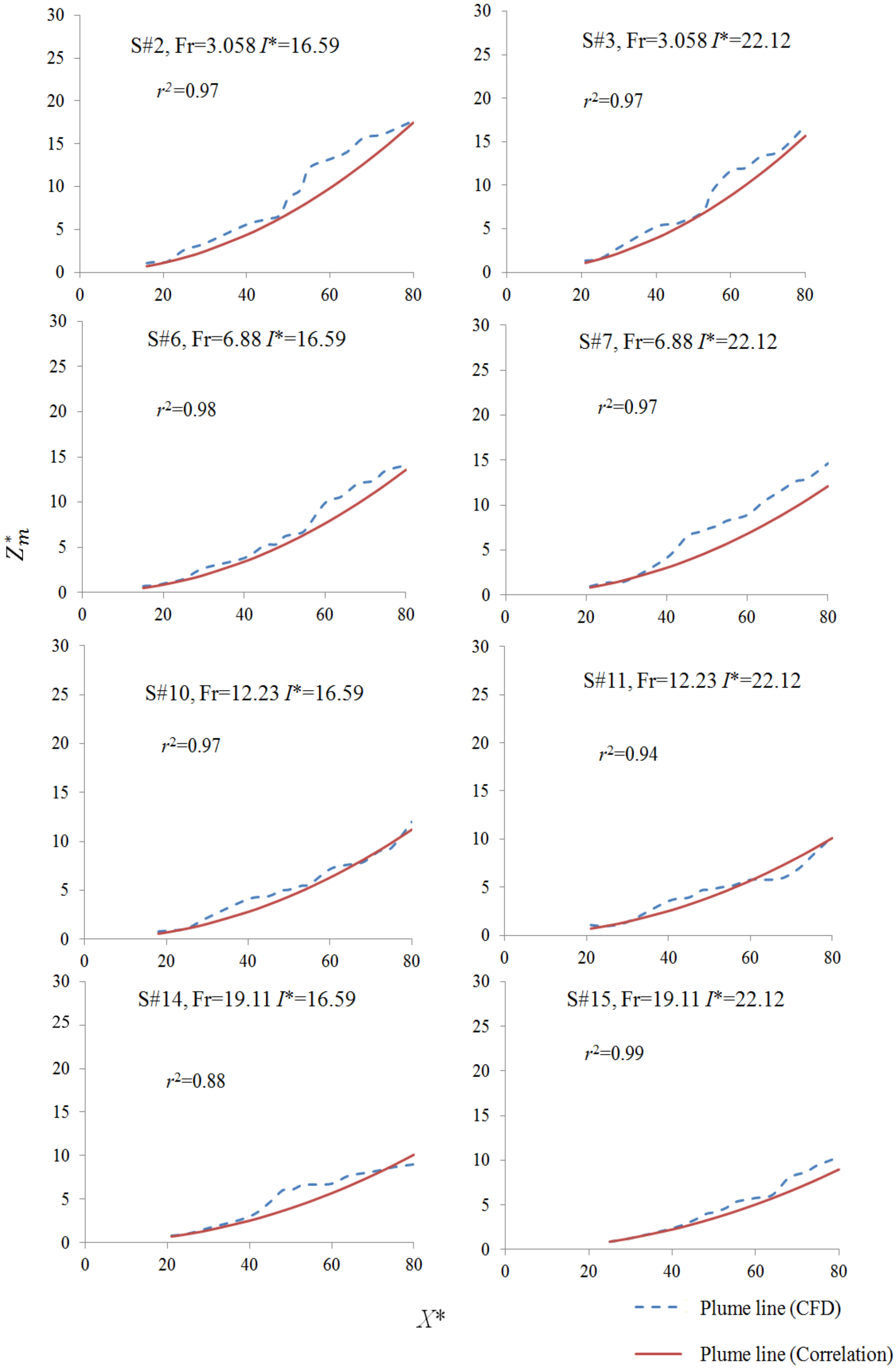

Figure 6-12 Comparison of wind enhancement plume line between CFD data and that of correlation [Eq.(6-13)] for different simulation scenarios

It was also found that a correlation can be developed for the longitudinal location at which maximum wind enhancement happens as a function of Fr number and *I**:

$$X^*_{e\_max} = m'\mathrm{Fr}^{n'} I^{*s'} \tag{6-14}$$

where, $X^*_{e\_max}$ is the location corresponding to the maximum wind enhancement ($U^*_{e\_max}$) and m', $n'$and s' are constant values determined based on Matlab (Inc 2016) regression tool. Equation (6-14) becomes:

$$X^*_{e\_max} = 2\mathrm{Fr}^{0.27} I^{*0.6} \tag{6-15}$$

Comparison of $X^*_{e\_max}$ of CFD results and that predicted by Eq. (6-15) is shown in Figure 6-13 that reveals there is a good agreement (regression coefficient of 0.95 and the average error of around 8%) between CFD data and the correlation prediction.

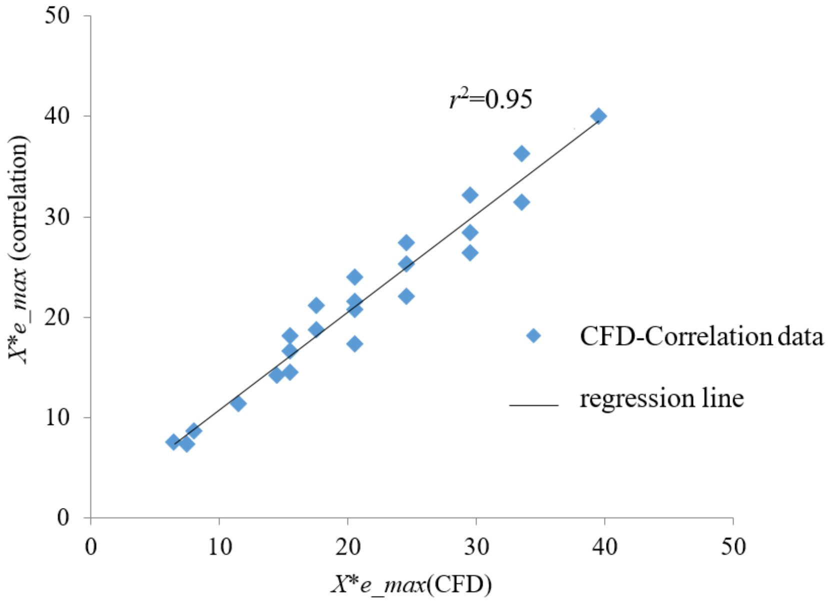

Figure 6-13 comparison of $\boldsymbol{X^*_{e\_max}}$ values by CFD and by correlation Eq. (6-15)

Although the investigation of the global maximum wind enhancement ($U^*_{e\_max}$) is the most critical velocity information in fire-wind interaction scenarios, the variation of local enhanced velocity along the longitudinal direction is worth investigating. Here also we define the normalized plume velocity as $U^*_p = \frac{U_p}{U_{e\_max}} = \frac{U_{max\_l}}{U_{e\_max}}, = \frac{U^*_{max\_l}}{U^*_{e\_max}}$, where *Up* is the *U*-component velocity along the plume line. In other words, U_p represents the local maximum wind enhancement at given *X**.

Figure 6-14 shows the variation of normalized plume velocity (U^*_p) along the wind enhancement plume line [Eq.(6-13)] for different simulation scenarios. The vertical axis represents the local wind enhancement velocity along the plume line (U_{max_l}) normalized with the global maximum wind enhancement velocity (U_{e_max}), while the horizontal axis indicates the normalized longitudinal position (X*) corresponding to the plume line. Figure 6-14 shows that for all examined simulation scenarios, the normalized enhanced velocity first increases and then reaches the maximum wind enhancement (U_{e_max}) followed by the decaying trend. To explain why wind enhancement undergoes decay after reaching a peak, it is necessary to address mechanisms through which wind is enhanced by fire. According to Eftekharian et al (2019), wind enhancement occurs due to the combined effects of fire-induced pressure gradient and density. Strongest wind enhancement happens in a region where fire-induced pressure force has the highest value and air density is minimum. Figures 6-5 and 6-6 confirm that in all simulation scenarios, strongest fire-induced pressure gradient occurs in low density region immediately downstream of the fire source, causing occurrence of maximum wind enhancement. Further downstream, gradually fire-induced pressure force starts to decrease and density increases along the plume line, causing decay of wind enhancement. Figure 6-14 reveals that the higher rate of decay velocity happens in the scenarios with the greater maximum wind enhancement. For example, the highest decay rate of velocity is observed in S#2 and S#3 possessing comparatively higher wind enhancement values (see Figure 6-4 and also Table 6-2).

The results obtained from the decaying velocity of different simulation scenarios were also fit to a correlation:

$$U_p^* = \exp(-r'X^*) + t' \qquad \text{For } X^* > X_{e\_max}^* \qquad (6\text{-}16)$$

where r' is the decay rate and t' is the asymptotic limit of decay such that when $X^* \rightarrow \infty$, $U_p^* \rightarrow t'$.

These two parameters are functions of normalized maximum wind enhancement as expressed below:

$$r' = 0.2\left(U_{e\_max}^*\right)^{-1} \qquad (6\text{-}17)$$

$$t' = \left(U_{e\_max}^*\right)^{-0.3} \qquad (6\text{-}18)$$

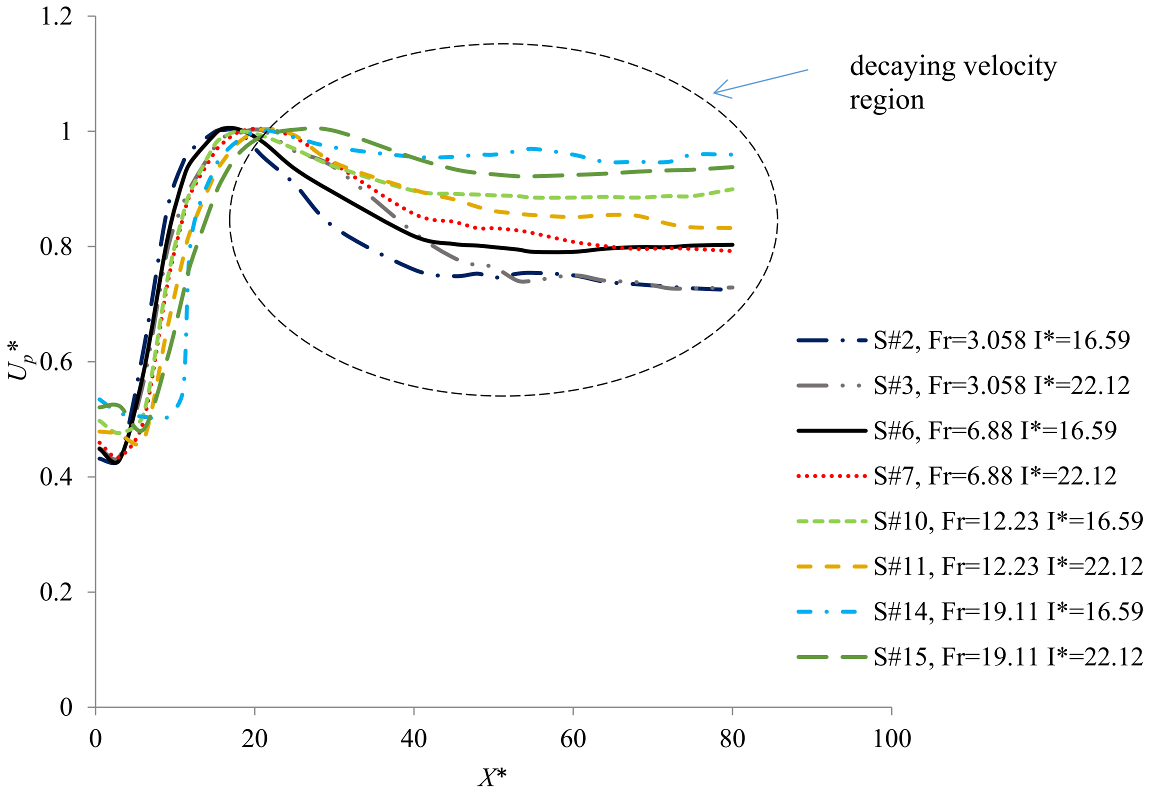

Figure 6-14 variations of normalized plume velocity along the wind enhancement plume line.

Figure 6-15 compares the normalized plume velocity of the CFD results and that predicted by the developed correlation [Eq. (6-16)]. Figure 6-15 shows that there is a good agreement (average error of less than 4%) between CFD results that those predicted by Eq.(6-16). Figure 6-15 also confirms that there is a higher decay of velocity in scenarios with a higher maximum wind enhancement.

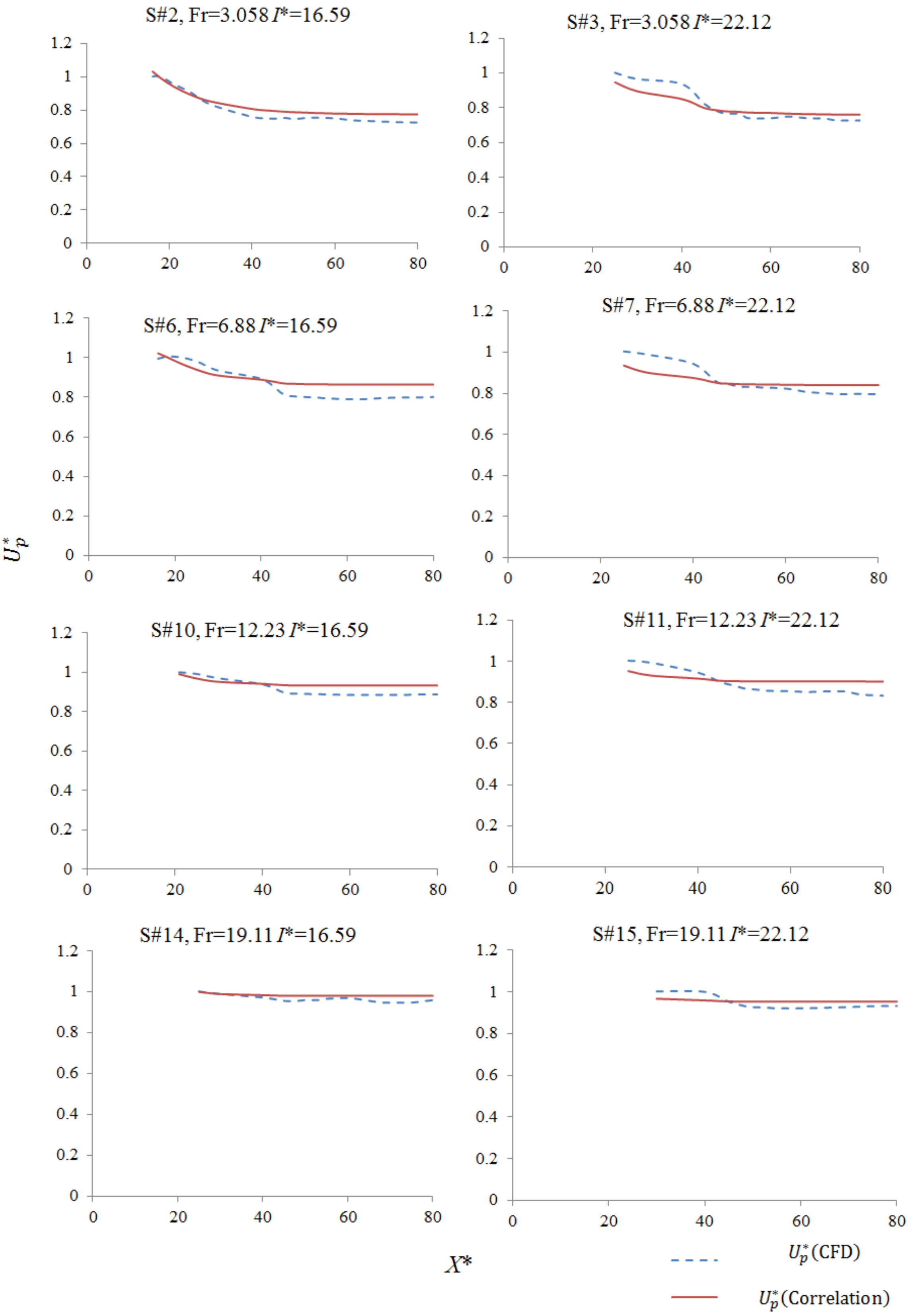

Figure 6-15 Comparison of normalized plume velocity (U_p^* for $X^* > X_{e\_max}^*$) between CFD data and the developed correlation [Eq. (6-16)].

6.8. Conclusion

LES study was conducted to determine the effects of free-stream wind velocity and fire intensity on fire-wind enhancement. A number of simulation scenarios with different combinations of free-stream wind velocity and fire intensity were performed to quantitatively determine the flow behavior under different wind and fire intensity conditions. Correlations were developed for fire-wind enhancement flow characteristics based on the predominant non-dimensional groups (Fr and I^*). Below are the main conclusions of this study.

- LES results showed that fire-wind enhancement increases with the increase of fire intensity and reduction of free-stream wind velocity.
- A correlation was developed for maximum wind enhancement ($U^*_{e\_max}$) by fire as a function of non-dimensional groups (Fr and I^*). LES results showed that maximum wind enhancement by fire increases with the increase of I^* and reduction in Fr number.
- A correlation was also developed as a function of Fr number and I^* to represent the longitudinal location ($X^*_{e\_\mathrm{max}}$) at which maximum wind enhancement by fire occurs.
- It was observed that at a given distance downstream of the fire source, there exists a local maximum wind enhancement, $U^*_{max\_l}$ (X^*, Z^*_m), whose vertical location (Z^*_m) was correlated with the normalized longitudinal distance X^* that represents the wind enhancement plume line.
- It was found that the wind enhancement gradually decays longitudinally along the plume line after reaching a peak downstream of the fire source. A correlation was also developed to determine the decay of the enhanced velocity as a function of the longitudinal distance downstream of the fire surface.

CHAPTER 7. INVESTIGATION OF TERRAIN SLOPE EFFECTS OF WIND ENHANCEMENT BY A LINE SOURCE FIRE

This chapter investigates the effects of terrain slope on wind enhancement by a line fire source based on the theoretical framework developed in Chapters 3 and 4. Four different terrain upslope angles and four terrain downslope angles are investigated and maximum wind enhancement is quantified. Furthermore, a trend for variation of maximum wind enhancement with slope angle is developed.

A reprint of this study entitled “Investigation of terrain slope effects on wind enhancement by a line source fire”, **Esmaeel Eftekharian**, Maryam Ghodrat, Yaping He, Robert H. Ong, Kenny C.S. Kwok, Ming Zhao, Bijan Samali published by the “*Case studies in Thermal Engineering”*, 2019; Volume 14, Article No 100467 (https://doi.org/10.1016/j.csite.2019.100467) is appended in Appendix A5.

7.1. Abstract

Wind enhancement triggered by fire-wind interaction can potentially pose significant damage to structures built in bushfire prone areas. The effect of terrain slope is one of the parameters contributing to the enhancement of wind by fire that needs to be taken into account. This study employs a validated model of Computational Fluid Dynamics to assess the effects of terrain slope on this phenomenon. A module was developed and appended to the FireFOAM solver to output individual component of flow acceleration. Multiple analyses were used to explain the effects of terrain upslope and downslope on the phenomenon. The results reveal that although the enhancement of wind velocity due to fire increases with an increase in terrain upslope, a terrain downslope reduces flow enhancement by fire. The results also established that while an upslope terrain reinforces the Coanda effects and intensifies attachment of the plume to the ground, the downslope condition mitigates Coanda effects and reduces the flow's tendency to attach to the ground downstream of the fire source. Furthermore, under a constant heat release rate and upstream wind velocity, the maximum magnitude of wind enhancement linearly increases with the increase of upslope angle.

Keywords: upslope, downslope, wind enhancement, fire, CFD, Coanda effects

7.2. Introduction

Interaction of wind and fire is a two-way interaction. On the one hand, wind leads to a change of fire plume geometrical structures and on the other, fire also influences the freestream (wind) aerodynamics. Many researchers have investigated the effects of wind on fire plume geometrical properties, such as fire plume tilt angle and flame length under the conditions of flat ground (Hu 2017; Hu, Liu, et al. 2013; Hu, Wu & Liu 2013) as well as sloped ground (Liu et al. 2014; Zhu et al. 2016) and unveiled a number of interesting fire behavior under the influence of wind (Welker & Sliepcevich 1996; Lin, Zhang, & Hu 2018; Tang, He & Wen 2019; Hu et.al 2017; Zhang et al. 2019; Lautkaski 1999; Rew, Hulbert & Deaves 1997; Shang et al. 2017; Zhen et.al 2011; Li, Hu & Shang 2018).

Flame base drag is one of the important phenomena that happens during fire-wind interaction in which flame is horizontally extended downstream of the fire source (Welker, J & Sliepcevich 1966). Experimental studies have been conducted to quantitatively investigate flame base drag phenomenon and it was found that flame extension first increases and then decreases with the increase of upstream wind velocity (Lin, Zhang & Hu 2018). Correlations were developed for flame base drag length (Lin, Zhang & Hu 2018; Tang, Fei, He & Wen 2019). The combined effects of cross-flow and sub-atmospheric pressure on flame base drag length were also investigated (Hu et al. 2017).

Flame sag is another phenomenon that occurs due to the interaction of cross-wind with pool fire above the ground surface (Zhang et al. 2019). In this phenomenon, the flame is deflected toward the ground at the leeward side of the lifted fire source (Zhang et al. 2019) primarily due to the complex pressure field in the wake flow in the lee of the pool. Flame sag phenomenon was initially reported in (Lautkaski 1992; Rew, Hulbert & Deaves 1997), however, a comprehensive experimental study has only recently been conducted to determine flame sag behavior under different wind velocity, fire heat release rate and pool fire height conditions (Zhang et al. 2019).

Another phenomenon involved in fire-wind interaction with more relevant industrial applications is flame downwash which is referred to as flame pulling by the wake produced at the burner nozzle leeward side (Shang et al. 2017). Flame downwash length is of great importance in designing industrial burners (Zhen et al. 2011). Recently, experimental investigations have been carried out to determine flame downwash length for different cross-wind and fuel jet velocities as well as nozzle diameters and a correlation for these parameters has been developed (Shang et al. 2017). A correlation was also developed for maximum flame downwash length (Li, Hu & Shang 2018).

The aforementioned studies primarily focused on the effects of wind on pool fire or point source fires. Some studies (Zhu et al. 2016; Liu et al. 2014) focused on the effect of terrain slope and wind on fire behavior. However, very few studies could be found in the literature that address the effects of terrain slope on aerodynamics change of wind during fire-wind interaction, particularly involving a line source fire setting that resembles bushfire (wildland fire) front.

Fire-wind enhancement is one of the detrimental effects of major bushfire attacks. Lambert (2010) and McRae et al. (2013) identified that wind can be magnified because of its interaction with bushfire. He et al. (2011a) and Kwok, He and Douglas (2012) studied bushfire-wind interaction numerically and revealed that it may elevate the near-ground wind velocity downstream of the bushfire source to a considerable extent. Owing to the escalation of wind velocity because of wind-fire interaction, the pressure coefficient around buildings downstream of the bush-fire source will be correspondingly increased. Recently, using numerical simulation, Eftekharian et al. (2019) fundamentally investigated the fire-wind enhancement phenomenon and revealed that as a result of the interaction of wind with fire, a negative streamwise pressure gradient is generated in the fire plume region which causes flow acceleration and increase of wind velocity downstream of the fire source. They also investigated the effects of heat release rate on the phenomenon and showed that wind enhancement is intensified as fire heat release rate increases. In a separate study, Eftekharian et al. (2018), investigated the effects of wind velocity on the enhancement of wind by fire. It was shown that under a constant fire heat release rate, the magnitude of flow enhancement decreases as the freestream wind velocity increases.

It has long been recognized that wildfire spread on uphill slopes is faster than on flat grounds (Hawley 1926; Show 1919). The rise in the fire spread rate was usually thought to be associated with the flames tilting towards or in direct contact with the ground fuel bed (Sharples 2009; Show 1919), but in fact, the total flame streamwise velocity profile and fire-induced flow are subjected to more fundamental variations in which the sloped terrain and some dangerous fire behavior were reported (Sharples 2009).

Some experimental studies have shed light on the effect of terrain slope on the kinematics of bushfires such as fire front shape and the relative fire propagation rate. The aforementioned terrain slope effects have commonly been assessed in conjunction with wind for various fuels (Mendes-Lopes, Ventura & Amaral 2003; Viegas 2004; Weise & Biging; 1996). Other studies produced useful sets of data to validate semi-empirical fire spread models (Balbi et al. 2009; Mendes-Lopes, Ventura & Amaral 2003). Lately, Dupuy et al. (2011) analyzed the influence of terrain slope and fuel bed geometry on the kinematics of the fire front to explain the mechanisms behind fire front shape and the pattern of line source fire. These researchers found that the fire-induced wind behind the fire was more intense when the terrain angle enlarged. Wind–slope correction models were developed by some researchers such as Sharples (Sharples 2008). These models are central to the idea of wind-slope corrections of fire spread rates based on the concepts of wind vector, topographic slope and other topographic aspects of the studied area. Their study (Sharples 2008) includes a systematic review of the techniques for merging the slope correction models with the rate of spread calculations and specified two main methods that can be applied to either empirical (Sullivan 2009b) or semi-physical models (Sullivan 2009a) of fire spread and slope interactions.

The effects of terrain slope in bushfire modeling approaches have been taken into account for years. Currently, with the development of computational fluid dynamics methods for simulating fire propagation scenarios (Dupuy, Jean-Luc & Morvan 2005; Linn & Cunningham 2005; Mell et al. 2010), there has been a renewed focus on developing an in-depth understanding of the effect of slope on fire-wind enhancement (Sharples 2008; Sullivan 2009a, 2009b). However, predicting the influence of terrain slope on fire-wind enhancement has been a challenging task that has neither been accurately identified nor sufficiently understood. Some researchers indicated air flow acceleration on windward terrain slopes may be responsible for fire propagation (Albini 1982; Jackson & Hunt 1975), whereas others claimed reduced angles between fuel and buoyant plume leads to an increase in heat flux (Luke & McArthur 1978; Pyne, Andrews & Laven 1996). Some other researchers such as Wu and Atkinson (2000) proposed the attachment of flames to the slope as the underlying mechanism for the rate of fire spread variation on slope terrain.

Although studies into this matter have been limited, yet, a number of laboratory scale researches have been carried out aiming at developing techniques to quantify the impact of terrain slope on propagation rate (Tritton 1988; Van Wagner 1977; Wu, Xing & Atkinson 2000). In spite of enhancement in computer simulation of the fire spread edge and improvements in three-dimensional information systems on geomorphology facilitated prediction of bushfire spread (Coleman & Sullivan 1996; Finney 2004; Johnston, Kelso & Milne 2008; Tolhurst, Shields & Chong 2008; Tymstra et al. 2010), fundamental understanding of the flow aerodynamics identifying the influences of terrain slope on the behavior of wind-fire enhancement is still in its early observation and empirical modeling stages.

One of the parameters that influence fire spread rate on the hilly terrains is the attachment of flames to the slope by the Coanda effect (Tritton 1988; Wu & Atkinson 2000). In fact, the Coanda effect is a reaction to the pressure difference induced by changes in the capacity for entrainment of air upslope and downslope of the fire and is considered as the main cause of plume attachment to the ground (Sharples, Gill & Dold 2010). For locations with a slope of about 40° ~ 42°, there is a possibility for unexpected wind to happen due to the Coanda effect. In other words, it is likely that the wind felt by firefighters in Tuolumne Fire event in California on a steep hill was actually sourced by flow within the buoyant plume itself as stated by Sharples, Gill and Dold (2010). They concluded that the experienced abrupt wind change in upslope terrain is compatible with what observed in the initial stage of plume attachment due to the Coanda effect.

The principal aim of this research is to shed light on the effects of sloped terrain on fire-wind enhancement and to investigate how flow accelerates during fire-wind interaction on hilly terrain.

This study attempts to fundamentally explain how the terrain slope affects the interaction between streamwise wind and vertical buoyant plume and alter the velocity profile near the ground. For this purpose, the flow acceleration is explicitly expressed in terms of contributions from pressure gradient, body force, and shear stress. A computational fluid dynamics method is used to quantitatively define the contribution of these terms.

7.3. Numerical approach

FireFOAM was used as a CFD solver in this study. This solver is a derivative of OpenFOAM (Greenshields 2015) platform, specifically designed for the fire dynamic simulations. OpenFOAM is an object-oriented open-source platform which allows the users to add self-developed modules to the main code. FireFOAM employs the LES (Large Eddy Simulation) scheme to solve Favre-filtered continuity, momentum, energy, species and state equations (Eqs 3-1 to 3-5) for compressible-flows (Wang, Chatterjee & de Ris 2011). FireFOAM uses PIMPLE scheme to couple velocity and pressure field. First order upwind was used as the differencing scheme and kEq model was used to model sub-grid scale turbulent structures. Eddy Dissipation Model (EDM) was applied as the combustion model. A module was added to the fireFOAM solver to extract fire-induced forces and acceleration to analyze the effects of terrain slope on enhancement of wind with fire. More details of this module is included in Section 3.3 and 4.3.

7.4. Model descriptions and boundary conditions

The computational domain consists of a rectangular box with the dimension of 34×9×15m as shown in Figure 7-1. The origin of the computational coordinate system is set at the center of the firebed which has a depth D of 0.3 m and a width W of 9 m extending to the full width of the computation domain. The firebed is flush with the ground and its leading edge is 3 m from the inlet of the domain. The domain inclination angle to the Earth horizontal, θ, is specified through the angle of gravitational acceleration to the z-coordinate of the computation domain. A negative value of θ indicates downslope. In such a specified computation domain, gravitational acceleration has two non-zero components:

$$g_x = -g\sin(\theta) \qquad and \qquad g_z = -g\cos(\theta) \tag{7-1}$$

Since buoyancy force is in opposite direction to gravitation acceleration, the heated fire plume will experience positive acceleration in x and z-direction under the upslope condition (θ>0); but the deceleration in x-direction and acceleration in z-direction under the downslope condition (θ<0).

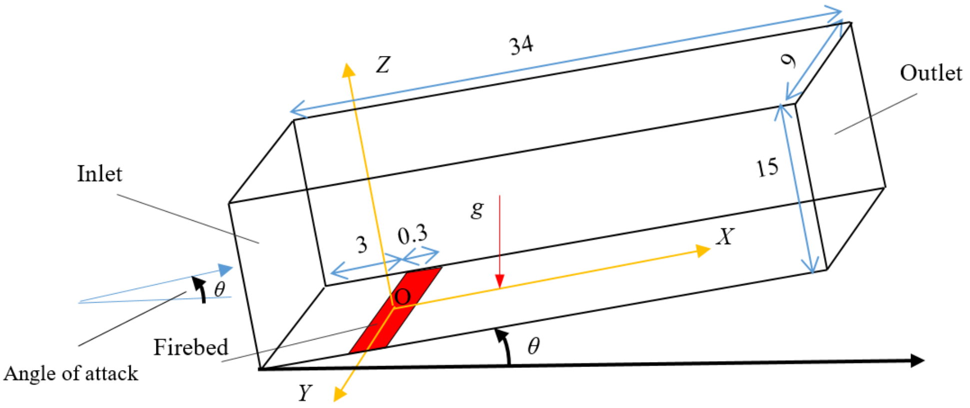

Figure 7-1. A schematic view of the computational domain at a slope angle θ from Earth horizontal direction (θ>0: upslope; θ=0: no slope; and θ<0: downslope). Dimensions are in meter.

A line source of fire with a width of 0.3m is introduced 3m downstream of the domain inlet. Methane was used as the fuel in the burner (fire source) to generate a 6.6 MW/m^2 heat release rate intensity which corresponds to a fire line intensity of I = 1.98 MW/m. Atmospheric boundary layer condition with power-law velocity profile was considered as in Eq. (7-2) for the domain inlet.

$$U(Z) = U_{ref}\left(\frac{Z}{Z_{ref}}\right)^{\alpha} \tag{7-2}$$

in which U_{ref} and Z_{ref} are respectively the reference velocity (4.5 m/s) and reference height (3 m). The value of the power exponent α is determined according to the terrain category and for the current study is taken to be 0.16. The two dimensional vortex method (Mathey et al. 2006) was used to take into account turbulent structures at the domain inlet. The initial temperature and velocity inside the whole domain were set to be 300 K and 0 m/s respectively.

Simulations were performed for no slope condition (θ=0°), four different terrain upslope angles (θ=5°, 15°, 10°, 20°) and four terrain downslope angles (θ=-5°, -15°, -10°, -20°) to evaluate the impact of terrain slope on fire-wind enhancement. The incoming flow direction for all cases is parallel with respect to the slope angle as shown in Figure 1; in other words, the angle of attack for incoming flow in each case is equal to the slope angle. Adiabatic boundary condition was used for the domain base.

No-slip wall boundary condition was prescribed for the domain base, while slip boundary was assigned to the domain sides. To treat the wall-bounded flow over the domain base, wall-function approach (Spalding 1961) was used. Open boundary condition was prescribed for the domain top to allow flows cross the boundary and a typical outflow boundary was applied to the domain outlet.

7.4.1. *Grid sensitivity analysis*

The grid sensitivity study was conducted with a grid similar to that used in our previous works (Eftekharian et al. 2018; Eftekharian et al. 2019). The grid system includes a structured non-uniform grid with the smaller cell size in the critical fire plume region. The three different grid sizes including coarse [600k (70×90×98)], medium [2.4 million, (127×149×130)] and fine [7 million, (197×163×220)] were tested. The results showed that negligible differences (<1%) in both streamwise velocity and density distributions were found between the results of the medium and fine grid, while the corresponding differences between the coarse and medium grid were about 1.7%. Hence, the medium grid was chosen for simulation in this study.

7.4.2. *Model validation*

The numerical model has been validated with two sets of experimental data, one involves diffusion flame in still air (McCaffrey 1979) and the other in cross-flow (Hirano & Kinoshita 1975) conditions. The details of the validation exercise were reported in our previous studies (Eftekharian et al. 2018; Eftekharian et al. 2019).

7.5. Results and discussion

7.5.1. *Upslope wind*

Domain travel time in the simulations is 12s. The simulation time for all simulation scenarios is 24s, which corresponds to the two domain travel cycle. The first travel cycle (12s) was considered as the transition period and therefore the data are averaged during the second cycle (last 12s).The streamwise velocity is defined as the velocity in the *X* direction in Figure 7-1.

Figure 7-2 depicts the influence of terrain upslope on different flow aerodynamic features including normalized streamwise velocity, pressure gradient, acceleration and buoyancy force on a plane passing the domain centerline (*Y*=0 in Figure 7-1). The normalized streamwise buoyancy force is defined as:

$$(F_b)_x = \left(\frac{\rho_\infty - \rho}{\rho_\infty}\right) \sin\theta \qquad (7\text{-}3)$$

Figure 7-2 (a) indicates that even in no slope condition (θ=0°) where the buoyancy force does not have any component in the streamwise direction, streamwise velocity is enhanced downstream of the fire source. This is mainly because when wind interacts with fire, a streamwise pressure gradient is generated along the wind direction and the fire-generated buoyant plume is tilted (Eftekharian et al. 2019). This fire-induced favorable pressure gradient according to Eq. (3-6) accelerates the flow and causes enhancement of the streamwise velocity.

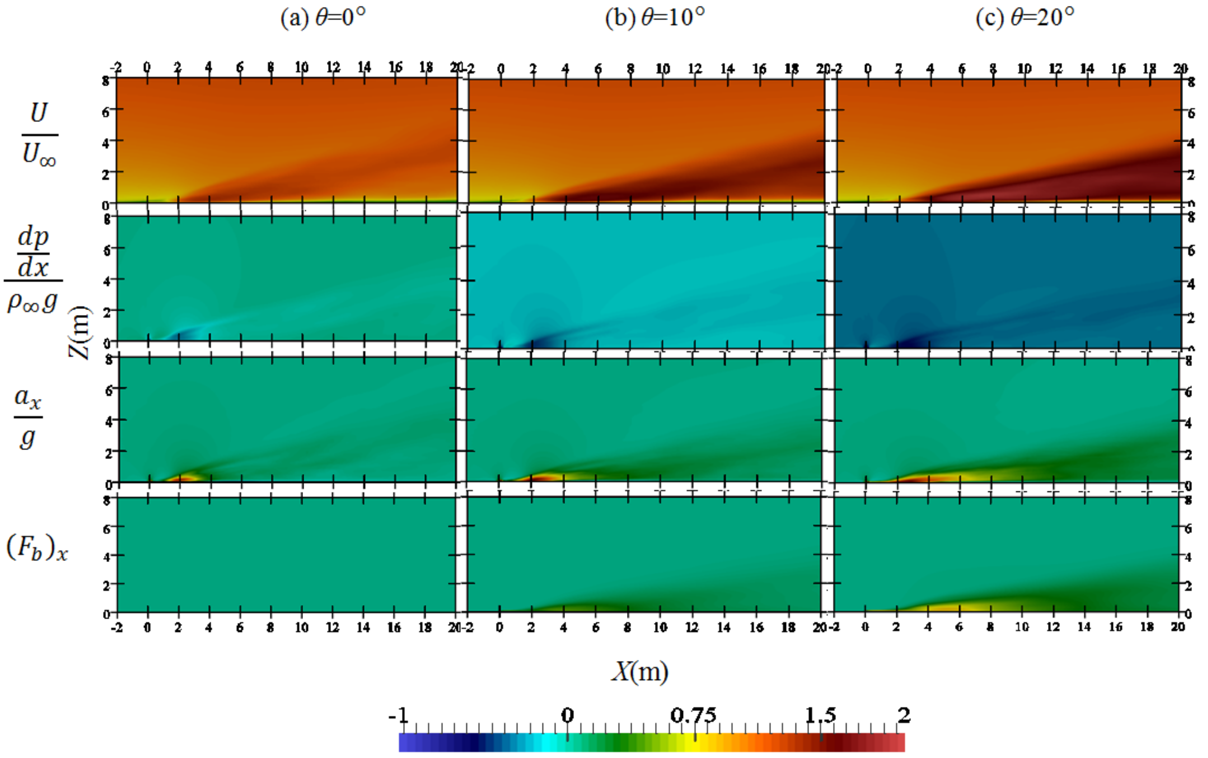

Figure 7-2 Comparison of normalized streamwise velocity $\left(\frac{U}{U_{ref}}\right)$, normalized streamwise pressure gradient$\left(\frac{\frac{dp}{dx}}{\rho_\infty g}\right)$, normalised streamwise acceleration $\left(\frac{a_x}{g}\right)$ and normalised streamwise component of buoyancy force $(F_b)_x$ at Y=0 for three inclination angles.

Comparison of Figure 7-2 (b) and (c) with (a) reveals that the streamwise buoyancy force intensifies the streamwise negative pressure gradient which leads to a greater magnitude of wind enhancement. Figure 7-2 also indicates that the higher upslope angle, the intensified streamwise negative pressure gradient which culminates in a greater magnitude of wind enhancement.

Figure 7-3 presents the cross-sectional streamwise normalized velocity at upstream and downstream of the fire source for no slope and upslope cases. The distance is normalized by the depth of the firebed. As shown in Figure 7-3, for all cases, the wind velocity is enhanced at a near ground region parallel to the fire source. Figure 7-3 also shows that fire plume is attached to the ground downstream of the fire source. Flame attachment to the ground downstream of the fire source was also observed in the previous studies investigating fire-wind interaction (Eftekharian et al. 2018; Eftekharian et al. 2019; Hu et al. 2017; Lin, Zhang & Hu 2018; Sharples, Gill & Dold 2010). It is also seen that the enhanced zone of velocity is expanded with the increase of distance from the fire source. Moreover, it is observed that the higher upslope angle leads to more intensified wind enhancement. However, the region of wind enhancement is thinner when the slope angle increases. It is believed that this is due to the Coanda effect which necessitates the plume to be inclined to the ground immediately downstream of the fire source. The Coanda effects become stronger in higher upslope angles, because in these cases, in addition to the wind force, a component of buoyancy force is created in wind direction, strengthening the Coanda effects and causing more inclination for the plume to be attached to the ground.

7.5.2. Downslope wind

Figure 7-4 shows the influence of terrain downslope on different flow aerodynamic characteristics. As can be observed, in contrast to the upslope, downslope terrain has an adverse effect on the enhanced wind by fire. The higher the downslope angle, the lower the wind enhancement. The reason behind this is that in downslope scenarios, a component of buoyancy force acts against wind direction which tends to decelerate the flow. In fact, in downslope conditions, the adverse effects of buoyancy force counteract the favorable pressure gradient being generated due to the fire-wind interaction. Immediately downstream of the fire source, the fire-induced pressure gradient (pressure force) which causes enhancement of wind by fire is strong. This pressure force prevails the adverse effects of buoyancy force and causes enhancement of wind as shown in Figure 7-4 (b) and (c). However, further downstream of the fire source where the fire-induced pressure force becomes weaker, the adverse effects of buoyancy become dominant and significantly reduce the wind velocity. In some regions, the overall effects of fire-induced pressure gradient and adverse effects of buoyancy force cause flow deceleration which leads to the reduction of the wind velocity to even lower than the freestream wind velocity

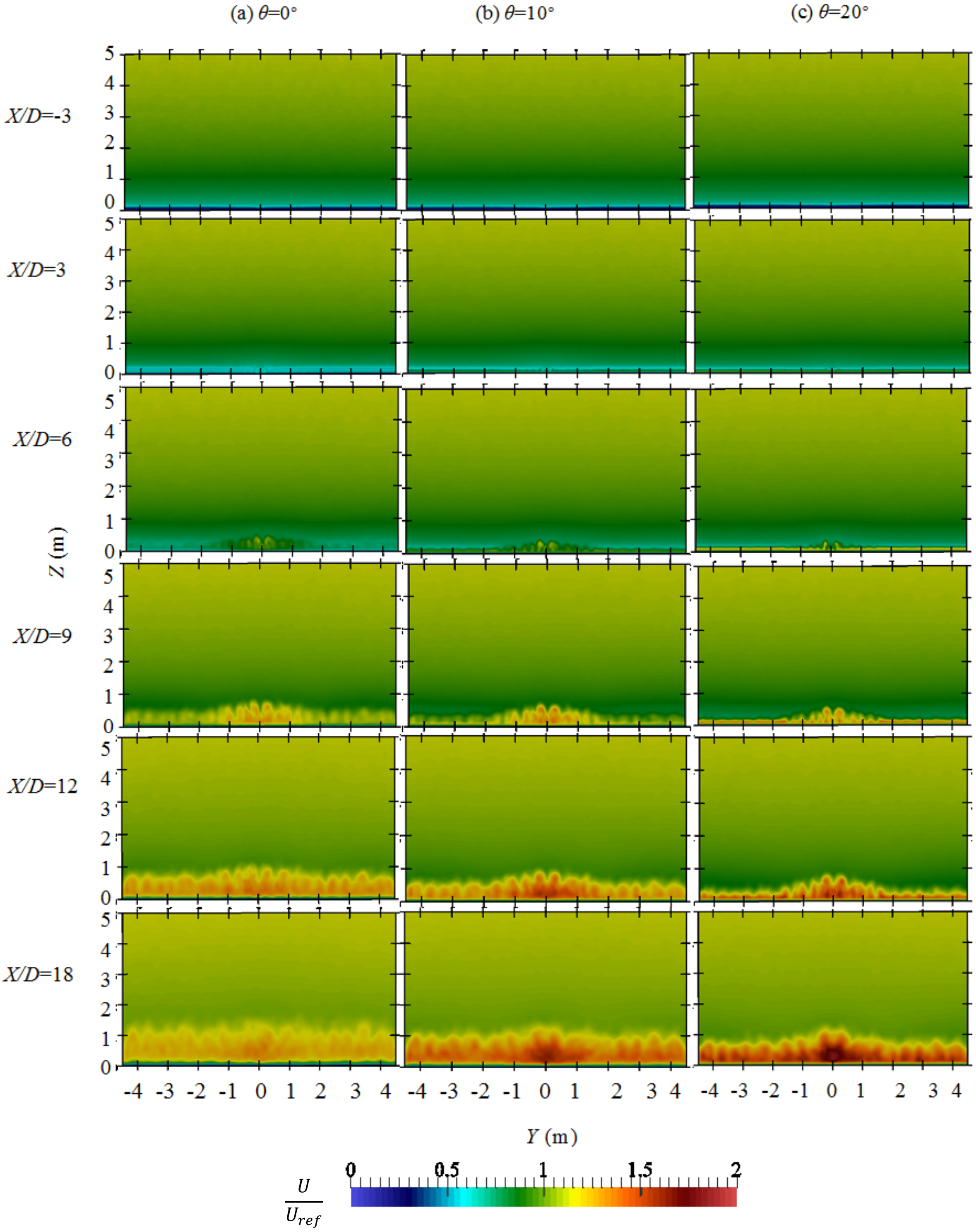

Figure 7-3 Cross-sectional normalized streamwise velocity $\left(\frac{U}{U_{ref}}\right)$ at different distances (*X/D*) from the fire source subjected to different slope conditions.

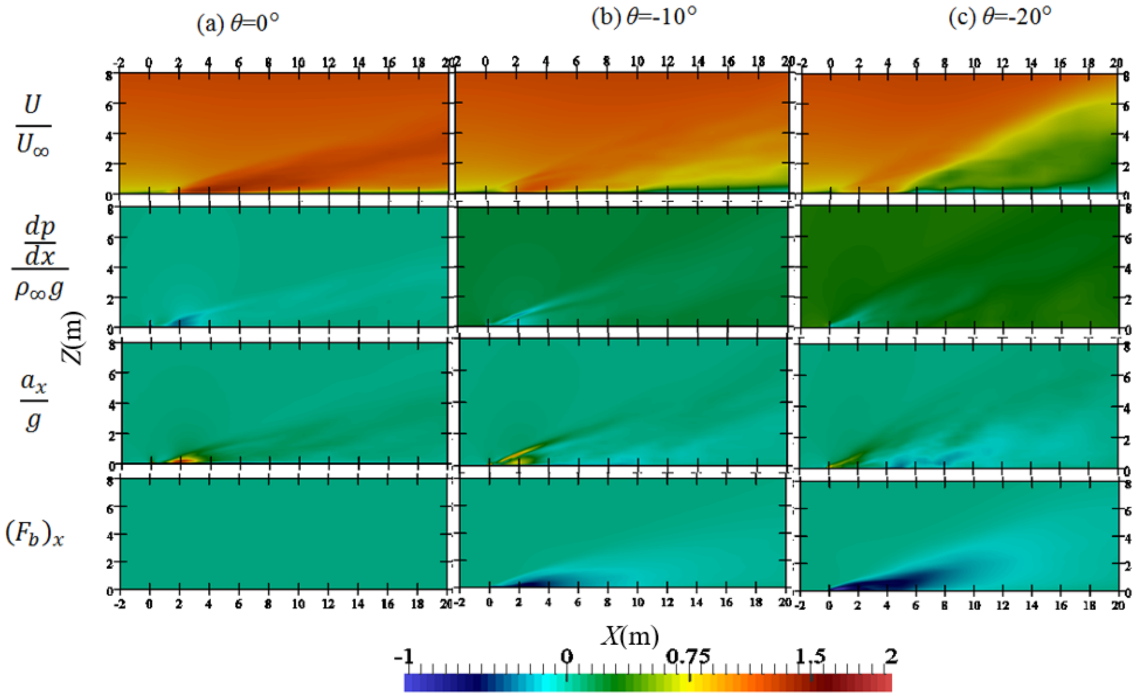

Figure 7-4. Comparison of normalized streamwise velocity $\left(\frac{U}{U_\infty}\right)$, normalized streamwise pressure gradient$\left(\frac{\frac{dp}{dx}}{\rho_\infty g}\right)$, normalized streamwise acceleration $\left(\frac{a_x}{g}\right)$ and normalized streamwise component of buoyancy force $(F_b)_x$ for (a) without slope (θ = 0°), (b) middle downslope (θ = -10°), high downslope (θ = -20°).

Figure 7-5 shows how downslope affects streamwise velocity. Cross-sectional normalized streamwise velocity distribution on Figure 7-5 shows that downslope may not only reduce the magnitude of flow enhancement by fire, but also the near ground flow velocity even lower than freestream wind velocity in relatively large downslope angles. For example, at 18D downstream of the fire source with the downslope angle of θ = -20°, the adverse buoyancy force causes a reduction in freestream wind velocity by almost 50%, creating a low-velocity region even lower than the freestream wind velocity. Moreover, in contrast to the upslope case, in the downslope scenario, the near-ground region of wind enhancement is thicker than that of no slope condition. This happens mainly because the adverse buoyancy force generated in downslope cases reduces the Coanda effects, the very effect which causes the attachment of plume to the ground immediately downstream of the fire source.

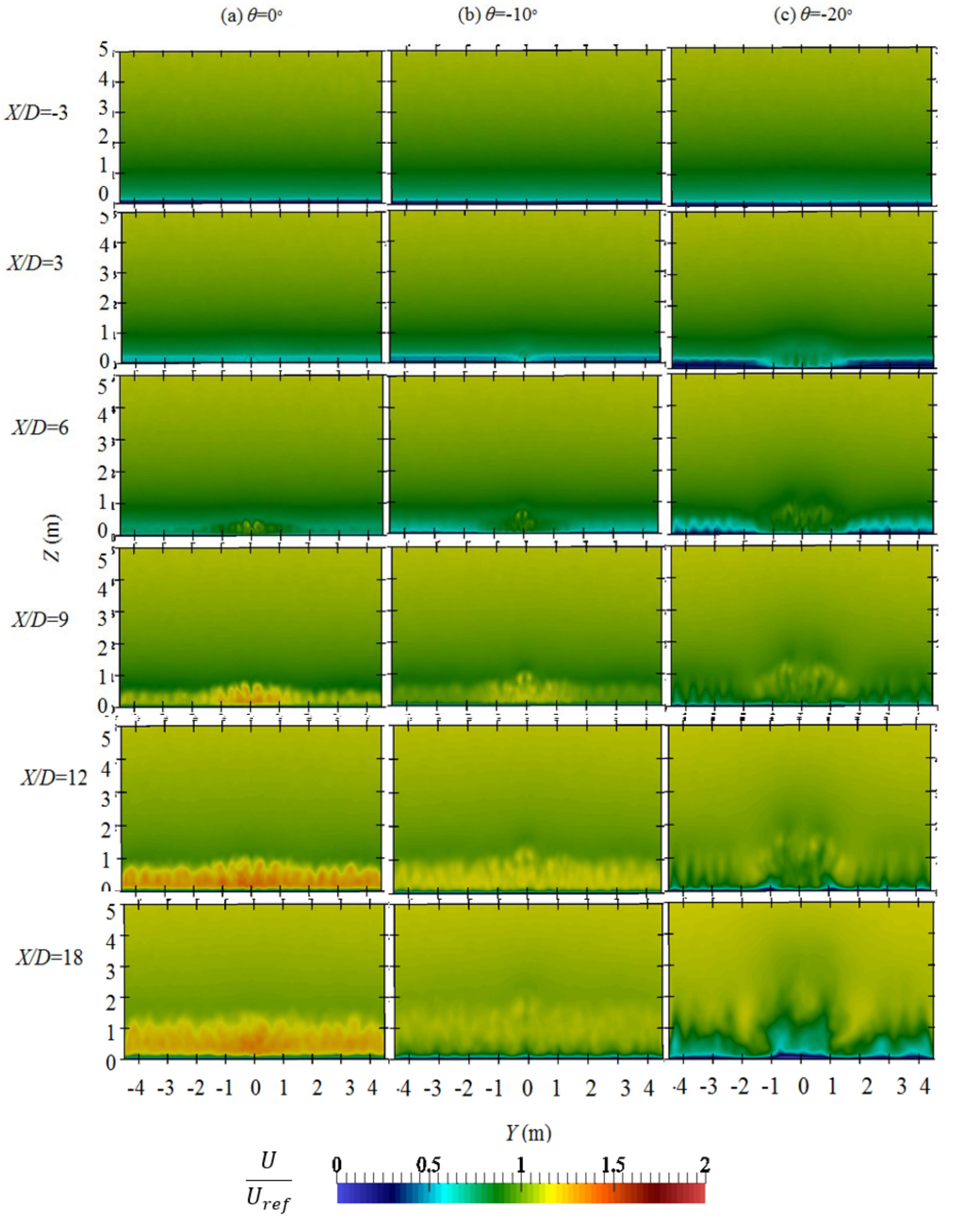

Figure 7-5 Cross-sectional normalized streamwise velocity $\left(\frac{U}{U_{ref}}\right)$ at different distances (*X/D*) from the fire source for the case without slope (θ=0°) and downslope (θ= -10°, θ= -20°) scenarios.

7.5.3. comparison of upslope and downslope

The location and the magnitude of the maximum velocity enhancement were searched in the flow filed for all simulations fire scenarios. Let U_{max} denotes the maximum streamwise velocity observed in the domain, L_x and L_z denote the *X* and *Z* coordinates of the location where U_{max} is observed. The normalized quantities of the above are listed in Table 7-1. As can be seen, for all upslope angles, the vertical distance L_z does not significantly increase, despite the increase of buoyancy force with the slope angle. This is mainly because of the dominance of Coanda effects which causes the plume to be attached to the ground immediately downstream of the fire source. However, in downslope cases, this distance (L_z) increases noticeably as the magnitude of the downslope angle increases. The major reason for this trend is that Coanda effects are weakened by the buoyancy force component against the flow in the streamwise direction. Consequently, the flow is shifted upward due to the dominance of the buoyancy force component in the vertical direction.

Table 7-1. Variation of maximum wind velocity enhancement and the corresponding location for different slope angles (degrees).

θ (°)	**$U_{\max}/Uref$**	**L_x/D (±0.38)***	**L_z/D (±0.19)**
-20	1.02	20.0	7.80
-15	1.04	14.0	4.43
-10	1.13	11.6	1.30
-5	1.22	11.0	1.06
0	1.34	12.5	0.65
5	1.47	16.0	0.85
10	1.58	19.5	1.00
15	1.77	22.5	1.30
20	1.90	26.0	1.60

* The half error band is determined by $\delta_x/(2D)$, where δ_x is the cell size.

The variation in L_x with θ appears to follow a similar trend. In order to visualize how the maximum magnitude of wind enhancement and the corresponding streamwise location change with the slope angle, these quantities are plotted in Figure 7-6. Figure 7-6 (a_1) shows that the maximum magnitude of wind enhancement is insensitive to θ in the range $-20° < \theta < -15°$. However, for $\theta > -15°$, $(U/U_{\text{ref}})_{\max}$ increases with θ almost linearly. Under the given constant wind velocity and fire intensity, an increase of 1° in slope angle approximately causes the maximum magnitude of wind enhancement to increase by approximately 2%. The L_x/D curve, however, exhibits a trough at about $\theta = -5°$ [See Figure 7-6 (a_2)]. It then increases almost linearly with θ for $\theta > 0°$.

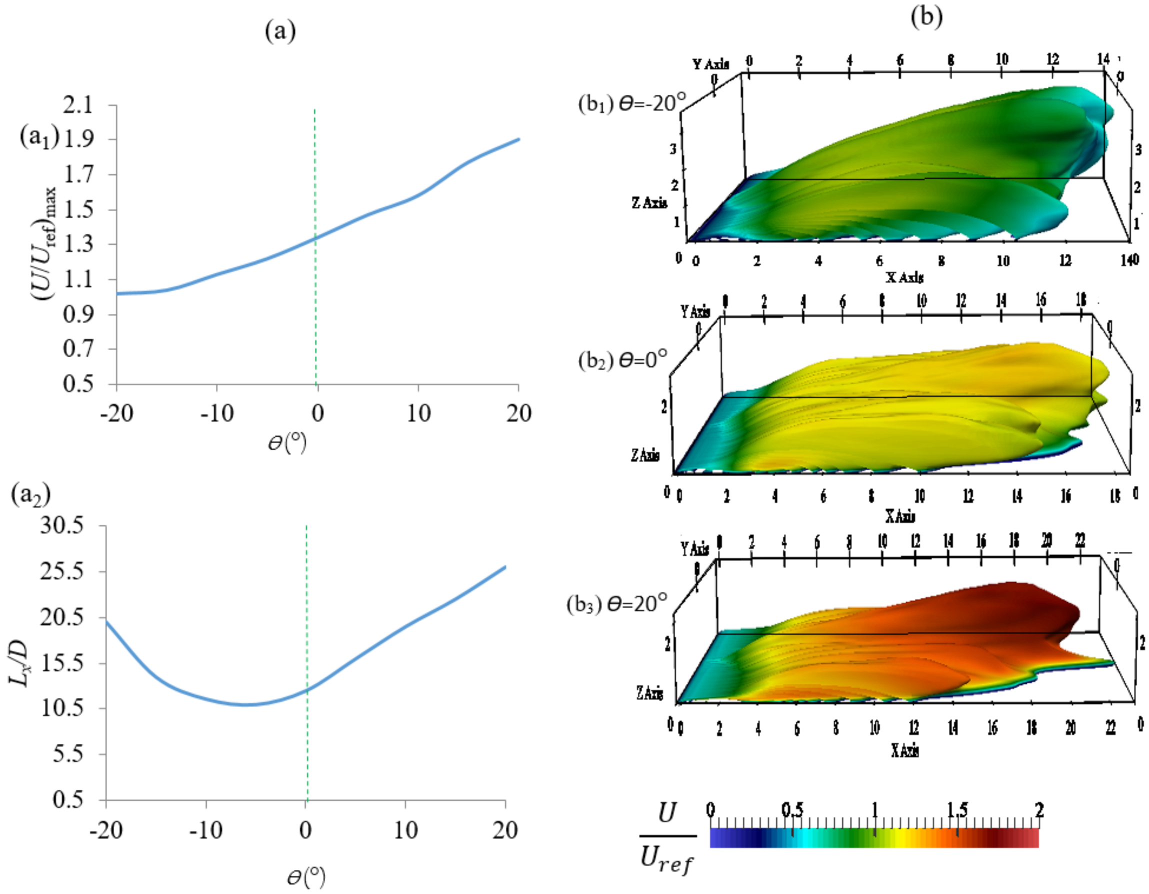

Figure 7-6 Left column (a): the trend of (a_1) maximum velocity enhancement and (a_2) its corresponding location with slope angle for all simulation cases; right column (b): Contour of plume region (the domain region where the density is less than half of the freestream density ($0.5\rho_\infty$) coloured by normalised streamwise velocity $\left(\frac{U}{U_{ref}}\right)$ for downslope (b_1), no-slope (b_2) and upslope (b_3) conditions.

Figure 7-6 (b) depicts the 3-D iso-contour of density distribution colored by the streamwise normalized wind velocity U/U_{ref} for downslope, upslope and no slope cases in the plume region. In other words, Figure 7-6 (b) shows a region of the domain where the flow density is lower than $0.5\rho_\infty$ (plume region) and these regions are coloured by normalized streamwise velocity.

Figure 7-6 (b) reveals that the enhancement of wind by fire happens in the plume region. Moreover, the upslope intensifies the magnitude of wind enhancement by fire, whereas the downslope counteracts the flow enhancement. Additionally, in contrast to the upslope scenarios, thickness growth is observed in the downslope plume region which leads to the wind enhancement in higher altitudes. All these observations are in agreement with the results observed in (Figure 7-2)-(Figure 7-5).

7.6. Conclusion

The effects of terrain slope on fire-wind enhancement phenomenon were investigated using Computational Fluid Dynamics approach, based on FireFOAM solver. Simulations were performed for 9 different slope angles ranging from -20° (downslope) to +20° (upslope) under constant freestream velocity profile and constant fire intensity. It was shown that in the upslope scenarios, streamwise buoyancy force intensifies the streamwise fire-induced negative pressure gradient which leads to a greater magnitude of wind enhancement. More specifically, the following conclusions have been drawn.

- Upslope terrain can intensify enhancement of wind by fire through the generation of a component of buoyancy force in the wind direction. In contrast, downslope terrain reduces the effects of wind enhancement by fire. In this latter case, a component of buoyancy force is generated opposite to the wind direction, which causes flow deceleration.
- Upslope terrain reinforces the Coanda effects and causes the flow to be more inclined to stay attached to the ground immediately downstream of the fire, while downslope terrain mitigates the Coanda effects, culminating in the fire plume detaching from the ground earlier.
- The simulation results revealed that the maximum magnitude of wind enhancement increases almost linearly with an increase of upslope angle.

The current study is limited to the idealized situation where the firebed is flush with the ground. In reality, both the firebed and the ground can be very rough. Their roughness and firebed protrusion above ground may have a strong influence on the turbulence intensity of the boundary layer flow, which, in turn, may alter the velocity profile downstream of the fire. These topics will be the subject of future studies.

7.7. Acknowledgment

This project is funded by Australian Research Council grant ARC-DP160103248.
The authors gratefully acknowledge OpenFOAM foundations for the provision of an open-source CFD platform. We also thank Dr. Yi Wang and Dr. Oluwayemisi Oluwole at FM Global Foundation for their technical advice on the validation part of this work.

CHAPTER 8. CONCLUSION

The enhancement of wind by fire is a complex phenomenon involving interaction of fire buoyant plume and wind cross-flow. Thermo-fluid governing equations were tailored to establish a theoretical framework to lay down the foundation for the analysis of wind enhanced by fire. Wind velocity enhancement through interacting with fire is rooted in the variation/generation of fire-induced forces at the interface of wind and fire along the wind direction, strengthening the wind velocity. Navier-Stokes equations consider these forces in three components: pressure force, gravitational force and viscous forces. A variation in one or more components of these forces causes wind enhancement in the corresponding flow velocity direction. The mechanisms of fire-wind enhancement phenomena were unraveled by numerical simulations using FireFOAM. FireFOAM solver was modified to enable it to extract all the fire-induced forces and the corresponding fire-induced acceleration contributing to the interface of fire and wind.

The developed numerical model was validated with experimental data of buoyant diffusion flame in still air and in cross-flow conditions. A good agreement was achieved for the velocity and temperature profile between experimental and numerical results.

Simulations were conducted for both point source and line source fires. The large eddy simulation results revealed that in both point and line source cases, due to the interaction of wind and fires, fire plumes are tilted toward wind direction and the longitudinal negative pressure gradient, generated by fire along the wind direction, accelerates the flow and causes wind enhancement. Simulation results also indicated that while fire-induced pressure forces are dominant, fire-induced viscous forces do not play a significant role in fire-wind interaction scenarios.

Simulations were conducted under various scenarios to study the contribution from different factors including free-stream wind velocity and fire intensity that affect the wind enhancement by point sources of fire. LES results proved that by keeping the wind velocity constant, an increase of the fire intensity increases fire-induced pressure force and consequently intensifies the enhanced wind by fire. In contrast, it was shown that under a constant fire intensity, an increase of the free-stream wind velocity causes reduction of the fire-wind enhancement. A new non-dimensional parameter, namely the modified Euler number, was introduced to explain wind enhancement behavior with variation in free-stream wind velocity. The modified Euler number represents the ratio of fire-induced pressure force to the incoming wind inertia force. It was shown that when wind velocity increases while fire intensity remains constant, the Euler number reduces and thereby fire-wind enhancement is mitigated. The variation of fire-wind enhancement with longitudinal distance from the fire source showed wind enhancement starts to increase immediately downstream of the fire source, reaching a maximum value before undergoing a gradual reduction further downstream. It was shown that the location at which maximum wind velocity enhancement happens in each simulation scenario depends on both the modified Euler number and Richardson number.

Simulations were also conducted with different combinations of fire intensity and free-stream wind velocity to quantitatively determine the extent to which wind enhancement is influenced by these two contributing factors in line fire-wind interaction scenarios. The simulation results indicated a similar trend to the point source fire scenarios: fire-wind enhancement by a line source increases with the increase of fire intensity and a reduction in free-stream wind velocity. Similarly, variation of fire-wind enhancement with longitudinal distance from the fire line source also shows that wind enhancement starts to increase immediately downstream of the fire source, reaching a maximum value, and then undergoes a gradual reduction at further downstream.

Using the contributing non-dimensional groups, a correlation was developed for maximum fire-wind velocity enhancement as a function of the Froude number and normalized fire intensity. A correlation was also developed for decaying wind enhancement after reaching the peak value as a function of maximum wind enhancement and normalized longitudinal direction. The developed correlations were satisfactorily matched (generally less than 5% margin error) with CFD data.

Once the effects of wind velocity and fire intensity on fire-wind interactions were understood for point source and line source fires respectively, a comparison was made between wind enhancement caused by the two kinds of fire sources. It was shown that under a constant fire heat release rate per unit area, a stronger pressure force is induced by the line source fire culminating in a greater fire-wind enhancement in line source fires. Aside from wind velocity enhancement in longitudinal directions, the fire-induced vertical velocity component was also investigated. In contrast to the longitudinal wind velocity enhancement, flow enhancement in vertical direction induced by a point source is higher than that of a line source. This is mainly because the overall fire-induced vertical forces in point source fires exceed that of line source fires. It was also shown that the region where wind enhancement happens is quite different in point source and line source fire scenarios. For point source cases, the region of enhancement is symmetrical horse-saddle shaped along the centreline, whereas line sources of fire generate a homogenous belt-shaped enhancement region parallel to the fire line source.

Finally, the effects of upslope and downslope terrain on a line source of fire were studied. The simulation results showed that upslope terrain creates a component of buoyancy force in wind direction and therefore intensifies the fire-induced pressure force, culminating in a stronger wind enhancement. It was also found that the higher the terrain upslope angle, the stronger the wind enhancement. In contrast, downslope terrain causes the generation of a buoyancy force component against the wind direction which counteracts fire-induced pressure forces and causes mitigation of wind enhancement. The simulation results showed that the higher the downslope angle, the less wind enhancement.

Followings are the recommendation for future work.

- Conducting full-scale experimental tests for wind-fire interaction to obtain flow aerodynamic data to be used for validation of numerical simulations.
- Conducting numerical simulation of fire-wind interaction in more complex scenarios including consideration of pyrolosis for solid fuel and modelling dynamic/moving fire source.
- Extending numerical simulation scenarios into full-scale wildland-fire/bushfire scales.
- Conducting experimental test for fire-wind-building interaction to obtain experimental data for the effects of fire-wind enhancement on pressure load of buildings.
- Developing and validating numerical models for fire-wind-building interaction and extending numerical model for more complex scenarios.

CHAPTER 9. REFERENCES

Aboje, AA, Hughes, KJ, Ingham, DB, Ma, L, Williams, A & Pourkashanian, M 2017, 'Numerical study of a wake-stabilized propane flame in a cross-flow of air', *Journal of the Energy Institute*, vol. 90, no. 1, pp. 145-58.

Albini, F 1982, 'Estimating upslope convective windspeeds for predicting wildland fire behavior', *24*, p. 1982.

Albini, FA 1981, 'A model for the wind-blown flame from a line fire', *Combustion and Flame*, vol. 43, pp. 155-74, DOI http://dx.doi.org/10.1016/0010-2180(81)90014-6

Ali, SM, Raghavan, V & Tiwari, S 2010, 'A study of steady laminar diffusion flame over methanol pool surface', *International Journal of Heat and Mass Transfer*, vol. 53, no. 21-22, pp. 4696-706.

Almeida, YP, Lage, PLC & Silva, LFLR 2015, 'Large eddy simulation of a turbulent diffusion flame including thermal radiation heat transfer', *Applied Thermal Engineering*, vol. 81, pp. 412-25, DOI https://doi.org/10.1016/j.applthermaleng.2015.02.027,

Apte VB, Bilger RW, Green AR, Quintiere JG. 1991 'Wind-aided turbulent flame spread and burning over large-scale horizontal PMMA surfaces'. *Combustion and Flame* 85(1):169-84.

AS3959 (2018), Construction of buildings in bushfire-prone areas, Standards Australia**:** 120

AS4055 (2012). Wind loads for housing. Standards Australia, SAI Global – Standards On-Line.

AS/NZS1170.2 (2011). Structural design actions Part 2: Wind actions. Standards Australia, SAI Global – Standards On-Line.

Ashe, B, McAneney, KJ & Pitman, AJ 2009, 'Total cost of fire in Australia', *Journal of Risk Research*, vol. 12, no. 2, pp. 121-36, DOI 10.1080/13669870802648528, <http://dx.doi.org/10.1080/13669870802648528>.

Balbi, JH, Rossi, JL, Marcelli, T & Santoni, P-A 2007, 'A 3D physical real-time model of surface fires across fuel beds', *Combustion Science and Technology*, vol. 179, no. 12, pp. 2511-37.

Balbi, JH, Morandini, F, Silvani, X, Filippi, JB & Rinieri, F 2009, 'A physical model for wildland fires', *Combustion and Flame*, vol. 156, no. 12, pp. 2217-30.

Batchelor, GK 2000, *An introduction to fluid dynamics*, Cambridge University Press, Cambridge.

Baum, H, McGrattan, KB & Rehm, RG 1994, 'Simulation of smoke plumes from large pool fires', *Elsevier*, vol. 25, no. 1, pp. 1463-9.

Baum, Hr, McGrattan, KB & Rehm, RG 1994, 'Simulation of smoke plumes from large pool fires', *Symposium (International) on Combustion*, vol. 25, no. 1, pp. 1463-9, DOI https://doi.org/10.1016/S0082-0784(06)80790-3.

Becker, HA & Liang, D 1978, 'Visible length of vertical free turbulent diffusion flames', *Combustion and Flame*, vol. 32, pp. 115-37, DOI https://doi.org/10.1016/0010-2180(78)90087-1.

Becker, HA & Yamazaki, S 1978, 'Entrainment, momentum flux and temperature in vertical free turbulent diffusion flames', *Combustion and Flame*, vol. 33, pp. 123-49, DOI https://doi.org/10.1016/0010-2180(78)90055-X.

Beer, T 1991, 'The interaction of wind and fire', *Boundary-Layer Meteorology*, vol. 54, no. 3, pp. 287-308, DOI 10.1007/bf00183958, <https://doi.org/10.1007/BF00183958>.

Beyler, CL 2008, 'Fire hazard calculations for large open hydrocarbon fires', *in SFPE Handbook of Fire Protection Engineering, 4th edn (eds P.J. Di Nenno et al .).*

Blanchi, R & Leonard, J 2005, *Investigation of bushfire attack mechanisms resulting in house loss in the ACT bushfire 2003.*

Blanchi, R, Lucas, C, Leonard, J & Finkele, K 2010, 'Meteorological conditions and wildfire-related houseloss in Australia', *International Journal of Wildland Fire*, vol. 19, no. 7, pp. 914-26, DOI http://dx.doi.org/10.1071/WF08175, <http://www.publish.csiro.au/paper/WF08175>.

Blocken, B & Gualtieri, C 2012, 'Ten iterative steps for model development and evaluation applied to computational fluid dynamics for environmental fluid mechanics', *Environmental Modelling & Software*, vol. 33, pp. 1-22, DOI http://dx.doi.org/10.1016/j.envsoft.2012.02.001.

Boirlaud, M, Couton, D & Plourde, F 2012, 'Direct numerical simulation of the turbulent wake behind a heated cylinder', *International Journal of Heat and Fluid Flow*, vol. 38, pp. 82-93, DOI https://doi.org/10.1016/j.ijheatfluidflow.2012.09.005, <http://www.sciencedirect.com/science/article/pii/S0142727X1200121X>.

BoM, BoM 2009, *Appendix 6 Submission to the Victorian Bushfire Royal Commission*, BoM, Melbourne, Australia.

Botros, PE & Brzustowski, TA 1979, 'An experimental and theoretical study of the turbulent diffusion flame in cross-flow', *Symposium (International) on Combustion*, vol. 17, no. 1, pp. 389-98, DOI https://doi.org/10.1016/S0082-0784(79)80040-5, <http://www.sciencedirect.com/science/article/pii/S0082078479800405>.

Bouhafid, A, Vantelon, J, Souil, J, Bosseboeuf, G & Rongere, F 1989, 'Characterisation of thermal radiation from freely burning oil pool fires', *Fire Safety Journal*, vol. 15, no. 5, pp. 367-90.

Bradstock, R & Gill, A 1993, 'Fire in semiarid, mallee shrublands-size of flames from discrete fuel arrays and their role in the spread of fire', *International Journal of Wildland Fire*, vol. 3, no. 1, pp. 3-12.

Briggs, GA 1975b, 'Plume rise predictions, lectures on air pollution and environment impact analysis.', *Am. Meteorol. Soc. 10. Boston, USA*.

Briggs, GA 1984, 'Plume rise and buoyancy effects', *Atmos. Sci. Power Prod*, pp. 327-66.

Broadwell, JE & Breidenthal, RE 1984, 'Structure and mixing of a transverse jet in incompressible flow', *Journal of Fluid Mechanics*, vol. 148, pp. 405-12, DOI 10.1017/S0022112084002408, <https://www.cambridge.org/core/article/div-class-title-structure-and-mixing-of-a-transverse-jet-in-incompressible-flow-div/4CBE40D45995546107B974DFA7661EA6>.

Butler, B, Cohen, J, Latham, D, Schuette, R, Sopko, P, Shannon, K et al. 2004, 'Measurements of radiant emissive power and temperatures in crown fires', *Canadian Journal of Forest Research*, vol. 34, no. 8, pp. 1577-87.

Byram, GM 1959, ‘Combustion of forest fuels’, in KP Davis (ed.) Forest fire: control and use, McGraw-Hill, New York, pp. 61-89.

Caulfield, C-CP & Woods, AW 1995, 'Plumes with non-monotonic mixing behaviour', *Geophysical & Astrophysical Fluid Dynamics*, vol. 79, no. 1-4, pp. 173-99, DOI 10.1080/03091929508228996, <http://dx.doi.org/10.1080/03091929508228996>.

Cetegen, B, Zukoski, EE & Kubota, T 1984, 'Entrainment in the near and far field of fire plumes', *Combustion Science and Technology*, vol. 39, no. 1-6, pp. 305-31, DOI 10.1080/00102208408923794, <http://dx.doi.org/10.1080/00102208408923794>.

Cetegen, BM & Kasper, KD 1996, 'Experiments on the oscillatory behavior of buoyant plumes of helium and helium-air mixtures', *Physics of Fluids*, vol. 8, no. 11, pp. 2974-84, DOI doi:http://dx.doi.org/10.1063/1.869075, <http://scitation.aip.org/content/aip/journal/pof2/8/11/10.1063/1.869075;jsessionid=sxt-HKA0bmzzqy-JNAm1kMtn.x-aip-live-03>.

Chai, J & Rath, P 2006, 'Discrete-ordinates and finite-volume methods for radiation heat transfer'. *presented at the International Workshop on Discrete- Ordinates and Finite-Volume Methods for Radiation Heat Transfer*, IIT, Guwahati, India, Jan. 2–3, 2006.

Chamberlin, D & Rose, A 1928, 'First symposium on combustion,' *Industrial Engineering Chemistry* vol. 20, pp. 1013-6.

Chen, Z, Wen, J, Xu, B & Dembele, S 2014a, 'Extension of the eddy dissipation concept and smoke point soot model to the LES frame for fire simulations', *Fire Safety Journal*, vol. 64, pp. 12-26.

Chen, Z, Wen, J, Xu, B & Dembele, S 2014b, 'Large eddy simulation of a medium-scale methanol pool fire using the extended eddy dissipation concept', *International Journal of Heat and Mass Transfer*, vol. 70, pp. 389-408, DOI http://dx.doi.org/10.1016/j.ijheatmasstransfer.2013.11.010, <http://www.sciencedirect.com/science/article/pii/S0017931013009642>.

Coleman, JR & Sullivan, AL 1996, 'A real-time computer application for the prediction of fire spread across the Australian landscape', *Simulation*, vol. 67, no. 4, pp. 230-40.

Consalvi, JL, Pizzo, Y & Porterie, B 2008, 'Numerical analysis of the heating process in upward flame spread over thick PMMA slabs', *Fire Safety Journal*, vol. 43, no. 5, pp. 351-62.

Cortelezzi, L & Karagozian, AR 2001, 'On the formation of the counter-rotating vortex pair in transverse jets', *Journal of Fluid Mechanics*, vol. 446, pp. 347-73, <https://www.cambridge.org/core/article/div-class-title-on-the-formation-of-the-counter-rotating-vortex-pair-in-transverse-jets-div/FDD69977A3C624C7152A9C8E023CF785>.

Drysdale, D 2011, *An introduction to fire dynamics*, A John Wiley & Sons, Ltd.

Dupuy, JL & Maréchal, J 2011, 'Slope effect on laboratory fire spread: contribution of radiation and convection to fuel bed preheating', *International Journal of Wildland Fire*, vol. 20, no. 2, pp. 289-307, DOI http://dx.doi.org/10.1071/WF09076, <http://www.publish.csiro.au/paper/WF09076>.

Dupuy, JL, Maréchal, J, Portier, D & Valette, JC 2011, 'The effects of slope and fuel bed width on laboratory fire behaviour', *International Journal of Wildland Fire*, vol. 20, no. 2, pp. 272-88, DOI http://dx.doi.org/10.1071/WF09075, <http://www.publish.csiro.au/paper/WF09075>.

Dupuy, JL & Morvan, D 2005, 'Numerical study of a crown fire spreading toward a fuel break using a multiphase physical model', *International Journal of Wildland Fire*, vol. 14, no. 2, pp. 141-51, DOI http://dx.doi.org/10.1071/WF04028, <http://www.publish.csiro.au/paper/WF04028>.

Eftekharian, E, Ghodrat, M, He, Y, Ong, RH, Kwok, KCS & Zhao, M 2019, 'Numerical analysis of wind velocity effects on fire-wind enhancement', *International Journal of Heat and Fluid Flow*, vol. 80 Article No 108471.

Eftekharian, E, Ghodrat, M, He, Y, Ong, RH, Kwok, KCS, Zhao, M. 2019, 'Investigation of terrain slope effects on wind enhancement by a line source fire', *Case Studies in Thermal Engineering*, vol. 14, DOI https://doi.org/10.1016/j.csite.2019.100467, <http://www.sciencedirect.com/science/article/pii/S2214157X19301121>.

Eftekharian, E, Ghodrat, M, Ong, R, He, Y & Kwok, K 2018, 'CFD investigation of cross-flow effects on fire-wind enhancement'. *Proceedings Of The 21St Australasian Fluid Mechanics Conference*, 10-13 December 2018, Adelaide, South Australia.

Eftekharian, E, He, Y, Kwok, KCS, Ong, RH & Yuan, J 2019, 'Investigation of fire-driven cross-wind velocity enhancement', *International Journal of Thermal Sciences*, vol. 141, pp. 84-95, DOI https://doi.org/10.1016/j.ijthermalsci.2019.03.033, <http://www.sciencedirect.com/science/article/pii/S1290072918311554>.

Eftekharian, E, Ghodrat, M, He, Y, Ong, RH, Kwok, KCS, Zhao, M 2019, 'Numerical analysis of the effect of fire source configuration on fire-wind enhancement', *Heat Transfer Engineering*, vol. 42, no. 1.

European & Commission 2014, 'Trends in global CO2 emissions: 2014 Report, Lead by the PBL Netherlands Environmental Assessment Agency', <Accessed at http://edgar.jrc.ec.europa.eu/news_docs/jrc-2014-trendsin-global-co2-emissions-2014-report-93171.pd>.

European & Commission 2013, *JRC Technical Report: Forest Fires in Europe, Middle East and North Africa 2012, Report EUR 26048 EN, pdf.* , Publications Office of the European Union,Luxembourg,, < Accessed at http://forest.jrc.ec.europa.eu/media/cms_page_media/9/FireReport2012_Final_2pdf_2.>.

Fang, J, Jiang, C, Wang, JW, Guan, JF, Zhang, YM & Wang, JJ 2016, 'Oscillation frequency of buoyant diffusion flame in cross-wind', *Fuel*, vol. 184, pp. 856-63, DOI http://dx.doi.org/10.1016/j.fuel.2016.07.084, <http://www.sciencedirect.com/science/article/pii/S0016236116306871>.

Ferrero, F, Munoz, M & Arnaldos, J 2007, 'Effects of thin-layer boilover on flame geometry and dynamics in large hydrocarbon pool fires', *Fuel Processing Technology*, vol. 88, no. 3, pp. 227-35.

Finney, M 2004. FARSITE: Fire Area Simulator–model development and evaluation, United States Department of Agriculture, Ogden.

Forthofer, JM & Goodrick, SL 2011, 'Review of vortices in wildland fire', *Journal of Combustion*, vol. 2011.

Fric, TF & Roshko, A 1994, 'Vortical structure in the wake of a transverse jet', *Journal of Fluid Mechanics*, vol. 279, pp. 1-47, DOI 10.1017/S0022112094003800, <https://www.cambridge.org/core/article/div-class-title-vortical-structure-in-the-wake-of-a-transverse-jet-div/79CFDA2A9200C76E5B16E2B2C4C2B515>.

Fuaad, PA, Baig, MF & Khan, BA 2016, 'Turbulent drag reduction using active control of buoyancy forces', *International Journal of Heat and Fluid Flow*, vol. 61, pp. 585-98, DOI https://doi.org/10.1016/j.ijheatfluidflow.2016.07.003, <http://www.sciencedirect.com/science/article/pii/S0142727X16303423>.

Fukumoto, K, Wang, C & Wen, J 2018, 'Large eddy simulation of upward flame spread on PMMA walls with a fully coupled fluid–solid approach', *Combustion and Flame*, vol. 190, pp. 365-87, DOI https://doi.org/10.1016/j.combustflame.2017.11.012, <http://www.sciencedirect.com/science/article/pii/S0010218017304510>.

Gallacher JR, Ripa B, Butler BW, Fletcher, TH. 2018 'Lab-scale observations of flame attachment on slopes with implications for firefighter safety zones'. Fire Safety Journal; 96:93-104. https://doi.org/10.1016/j.firesaf.2018.01.002

Ganji, AR & Sawyer, RF 1980, 'Experimental study of the flow-field of a two-dimensional premixed turbulent flame', *American Institute of Aeronautics and Astronautics* Journal., vol. 18, no. 7.

Gannouni, S, Zinoubi, J & Maad, RB 2019, 'Numerical study on the thermal buoyant flow stratification in tunnel fires with longitudinal imposed airflow: Effect of an upstream blockage', *International Journal of Thermal Sciences*, vol. 136, pp. 230-42.

Gentle, N, Kierce, S & Nitze, A 2001, 'Economic costs of natural disasters in Australia', *Australian Journal of Emergency Management,*EMA, Canberra.

Gollahalli, SR, Brzustowski, TA & Sullivan, HF 1975, 'Characteristics of a turbulent propane diffusion flame in a cross-wind', *Transactions of the Canadian Society for Mechanical Engineering*, vol. 3, no. 4, pp. 205-14, viewed 19 Jun 2018, DOI 10.1139/tcsme-1975-0028, <https://doi.org/10.1139/tcsme-1975-0028>.

Gould, JS, McCaw, WL & Cheney, NP 2007, *Project Vesta. Fire in Dry Eucalypt Forest: Fuel Structure, Fuel Dynamics and Fire Behaviour.*, Ensis-CSIRO, Canberra, Australia and WA Department of Environment and Conservation, Perth, Australia.

Gould, JS, McCaw, WL, Ensis, Conservation, WADo, Management, L, CSIRO et al. 2007, *Project Vesta: Fire in Dry Eucalypt Forest : Fuel Structure, Fuel Dynamics and Fire Behaviour*, Ensis.

Grant, AJ & Jones, JM 1975, 'Low-frequency diffusion flame oscillations', *Combustion and Flame*, vol. 25, pp. 153-60, DOI http://dx.doi.org/10.1016/0010-2180(75)90081-4, <http://www.sciencedirect.com/science/article/pii/0010218075900814>.

Greenshields, CJ 'Openfoam user guide', *OpenFOAM Foundation Ltd,* [Online] Available https://www.openfoam.com/documentation/userguide. Accessed: Jul. 3, 2019.

Hamins, A, Kashiwagi, T & Buch, RR 1996, 'Characteristics of pool fire burning', in *Fire resistance of industrial fluids*, ASTM International.

Hamins, A, Yang, JC & Kashiwagi, T 1992, 'An experimental investigation of the pulsation frequency of flames', *Symposium (International) on Combustion*, vol. 24, no. 1, pp. 1695-702, DOI http://dx.doi.org/10.1016/S0082-0784(06)80198-0, <http://www.sciencedirect.com/science/article/pii/S0082078406801980>.

Hasemi, Y & Nishihata, M 1989, 'Fuel shape effect on the deterministic properties of turbulent diffusion flames ', *Fire Safety Science*. Vol. 2, pp. 275–286.

Hattori, T, Norris, SE, Kirkpatrick, MP & Armfield, SW 2013, 'Simulation and analysis of puffing instability in the near field of pure thermal planar plumes', *International Journal of Thermal Sciences*, vol. 69, pp. 1-13, DOI https://doi.org/10.1016/j.ijthermalsci.2013.01.016, <http://www.sciencedirect.com/science/article/pii/S1290072913000252>.

Hawley, LF 1926, 'Theoretical considerations regarding factors which influence forest fires', *Journal of Forestry*, vol. 24, no. 7, pp. 756-63, viewed 14 Feb 2019, DOI 10.1093/jof/24.7.756, <https://dx.doi.org/10.1093/jof/24.7.756>.

He, Y, Kwok, K, Douglas, G & Razali, I 2011a, 'Numerical investigation of bushfire-wind interaction and its impact on building structure', *Fire Safety Science*, vol. 10, pp. 1449-62.

He, Y, Kwok, KCS, Douglas, G & Razali, IM 2011b, *Numerical Investigation of Bushfire-Wind Interaction and its Impact on Building Structure*, vol. 10.

Herwig, H, Gloss, D & Wenterodt, T 2010, 'Flow in channels with rough walls—old and new concepts', *Heat Transfer Engineering*, vol. 31, no. 8, pp. 658-65.

Heskestad, G 2016 ‘Fire plumes, flame height and air entrainment’, in MJ Hurley (ed.), SFPE handbook of fire protection engineering, Springer, New York. – provide page references for relevant chapter if possible.

Hilton, J, Miller, C, Sullivan, A & Rucinski, C 2015, 'Effects of spatial and temporal variation in environmental conditions on simulation of wildfire spread', *Environmental Modelling & Software*, vol. 67, pp. 118-27.

Hirano, T & Kanno, Y 1973, 'Aerodynamic and thermal structures of the laminarboundary layer over a flat plate with a diffusion flame', *Symposium (International) on Combustion*, vol. 14, no. 1, pp. 391-8, DOI https://doi.org/10.1016/S0082-0784(73)80038-4, <http://www.sciencedirect.com/science/article/pii/S0082078473800384>.

Hirano, T & Kinoshita, M 1975, 'Gas velocity and temperature profiles of a diffusion flame stabilized in the stream over liquid fuel', *Symposium (International) on Combustion*, vol. 15, no. 1, pp. 379-87, DOI https://doi.org/10.1016/S0082-0784(75)80312-2, <http://www.sciencedirect.com/science/article/pii/S0082078475803122>.

Hottel, HC & Hawthorne, WR 1948, Diffusion in laminar flame jets ‘*Symposium on Combustion and Flame, and Explosion Phenomena*', Vol. 3 PP. 254-266.

Hu, L 2017, 'A review of physics and correlations of pool fire behaviour in wind and future challenges', *Fire Safety Journal*, vol. 91, no. Supplement C, pp. 41-55, DOI https://doi.org/10.1016/j.firesaf.2017.05.008, <http://www.sciencedirect.com/science/article/pii/S0379711217303405>.

Hu, L, Hu, J & de Ris, JL 2015, 'Flame necking-in and instability characterization in small and medium pool fires with different lip heights', *Combustion and Flame*, vol. 162, no. 4, pp. 1095-103, DOI http://dx.doi.org/10.1016/j.combustflame.2014.10.001, <http://www.sciencedirect.com/science/article/pii/S0010218014003101>.

Hu, L, Kuang, C, Zhong, X, Ren, F, Zhang, X & Ding, H 2017, 'An experimental study on burning rate and flame tilt of optical-thin heptane pool fires in cross flows', *Proceedings of the Combustion Institute*, vol. 36, no. 2, pp. 3089-96.

Hu, L, Liu, S, de Ris, JL & Wu, L 2013, 'A new mathematical quantification of wind-blown flame tilt angle of hydrocarbon pool fires with a new global correlation model', *Fuel*, vol. 106, pp. 730-6, DOI http://dx.doi.org/10.1016/j.fuel.2012.10.075, <http://www.sciencedirect.com/science/article/pii/S0016236112008721>.

Hu, L, Liu, S & Wu, L 2013, 'Flame radiation feedback to fuel surface in medium ethanol and heptane pool fires with cross air flow', *Combustion and Flame*, vol. 160, no. 2, pp. 295-306, Scopus, DOI 10.1016/j.combustflame.2011.11.008, <https://www.scopus.com/inward/record.url?eid=2-s2.0-84875875578&partnerID=40&md5=896ea91d718c70b458ea2a228fd18e8e>.

Hu, L, Liu, S, Xu, Y & Li, D 2011, 'A wind tunnel experimental study on burning rate enhancement behavior of gasoline pool fires by cross air flow', *Combustion and Flame*, vol. 158, no. 3, pp. 586-91, Scopus, DOI 10.1016/j.combustflame.2010.10.013, <https://www.scopus.com/inward/record.url?eid=2-s2.0-78751567729&partnerID=40&md5=cf194436b0e9540355154eeafabdf74f>.

Hu, L, Tang, F, Wang, Q & Qiu, Z 2013, 'Burning characteristics of conduction-controlled rectangular hydrocarbon pool fires in a reduced pressure atmosphere at high altitude in Tibet', *Fuel*, vol. 111, pp. 298-304.

Hu, L, Wu, L & Liu, S 2013, 'Flame length elongation behavior of medium hydrocarbon pool fires in cross air flow', *Fuel*, vol. 111, pp. 613-20, Scopus, DOI 10.1016/j.fuel.2013.03.025, <https://www.scopus.com/inward/record.url?eid=2-s2.0-84879050099&partnerID=40&md5=613a8d8231db0a6ca60736c9fc40889a>.

Hu, L, Zhang, X, Delichatsios, MA, Wu, L & Kuang, C 2017, 'Pool fire flame base drag behavior with cross flow in a sub-atmospheric pressure', *Proceedings of the Combustion Institute*, vol. 36, no. 2, pp. 3105-12, DOI https://doi.org/10.1016/j.proci.2016.06.139, <http://www.sciencedirect.com/science/article/pii/S1540748916301973>.

Hunt, GR & Kaye, NB 2005, 'Lazy plumes', *Journal of Fluid Mechanics*, vol. 533, pp. 329–38.
Inc, M 2016, 'MATLAB–MathWorks'.

Iqbal, N & Quintiere, JG 1994, 'Flame heat fluxes in PMMA pool fires', *Journal of Fire Protection Engineering*, vol. 6, pp. 153–62.

Jackson, P & Hunt, J 1975, 'Turbulent wind flow over a low hill', *Quarterly Journal of the Royal Meteorological Society*, vol. 101, no. 430, pp. 929-55.

Jiang, P & Lu, S-x 2016, 'Pool Fire Mass Burning Rate and Flame Tilt Angle under Crosswind in Open Space', *Procedia Engineering*, vol. 135, pp. 261-74, DOI http://dx.doi.org/10.1016/j.proeng.2016.01.122, <http://www.sciencedirect.com/science/article/pii/S1877705816001260>.

Johnson, A 1993, 'A model for predicting thermal radiation hazards from large-scale LNG pool fires', *Hemsphere Publishing Corporation*, vol. 130, pp. 507-.

Johnston, P, Kelso, J & Milne, GJ 2008, 'Efficient simulation of wildfire spread on an irregular grid', *International Journal of Wildland Fire*, vol. 17, no. 5, pp. 614-27.

Kazemipour, A, Afshin, H & Farhanieh, B 2017, 'Numerical–Analytical Assessment of Fire and Ventilation Interaction in Longitudinally Ventilated Tunnels Using Jet Fans', *Heat Transfer Engineering*, vol. 38, no. 5, pp. 523-37.

Kelso, RM, Lim, TT & Perry, AE 1996, 'An experimental study of round jets in cross-flow', *Journal of Fluid Mechanics*, vol. 306, pp. 111-44, DOI 10.1017/S0022112096001255, <https://www.cambridge.org/core/article/div-class-title-an-experimental-study-of-round-jets-in-cross-flow-div/4301861CE913C315D60B390A77053977>.

Koo, E, Pagni, P, Stephens, S, Huff, J, Woycheese, J & Weise, D 2005, 'A simple physical model for forest fire spread rate', *Fire Safety Science*, vol. 8, pp. 851-62.

Krishnamoorthy, G 2012, 'A comparison of angular discretization strategies for modeling radiative transfer in pool fire simulations', *Heat Transfer Engineering*, vol. 33, no. 12, pp. 1040-51.

Kumar, R & Dewan, A 2014, 'Computational models for turbulent thermal plumes: recent advances and challenges', *Heat Transfer Engineering*, vol. 35, no. 4, pp. 367-83.

Kwok, K, He, Y & Douglas, G 2012, 'Bushfire-enhanced wind load on structures', *Proceedings of the Institution of Civil Engineers-Engineering and Computational Mechanics*, vol. 165, no. 4, pp. 253-63.

Kwok, KC, He, Y & Douglas, GB 2010, 'Wind impacts on fire spread and structural failure during bushfire in complex terrain', *Proceedings of 9th United Kingdom Conference on Wind Engineering* pp. 3-14.

Lam, CS & Weckman, EJ 2015, 'Wind-blown pool fire, Part II: Comparison of measured flame geometry with semi-empirical correlations', *Fire Safety Journal*, vol. 78, pp. 130-41, DOI http://dx.doi.org/10.1016/j.firesaf.2015.08.004, <http://www.sciencedirect.com/science/article/pii/S037971121530014X>.

Lambert, K 2010, 'Extreme bushfire/firestorm impact and the bush/urban interface, Black Saturday 7th February 2009', 13th Feb. 2014, 2009 Victorian Bushfires Royal Commission, <www.royalcommission.vic.gov.au/Submissions/SubmissionDocuments/SUBM-002-059-0366_01_R.pdf. >.

Landahl, MT, Landahl, M & Mollo-Christensen, E 1992, *Turbulence and random processes in fluid mechanics*, Cambridge University Press.

Lautkaski, R 1992, 'Validation of flame drag correlations with data from large pool fires', *Journal of Loss Prevention in the Process Industries*, vol. 5, no. 3, pp. 175-80.

Lawal, MS, Fairweather, M, Ingham, DB, Ma, L, Pourkashanian, M & Williams, A 2010, 'Numerical study of emission characteristics of a jet flame in cross-flow', *Combustion Science and Technology*, vol. 182, no. 10, pp. 1491-510, DOI 10.1080/00102202.2010.496379, <https://doi.org/10.1080/00102202.2010.496379>.

Li, M, Wang, C, Li, Z, Yang, S, Fukumoto, K & Fan, C 2018, 'Combustion and flame spreading characteristics of diesel fuel with forced air flows', *Fuel*, vol. 216, pp. 390-7.

Li, X, Hu, L & Shang, F 2018, 'Flame downwash transition and its maximum length with increasing fuel supply of non-premixed jet in cross flow', *Energy*, vol. 164, pp. 298-305, DOI https://doi.org/10.1016/j.energy.2018.08.133, <http://www.sciencedirect.com/science/article/pii/S0360544218316670>.

Li, YZ, Huang, C, Anderson, J, Svensson, R, Haukur, I, Husted, B et al. 2017, 'Verification, validation and evaluation of FireFOAM as a tool for performance design'. Lund University, Lund Sweden, Rep 3208, 2017

Liesowska, A 2015, 'Fire rages on as death toll from two blazes reaches 33, *The Siberian Times*, 16 April 2015,' <Accessed at http://siberiantimes.com/ecology/casestudy/news/n0187-fire-rages-on-as-death-toll-from-two-blazesreaches-33/.>.

Lin, Y, Delichatsios, M. A., Zhang, X. and Hu, L. 2019 'Experimental study and physical analysis of flame geometry in pool fires under relatively strong cross flows,' *Combustion and Flame*, vol. 205, pp. 422-433.

Lin, Y, Zhang, X & Hu, L 2018, 'An experimental study and analysis on maximum horizontal extents of buoyant turbulent diffusion flames subject to relative strong cross flows', *Fuel*, vol. 234, pp. 508-15.

Linn, RR & Cunningham, P 2005, 'Numerical simulations of grass fires using a coupled atmosphere–fire model: basic fire behavior and dependence on wind speed', *Journal of Geophysical Research: Atmospheres*, vol. 110, no. D13.

Liu, S & Hu, L 2019, 'An experimental study on flame envelope morphologic characteristics of downward-orientated buoyant turbulent jet fires', *Proceedings of the Combustion Institute*, vol. 37, no. 3, pp. 3935-42.

Liu, N & de Ris, JL 2013, '9th Asia-Oceania symposium on fire science and technology mechanism of buoyant turbulent diffusion flames', *Procedia Engineering*, vol. 62, pp. 13-27, DOI http://dx.doi.org/10.1016/j.proeng.2013.08.040, <http://www.sciencedirect.com/science/article/pii/S1877705813012228>.

Liu, N, Wu, J, Chen, H, Xie, X, Zhang, L, Yao, B et al. 2014, 'Effect of slope on spread of a linear flame front over a pine needle fuel bed: experiments and modelling', *International Journal of Wildland Fire*, vol. 23, no. 8, pp. 1087-96, DOI https://doi.org/10.1071/WF12189, <https://www.publish.csiro.au/paper/WF12189>.

Lois, E & Swithenbank, J 1979, 'Fire hazards in oil tank arrays in a wind', *Elsevier*, vol. 17, no. 1, pp. 1087-98.

Lu, Y, Huang, X, Hu, L & Fernandez-Pello, C 2019, 'The interaction between fuel inclination and horizontal wind: Experimental study using thin wire', *Proceedings of the Combustion Institute*, vol. 37, no. 3, pp. 3809-16.
Luke, RH & McArthur, AG 1978, *Bushfires in Australia*, Australian Government Publishing Service, Canberra.

Magnussen, BF 2005, 'The Eddy Dissipation Concept—A Bridge Between Science and Technology', pp. *ECCOMAS thematic conference on computational combustion* 21-24.

Mahalingam, S, Thévenin, D, Candel, S & Veynante, D 1999, 'Analysis and numerical simulation of a nonpremixed flame in a corner', *Combustion and Flame*, vol. 118, no. 1, pp. 221-32, DOI https://doi.org/10.1016/S0010-2180(98)00142-4, <http://www.sciencedirect.com/science/article/pii/S0010218098001424>.

Mahesh, K 2013, 'The interaction of jets with crossflow', *Annual Review of Fluid Mechanics*, vol. 45 pp. 379–407.

Majeski, AJ, Wilson, DJ & Kostiuk∗, LW 2004, 'Predicting the length of low-momentum jet diffusion flames in crossflow', *Combustion Science and Technology*, vol. 176, no. 12, pp. 2001-25, DOI 10.1080/00102200490514769, <http://dx.doi.org/10.1080/00102200490514769>.

Malalasekera, W, Ibrahim, SS, Masri, AR, Gubba, SR & Sadasivuni, S 2013, 'Experience with the Large Eddy Simulation (LES) technique for the modeling of premixed and non-premixed combustion', *Heat Transfer Engineering*, vol. 34, no. 14, pp. 1156-70.

Malalasekera, WMG, Versteeg, HK & Gilchrist, K 1996, 'A review of research and an experimental study on the pulsation of buoyant diffusion flames and pool fires', *Fire and Materials*, vol. 20, no. 6, pp. 261-71, DOI 10.1002/(SICI)1099-1018(199611)20:6<261::AID-FAM578>3.0.CO;2-M, <http:https://dx.doi.org/10.1002/(SICI)1099-1018(199611)20:6<261::AID-FAM578>3.0.CO;2-M>.

Maragkos, G, Beji, T & Merci, B 2017, 'Advances in modelling in CFD simulations of turbulent gaseous pool fires', *Combustion and Flame*, vol. 181, pp. 22-38, DOI https://doi.org/10.1016/j.combustflame.2017.03.012, <http://www.sciencedirect.com/science/article/pii/S0010218017301049>.

Margason, RJ 1993, 'Fifty years of jet in cross flow research', *Advisory Group for Aerospace Research and Development-CP*, vol. 534 Paper 1.

Margerit, J & Séro-Guillaume, O 2002, 'Modelling forest fires. Part ii: reduction to two-dimensional models and simulation of propagation', *International Journal of Heat and Mass Transfer*, vol. 45, no. 8, pp. 1723-37, DOI https://doi.org/10.1016/S0017-9310(01)00249-6, <http://www.sciencedirect.com/science/article/pii/S0017931001002496>.

Mathey, F, Cokljat, D, Bertoglio, JP & Sergent, E 2006, 'Assessment of the vortex method for large eddy simulation inlet conditions', *Progress in Computational Fluid Dynamics*, vol. 6, no. 1-3, pp. 58-67, Scopus, DOI 10.1504/PCFD.2006.009483, <https://www.scopus.com/inward/record.uri?eid=2-s2.0-33744455756&doi=10.1504%2fPCFD.2006.009483&partnerID=40&md5=c3ddaa144fe30bfb688f19205cc642fc>.

McCaffrey, BJ 1979, 'Purely buoyant diffusion flames: some experimental results', Center for Fire Research National Engineering Laboratory National Bureau of Standards, Washington, DC, USA, NBSIR 79-1910,1979.

McRae, RHD, Sharples, JJ, Wilkes, SR & Walker, A 2013, 'An Australian pyro-tornadogenesis event', *Natural Hazards*, vol. 65, no. 3, pp. 1801-11, DOI 10.1007/s11069-012-0443-7, <http://dx.doi.org/10.1007/s11069-012-0443-7>.

Megerian, S, Davitian, J, De B, Alves, LS & Karagozian, AR 2007, 'Transverse-jet shear-layer instabilities. Part 1. Experimental studies', *Journal of Fluid Mechanics*, vol. 593, pp. 93-129, DOI 10.1017/S0022112007008385, <https://www.cambridge.org/core/article/div-class-title-transverse-jet-shear-layer-instabilities-part-1-experimental-studies-div/E1B78073918630A6BF25E6DCC8FD0DED>.

Mell, W, Charney, J, Jenkins, MA, Cheney, P & Gould, J 2013, 'Numerical simulations of grassland fire behavior from the LANL-FIRETEC and NIST-WFDS models', in *Remote Sensing and Modeling Applications to Wildland Fires*, Springer, pp. 209-25.

Mell, W, Manzello, SL, Maranghides, A, Butry, D & Rehm, RG 2010, 'The wildland–urban interface fire problem–current approaches and research needs', *International Journal of Wildland Fire*, vol. 19, no. 2, pp. 238-51.

Mendes-Lopes, JM, Ventura, JM & Amaral, JM 2003, 'Flame characteristics, temperature–time curves, and rate of spread in fires propagating in a bed of Pinus pinaster needles', *International Journal of Wildland Fire*, vol. 12, no. 1, pp. 67-84.

Meroney, RN 2011, 'Wind effects on atria fires', *Journal of Wind Engineering and Industrial Aerodynamics*, vol. 99, no. 4, pp. 443-7, DOI http://dx.doi.org/10.1016/j.jweia.2010.11.003, <http://www.sciencedirect.com/science/article/pii/S0167610510001212>.

Mills, G 2009, 'Changes of wind and fire', *Fire Australia, available at<http://www.bushfirecrc.com>*, Winter 2009.

Modak, AT & Croce, PA 1977, 'Plastic pool fires', *Combustion and Flame*, vol. 30, pp. 251-65, DOI http://dx.doi.org/10.1016/0010-2180(77)90074-8, <http://www.sciencedirect.com/science/article/pii/0010218077900748>.

Montorfano, A, Piscaglia, F & Ferrari, G 2013, 'Inlet boundary conditions for incompressible LES: a comparative study', *Mathematical and Computer Modelling*, vol. 57, no. 7, pp. 1640-7, DOI https://doi.org/10.1016/j.mcm.2011.10.077, <http://www.sciencedirect.com/science/article/pii/S0895717711006820>.

Moorhouse, J 1982, 'Scaling criteria for pool fires derived from large-scale experiments', *The Assessment of Major Hazards, Symposium Series* vol. 71, pp. 165-79.

Morandini, F, Silvani, X, Honoré, D, Boutin, G, Susset, A & Vernet, R 2014, 'Slope effects on the fluid dynamics of a fire spreading across a fuel bed: PIV measurements and OH chemiluminescence imaging', *Experiments in Fluids*, vol. 55, no. 8, p. 1788, DOI 10.1007/s00348-014-1788-3, <http://dx.doi.org/10.1007/s00348-014-1788-3>.

Morandini, F, Simeoni, A, Santoni, P-A & Balbi, J-H 2005, 'A model for the spread of fire across a fuel bed incorporating the effects of wind and slope', *Combustion Science and Technology*, vol. 177, no. 7, pp. 1381-418.

Morton, BR 1959, 'Forced plumes', *Journal of Fluid Mechanics*, vol. 5, pp. 151–63.

Morton, BR 1965, 'Tenth symposium (international) on combustion modeling fire plumes', *Symposium (International) on Combustion*, vol. 10, no. 1, pp. 973-82, DOI http://dx.doi.org/10.1016/S0082-0784(65)80240-5, <http://www.sciencedirect.com/science/article/pii/S0082078465802405>.

Morton, BR & Middleton, J 1973, 'Scale diagrams for forced plumes', *Journal of Fluid Mechanics*, vol. 58, pp. 165–76.

Morton, BR, Taylor, G & Turner, JS 1956, 'Turbulent gravitational convection from maintained and instantaneous sources', *Proceedings of the Royal Society of London. Series A. Mathematical and Physical Sciences*, vol. 234, no. 1196, pp. 1-23, DOI 10.1098/rspa.1956.0011.

Morvan, D & Dupuy, J 2001, 'Modeling of fire spread through a forest fuel bed using a multiphase formulation', *Combustion and Flame*, vol. 127, no. 1-2, pp. 1981-94.

Morvan, D & Dupuy, J 2004, 'Modeling the propagation of a wildfire through a Mediterranean shrub using a multiphase formulation', *Combustion and Flame*, vol. 138, no. 3, pp. 199-210.

Morvan, D, Porterie, B, Larini, M & Loraud, JC 1998, 'Numerical simulation of turbulent diffusion Flame in Cross Flow', *Combustion Science and Technology*, vol. 140, no. 1-6, pp. 93-122, Scopus, <https://www.scopus.com/inward/record.url?eid=2-s2.0-0002917769&partnerID=40&md5=29e8482f69739a9a23eb7526543fdca2>.

Muppidi, S & Mahesh, K 2007, 'Direct numerical simulation of round turbulent jets in crossflow', *Journal of Fluid Mechanics*, vol. 574, pp. 59-84, DOI 10.1017/S0022112006004034, <https://www.cambridge.org/core/article/div-class-title-direct-numerical-simulation-of-round-turbulent-jets-in-crossflow-div/4714E5D0402432284F4E8593239643C2>.

Nelson Jr, RM & Adkins, CW 1986, 'Flame characteristics of wind-driven surface fires', *Canadian Journal of Forest Research*, vol. 16, no. 6, pp. 1293-300.

Nelson, RM 1980, 'Flame characteristics for fires in southern fuels', *Research Paper SE-RP-205. Asheville, NC: USDA-Forest Service, Southeast Forest Experiment Station.*, vol. 205, pp. 1-14.

Nelson, RM, Butler, BW & Weise, DR 2012, 'Entrainment regimes and flame characteristics of wildland fires', *International Journal of Wildland Fire*, vol. 21, no. 2, pp. 127-40, DOI http://dx.doi.org/10.1071/WF10034, <http://www.publish.csiro.au/paper/WF10034>.

NIFC 2015a, *(National Interagency Fire Center) Internation Agreements - Australia,*, < http://www.nifc.gov/nicc/logistics/International%20Agreements/Australia%20Support.pdf.>.

Nmira, F, Consalvi, J, Boulet, P & Porterie, B 2010, 'Numerical study of wind effects on the characteristics of flames from non-propagating vegetation fires', *Fire Safety Journal*, vol. 45, no. 2, pp. 129-41.

NSWRFS 2006, 'NSW Rural Fire Service Planning for Bush Fire Protection 2006'.

Orloff, L, De Ris, J & Markstein, G 1975, 'Upward turbulent fire spread and burning of fuel surface', *Elsevier*, vol. 15, no. 1, pp. 183-92.

Penttinen, O & Nilsson, H 2015, 'A fully synthetic turbulent boundary condition with a homogeneous vortex distribution', *Computer Physics Communications*, vol. 190, pp. 23-32, DOI https://doi.org/10.1016/j.cpc.2015.01.002, <http://www.sciencedirect.com/science/article/pii/S0010465515000041>.

Ping, P, He, X, Kong, D, Wen, R, Zhang, Z & Liu, P 2018, 'An experimental investigation of burning rate and flame tilt of the boilover fire under cross air flows', *Applied Thermal Engineering*, vol. 133, pp. 501-11.

Pipkin, OA & Sliepcevich, CM 1964, 'The effect of wind on buoyant diffusion flames', *Industrial and Engineering Chemistry: Fundamentals*, vol. 3, pp. 147–54.

Pipkin, OA & Sliepcevich, CM 1964, 'Effect of wind on buoyant diffusion flames. Initial correlation', *Industrial & Engineering Chemistry Fundamentals*, vol. 3, no. 2, pp. 147-54, DOI 10.1021/i160010a011, <http://dx.doi.org/10.1021/i160010a011>.

Plourde, F, Pham, MV, Kim, SD & Balachandar, S 2008, 'Direct numerical simulations of a rapidly expanding thermal plume: structure and entrainment interaction', *Journal of Fluid Mechanics*, vol. 604, pp. 99-123, Cambridge Core, Cambridge University Press, DOI 10.1017/S0022112008001006, <https://www.cambridge.org/core/article/direct-numerical-

simulations-of-a-rapidly-expanding-thermal-plume-structure-and-entrainment-interaction/2AFFFD091EB3454CD1BE9432BFF8F9A3>.

Pope, SB & Pope, SB 2000, *Turbulent flows*, Cambridge University Press.

Porterie, B, Morvan, D, Loraud, JC & Larini, M 2000, 'Firespread through fuel beds: Modeling of wind-aided fires and induced hydrodynamics', *Physics of Fluids*, vol. 12, no. 7, pp. 1762-82, DOI 10.1063/1.870426, <https://aip.scitation.org/doi/abs/10.1063/1.870426>.

Putnam, AA 1965, 'A model study of wind-blown free-burning fires', *Elsevier*, vol. 10, no. 1, pp. 1039-46.

Pyne, S, Andrews, P & Laven, RD 1996, 'Introduction to Wildland Fire, John Wiley and Sons', *New York*.

Quintiere, J, Harkleroad, M & Hasemi, Y 1986, 'Wall flames and implications for upward flame spread', *Combustion Science and Technology*, vol. 48, no. 3-4, pp. 191-222.

Quintiere, JG & Grove, BS 1998, 'A unified analysis for fire plumes', *Symposium (International) on Combustion*, vol. 27, no. 2, pp. 2757-66, DOI https://doi.org/10.1016/S0082-0784(98)80132-X, <http://www.sciencedirect.com/science/article/pii/S008207849880132X>.

Raj, PK 2010, 'A physical model and improved experimental data correlation for wind induced flame drag in pool fires', *Fire Technology*, vol. 46, no. 3, pp. 579-609.

Ramsay, GC, Mcarthur, NA & Dowling, V 1987, 'Preliminary results from an examination of house survival in the 16 February 1983 bushfires in Australia', *Fire and Materials*, vol. 11, no. 49-51.

Rew, P, Hulbert, W & Deaves, D 1997, 'Modelling of thermal radiation from external hydrocarbon pool fires', *Process Safety and Environmental Protection*, vol. 75, no. 2, pp. 81-9.

Rossa, CG, Davim, DA & Viegas, DX 2015, 'Behaviour of slope and wind backing fires', *International Journal of Wildland Fire*, vol. 24, no. 8, pp. 1085-97.

Satoh, K, Liu, N, Xie, X, Zhou, K, Chen, H-C, Wu, J et al. 2011, 'CFD study of huge oil depot fires-generation of fire merging and fire whirl in (7 x 7) arrayed oil tanks', *Fire Safety Science*, vol. 10, pp. 693-705.

Scesa, S 1957b, *Transfer of heat by forced convection from a line combustion source--the influence of atmospheric stability and surface roughness*, Forest service Washington DC.

Scesa, S & Sauer, F 1954, 'Possible effects of free convection on fire behavior-laminar and turbulent line and point sources of heat', *Tech. Pap. 12. Berkeley, CA: US Department of Agriculture, Forest Service, California Forest and Range Experiment Station. 47 p.*, vol. 12.

Sedano, CA, Pez, OD, Ladino, A & Muoz, F 2017, 'Prediction of a small-scale pool fire with FireFoam', *International Journal of Chemical Engineering*, vol. 2017, p. 12, DOI 10.1155/2017/4934956, <https://doi.org/10.1155/2017/4934956>.

Sergent, ME 2002, *Vers une Méthodologie de Couplage Entre la Simulation des Grandes Echelles et les Modèles Statistiques*, Thesis, Ecole Central de Lyon.

Shang, F, Hu, L, Sun, X, Wang, Q & Palacios, A 2017, 'Flame downwash length evolution of non-premixed gaseous fuel jets in cross-flow: experiments and a new correlation', *Applied Energy*, vol. 198, pp. 99-107, DOI https://doi.org/10.1016/j.apenergy.2017.04.043, <http://www.sciencedirect.com/science/article/pii/S0306261917304439>.

Sharples, JJ 2008, 'Review of formal methodologies for wind–slope correction of wildfire rate of spread', *International Journal of Wildland Fire*, vol. 17, no. 2, pp. 179-93.

Sharples, JJ 2009, 'An overview of mountain meteorological effects relevant to fire behaviour and bushfire risk', *International Journal of Wildland Fire*, vol. 18, no. 7, pp. 737-54.

Sharples, JJ, Gill, AM & Dold, JW 2010, The trench effect and eruptive wildfires: lessons from the King's Cross underground disaster, Proceedings of Australian Fire and Emergency Service Authorities Council 2010 Conference. pp. 8-10.

Shi, L, Shi, L & Yeo, D 2016, *OpenFOAM large-eddy simulations of atmospheric boundary layer turbulence for wind engineering applications*, US Department of Commerce, National Institute of Standards and Technology.

Show, SB 1919, 'Climate and forest fires in northern California', *Journal of Forestry*, vol. 17, no. 8, pp. 965-79, viewed 2 Feb 2019, DOI 10.1093/jof/17.8.965, <https://dx.doi.org/10.1093/jof/17.8.965>.

Sikanen, T & Hostikka, S 2016, 'Modeling and simulation of liquid pool fires with in-depth radiation absorption and heat transfer', *Fire Safety Journal*, vol. 80, pp. 95-109.

Silvani, X, Morandini, F & Dupuy, J-L 2012, 'Effects of slope on fire spread observed through video images and multiple-point thermal measurements', *Experimental Thermal and Fluid Science*, vol. 41, pp. 99-111, DOI http://dx.doi.org/10.1016/j.expthermflusci.2012.03.021, <//www.sciencedirect.com/science/article/pii/S089417771200088X>.

Sinai, YL & Owens, MP 1995, 'Validation of CFD modelling of unconfined pool fires with cross-wind: Flame geometry', *Fire Safety Journal*, vol. 24, no. 1, pp. 1-34, Scopus, DOI 10.1016/0379-7112(94)00028-E, <https://www.scopus.com/inward/record.url?eid=2-s2.0-0029228802&partnerID=40&md5=cb2f252c2e611effa130631f9d39d4cf>.

Singh, AV & Gollner, MJ 2016, 'Experimental methodology for estimation of local heat fluxes and burning rates in steady laminar boundary layer diffusion flames', *Journal of visualized experiments: JoVE*, no. 112.

Smith, SH & Mungal, MG 1998, 'Mixing, structure and scaling of the jet in crossflow', *Journal of Fluid Mechanics*, vol. 357, pp. 83-122, DOI 10.1017/S0022112097007891, <https://www.cambridge.org/core/article/div-class-title-mixing-structure-and-scaling-of-the-jet-in-crossflow-div/56E842386D96423BCD11C26DEBA8D8F6>.

Snegirev, AY 2004, 'Statistical modeling of thermal radiation transfer in buoyant turbulent diffusion flames', *Combustion and Flame*, vol. 136, no. 1-2, pp. 51-71.

Souil, JM, Joulain, P & Gengembre, E 1984, 'Experimental and theoretical study of thermal radiation from turbulent diffusion flames to vertical target surfaces', *Combustion Science and Technology*, vol. 41, no. 1-2, pp. 69-81, DOI 10.1080/00102208408923823, <https://doi.org/10.1080/00102208408923823>.

Spalding, D 1961, 'A single formula for the “law of the wall”', *Journal of Applied Mechanics*, vol. 28, no. 3, pp. 455-8.

Sreenivas, KR & Prasad, AK 2000, 'Vortex-dynamics model for entrainment in jets and plumes', *Physics of Fluids*, vol. 12, no. 8, pp. 2101-7, DOI doi:http://dx.doi.org/10.1063/1.870455, <http://scitation.aip.org/content/aip/journal/pof2/12/8/10.1063/1.870455>.

Steward, FR 1964, 'Linear flame heights for various fuels', *Combustion and Flame*, vol. 8, no. 3, pp. 171-8, DOI http://dx.doi.org/10.1016/0010-2180(64)90063-X, <http://www.sciencedirect.com/science/article/pii/001021806490063X>.

Su, LK & Mungal, MG 2004, 'Simultaneous measurements of scalar and velocity field evolution in turbulent crossflowing jets', *Journal of Fluid Mechanics*, vol. 513, pp. 1-45, DOI 10.1017/S0022112004009401, <https://www.cambridge.org/core/article/div-class-title-simultaneous-measurements-of-scalar-and-velocity-field-evolution-in-turbulent-crossflowing-jets-div/9A7D5953C0E4A66E478EA5F33A0B8622>.

Sullivan, A 2004, *Nature of Severe Fire Events*. Department of Urban Services ACT Government. CSIRO. Canberra.

Sullivan, AL 2009a, 'Wildland surface fire spread modelling, 1990–2007. 2: empirical and quasi-empirical models', *International Journal of Wildland Fire*, vol. 18, no. 4, pp. 369-86.

Sullivan, AL 2009b, 'Wildland surface fire spread modelling, 1990–2007. 3: simulation and mathematical analogue models', *International Journal of Wildland Fire*, vol. 18, no. 4, pp. 387-403.

Sun, B, Guo, K & Pareek, VK 2014, 'Computational fluid dynamics simulation of LNG pool fire radiation for hazard analysis', *Journal of Loss Prevention in the Process Industries*, vol. 29, pp. 92-102, DOI http://dx.doi.org/10.1016/j.jlp.2014.02.003, <http://www.sciencedirect.com/science/article/pii/S0950423014000266>.

Sun, X, Zhang, X, Hu, L & Kuwana, K 2019, 'Temperature evolution and transition inside fire compartment with an opening subject to external sideward wind', *Proceedings of the Combustion Institute*, vol. 37, no. 3, pp. 3869-77.

Tang, F, Hu, L, Zhang, X, Zhang, X & Dong, M 2015, 'Burning rate and flame tilt characteristics of radiation-controlled rectangular hydrocarbon pool fires with cross air flows in a reduced pressure', *Fuel*, vol. 139, pp. 18-25.

Tang, F, He, Q & Wen, J 2019, 'Effects of crosswind and burner aspect ratio on flame characteristics and flame base drag length of diffusion flames', *Combustion and Flame*, vol. 200, pp. 265-75.

Tang, F, Li, L, Wang, Q & Shi, Q 2016, 'Effect of cross-wind on near-wall buoyant turbulent diffusion flame length and tilt', *Fuel*, vol. 186, pp. 350-7, DOI http://dx.doi.org/10.1016/j.fuel.2016.08.095, <http://www.sciencedirect.com/science/article/pii/S001623611630833X>.

Tang, F, Li, LJ, Zhu, KJ, Qiu, ZW & Tao, CF 2015, 'Experimental study and global correlation on burning rates and flame tilt characteristics of acetone pool fires under cross air flow', *International Journal of Heat and Mass Transfer*, vol. 87, pp. 369-75, DOI http://dx.doi.org/10.1016/j.ijheatmasstransfer.2015.04.019, <http://www.sciencedirect.com/science/article/pii/S0017931015003798>.

Tang, W, Miller, CH & Gollner, MJ 2017, 'Local flame attachment and heat fluxes in wind-driven line fires', *Proceedings of the Combustion Institute*, vol. 36, no. 2, pp. 3253-61.

Tao, C, Liu, Y, Tang, F & Wang, Q 2018, 'An experimental investigation of the flame height and air entrainment of ring pool fire', *Fuel*, vol. 216, pp. 734-7.

Tewarson, A 1972, 'Some observations on experimental fires in enclosures, part II-ethyl alcohol and paraffin oil', *Combustion and Flame*, vol. 19, no. 3, pp. 363-71, DOI http://dx.doi.org/10.1016/0010-2180(72)90006-5, <http://www.sciencedirect.com/science/article/pii/0010218072900065>.

Tewarson, A 1982, 'Experimental evaluation of flammability parameters of polymeric materials', in M Lewin, SM Atlas & EM Pearce (eds), *Flame - Retardant Polymeric Materials: Volume 3*, Springer New York, Boston, MA, pp. 97-153.

Thomas P, Pickard R, and Wraight H, "On the size and orientation of buoyant diffusion flames and the effect of wind." Int. Assoc. Fire Saf. Sci. [Online]. Available: https://www.iafss.org/publications/frn/516/-1/view/frn_516.pdf. Accessed: Jul. 3, 2019.

Thomas, PH 1963a, 'The size of flames from natural fires', *Symposium (International) on Combustion*, vol. 9, no. 1, pp. 844-59, DOI https://doi.org/10.1016/S0082-0784(63)80091-0, <http://www.sciencedirect.com/science/article/pii/S0082078463800910>.

Thomas, PH 1963b, 'The size of flames of natural fires', *Proceedings of the Combustion Institute 9*.

Thomas, PH & Bowes, PC 1961b, 'Thermal ignition in a slab with one face at a constant high temperature', *Transactions of the Faraday Society*, pp. 2007–16.

Tlili, O, Mhiri, H & Bournot, P 2015, 'Airflow induced by a room fire: Effect of roof shape and source location', *International Journal of Thermal Sciences*, vol. 90, pp. 135-49, DOI http://dx.doi.org/10.1016/j.ijthermalsci.2014.12.003, <http://www.sciencedirect.com/science/article/pii/S1290072914003482>.

Tolhurst, K, Shields, B & Chong, D 2008, 'Phoenix: development and application of a bushfire risk management tool', *Australian Journal of Emergency Management,* vol. 23, no. 4, p. 47.

Tominaga, Y, Mochida, A, Yoshie, R, Kataoka, H, Nozu, T, Yoshikawa, M et al. 2008, 'AIJ guidelines for practical applications of CFD to pedestrian wind environment around buildings', *Journal of Wind Engineering and Industrial Aerodynamics*, vol. 96, no. 10-11, pp. 1749-61, DOI 10.1016/j.jweia.2008.02.058.

Tritton, D 1988, 'Physical fluid dynamics, Clarendon', Oxford.

Tymstra, C, Bryce, R, Wotton, B, Taylor, S & Armitage, O 2010, 'Development and structure of Prometheus: the Canadian wildland fire growth simulation model', *Natural Resources Canada, Canadian Forest Service,* Northern Forestry Centre, Information Report NOR-X-417.*(Edmonton, AB)*.

US Department of Agriculture 2015, Forest service chief predicts "above normal" wildland fire potential in much of the west 012.15, 5 May, <Accessed at http://www.usda.gov/wps/portal/usda/usdamediafb?contentid=2015/05/0126.xml&printable=true&contentidonly=true.>.

Van Wagner, C 1977, 'Effect of slope on fire spread rate', *Canadian Forestry Service Bi-monthly Research Notes*, vol. 33, no. 1.

Vasanth, S, Tauseef, SM, Abbasi, T & Abbasi, SA 2013, 'Assessment of four turbulence models in simulation of large-scale pool fires in the presence of wind using computational fluid dynamics (CFD)', *Journal of Loss Prevention in the Process Industries*, vol. 26, no. 6, pp. 1071-84, DOI http://dx.doi.org/10.1016/j.jlp.2013.04.001, <http://www.sciencedirect.com/science/article/pii/S0950423013000879>.

Vasanth, S, Tauseef, SM, Abbasi, T & Abbasi, SA 2015, 'CFD simulation of pool fires situated at differing elevation', *Process Safety and Environmental Protection*, vol. 94, pp. 89-95, DOI https://doi.org/10.1016/j.psep.2015.01.001, <http://www.sciencedirect.com/science/article/pii/S0957582015000026>.

Vasanth, S, Tauseef, SM, Abbasi, T & Abbasi, SA 2017, 'Simulation of multiple pool fires involving two different fuels', *Journal of Loss Prevention in the Process Industries*, vol. 48, pp. 289-96, DOI https://doi.org/10.1016/j.jlp.2017.04.031, <http://www.sciencedirect.com/science/article/pii/S0950423017303741>.

Viegas, DX 2004, 'Slope and wind effects on fire propagation', *International Journal of Wildland Fire*, vol. 13, no. 2, pp. 143-56, DOI http://dx.doi.org/10.1071/WF03046, <http://www.publish.csiro.au/paper/WF03046>.

Vilfayeau, S 2015, *Large eddy simulation of fire extinction phenomena*, University of Maryland, College Park.

Vilfayeau, S, White, JP, Sunderland, PB, Marshall, AW & Trouvé, A 2016, 'Large eddy simulation of flame extinction in a turbulent line fire exposed to air-nitrogen co-flow', *Fire Safety Journal*, vol. 86, pp. 16-31, DOI http://dx.doi.org/10.1016/j.firesaf.2016.09.003, <http://www.sciencedirect.com/science/article/pii/S0379711216301175>.

Viskanta, R 2008, 'Overview of some radiative transfer issues in simulation of unwanted fires', *International Journal of Thermal Sciences*, vol. 47, no. 12, pp. 1563-70, DOI https://doi.org/10.1016/j.ijthermalsci.2008.01.008, <http://www.sciencedirect.com/science/article/pii/S129007290800032X>.

Volchkov, E, Terekhov, V & Terekhov, V 2004, 'Flow structure and heat and mass transfer in boundary layers with injection of chemically reacting substances', *Combustion, Explosion and Shock Waves*, vol. 40, no. 1, pp. 1-16.

Volchkov, ÉP, Terekhov, VI & Terekhov, VV 2004, 'Flow Structure and Heat and Mass Transfer in Boundary Layers with Injection of Chemically Reacting Substances (Review)', *Combustion, Explosion and Shock Waves*, vol. 40, no. 1, pp. 1-16, DOI 10.1023/B:CESW.0000013663.27112.ab, <https://doi.org/10.1023/B:CESW.0000013663.27112.ab>.

Walton, WD & Thomas, PH 2008, *Estimating temperatures in compartment fires*, 4th edn edn.

Wang, C, Wang, Z, Wang, L, Luo, L & Sundén, B 2019, 'Experimental study of fluid flow and heat transfer of jet impingement in cross-flow with a vortex generator pair', *International Journal of Heat and Mass Transfer*, vol. 135, pp. 935-49, DOI https://doi.org/10.1016/j.ijheatmasstransfer.2019.02.024, <http://www.sciencedirect.com/science/article/pii/S0017931018349937>.

Wang, C, Wen, J & Chen, Z 2014, 'Simulation of large-scale LNG pool fires using FireFoam', *Combustion Science and Technology*, vol. 186, no. 10-11, pp. 1632-49.

Wang, CJ, Liu, HR & Wen, JX 2018, 'An improved PaSR-based soot model for turbulent fires', *Applied Thermal Engineering*, vol. 129, pp. 1435-46, DOI https://doi.org/10.1016/j.applthermaleng.2017.10.129, <http://www.sciencedirect.com/science/article/pii/S135943111633900X>.

Wang, CJ, Wen, JX, Chen, ZB & Dembele, S 2014, 'Predicting radiative characteristics of hydrogen and hydrogen/methane jet fires using FireFOAM', *International Journal of Hydrogen Energy*, vol. 39, no. 35, pp. 20560-9, DOI http://dx.doi.org/10.1016/j.ijhydene.2014.04.062, <http://www.sciencedirect.com/science/article/pii/S0360319914010830>.

Wang, J, Fang, J, Zhao, L, Guan, J, Zhang, Y, Sun, J & Hu, L 2019, 'Sooting tendencies of propane jet diffusion flame under crossflow', *Fuel*, vol. 245, pp. 247-52.

Wang, H 2006, 'Ember attack: its role in the destruction of houses during ACT bushfire in 2003', *Life in A Fire-Prone Environment: Translating Science into Practice, Proceedings of Bushfire Conference, Griffith University, Brisbane, Australia*, <http://www.griffith.edu.au/conference/>.

Wang, Y, Chatterjee, P & de Ris, JL 2011, 'Large eddy simulation of fire plumes', *Proceedings of the Combustion Institute*, vol. 33, no. 2, pp. 2473-80, DOI http://dx.doi.org/10.1016/j.proci.2010.07.031, <http://www.sciencedirect.com/science/article/pii/S1540748910002944>.

Wang, YF, Sun, XF, Liu, S, Yan, PN, Qin, T & Zhang, B 2016, 'Simulation of back-layering length in tunnel fire with vertical shafts', *Applied Thermal Engineering*, vol. 109, pp. 344-50, DOI https://doi.org/10.1016/j.applthermaleng.2016.08.081, <http://www.sciencedirect.com/science/article/pii/S1359431116314405>.

Weise, DR & G.S, B 1996, 'Effects of wind velocity and slope on flame properties', *Canadian Journal of Forest Research*, vol. 26, pp. 1849–58.

Weise, DR, Koo, E, Zhou, X, Mahalingam, S, Morandini, F & Balbi, JH 2016, 'Fire spread in chaparral–a comparison of laboratory data and model predictions in burning live fuels', *International Journal of Wildland Fire*, vol. 25, no. 9, pp. 980-94.

Welker, J & Sliepcevich, C 1966, 'Bending of wind-blown flames from liquid pools', *Fire Technology*, vol. 2, no. 2, pp. 127-35.

Welker, JR 1965, *The effect of wind on uncontrolled buoyant diffusion flames from burning liquids*, The University of Oklahoma.

Woods, JA, Fleck, BA & Kostiuk, LW 2006, 'Effects of transverse air flow on burning rates of rectangular methanol pool fires', *Combustion and Flame*, vol. 146, no. 1-2, pp. 379-90.

Wu, Y, Xing, H & Atkinson, G 2000, 'Interaction of fire plume with inclined surface', *Fire Safety Journal*, vol. 35, no. 4, pp. 391-403.

Xie, B, Gao, F, Boudet, J, Shao, L & Lu, L 2018, 'Improved vortex method for large-eddy simulation inflow generation', *Computers & Fluids*, vol. 168, pp. 87-100, DOI https://doi.org/10.1016/j.compfluid.2018.03.069, <http://www.sciencedirect.com/science/article/pii/S0045793018301737>.

Xie, W & DesJardin, PE 2009, 'An embedded upward flame spread model using 2D direct numerical simulations', *Combustion and Flame*, vol. 156, no. 2, pp. 522-30.

Yeoh, G-H & Yuen, KK 2009, *Computational fluid dynamics in fire engineering: theory, modelling and practice*, Butterworth-Heinemann.

Yoshihara, N, Ito, A & Torikai, H 2013, 'Flame characteristics of small-scale pool fires under low gravity environments', *Proceedings of the Combustion Institute*, vol. 34, no. 2, pp. 2599-606.

Yoshizawa, A 1986, 'Statistical theory for compressible turbulent shear flows, with the application to subgrid modeling', *The Physics of fluids*, vol. 29, no. 7, pp. 2152-64.

Yuana, L-M & Cox, G 1996, 'An experimental study of some line fires', *Fire Safety Journal*, vol. 27, no. 2, pp. 123-39, DOI http://dx.doi.org/10.1016/S0379-7112(96)00047-1, <http://www.sciencedirect.com/science/article/pii/S0379711296000471>.

Zhang, X, Xu, W, Hu, L, Liu, X, Zhang, X & Xu, W 2016, 'A new mathematical method for quantifying trajectory of buoyant line-source gaseous fuel jet diffusion flames in cross air flows', *Fuel*, vol. 177, pp. 107-12, DOI http://dx.doi.org/10.1016/j.fuel.2016.02.092, <http://www.sciencedirect.com/science/article/pii/S0016236116300278>.

Zhang, X, Zhang, X, Hu, L, Tu, R & Delichatsios, MA 2019, 'An experimental investigation and scaling analysis on flame sag of pool fire in cross flow', *Fuel*, vol. 241, pp. 845-50, DOI https://doi.org/10.1016/j.fuel.2018.12.020, <http://www.sciencedirect.com/science/article/pii/S0016236118320714>.

Zhang, X, Hu, L, Zhang, X, Yang, L & Wang, S 2014, 'Non-dimensional correlations on flame height and axial temperature profile of a buoyant turbulent line-source jet fire plume', *Journal of Fire Sciences*, vol. 32, no. 5, pp. 406-16, DOI doi:10.1177/0734904114529258, <http://journals.sagepub.com/doi/abs/10.1177/0734904114529258>.

Zhen, HS, Choy, YS, Leung, CW & Cheung, CS 2011, 'Effects of nozzle length on flame and emission behaviors of multi-fuel-jet inverse diffusion flame burner', *Applied Energy*, vol. 88, no. 9, pp. 2917-24, DOI https://doi.org/10.1016/j.apenergy.2011.02.040, <http://www.sciencedirect.com/science/article/pii/S0306261911001528>.

Zhou, B, Sobiesiak, A & Quan, P 2006, 'Flame behavior and flame-induced flow in a closed rectangular duct with a 90° bend', *International Journal of Thermal Sciences*, vol. 45, no. 5, pp. 457-74, DOI https://doi.org/10.1016/j.ijthermalsci.2005.07.001, <http://www.sciencedirect.com/science/article/pii/S1290072905001638>.

Zhou, T, Li, H, Chen, Q, Wei, R & Wang, J 2018, 'Understanding sidewall constraint involving ventilation effects on temperature distribution of fire-induced thermal flow under a tunnel ceiling', *International Journal of Thermal Sciences*, vol. 129, pp. 290-300.

Zhou, X, Mahalingam, S & Weise, D 2005, 'Modeling of marginal burning state of fire spread in live chaparral shrub fuel bed', *Combustion and Flame*, vol. 143, no. 3, pp. 183-98.

Zhu, P, Wang, XS, He, YP, Tao, CF & Ni, XM 2016, 'Flame characteristics and burning rate of small pool fires under downslope and upslope oblique winds', *Fuel*, vol. 184, pp. 725-34, DOI https://doi.org/10.1016/j.fuel.2016.07.059, <http://www.sciencedirect.com/science/article/pii/S0016236116306627>.

Appendix A1

Esmaeel Eftekharian, Yaping He, Robert H. Ong, Kenny C. S. Kwok, Jianping Yuan. "**Investigation of fire-driven cross-wind velocity enhancement**" **.** *International Journal of Thermal Sciences.* 2019; Volume 141, Pages 84-95. *https://doi.org/10.1016/j.ijthermalsci.2019.03.033*

International Journal of Thermal Sciences 141 (2019) 84–95

Contents lists available at ScienceDirect

International Journal of Thermal Sciences

journal homepage: www.elsevier.com/locate/ijts

Investigation of fire-driven cross-wind velocity enhancement

Esmaeel Eftekharian[a,*], Yaping He[a], Kenny C.S. Kwok[b], Robert H. Ong[b], Jianping Yuan[c]

[a] Centre for Infrastructure Engineering, School of Computing Engineering and Mathematics, Western Sydney University, Penrith, NSW, 2751, Australia
[b] School of Civil Engineering, The University of Sydney, NSW, Australia
[c] School of Civil Engineering, Wuhan University, Wuhan, 430072, PR China

ARTICLE INFO

Keywords:
Flow aerodynamics
Fire-wind enhancement
Flow acceleration
Pressure gradient
Fire plume

ABSTRACT

Understanding the aerodynamics associated with the interaction of fire and cross-wind flow is of great importance because the consequence may have major implications in building design against bushfire (or wildland fire) attacks. However, a fundamental understanding of how the interaction of fire and wind can alter free stream flow aerodynamic properties has remained elusive. The scope of this study is to examine the pool fire and wind interaction under fixed wind velocity condition. This study dissects the fundamental mechanisms of how the interaction of horizontal momentum flow with a vertical buoyant plume leads to enhancement of wind velocity in the horizontal direction at a certain elevation. Changes in flow aerodynamics caused by the interaction of fire and wind were analysed using the computational fluid dynamics approach. The mechanisms causing the changes were explained. A module was developed and added to the FireFOAM solver to evaluate flow acceleration due to the pressure gradient, gravity, and viscous effects. The chosen computational model was validated against two sets of experimental data, namely, a buoyant diffusion fire plume in still air and the other in cross-wind condition. The numerical simulation revealed that due to the interaction of fire and wind, there is a negative longitudinal pressure gradient across the plume axis, causing the flow to accelerate and the velocity profile to alter. It was also shown that the distortion in velocity profile depends on the location downstream of the fire plume. The height of the distortion increases whilst the magnitude of the distortion diminishes as the longitudinal distance from the fire source increases. Investigation of the effects of heat release rate on wind enhancement further showed that fire with a higher heat release rate causes a greater pressure gradient and a lower density, culminating in higher flow acceleration and consequently increase of wind enhancement.

1. Introduction

The interaction of fire and wind has long been a subject of interest. The effects of fire-wind interaction on the spread rate of fire-front were investigated in Refs. [1–3] and it was demonstrated that wind can significantly increase the spread rate of fire-front in unstable conditions [1]. The role of convective and radiative heat transfer mechanism in fire spread rate has been experimentally investigated [4,5]. Details of flame heat flux characteristics in the flame region have also been experimentally determined [6]. In addition to experimental investigations, computational fluid dynamics have also been used to model fire spread rate [7,8]. Numerical studies based on Large Eddy Simulation (LES) was used to simulate smoke plumes from the interaction of large pool fires and cross-wind [9,10]. Extensive numerical works have also been done to effectively modify combustion model [11] as well as radiative heat transfer and soot modelling in pyrolysis calculation [12] used in FireFOAM solver.

Direct Numerical Simulation (DNS) was also employed to investigate puffing instability and vortical structure generated during interaction of buoyant plume with free-stream cross flow [13]. A critical Reynolds and Froude number were used to determine thresholds for formation of these structures. Fire-induced flow in enclosures has also been numerically investigated [14,15].

Many other studies also have concentrated on the effects of wind on flame characteristics such as geometry including length and tilt angle [16–20]. Air entrainment mechanism for different fire-wind flow regimes was investigated in Ref. [21] and an approximation for entrainment velocity in different wind-fire conditions was developed based on the convection number. However, much fewer numbers of studies have been carried out to investigate the opposite effect, i.e., the effect of fire on the wind, or the changes in flow aerodynamics caused by the interaction of cross-flow with diffusion flame. It was experimentally shown that velocity profile immediately after the fire source is distorted and there is an increase in velocity near the flame zone because of the

---

[*] Corresponding author.
E-mail address: e.eftekharian@westernsydney.edu.au (E. Eftekharian).

https://doi.org/10.1016/j.ijthermalsci.2019.03.033
Received 2 August 2018; Received in revised form 14 January 2019; Accepted 25 March 2019

Nomenclatures

a	acceleration (m/s^2)
a_i	acceleration in direction i (m/s^2)
a_p	pressure acceleration (m/s^2)
a_v	viscous acceleration (m/s^2)
a_t	total acceleration (m/s^2)
c_p	specific heat at constant pressure (kJ/kgK)
D	fuel bed characteristic length (0.3 m)
D_m	diffusion coefficient
g	gravitational acceleration (9.81 m/s^2)
h	specific enthalpy per unit volume (kJ/m^3)
I	radiation intensity (W/m^2)
L	flame length (m)
p	static pressure (Pa)
Pr	Prandtl number
Q	heat release rate (kW)
Q^*	normalised heat release rate
q_r''	radiation flux (W/m^2)
$\dot{q}'''$	fuel heat release rate per unit volume (W/m^3)
q_c'''	local heat release rate per unit volume (W/m^3)
q_r'''	radiative heat transfer per unit volume (W/m^3)
R	gas constant (J/kgK)
Ri	Richardson number
s	distance along a special ray (m)
t	time (s)
T	temperature (K)
T_f	flame temperature (K)
u	velocity (m/s)
U_{ref}	reference velocity (m/s)
X, Y, Z	coordinates of computational domain (m)
Y	mass fraction of mixture

Symbols

−	spatial filtering
−	favre filtering
→	vector variable

Subscripts

ref	reference value
∞	free stream
t	turbulent
p	pressure
v	viscous

Greek

α	terrain coefficient
β	Thermal expansion coefficient (1/K)
δ	Kronecker delta
$\varkappa$	absorption coefficient
$\varkappa_p$	Plank mean absorption coefficient
N	kinematic viscosity (m^2/s)
P	density (kg/m^3)
σ	stress (Pa)
σ_r	Stefan-Boltzmann constant (W/m^2K^4)
χ	radiation fraction
Φ	viscous stress tensor (kg/m^2s^2)
Ω	mass rate of production of species
ρ	density (kg/m^3)

interaction of free-stream velocity and buoyant diffusion flame [22]. Based on analysis of experimental data, thermal expansion and low-density in the flame zone were speculated to be responsible for distortion in velocity profile [23]. It was shown recently, based on an analytical solution for flame acceleration and velocity, that buoyancy force plays a role in flow acceleration of cross-wind [24].

Investigation of wind and pool fire interaction is highly applicable to fire safety of scenarios associated with burning industrial oil tank [25,26]. A theoretical model was developed to characterise temperature and air entrainment in pool fire scenarios in windy conditions [25]. It was shown that when multiple fire tanks are subjected to cross-wind, strong fire whirs can be generated causing huge influences on the flow field [27]. The effects of wind on burning rate of methanol pool fire was investigated and also it was shown that the flow characteristics is determined by ratio of momentum to buoyancy force (Richardson number) [28]. The interaction of pool fire source with free stream velocity was also investigated to simulate burning vehicles in tunnels [29,30]. However, the majority of these studies focused on temperature distribution, rather than velocity profile. Hence, little information is discernible as to how pool fires affect free stream wind velocity profiles.

The implication of enhancement of free-stream velocity with fire can be found in the phenomenon of wind enhancement by bushfire (forest fire or wild fire). That is the increase of local wind velocity by bushfire. Bushfire enhanced wind is believed to be one of the destructive forces in bushfire events. It is generally accepted that the wind can enhance bushfire spread rate as well as flame characteristics [31]. In contrast, there is only some anecdotal evidence in the literature to indicate the contribution of bushfire to wind enhancement [32]. The role of bushfire in wind enhancement has been preliminarily investigated using CFD (Computational Fluid Dynamics) technique [33]. It was shown that bushfire can significantly increase near-ground wind as well as pressure load on buildings located downstream of bushfire front. Coanda or trench effects were postulated to account for the attachment of plume to the ground immediately downstream of bushfire front, while further downstream, buoyancy force dominates and eventually lifts the plume above the ground. However, the results presented in Ref. [33] are crude and no information was reported regarding mechanisms that explain the phenomenon.

The presented literature review indicates that in spite of a number of studies performed in the domain of wind-fire interaction, the basic understanding of aerodynamic effects of fire on wind requires further investigation, particularly in respect to the enhancement of near-ground wind by fire. Previous works provide invaluable experimental and numerical data into the impacts of buoyant diffusion flame on flow aerodynamics. However, the fundamental reasons as to how the interaction of fire and wind leads to enhancement of wind are unclear. This work aims to fill the gap by providing quantitative and systematic analysis into the factors contributing to distortion of the velocity profile in the interaction of wind and fire scenarios. The main objectives of this study are to provide an insight of flow acceleration during fire-wind interactions and to fundamentally explain how the interaction of horizontal wind and vertical buoyant plume leads to increase of wind horizontal velocity. For this purpose, the flow acceleration is explicitly expressed in terms of contributions from the pressure gradient, body force, and shear stress. The computational fluid dynamics method is used to quantitatively delineate each contribution term.

Bushfire almost always starts with a small ignition source which closely resembles a pool fire and then evolves into a line source of fire. Hence, the first step is to understand pool fire behaviour for a given dimension. The fundamental mechanisms governing pool fire-wind interaction are applicable to better understand the mechanisms involved in bushfire wind enhancement phenomenon. Therefore, the interaction between pool fire and wind is the focus of the current study.

2. The numerical modelling approach

2.1. The modelling software and the governing equations

FireFOAM was used as a CFD solver in this study. This solver is a derivative of OpenFOAM [34] platform, specifically designed for fire dynamic simulations. OpenFOAM is an object-oriented open-source platform which allows the users to add self-developed modules to the main code. It has been validated with many experimental results including methane diffusion flames [35,36], methanol pool fire [37] and hydrogen-methane jet fire [38]. FireFOAM is a transient solver that uses the LES (Large Eddy Simulation) scheme to solve Favre-filtered continuity, momentum, energy, species and state equations for compressible-flow [35]:

$$\frac{\partial\bar{\rho}}{\partial t}+\frac{\partial(\bar{\rho}\tilde{u}_i)}{\partial x_i}=0 \tag{1}$$

$$\frac{\partial(\bar{\rho}\tilde{u}_i)}{\partial t}+\frac{\partial(\bar{\rho}\tilde{u}_i\tilde{u}_j)}{\partial x_j}=\frac{\partial}{\partial x_j}\left[\bar{\rho}(\nu+\nu_t)\left(\frac{\partial(\tilde{u}_i)}{\partial x_j}+\frac{\partial(\tilde{u}_j)}{\partial x_i}-\frac{2}{3}\frac{\partial\tilde{u}_k}{\partial x_k}\delta_{ij}\right)-\bar{p}\delta_{ij}\right]+\bar{\rho}g_i \tag{2}$$

$$\frac{\partial(\bar{\rho}\tilde{h})}{\partial t}+\frac{\partial(\bar{\rho}\tilde{u}_j\tilde{h})}{\partial x_j}=\frac{D\bar{p}}{Dt}+\frac{\partial}{\partial x_j}\left[\bar{\rho}\left(D_m+\frac{\nu_t}{\mathrm{Pr}_t}\right)\left(\frac{\partial\tilde{h}}{\partial x_j}\right)\right]+\dot{q}'''-\nabla\cdot\dot{q}_r'' \tag{3}$$

$$\frac{\partial\bar{\rho}\tilde{Y}_m}{\partial t}+\frac{\partial(\bar{\rho}\tilde{u}_j\tilde{Y}_m)}{\partial x_j}=\frac{\partial}{\partial x_j}\left[\bar{\rho}+\left(D_m+\frac{\nu_t}{\mathrm{Pr}_t}\right)\frac{\partial\tilde{Y}_m}{\partial x_j}\right]+\omega_m \tag{4}$$

$$\bar{p}=\bar{\rho}R\tilde{T} \tag{5}$$

where the superscripts "−" and "∼" indicates spatial and Favre filtering. Also, ρ, p, h, Y_m, g, ν, ν_t, D_m, R, Pr_t, δ and ω_m are respectively, density, static pressure, specific enthalpy, mass fraction of species m in the gas mixture, gravitational acceleration, laminar viscosity, turbulent viscosity, laminar diffusion coefficient, gas constant, Prandtl number, Kronecker delta and production/sink rate of species m due to chemical reaction. The heat release rate per unit volume (W/m^3) from a chemical reaction and the radiation emission intensity (W/m^2) of the gas mixture are represented by $\dot{q}'''$ and $\dot{q}_r''$ respectively.

For ease of explanation, the momentum equation, i.e., Eq. (2), can be simply expressed in terms of acceleration vector:

$$\vec{a}=\frac{D\vec{u}}{Dt}=\frac{-\nabla p}{\rho}+\vec{g}+\frac{\Phi}{\rho}=\vec{a}_p+\vec{g}+\vec{a}_v \tag{6}$$

where $\vec{a}$ is flow acceleration, $\vec{u}$ is velocity vector, $\vec{g}$ is the gravitational acceleration vector, and Φ is the viscous shear stress tensor $\left(\Phi_i=\frac{\partial(\sigma_{ij})}{\partial x_j}\right)$ in which σ is the components of stress. The first, second and third term on the RHS (Right Hand Side) of Eq. (6) account for the accelerations due to respectively, pressure gradient, gravity and viscous forces. For simplicity, the three components are referred as pressure acceleration, gravitational acceleration and viscous acceleration respectively in the remaining discussions of this paper. The directional components of $\vec{a}$ is presented individually as:

$$a_{ti}=a_{pi}+g_i+a_{vi} \tag{7}$$

where index $i=1, 2, 3$ correspond to acceleration in X, Y and Z directions. In the current discussion, we are mainly concerned with velocity and acceleration in the longitudinal direction i.e., $i=1$.

FireFOAM iteratively solves Eqs. (1)–(5) to determine the flow prime variables. In order to conduct a quantitative analysis of flow acceleration, a module has been prepared and added to the FireFOAM platform to sort and output individual components of the total acceleration [see Eq. (6)] at the end of each iteration cycle.

The kEq model [39] was used to treat sub-grid scale turbulence structures. This model solves a transport equation for sub-grid scale turbulent kinetic energy to model sub-grid turbulent structures.

The combustion simulation is based on the eddy dissipation concept [40]. Simulations of the current study use Eddy Dissipation Model (EDM) which assumes that the combustion process is infinitely fast and chemical reaction time scale is negligible compared to the turbulent time-scale. Therefore, turbulent mixing time-scale is controlling the combustion rate. The infinitely fast chemistry and single-step global reaction model was selected to model the combustion process.

Radiation is one of the most challenging parts of fire-related numerical simulations [41]. FireFOAM solves radiative heat transfer equation based on grey gas assumption [Eq. (8)], [42].

$$\frac{dI}{ds}=\overline{\kappa I_b}-\overline{\kappa I} \tag{8}$$

In which I is the radiation intensity, I_b is the black body radiation intensity ($I_b=\sigma_r T^4/\pi$) and κ is absorption coefficient of the grey gas, s is the distance along a special ray and σ_r is Stefan-Boltzmann constant (W/m^{2}K^4). Grey model assumes that radiation does not change with the wavelength and therefore, κ is replaced by Plank mean absorption coefficient (κ_p).

FireFoam uses finite volume discrete ordinates model (fvDOM) [43] to solve radiation heat transfer equation [Eq. (8)]. This model solves radiative heat transfer equation for a discrete number of finite solid angles. Also, it was assumed that the grey model is non-absorbing and non-scattering thin medium. This assumption makes the second term in the right hand side of Eq. (8) zero ($\overline{\kappa I}=0$). Assuming isotropic radiation

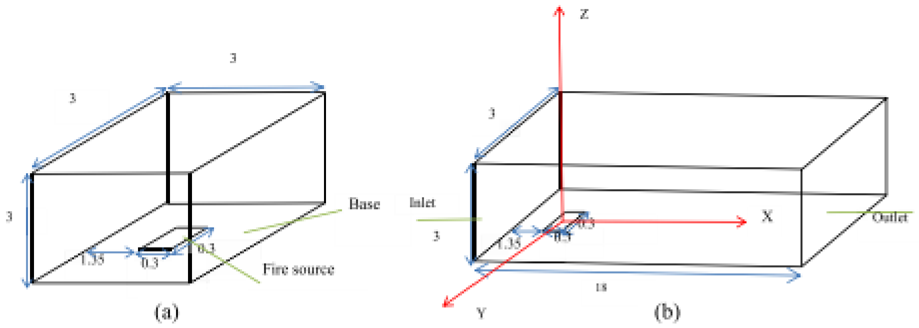

Fig. 1. Schematic views of the computational domain for (a) validation (b) cross-wind fire scenarios.

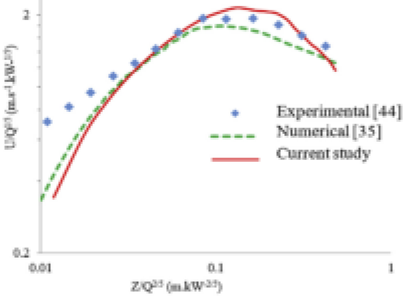

Fig. 2. Comparison of the normalised centreline velocity profile of the current study with numerical and experimental data available in the literature.

emission for the flame $\left(\kappa I_b = \frac{\dot{q}'''}{4\pi}\right)$, Eq. (8) will be simplified to Eq. (9) [42],:

$$\frac{dI}{ds} = \frac{\chi_{rad}\dot{q}_i'''}{4\pi} \tag{9}$$

In which, $\dot{q}_i'''$ is the local heat release rate per unit volume and χ_{rad} is the radiant fraction. In this study, radiant fraction of 0.2 was considered as used in previous studies for simulation of methane-diffusion flame [35]. Finally, the radiant heat transfer source term ($\nabla\cdot\dot{q}_r''$) in the energy equation [Eq. (3)] can be calculated by integrating from the right hand side of Eq. (9) in the polar coordinates [(Eq. (10)] [42],:

$$\nabla\cdot\dot{q}_r'' = \dot{q}_r''' = \int\left(\frac{\chi_{rad}\dot{q}_i'''}{4\pi}\right)d\Omega = \chi_{rad}\dot{q}_i'''4\pi \tag{10}$$

2.2. Geometrical model and simulation conditions

Two computational domains have been separately prepared for a buoyant diffusion (for validating the model) and a cross-wind fire scenario. In the context of this paper, cross-wind means the flow in longitudinal direction that makes the right-angle with vertical buoyant plume. Fig. 1 displays schematic views of the domains.

For the simulation of the buoyancy diffusion flame experiment by McCaffrey [44], the domain size in all directions was set at 3 m [see Fig. 1(a)] and the number of cells in horizontal, spanwise and vertical direction are, 154, 154 and 100, respectively. A non-uniform grid was used to keep the smallest cell size the same as that suggested in Ref. [35]. Similar to Ref. [35], the burner was simulated by a 0.3 × 0.3 m square placed at the centre of the domain. The surface of the burner abutted the base of the domain. The domain boundary conditions for the buoyant diffusion geometry were similar to those suggested by Wang et al. [35].

For the simulation of the cross-wind fire interaction scenarios, the domain dimension in X direction was extended to 18 m, while other geometrical dimensions, including the fuel bed size, were the same as the computational domain prepared for buoyant diffusion scenarios [see Fig. 1(b)]. The origin of the XYZ coordinate system was set at the centre of the fuel bed. Methane was chosen to be injected from the fire source to generate heat release rate (HRR) of 58 kW, 580 kW and 1.16 MW for different scenarios. As for the other domain boundaries, outflow and open boundary conditions were prescribed for the domain outlet on the right and the ceiling, respectively. Slip and no-slip boundary condition were applied respectively to the domain sides and base. To treat the near-wall flow region, the wall function approach [45] was applied. A power law velocity profile was used at the inlet on the left of the domain:

$$U(Z) = U_{ref}\left(\frac{Z}{Z_{ref}}\right)^{\alpha} \tag{11}$$

where, U_{ref} and Z_{ref} are, respectively, the reference velocity (6 m/s) and height (3 m), α is determined based on terrain category (here 0.16) [46]. In order to consider turbulent fluctuations in the domain inlet, the "2D vortex method" [47] was used.

The initial temperature was considered to be 300 K, while adiabatic boundary was suggested for the domain base.

3. Results and discussion

3.1. Result of validation

Two sets of experimental data were used to validate numerical model of the current study. The first experiment involved a buoyant diffusion flame of methane in still air and was performed by McCaffery [44]. The second experiment was case of buoyant diffusion flame interacting with free-stream cross-flow reported by Hirano and Kinoshita [22]. In the first benchmarking case, a simulation with a constant HRR of 58 kW was performed and then compared with numerical results of [35] and experimental data of [44].

McCaffery's [44] experiment was also simulated by Wang et al. [35]

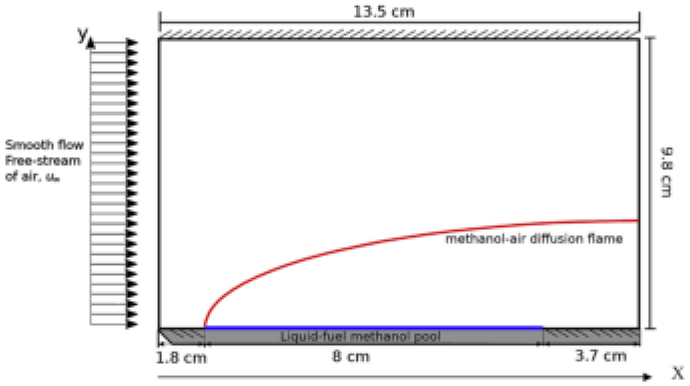

Fig. 3. Schematic of Hirano and Kinoshita's experimental configuration [22].

using an early version of FireFOAM. Their total simulation time was 20 s and it took 7 s for the simulation to reach the quasi-steady conditions. They also collected and averaged data during the remaining part of their simulation (13 s). The same simulation and average times were used in the current study. The predicted fire plume centreline velocity is plotted in a log-log coordinate in Fig. 2 which compares the results predicted in Ref. [35] and measured in Ref. [44].

The mean absolute error (MAE) associated with the current study and numerical results reported in Ref. [35] are 0.156 and 0.179, respectively. These statistics show that in spite of similarities in the geometrical model, boundary conditions and simulation time in the two studies, the current study shows slightly better agreement with the experimental data than the previous study [35]. The reason might be rooted in the version difference of FireFOAM in the two studies. The older versions of FireFOAM (based on OpenFOAM V.1.7) was used in Ref. [35]. This version of FireFOAM employed the mixture fraction combustion model, whereas, the version used in the current study is based on OpenFOAM V.4.1 which uses eddy dissipation combustion model.

The second numerical model validation was against the experimental data of a steady burning of a liquid-fuel methanol pool in a forced convective environment [22]. The flow velocity and temperature profiles across the laminar boundary layer with a methanol-air diffusion flame were measured in a combustion chamber with 3 × 9.8 cm (width × height) cross-section and 13.5 cm in length.

Fig. 3 shows the 2-D schematic of experimental setup of Hirano and Kinoshita [22].

Considering the symmetry in the spanwise direction, a 2-D model was used for validation of cross-wind fire in the current study to solve the mass, momentum, energy, and species equations in Cartesian coordinates as was outlined earlier. Ali et al. [48] also used a 2-D approach to validate their numerical model with the experimental data of Hirano and Kinoshita [22]. The computation domain coincides with the chamber boundary. A smooth and uniform fixed velocity of air was imposed at the inlet, while the flow of diffusion flame leaves to the atmosphere at the exit boundary of the domain. A constant temperature of 300 K was set for the initial condition. The pressure outlet boundary conditions utilise the initialisation of the pressure field and density. The top and bottom walls were fixed with no-slip velocity conditions and adiabatic conditions for the temperature. The uniform grid of 550 × 400 cells in streamwise (X) and spanwise (Y) directions was considered to balance the solution accuracy and computational cost.

In Fig. 4, both the measured and the CFD simulated velocity profiles downstream of the leading flame edge across the boundary layer over the burning liquid methanol revealed the result of flow acceleration or flow enhancement due to the local pressure gradient generated by the local temperature gradient and distortion of the streamline due to the chemical reaction [22]. Furthermore, the aerodynamic structure of the region near the trailing flame edge showing a shift in its shape change and the maximum velocity in this higher velocity region increases with the downstream distance [22].

Fig. 5 also compares the measured temperature profile [22] with the current numerical results at different distances downstream of the fire. Both Figs. 4 and 5 show reasonably good agreements between the current numerical results and experimental data [22].

3.2. Grid sensitivity analysis

For the 3-D simulation of the tunnel fire flow depicted in Fig. 1(b), a grid sensitivity study with three different cell numbers of 400 k (coarse), 800 k (medium) and 1200 k (fine) was conducted for the $Q = 580$ kW case. In all cases, non-uniform grid was used to generate smaller cells near the burner, resulting in the near-burner cell sizes of $1 \times 10^{-5}\,\mathrm{m}^3$, $5 \times 10^{-6}\,\mathrm{m}^3$ and $2.5 \times 10^{-6}\,\mathrm{m}^3$ for the coarse, medium and fine grid, respectively. Velocity and density profile for different grid sizes were compared as shown in Fig. 6. The relative mean velocity difference between fine and medium grids was 1.5% while this was 10.5% between medium and coarse grids. The corresponding relative air density difference was 0.78% and 1.69%, respectively. Hence, the medium grid was chosen for this study.

3.3. Result of wind-fire simulation

3.3.1. General description and observation

Numerical simulations were performed for three heat release rates (58 kW, 580 kW, and 1.16 MW) under the constant free stream velocity of 6 m/s. Tang et al. [49] suggests that fire wind interaction scenarios can be divided into three major categories based on the dominant contributing force (i.e, inertia or buoyancy). Richardson number $\left[\mathrm{Ri}_x = \frac{g\beta(T_f - T_\infty)x}{U_\infty^2}\right]$ was used to show that whether the flow is controlled by force convection ($\mathrm{Ri} < 0.1$), mixed convection ($0.1 < \mathrm{Ri} < 10$), or natural convection ($\mathrm{Ri} > 10$). Based on the suggested boundaries for heat and velocity, the results showed that flow regime of all fire-wind simulation scenarios in this study can be considered as mixed convection in which both the effects of buoyancy and inertia are important.

The simulated time period for all flow scenarios was 20s. It took about 7 s of the simulated time period for the flow to reach quasi-steady state. Hence, all the presented results in this section are the time-averaged values over the last 13s of the simulated period.

In the presentation of the results, all length dimensions are normalised over the characteristic dimension D which is defined as the dimension of the fire source (0.3 m).

3.3.2. Velocity and acceleration profiles

Planar distributions of normalised longitudinal velocity at different longitudinal distances are depicted in Fig. 7. By comparing the free-stream, or ambient, velocity distribution [Fig. 7(a)] with that downstream of the fire source [Fig. 7 (b), (c), (d), (e) and (f)], it is seen that velocity is significantly enhanced at different regions downstream of the fire source. For example, at $X/D = 10$ the longitudinal velocity has increased by almost 40% in the neighbourhood of the plume centre [Fig. 7(d)], compared to the velocity upstream of the fire source at the same height. It is believed that the mushroom structure being formed initially in the near ground region at each side of the fire source [Fig. 7 (b)] is due to the Rayleigh–Taylor instability. This mushroom structure grows along the central column further downstream of the fire source and form vortical structures [Fig. 7 (d),(e) and (f)]. This observation is consistent with those reported in Refs. [13,50].

For detailed investigation of the phenomenon, normalised longitudinal velocity and total acceleration profiles along the domain centre plane at various distances from the fire source under the cross-wind

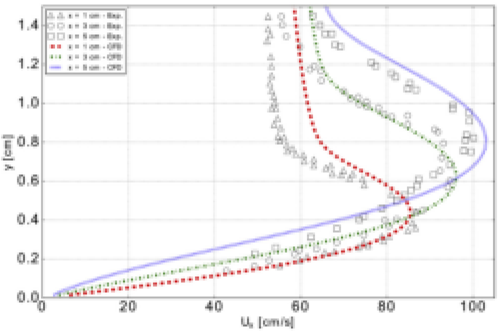

Fig. 4. Comparison between experiment [22] and CFD of the velocity profiles taken downstream the boundary layer of methanol-air diffusion flame, $u_\infty = 0.5$ m/s.

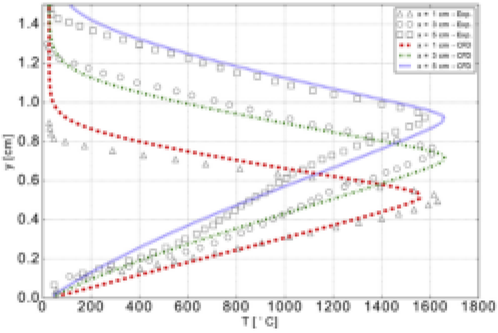

Fig. 5. Comparison between experiment [22] and CFD of the temperature profiles taken downstream the boundary layer of methanol-air diffusion flame, $u_\infty = 0.5$ m/s.

condition are plotted in Fig. 8. Note that the profiles corresponding to $X/D = -3$ are the free-stream profiles. The distortions of the longitudinal velocity vertical profiles downstream of the fire can be clearly seen in Fig. 8(a). At $X/D = 6$, the velocity profile exhibits a bulge which is encircled at the height of Z/D˜1.2. This bulge represents the centre of the tilted plume and also reveals that the local velocity there exceeds that of the free stream as a result of the enhancement due to the interaction of the cross-wind and the buoyant plume. At the near ground level ($0 < Z/D < 0.2$), the longitudinal velocity downstream of the fire is also seen to exceed that of the free-stream. As X/D increases, the plume rises from the ground and the location of the bulge in the velocity profile, though becoming weaker, is lifted further.

Under the influence of buoyancy, the fire plume accelerates upwards. The longitudinal wind flow, on the other hand, interacts with the plume, bending it by pressure and viscous force towards downstream. This is indicated by the longitudinal acceleration presented in Fig. 8(b) and (c). As observed in Fig. 8(b), at all distances downstream of the fire, wind accelerates at two regions: (1) very close to the ground (Z/D˜0.2) and (2) above the ground at the plume region. At further downstream when $X/D > 6$, near ground (Z/D˜0.2) longitudinal acceleration is dominant, resulting in an increase of wind velocity in that region. All these confirm the observations previously reported in Refs. [22,33,51], though the extents of the velocity enhancement are different due to the differences in the simulated fire source configurations.

Further downstream of the fire source ($X/D > 10$), the longitudinal velocity profiles appear to be lower than that of free-stream for the elevation within the range $0.3 < Z/D < 4.5$.

During fire-wind interaction, fire buoyant plume acts as a jet blockage against wind and causes formation of wake and low velocity region around the domain centreline downstream of the fire source. As shown in Fig. 9, when wind velocity impinges the buoyant plume, the longitudinal velocity is significantly reduced at the point of impact as well as downstream of the fire align with the domain centreline. The formation of counter-rotating vortex pair (CVP), generated due to interaction of cross flow with buoyant plume [13,52], can be clearly observed in Fig. 9. Formation of CVP creates a wake region through flow entrainment, reducing the longitudinal velocity along the domain centreline downstream of the fire source. Similar phenomena have also been observed in cross-wind-jet interaction studies [53]. However, just below and above the plume region [before and after the bulge in Fig. 8(a)], flow entrainment is the main cause of flow deceleration and reduction of longitudinal velocity.

The variations in velocity profiles are consistent with variations in the normalised total horizontal acceleration a_{t1} profiles shown in Fig. 8(b). For example, at $Z/D = 1.2$ for $X/D = 6$, the increase in velocity is accompanied by the large acceleration at the same elevation around $Z/D = 1$.

According to Eq. (6), acceleration vector field can be decomposed into three different components, namely, pressure acceleration $\left(\frac{-\nabla p}{\rho}\right)$, gravitational acceleration (g) and viscous acceleration $\left(\frac{\varphi}{\rho}\right)$. The vertical distribution of the longitudinal total acceleration and each of the components at the $6D$ distance downstream of the fire source for the $Q = 580$ kW case are plotted in Fig. 8(c). Gravitational acceleration is non-existent in the longitudinal direction, i.e., $g_1 = 0$ and therefore, is not shown in Fig. 8(c). In the region up to the height of $Z/D = 0.5$, because of the dominance of viscous effects in the boundary layer, flow acceleration is only limited to viscous forces. Flow acceleration gradually declined in this region as velocity gradient and correspondingly viscous acceleration reduces with height. This is followed by the dominance of pressure acceleration which experiences a sharp increase, reaching its maximum value at Z/D˜1 and then drops to zero at Z/D˜1.8. In the region above $Z/D = 1.8$, total acceleration almost remains zero as there is neither buoyant plume to create pressure acceleration nor shear stress gradient to create viscous acceleration.

Pressure acceleration term is the dominant acceleration component in velocity enhancement region $0.3 < Z/D < 1.5$ for $X/D = 6$. Immediately downstream of the fire source, because of thermal expansion, the magnitude of longitudinal pressure gradient is high, while density has the lowest value because of high temperature and its value increases further downstream as shown in Fig. 10(b). Accompanied by density changes is a gradual reduction in the magnitude of longitudinal pressure gradient as shown in Fig. 10(a). Hence, immediately

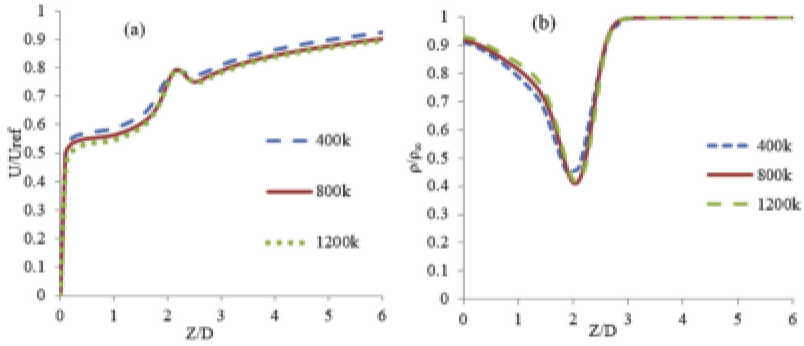

Fig. 6. Vertical distribution of normalised (a) horizontal velocity (b) density for different grid sizes at $X = 6D$ when $Q = 580$ kW.

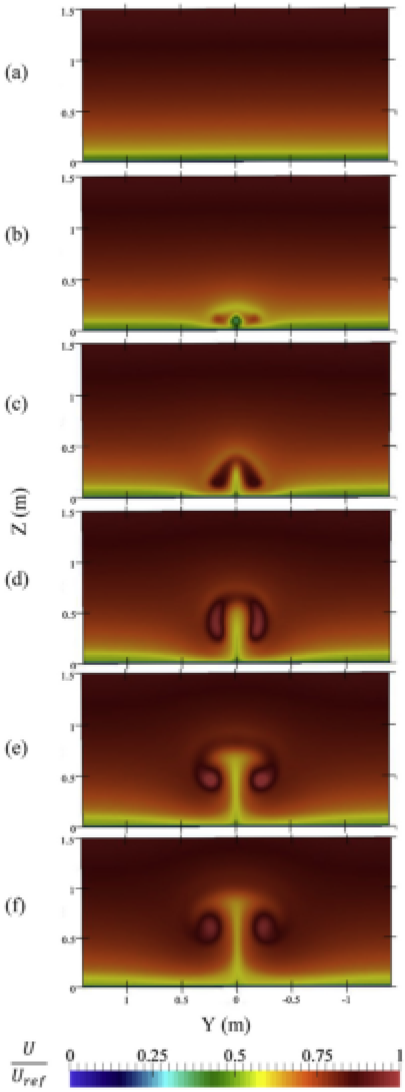

Fig. 7. Cross sectional longitudinal normalised velocity $\left(\frac{U}{U_{ref}}\right)$ at (a) $X/D = -3$, (b) $X/D = 3$, (c) $X/D = 6$, (d) $X/D = 10$, (e) $X/D = 13$ and (f) $X/D = 16$, for $Q = 580$ kW case.

downstream of the fire source, the combined effects of large magnitude of longitudinal pressure gradient and low density create a large acceleration which causes a significant distortion of velocity profile as shown in Fig. 8(a).

3.3.3. *Sensitivity to heat release rate*

Higher heat release rates create greater distortion in the velocity profile as revealed in Fig. 11. The peak of velocity enhancement or the bulge in the velocity profile also shifts upwards in Z direction as the heat release rate increases. Different heat release rates generate different longitudinal pressure acceleration, density, and total acceleration profiles, as shown in Fig. 12 (a), (b) and (c). Lower density means greater thermal expansion which is associated with velocity increase as shown in Fig. 11.

Fig. 12 also shows that as heat release rate increases, the peaks in the horizontal pressure gradient, density and consequently acceleration profile move upwards in the Z direction. Such shifts are driven by the increased buoyancy force associated with the increased heat release rate.

Negative values of near ground ($Z/D < 2$) longitudinal pressure gradient not far downstream of fire source are due to the attachment of the plume to the ground, which prevents or hinders flow entrainment from the region below the plume. However, further downstream of the fire plume, where the plume starts to lift from the ground, it can entrain flow from either side. Hence, in the near ground region, the plume imposes a positive pressure gradient to the surrounded air. This positive pressure gradient increases along with vertical direction up to just underneath the plume region where there exists negative pressure gradient as shown in Fig. 13(a).

Fig. 13(a) also reveals that the maximum value for the magnitude of the positive longitudinal pressure gradient at the up side of the plume (vertically above the plume) happens immediately after the fire source, while the corresponding maximum value at the downside of the plume (vertically underneath the plume) occurs in further downstream of the fire source where the plume is detached from the ground. This is because initially, plume imposes a positive pressure gradient to the surrounding flow only in the up side of the plume to complete the flow entrainment process. In this region, because plume is attached to the ground, the flow is not entrained from the downside of the plume and therefore all the flow entrainment is only supplied from the plume up side. Hence, the maximum positive pressure gradient for the up side of the plume is observed immediately downstream of the fire. Further downstream, as the plume is detached from the ground, because of the low-velocity in the downside region of the plume, the plume is inclined to entrain flow from this region rather than the up side. Thus, the magnitude of the positive pressure gradient in the region downside of the plume exceeds that in the region above the plume.

During the interaction of cross-wind with fire, viscous forces also undergo changes. As viscous forces in the longitudinal direction increases, correspondingly the longitudinal viscous acceleration increases, as shown in Fig. 13(b). Furthermore, the magnitude of longitudinal viscous acceleration increases as the heat release rate increases. This is because the fire changes the turbulent mixing process and increases the turbulent shear stress of the free stream airflow. Along the plume region for all heat release rates, as longitudinal pressure acceleration increases [Fig. 13(c)], the magnitude of viscous acceleration also increases [Fig. 13(b)]. The main reason is that the flow viscous acceleration is correlated with velocity gradient [according to Eq. (2)]. Velocity gradient itself is generated due to the pressure acceleration. Consequently, when pressure acceleration increases, viscous forces and correspondingly viscous acceleration increase.

3.3.4. *Heat release rate effects on flame length*

One of the ways to recognize the flame region and length is to plot the distribution of combustion products (e.g CO_2) where the point corresponding to the maximum (threshold) value of CO_2 can determine the flame length [37]. The value of CO_2 in different planes was reviewed and it was found that the maximum value of CO_2 occurs at the plane $Y/D = 0.2$, $Y/D = 0.5$ and $Y/D = 0.7$, respectively for the cases $Q = 58$ kW, $Q = 580$ kW and $Q = 1.16$ MW in this study. Hence, the distribution of CO_2 and the normalised longitudinal velocity were plotted in these planes in Fig. 14. Fig. 14(a) shows that the highest value of CO_2 happens at around $X = 1$ m, $X = 3$ m and $X = 4$ m which approximate the flame length for $Q = 58$ kW $Q = 580$ kW and

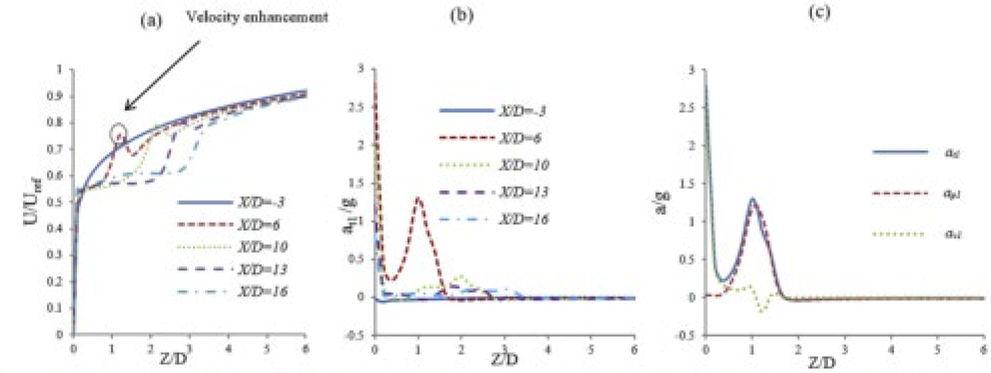

Fig. 8. Distributions of normalised longitudinal (a) velocity, (b) total acceleration along the domain centre plane at various distances and (c) components of acceleration at $X/D = 6$, downstream of the fire source for $Q = 380$ kW case.

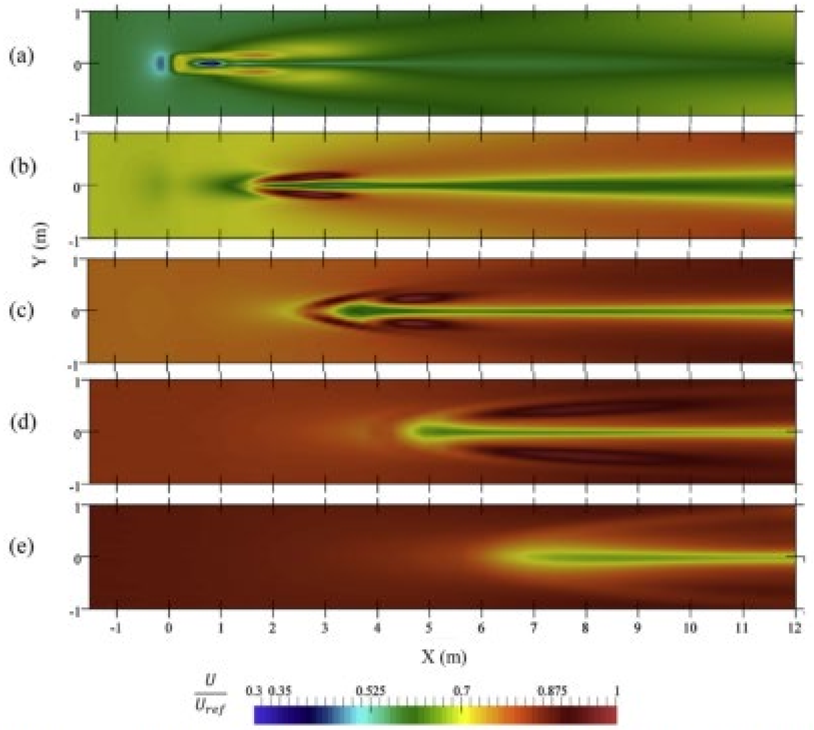

Fig. 9. Distribution of normalised longitudinal velocity $\left(\frac{U}{U_{ref}}\right)$ at different horizontal plane: (a) $Z/D = 0.3$, (b) $Z/D = 1$, (c) $Z/D = 2$, (d) $Z/D = 3$ and (e) $Z/D = 4$ for the case $Q = 380$ kW.

$Q = 1.16$ MW, respectively.

Heskestad [54] presented a correlation for flame length for pool fire in still condition based on experimental data:

$$\frac{L}{D} = -1.02 + 3.7\dot{Q}^{*2/5} \tag{12}$$

where L is the flame length, D is the characteristic length of square pool (here 0.3). Parameter Q^* is the normalised heat release rate.

$$Q^* = \frac{Q}{T_\infty \rho_\infty c_p \sqrt{g} D^{5/2}} \tag{13}$$

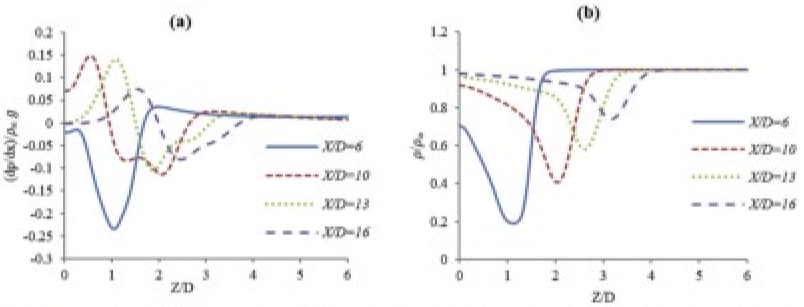

Fig. 10. Distribution of normalised (a) longitudinal pressure gradient (b) density at different distances downstream of the fire source centreline for $Q = 580$ KW case.

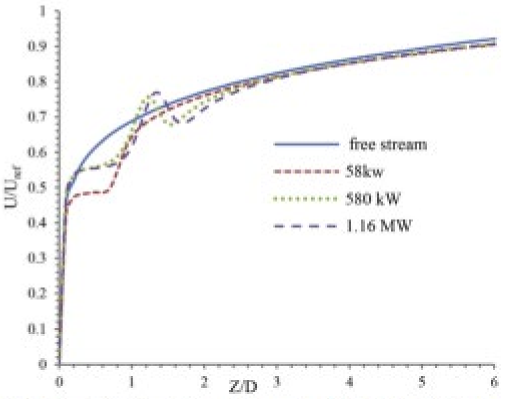

Fig. 11. Normalised Longitudinal velocity profile at $X/D = 6$ for different heat release rates.

where c_p is specific heat at constant pressure.

The flame lengths estimated from the current study are compared with the values determined by Eq. (12) and presented in Table 1.

As can be seen in Table 1, flame length in the presence of wind is slightly higher than that in still condition. This trend is in agreement with the observation reported in Ref. [20] for a range of strong cross-wind flame interaction.

Fig. 14 reveals that the flame is attached to the ground and horizontally extended immediately downstream of the fire source. This phenomenon is referred as the flame base drag and has been observed in many previous studies [16,33,52,55–57]. Fig. 14(b) shows that accompanied by the horizontal flame extension, the enhanced longitudinal velocity region is also horizontally extended immediately downstream of the fire source and then lifts from the ground further downstream.

The flame base drag phenomenon was attributed by some researchers [58] to the fuel gas density being greater than air. It is noted that in the present study, the fuel gas is methane of which the density is less than air. Therefore, the possible explanation of the flame base drag phenomenon is the Coanda-effect as speculated in Ref. [31].

4. Conclusion

This paper presents a numerical investigation of the phenomenon of wind enhancement by fire and provides fundamental explanation of longitudinal wind flow acceleration as a result of actions induced by a buoyant plume. The changes in flow characteristics by the interaction of cross-wind and fire are revealed by examining flow accelerations due to the pressure gradient, gravity and shear stress. Negative longitudinal pressure gradient and low-density values within the plume region are

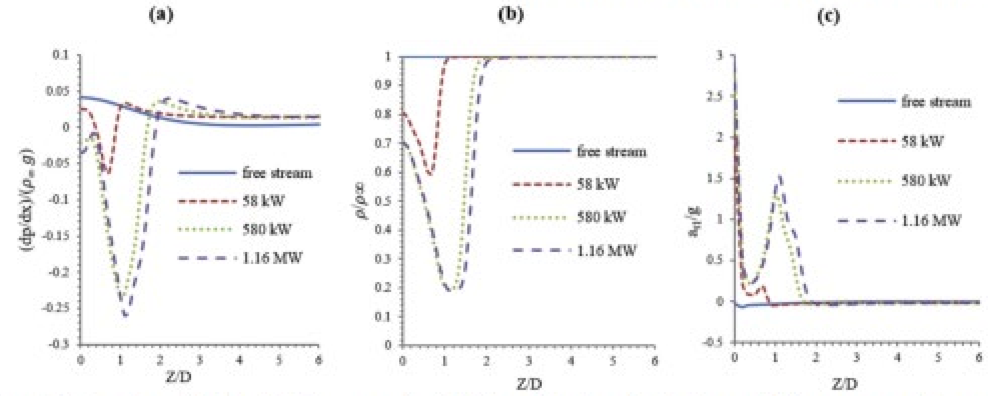

Fig. 12. Distribution of normalised (a) longitudinal pressure gradient (b) density and (c) total acceleration along a vertical line at $X/D = 6$ and free stream for different heat release rates.

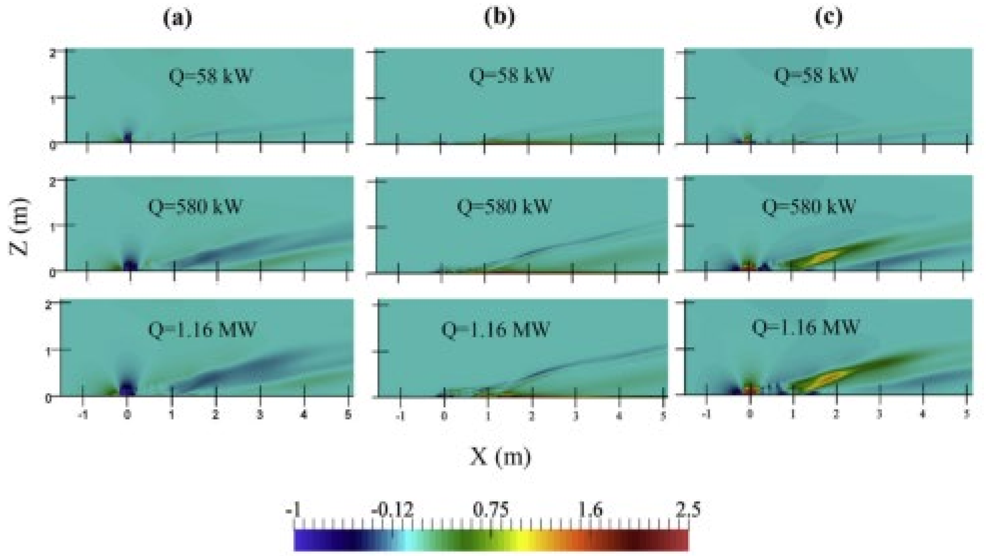

Fig. 13. Normalised longitudinal (a) pressure gradient $(dp/dx)/(\rho_{\infty}g)$, (b) viscous acceleration $a_{\nu,x}/g$ and (c) pressure acceleration $a_{p,x}/g$, planar distribution at $Y = 0$ for different heat release rates.

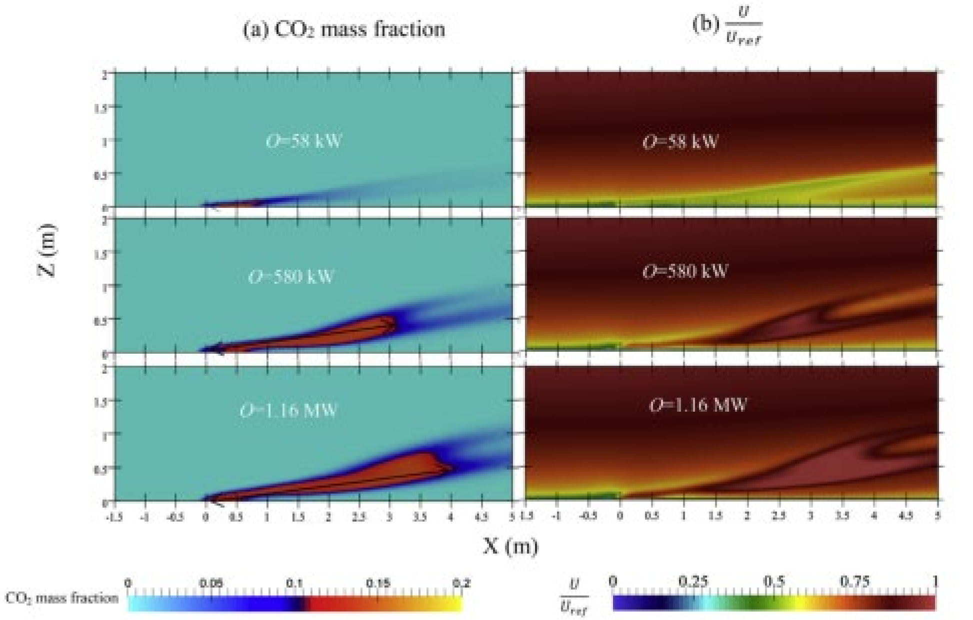

Fig. 14. Distribution of (a) CO_2 mass fraction and (b) normalised longitudinal velocity $\left(\frac{U}{U_{ref}}\right)$ at $Y/D = 0.2$, $Y/D = 0.5$ and $Y/D = 0.7$ respectively for $Q = 58$ kW, $Q = 580$ kW and $Q = 1.16$ MW.

Table 1
Comparison of estimated flame length (m).

Method	Q (kW)		
	58	580	1160
Without wind, Eq. (12)	0.83	2.55	3.46
With wind, CO_2 mapping	0.95	3.04	4.03

found to act as a driving force to accelerate the flow and cause the wind enhancement downstream of the fire source. It was also revealed that interaction between pool fire and wind in a mixed convection flow regime can increase the horizontal velocity by up to 40%. It is also found that in the near ground region downstream of the fire source, the magnitude of longitudinal acceleration, as well as density difference, increases with increasing heat release rate, leading to a higher flow enhancement. Also, the results reveal that elevation of the peak of enhanced wind velocity increases with the increasing heat release rate of the fire.

The results of the current study support the findings of some previous studies in the sense that interaction of wind and fire can lead to enhancement of wind. However, this study fundamentally investigated the mechanisms involved in the phenomenon.

Although the current study focuses on the pool fires with the finite burning surface area, the outcomes have the implications to the understanding of bushfire wind enhancement phenomenon in the larger scales. Experiments are being prepared in a wind tunnel using a line-source fire to simulate a bushfire front. The results will be used to validate the FireFOAM model and verify the findings of the numerical studies.

Acknowledgement

This project is funded by Australian Research Council grant ARC-DP160103248.

The authors gratefully acknowledge OpenFOAM foundations for the provision of an open-source CFD platform. We also thank Dr. Yi Wang and Dr. Oluwayemisi Oluwole at FM Global Foundation for their technical advice on the validation part of this work.

References

[1] T. Beer, The interaction of wind and fire, Boundary-Layer Meteorol. 54 (February 1 1991) 287–308.

[2] B. Porterie, D. Morvan, J.C. Loraud, M. Larini, Firespread through fuel beds: modeling of wind-aided fires and induced hydrodynamics, Phys. Fluids 12 (2000) 1762–1782.

[3] M. Li, C. Wang, Z. Li, S. Yang, K. Fukumoto, C. Fan, Combustion and flame spreading characteristics of diesel fuel with forced air flows, Fuel 216 (2018) 390–397.

[4] L. Orloff, J. De Ris, G. Markstein, Upward turbulent fire spread and burning of fuel surface, Symposium (International) on Combustion, 1975, pp. 183–192.

[5] J. Quintiere, M. Harkleroad, Y. Hasemi, Wall flames and implications for upward flame spread, Combust. Sci. Technol. 48 (1986) 191–222.

[6] A.V. Singh, M.J. Gollner, Experimental methodology for estimation of local heat fluxes and burning rates in steady laminar boundary layer diffusion flames, J. Visual. Exp. JoVE (112) (2016).

[7] J.-L. Consalvi, Y. Pizzo, B. Porterie, Numerical analysis of the heating process in upward flame spread over thick PMMA slabs, Fire Saf. J. 43 (2008) 351–362.

[8] W. Xie, P.E. DesJardin, An embedded upward flame spread model using 2D direct numerical simulations, Combust. Flame 156 (2009) 522–530.

[9] H. Baum, K.B. McGrattan, R.G. Rehm, Simulation of smoke plumes from large pool fires, Symposium (International) on Combustion, 1994, pp. 1463–1469.

[10] C. Wang, J. Wen, Z. Chen, Simulation of large-scale LNG pool fires using FireFoam, Combust. Sci. Technol. 186 (2014) 1632–1649.

[11] Z. Chen, J. Wen, B. Xu, S. Dembele, Extension of the eddy dissipation concept and smoke point soot model to the LES frame for fire simulations, Fire Saf. J. 64 (2014) 12–26.

[12] K. Fukumoto, C. Wang, J. Wen, Large eddy simulation of upward flame spread on PMMA walls with a fully coupled fluid–solid approach, Combust. Flame 190 (2018) 365–387 2018/04/01.

[13] T. Hattori, S.E. Norris, M.P. Kirkpatrick, S.W. Armfield, Simulation and analysis of puffing instability in the near field of pure thermal planar plumes, Int. J. Therm. Sci. 69 (2013) 1–13 2013/07/01.

[14] O. Tlili, H. Mhiri, P. Bournot, Airflow induced by a room fire: effect of roof shape and source location, Int. J. Therm. Sci. 90 (2015) 135–149 4.

[15] B. Zhou, A. Sobiesiak, P. Quan, Flame behavior and flame-induced flow in a closed rectangular duct with a 90° bend, Int. J. Therm. Sci. 45 (2006) 457–474 2006/05/01.

[16] F. Tang, L.J. Li, K.J. Zhu, Z.W. Qiu, C.F. Tao, Experimental study and global correlation on burning rates and flame tilt characteristics of acetone pool fires under cross air flow, Int. J. Heat Mass Transf. 87 (2015) 369–375 8.

[17] L. Hu, L. Wu, S. Liu, Flame length elongation behavior of medium hydrocarbon pool fires in cross air flow, Fuel 111 (2013) 613–620.

[18] P.H. Thomas, The size of flames of natural fires, Presented at the Proceedings of the Combustion Institute 9, 1963.

[19] L. Hu, A review of physics and correlations of pool fire behaviour in wind and future challenges, Fire Saf. J. 91 (2017) 41–55 2017/07/01.

[20] F. Tang, L. Li, Q. Wang, Q. Shi, Effect of cross-wind on near-wall buoyant turbulent diffusion flame length and tilt, Fuel 186 (12/15/2016) 350–357.

[21] R.M. Nelson, B.W. Butler, D.R. Weise, Entrainment regimes and flame characteristics of wildland fires, Int. J. Wildland Fire 21 (2012) 127–140.

[22] T. Hirano, M. Kinoshita, Gas velocity and temperature profiles of a diffusion flame stabilized in the stream over liquid fuel, Symposium (International) on Combustion, vol. 15, 1975, pp. 379–387 1975/01/01.

[23] E.P. Volchkov, V.I. Terekhov, V.V. Terekhov, Flow structure and heat and mass transfer in boundary layers with injection of chemically reacting substances (review), Combust. Explos. Shock Waves 40 (2004) 1–16 2004/01/01.

[24] J. Fang, C. Jiang, J.-w. Wang, J.-f. Guan, Y.-m. Zhang, J.-j. Wang, Oscillation frequency of buoyant diffusion flame in cross-wind, Fuel 184 (11/15/2016) 856–863.

[25] E. Lois, J. Swithenbank, Fire hazards in oil tank arrays in a wind, Symposium (International) on Combustion, 1979, pp. 1087–1098.

[26] R. Lautkaski, Validation of flame drag correlations with data from large pool fires, J. Loss Prev. Process. Ind. 5 (1992) 175–180.

[27] K. Satoh, N. Liu, X. Xie, K. Zhou, H.-C. Chen, J. Wu, et al., CFD study of huge oil depot fires-generation of fire merging and fire whirl in (7 x 7) arrayed oil tanks, Fire Saf. Sci. 10 (2011) 693–705.

[28] J.A. Woods, B.A. Fleck, L.W. Kostiuk, Effects of transverse air flow on burning rates of rectangular methanol pool fires, Combust. Flame 146 (2006) 379–390.

[29] T. Zhou, H. Li, Q. Chen, R. Wei, J. Wang, Understanding sidewall constraint involving ventilation effects on temperature distribution of fire-induced thermal flow under a tunnel ceiling, Int. J. Therm. Sci. 129 (2018) 290–300.

[30] S. Gannouni, J. Zinoubi, R.B. Maad, Numerical study on the thermal buoyant flow stratification in tunnel fires with longitudinal imposed airflow: effect of an upstream blockage, Int. J. Therm. Sci. 136 (2019) 230–242.

[31] J. Gould, W. McCaw, N. Cheney, Project Vesta. Fire in Dry Eucalypt Forest: Fuel Structure, Fuel Dynamics and Fire Behaviour. Ensis-CSIRO, Canberra, Australia and WA Department of Environment and Conservation, Perth, Australia, (2007).

[32] H. Wang, Ember attack: its role in the destruction of houses during ACT bushfire in 2003, Life in A Fire-Prone Environment: Translating Science into Practice, Proceedings of Bushfire Conference, Griffith University, Brisbane, Australia, 2006.

[33] Y. He, K. Kwok, G. Douglas, I. Razali, Numerical investigation of bushfire-wind interaction and its impact on building structure, Fire Saf. Sci. 10 (2011) 1449–1462.

[34] C.J. Greenshields, Openfoam User Guide vol. 3, OpenFOAM Foundation Ltd, version, 2015.

[35] Y. Wang, P. Chatterjee, J.L. de Ris, Large eddy simulation of fire plumes, Proc. Combust. Inst. 33 (2011) 2473–2480.

[36] Y.P. Almeida, P.L.C. Lage, L.F.L.R. Silva, Large eddy simulation of a turbulent diffusion flame including thermal radiation heat transfer, Appl. Therm. Eng. 81 (2015) 412–425 2015/04/25.

[37] C.A. Sedano, O.D. Paz, A. Ladino, F. Muoz, Prediction of a small-scale pool fire with FireFoam, Int. J. Chem. Eng. 2017 (2017) 12.

[38] C.J. Wang, J.X. Wen, Z.B. Chen, S. Dembele, Predicting radiative characteristics of hydrogen and hydrogen/methane jet fires using FireFOAM, Int. J. Hydrogen Energy 39 (12/3/2014) 20560–20569.

[39] A. Yoshizawa, Statistical theory for compressible turbulent shear flows, with the application to subgrid modeling, Phys. Fluid. 29 (1986) 2152–2164.

[40] B.F. Magnussen, The eddy dissipation concept—a bridge between science and technology, ECCOMAS Thematic Conference on Computational Combustion, 2005, pp. 21–24.

[41] R. Viskanta, Overview of some radiative transfer issues in simulation of unwanted fires, Int. J. Therm. Sci. 47 (2008) 1563–1570 2008/12/01.

[42] S. Vilfayeau, Large Eddy Simulation of Fire Extinction Phenomena, University of Maryland, College Park, 2015.

[43] J. Chai, P. Rath, Discrete-ordinates and Finite-Volume Methods for Radiation Heat Transfer, (2006).

[44] B.J. McCaffrey, Purely Buoyant Diffusion Flames: some Experimental Results vol. NBSIR 79-1910, (1979).

[45] D. Spalding, A single formula for the "law of the wall", J. Appl. Mech. 28 (1961) 455–458.

[46] Y. Tominaga, A. Mochida, R. Yoshie, H. Kataoka, T. Nozu, M. Yoshikawa, et al., AIJ guidelines for practical applications of CFD to pedestrian wind environment around buildings, J. Wind Eng. Ind. Aerod. 96 (2008) 1749–1761.

[47] F. Mathey, D. Cokljat, J.P. Bertoglio, E. Sergent, Assessment of the vortex method for large eddy simulation inlet conditions, Prog. Comput. Fluid Dynam. Int. J. 6 (2006) 58–67.

[48] S.M. Ali, V. Raghavan, S. Tiwari, A study of steady laminar diffusion flame over methanol pool surface, Int. J. Heat Mass Transf. 53 (2010) 4696–4706.

[49] W. Tang, C.H. Miller, M.J. Gollner, Local flame attachment and heat fluxes in wind-

driven line fires, Proc. Combust. Inst. 36 (2017) 3253–3261 2017/01/01.

[50] F. Plourde, M.V. Pham, S.D. Kim, S. Balachandar, Direct numerical simulations of a rapidly expanding thermal plume: structure and entrainment interaction, J. Fluid Mech. 604 (2008) 99–123.

[51] K. Kwok, Y. He, G. Douglas, Bushfire-enhanced wind load on structures, Proceedings of the Institution of Civil Engineers-Engineering and Computational Mechanics, vol. 165, 2012, pp. 253–263.

[52] Y. Lin, X. Zhang, L. Hu, An experimental study and analysis on maximum horizontal extents of buoyant turbulent diffusion flames subject to relative strong cross flows, Fuel 234 (2018) 508–515.

[53] R.J. Margason, Fifty years of jet in cross flow research, AGARD-CP, vol. 534, 1993 Paper 1.

[54] G. Heskestad, Fire plumes, flame height and air entrainment, in: M.J. Hurley (Ed.), SFPE Handbook of Fire Protection Engineering, Springer., New York, 2016.

[55] K. Kwok, Y. He, G. Douglas, Bushfire-enhanced wind load on structures, Proceedings of the Institution of Civil Engineers - Engineering and Computational Mechanics, vol. 165, 2012, pp. 253–263.

[56] L. Hu, X. Zhang, M.A. Delichatsios, L. Wu, C. Kuang, Pool fire flame base drag behavior with cross flow in a sub-atmospheric pressure, Proc. Combust. Inst. 36 (2017) 3105–3112 2017/01/01.

[57] F. Tang, Q. He, J. Wen, Effects of crosswind and burner aspect ratio on flame characteristics and flame base drag length of diffusion flames, Combust. Flame 200 (2019) 265–275 2019/02/01.

[58] J. Welker, C. Sliepcevich, Bending of wind-blown flames from liquid pools, Fire Technol. 2 (1966) 127–135.

Appendix A2

Esmaeel Eftekharian, Maryam Ghodrat, Yaping He, Robert H. Ong, Kenny C. S. Kwok, Ming Zhao. **Numerical analysis of wind velocity effects on fire-wind enhancement.** *International Journal of Heat and Fluid Flow.* 2019; Vol 80, Article No, 108471. *https://doi.org/10.1016/j.ijheatfluidflow.2019.108471.*

International Journal of Heat and Fluid Flow 80 (2019) 108471

Contents lists available at ScienceDirect

International Journal of Heat and Fluid Flow

journal homepage: www.elsevier.com/locate/ijhff

Numerical analysis of wind velocity effects on fire-wind enhancement

Esmaeel Eftekharian[a,*], Maryam Ghodrat[a], Yaping He[a], Robert H. Ong[b], Kenny C.S. Kwok[b], Ming Zhao[a]

[a] *Center for Infrastructure Engineering, School of Computing Engineering and Mathematics, Western Sydney University, Penrith, NSW 2751, Australia*
[b] *School of Civil Engineering, The University of Sydney, NSW, Australia*

ARTICLE INFO

Keywords:
Fire-induced forces
Fire-wind enhancement
Wind velocity distortion
Wind effects
Buoyant plume

ABSTRACT

Variation in flow characteristics triggered through the fire-wind interface can potentially damage the buildings during bushfires. Fire-wind enhancement which is referred to as the increase of wind velocity, caused by the fire-wind interaction, is one of the destructive phenomena in this regard. In spite of the significance, the underlying mechanism contributing to this phenomenon is still not well understood. This study employs computational fluid dynamic (CFD) simulation to fundamentally investigate the effects of free-stream wind velocity on fire-wind enhancement through analyzing the momentum and buoyancy of fluid. Fire-wind interaction is shown to cause the generation of fire-induced longitudinal negative pressure gradient which results in fire-induced pressure and viscous forces in longitudinal direction. These forces are further found as the prime reason for the distortion of the wind velocity profile. A module is implemented to the FireFOAM solver to calculate and extract these forces quantitatively. The results reveal that under a constant fire intensity, the level of distortion and/or enhancement in the wind velocity profile comparatively reduces with the increase of free-stream wind velocity. A new non-dimensional group (modified Euler number) is introduced to take into account dominant fire-induced forces causing fire-wind enhancement. Richardson number and the modified Euler number are employed to determine the influence of free-stream wind velocity and longitudinal distance from the fire source on wind velocity enhancement. Large-eddy simulation (LES) results indicate that while the level of enhancement generally depends on both Richardson and the modified Euler number, the location of the maximum level of enhancement along the plume centreline coincides with the maximum value of modified Euler number under a constant free-stream wind velocity scenario.

1. Introduction

Understanding the interaction between fire and wind has always been a significant challenge (Scesa and Sauer, 1954; Scesa, 2019, 1957). Several studies have been devoted to the burning behavior of pool fires in wind condition and the effects of wind on flame features (Hu et al., 2011; Tang et al., 2015; Hu et al., 2013; Thomas, 1963; Kwok et al., 2010; Yeoh and Yuen, 2009; Meroney, 2011; Hirano and Kinoshita, 1975). However, the studies investigating the changes in flow aerodynamics caused by the interaction of wind and fire are very limited. Hirano and Kinoshita (1975) studied the interaction of fire and wind and revealed that the wind velocity profile is deformed immediately after the fire source and the interaction of free-stream velocity and buoyant diffusion flame led to an increase in velocity close to the flame zone. Entrainment regimes and flame characteristics of wildland fires were studied by Nelson et al. (2012). Their research revealed that buoyancy and convection-controlled regimes for line source of fire can be divided into three categories based on the convection number that is defined as the ratio of fire buoyancy force to the free-stream wind momentum force. This number can be used to determine the extent to which flow regime is buoyant or wind dominant. They also presented a correlation between plume tilt angle and the convection number. Detailed analysis by Volchkov et al. (2004) and the experimental results of Hirano and Kanno (1973) indicate the association of thermal expansion with low-density value in the flame zone accountable for deformation of the free-stream velocity profile.

Wind has been observed to increase the burning rate of pool fires (Tang et al., 2015). A correlation was developed in Tang et al. (2015) to describe the burning behavior of pool fire within a specific range of cross-wind and it was shown that with the increase of the cross-air flow speed, the enhancement rate of the mass burning rate (The difference between mass burning rate in wind and still condition divided by the cross-wind velocity) was higher for smaller pool fires.

A numerical model was used by Ali et al. (2010) to investigate the

---

[*] Corresponding author.
E-mail address: e.eftekharian@westernsydney.edu.au (E. Eftekharian).

https://doi.org/10.1016/j.ijheatfluidflow.2019.108471
Received 29 October 2018; Received in revised form 31 July 2019; Accepted 15 September 2019
0142-727X/

Nomenclature

a	acceleration
D	fuel bed characteristic length (0.3 m)
D_c	diffusion coefficient
Eu	Euler number
Eu_x	modified local Euler number
f_p	fire-induced pressure force per unit volume
f_v	fire-induced viscous force per unit volume
f_T	fire-induced total force per unit volume
F_p	pressure force
F_v	viscous force
F_T	total force
g	gravitational acceleration (9.81 m/s^2)
h	specific enthalpy per unit volume
LE	level of enhancement
n	frequency
p	static pressure
Q	heat release rate
$\dot{q}'''$	fuel heat release rate per unit volume
$\dot{q}_r''$	radiation heat transfer
R	gas constant
Ri	Richardson number
S_{uu}	Power spectrum density
T	temperature
u	velocity
U	longitudinal velocity
U_f	maximum velocity of the bulge in the wind velocity profile
U_w	Free-stream wind velocity in the same elevation where maximum velocity of the bulge happens.
W	Fire source width
X, Y, Z	coordinates of computational domain
x	Downstream longitudinal distance from the fire source ($x = X\text{-}D/2$)
X^*	normalised longitudinal distance (X/D)
Y_m	mass fraction of mixture
Y^*	normalized spanwise distance (Y/D)
$\forall$	volume
Z^*	normalized vertical distance (Z/D)

Symbols

−	spatial filtering
−	Favre filtering
→	vector variable
< >	Mean (time-averaged)

Subscripts

ref	reference value
res	resolved
∞	free-stream
t	turbulent
N	normalized
p	pressure
T	total
sgs	sub grid scale
v	viscous

Greek

α	terrain coefficient
α_{th}	thermal diffusivity
β	thermal expansion coefficient
γ	tilt angle
δ	Kronecker delta
Δ	grid spacing
ϵ	Dissipation rate of turbulent kinetic energy
η_k	Kolmogorov length scale
ν	kinematic viscosity
ρ	density
σ	stress
Φ	viscous shear stress tensor
ω	mass rate of production of species

influence of free-stream air velocity on the burning behavior of pool fires. After a 2-D numerical model was validated with experimental data of Hirano and Kinoshita (1975), Ali et al. (2010) focused on fuel mass burning rate, flame stand-off distance, temperature and flow fields behind the fire source. In their study, the flame stand-off distance was considered as a distance from the pool surface to the flame zone center where the temperature has the highest value. Ali et al. (2010) results showed that with the increase in air velocity, the average fuel mass burning rate increases but the flame stand-off distance decreases. However, the flame stand-off distance and the velocity profile remain almost invariant once the free-stream velocity increases beyond a threshold.

In another study, the effects of fuel exit velocity and cross-flow variation on the radiant fraction of a high-momentum jet flame were investigated numerically (Lawal et al., 2010). The results indicated a good agreement with experimental measurement for the jet-to-cross-flow momentum flux ratio of 100 to 800. Majeski et al. (2004) developed a theoretical method to relate the length of the flame to the diameter and velocity of the jet as well as cross-flow velocity.

Most recently, analytical studies for flow acceleration and velocity showed that buoyancy force has a significant effect on the flow acceleration of cross-wind (Fang et al., 2016).

Bushfire-wind enhancement phenomenon is one of the most destructive consequences of bushfire attacks. It is well understood that bushfires can be regarded as energy sources which inject thermal energy into the atmosphere and wind can increase bushfire spread rate as well as influencing other flame characteristics (Gould et al., 2007). Field data analysis also indicates that the enhanced wind by bushfire can play a significant role in ember attack mechanism (Wang, 2006).

Application of Computational Fluid Dynamics (CFD) models has gained popularity due to the rapid advancement of numerical methods and computational power. For example, large-scale pool fires in the presence of wind have been modeled using computational fluid dynamics approach by many researchers (Vasanth et al., 2013, 2015, 2017; Sun et al., 2014; Sikanen and Hostikka, 2016; Wang et al., 2016).

The influence of bushfire on wind enhancement has been studied by Kwok et al., 2012) using CFD. The outcome of their studies indicated that bushfire significantly intensifies the wind velocity at the near-ground region and considerably escalates pressure load on buildings situated at a certain distance downstream of the bushfire front. Coanda effect was claimed to be responsible for the attachment of plume to the ground immediately downstream of bushfire front, while further downstream, buoyancy force is in control and ultimately lifts up the plume.

Recently, Eftekharian et al., 2019) performed large eddy simulation analysis to fundamentally investigate the enhancement of wind caused by fire-wind interaction. It was found that as a result of the interaction of wind with fire, a longitudinal negative pressure gradient is generated in the fire plume region which accelerates the wind and causes wind enhancement. They also revealed that enhancement of wind is intensified with the increase of fire heat release rate. In another study, Eftekharian et al., 2019) investigated the effects of terrain slope on the enhancement of wind by line source of fire and showed that while upslope terrain intensifies wind enhancement, the existence of downslope reduces the effects of fire-induced negative pressure gradient and causes mitigation of fire-wind enhancement effects.

A detailed survey of the existing literature reveals that how variation of free-stream wind velocity affects fire-wind enhancement still requires further study. This study aims to investigate the effects of free-stream wind velocity on fire-wind enhancement by conducting a systematic analysis. The objective of this study is, therefore, to investigate how the distortion in the wind velocity profile, caused by fire, is affected by the upstream wind velocity. For this purpose, the longitudinal forces generated due to the interaction of fire and wind are explicitly expressed in terms of fire-induced pressure and viscous forces.

2. Numerical modeling

2.1. Simulation method

In the current study, FireFOAM was employed to simulate a series of small-scale buoyant fire plumes with a heat release rate of 580 kW. The FireFOAM (Wang et al., 2011) code is developed based on OpenFOAM platform and applied to the CFD model. OpenFOAM is an object-oriented open-source code which employs the finite volume method to solve complex problems in fluid mechanics (Greenshields, 2019). The OpenFOAM platform permits users to add self-developed modules to the main code. Its applicability has been confirmed and validated by different experimental studies in fire engineering including methane diffusion flames (Wang et al., 2011; Almeida et al., 2015), heptane and turbulent pool fire (Wang et al., 2018) methanol pool fire (Maragkos et al., 2017; Chen et al., 2014) and real fire tests (Li et al., 2017). FireFOAM uses the LES (Large Eddy Simulation) scheme to solve Favre-filtered continuity, momentum, energy, state and species equations for compressible-flow (Wang et al., 2011; Wang et al., 2014):

$$\frac{\partial\bar{\rho}}{\partial t}+\frac{\partial(\bar{\rho}\tilde{u}_i)}{\partial x_i}=0 \tag{1}$$

$$\frac{\partial(\bar{\rho}\tilde{u}_i)}{\partial t}+\frac{\partial(\bar{\rho}\tilde{u}_i\tilde{u}_j)}{\partial x_j}=\frac{\partial}{\partial x_j}\left[\bar{\rho}(\nu+\nu_t)\left(\frac{\partial(\tilde{u}_i)}{\partial x_j}+\frac{\partial(\tilde{u}_j)}{\partial x_i}-\frac{2}{3}\frac{\partial\tilde{u}_k}{\partial x_k}\delta_{ij}\right)\right]-\frac{\partial\bar{p}}{\partial x_i}+\bar{\rho}g_i \tag{2}$$

$$\frac{\partial(\bar{\rho}\tilde{h})}{\partial t}+\frac{\partial(\bar{\rho}\tilde{u}_j\tilde{h})}{\partial x_j}=\frac{D\bar{p}}{Dt}+\frac{\partial}{\partial x_j}\left[\bar{\rho}\left(\alpha_{th}+\frac{\nu_t}{\mathrm{Pr}_t}\right)\left(\frac{\partial\tilde{h}}{\partial x_j}\right)\right]+\dot{q}'''-\nabla.\dot{q}_r'' \tag{3}$$

$$\frac{\partial\bar{\rho}\tilde{Y}_m}{\partial t}+\frac{\partial(\bar{\rho}\tilde{u}_j\tilde{Y}_m)}{\partial x_j}=\frac{\partial}{\partial x_j}\left[\bar{\rho}\left(D_c+\frac{\nu_t}{\mathrm{Pr}_t}\right)\frac{\partial(\tilde{Y}_m)}{\partial x_j}\right]+\omega_m \tag{4}$$

$$\bar{p}=\bar{\rho}R\tilde{T} \tag{5}$$

where the symbols "$-$" and "$\sim$" specifies spatial and Favre filtering. p, h, Y_m, g, ν, ν_t, D_c, R, Pr, δ, α_{th} and ω_m are static pressure, specific enthalpy, mass fraction of species m in the gas mixture, gravitational acceleration, laminar viscosity, turbulent viscosity, laminar diffusion coefficient, gas constant, Prandtl number, Kronecker delta, thermal diffusivity and reaction rate of species m due to gas reaction respectively. $\dot{q}'''$ is heat release rate per unit volume (W/m^3) from chemical reactions and $\dot{q}_r''$ is the total radiation emission intensity (W/m^2) of the gas mixture, $\nabla.$ is the divergence operator.

FireFOAM numerically solves Eqs. (1) – (5) to determine the flow prime variables. kEq model (Yoshizawa, 1986) was applied to treat subgrid scale turbulent structures. The combustion is controlled by the eddy dissipation concept (Magnussen, 2005) and the infinitely-fast chemical reactions are assumed. Finite volume discrete ordinates model (fvDOM) was employed to model radiation heat transfer. More details about the radiation models used in FireFOAM can be found in Vilfayeau (2015).

PIMPLE (combined PISO and SIMPLE) algorithm was used to couple velocity and pressure field. Adjustable time step approach was used to keep Courant-Friedrichs-Lewy (CFL) number below 0.6. As for the temporal discretization, the first order Euler was used. Central differences were used to discretize gradients and diffusive terms, while unbounded Linear-Upwind Stabilised Transport (LUST) scheme was used for the advective terms. Pre-conditioned Bi-Conjugate Gradient (PBiCG) algorithm was used to solve momentum, energy and species and SGS turbulent kinetic energy equations.

According to the momentum equation, the force imposed on the infinitesimal fluid parcel is equal to the fluid parcel mass multiplied by the acceleration. Generally:

$$\begin{aligned} d\vec{F} &= \vec{a}\,dm = \rho\vec{a}\,d\forall = \rho(\vec{a}_p+\vec{g}+\vec{a}_v)d\forall \\ &= \vec{f}_p\,d\forall + \vec{f}_g\,d\forall + \vec{f}_v\,d\forall = d\vec{F}_p + d\vec{F}_g + d\vec{F}_v \end{aligned} \tag{6}$$

where ρ is density, $\forall$ is volume, $\vec{a}$ is flow acceleration, $\vec{g}$ is gravitational acceleration and f is the force per unit volume.

The flow acceleration in the Eulerian system can be expressed as (based on momentum equation):

$$\vec{a}=\frac{D\vec{u}}{Dt}=\frac{-\nabla p}{\rho}+\vec{g}+\frac{\Phi}{\rho}=\vec{a}_p+\vec{g}+\vec{a}_v \tag{7}$$

where $\vec{u}$ is velocity vector, $\vec{g}$ is the gravitational acceleration vector, and Φ is the viscous shear stress vector $(\Phi_i)=\frac{\partial(\sigma_{ji})}{\partial x_j}$ in which σ_{ji} is the components of stress. The first, second and third terms on the right-hand side of Eq. (7) represents the accelerations due to the pressure gradient, gravity, and viscous forces, respectively. The three components are referred to as pressure acceleration, gravitational acceleration, and viscous acceleration respectively hereafter in this paper. Similarly, $\vec{f}_p$, $\vec{f}_g$ and $\vec{f}_v$ are referred to as fire-induced pressure force,

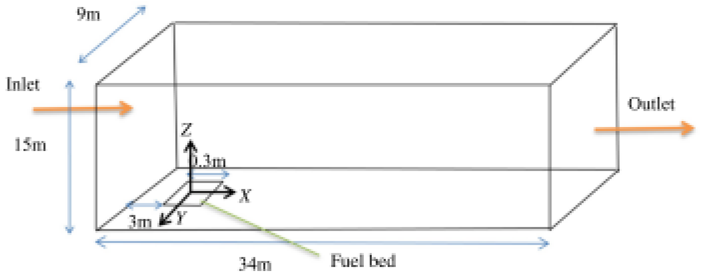

Fig. 1. Schematic views of the computational domain for the cross-wind and fire simulations.

gravitational force and fire-induced viscous force. The directional components of $\vec{f}$ and $\vec{a}$ are presented separately:

$$a_{Ti} = a_{pi} + g_i + a_{vi} \tag{8}$$

$$\vec{f}_{Ti} = \vec{f}_{pi} + \vec{f}_{gi} + \vec{f}_{vi} \tag{9}$$

where index $i = 1, 2, 3$ accounts for forces and acceleration in X, Y and Z directions. In the current discussion, the focus is on velocity, force, and acceleration in the longitudinal direction, i.e., $i = 1$.

A module has been developed and attached to the FireFOAM platform in the current study to generate individual output components of the total fire-induced forces and acceleration [Eq. (7)] at the end of each computational time step.

2.2. Geometrical model and simulation conditions

A computational domain with the dimension of 34 m, 9 m, and 15 m has been generated for simulation of cross-wind fire scenarios as shown in Fig. 1. A square burner with the dimension of 0.3 m was placed on the bottom surface 3 m downstream of the domain inlet.

Cross-wind was specified as the flow entering the domain at the inlet. See Fig. 1. Methane was selected as the fuel injected from the fire source to produce heat release rate (HRR) of 580 kW for different reference wind velocities (3, 4.5, 6, 7.5 and 9 m/s). A fixed fuel mass flow rate was suggested for the burner in all simulation scenarios to achieve a constant HRR of 580 kW. A summary of different simulation scenarios was shown in Table 1.

For simplicity, non-dimensional distances are introduced as $X^* = X/D$, $Y^* = Y/D$, and $Z^* = Z/D$, where X, Y, and Z are distances respectively in longitudinal, transverse (spanwise) and vertical directions and D is the fire source dimension ($D = 0.3$ m).

In the study of momentum and buoyancy flow interactions, Richardson number is used to characterize flow regimes as to whether it is a buoyancy or momentum dominant. Richardson number is the ratio of buoyancy and inertial forces (Boirlaud et al., 2012; Fuaad et al., 2016) and is used in fire-wind flow regimes (Tang et al., 2017):

$$\mathrm{Ri}_x = \frac{g\beta(\mathrm{T_f} - \mathrm{T_\infty})\mathrm{x}}{\mathrm{U_{ref}}^2} \tag{10}$$

where $\mathrm{Ri}_x$is the local Richardson number, g is gravitational acceleration, β is thermal expansion coefficient, T_f is the flame temperature, $T_\infty$is the ambient temperature, x is the downstream distance from the fire source ($x = X\text{-}D/2$) and U_{ref} is the ambient wind reference velocity.

Outflow and open boundary (total pressure) conditions were set for domain outlet on the right and the domain ceiling, respectively. Therefore, the flow can freely get in and out of the domain top surface. The slip and no-slip boundary condition were applied respectively to the domain sides and base. The adiabatic condition was assumed for the domain base. As for the initial condition for temperature, a constant temperature of 298 K was applied. A power law velocity profile was employed at the inlet on the left of the domain:

$$U(Z) = U_{ref}\left(\frac{Z}{Z_{ref}}\right)^{\alpha} \tag{11}$$

where, U_{ref} and Z_{ref} are the reference velocity and reference height (3 m) respectively, the value of power α depends on terrain category (here 0.16). In order to consider turbulent fluctuations in the domain inlet, the "2D vortex method" (Mathey et al., 2006) was utilized.

3. Validation and numerical settings

3.1. Validation

Two sets of experimental data have been used to validate the numerical model in the current study. The first validation is associated with the simulation of McCaffrey experiment (McCaffrey, 1979) which includes experimental data of buoyant diffusion flame in a still environment. In order to validate the numerical model utilized in this study, a simulation with constant HRR of 58 kW was carried out. The simulation results were then assessed against the numerical results of Wang et al. (2011) and experimental data of McCaffrey (1979). In their research, McCaffrey (1979) used a natural gas burner and measured the centreline of flow velocity for various heat release rates including 58 kW. Wang et al. (2011) used FireFOAM to simulate this experiment. They conducted a simulation of the 20 s burning time and showed that it takes 7 s of the simulated period for the buoyancy diffusion flame to reach a quasi-steady condition. They also gathered data and averaged them during the last 13 s of the analysis and compared with the experimental results. The same simulation and average time were employed in the present study. A schematic view of the computational domain used in the current study to simulate McCaffrey's experiment (McCaffrey, 1979) is presented in Fig. 2. In order to model the buoyancy diffusion flame experiment done by McCaffrey (1979), the domain size in the X direction is set at 3 m and the grid size of 0.019 m × 0.019 m × 0.03 m was utilized to maintain the smallest cell size similar to that suggested in Wang et al. (2011). The burner is simulated by a 0.3 × 0.3 m square placed at the center of the domain (Wang et al., 2011). It is assumed that the surface of the burner touches the base of the domain. The domain boundary conditions for the buoyant diffusion geometry are similar to those proposed by Wang et al. (2011).

Fig. 3 shows the velocity corresponds to fire plume centreline in a log-log coordinate, and compares with the results predicted in Wang et al. (2011) and measured in McCaffrey (1979).

Despite similarities in the geometrical model, boundary conditions and simulation time in the two studies, it was observed that MAE (mean absolute error) for the present study is 0.15, while this value is 0.17 for the and numerical results of Wang et al. (2011) which highlights a slightly better agreement of the current numerical results with the experimental data than the previous study (Wang et al., 2011). The reason might be the difference in the FireFOAM version used in the two studies. The current study uses FireFOAM solver based on OpenFOAM V.4.1 while OpenFOAM V.1.6 was used in Wang et al. (2011). The older versions of FireFOAM, utilized in Wang et al. (2011), employed the mixture fraction combustion model, whereas, the current version uses eddy dissipation combustion model.

The numerical model was further validated with the results of Hirano and Kinoshita's experiment (Hirano and Kinoshita, 1975), that involved a steady burning of a liquid-fuel methanol pool in a forced convective media. The combustion chamber where methanol-air diffusion flame was measured was 13.5 cm long and 3 cm × 9.8 cm in cross-section. The gas velocity and temperature profiles across the laminar boundary layer were measured in the chamber.

Fig. 4 presents a 2-D schematic diagram of Hirano and Kinoshita's experimental setup (Hirano and Kinoshita, 1975). The inlet uniform airflow was provided by a blower. The fuel pan was 8 cm long and 2.8 cm wide. The methanol fuel was fed into the pan from another vessel through gravity. A wire diameter thermocouple was used to measure the temperature profiles across the boundary layer. The local gaseous velocities have been measured and estimated by suspended magnesium oxide particles under a light beam and concave mirrors.

Table 1
Demonstration of different simulation scenarios.

Scenario ID (S#)	U_{ref} (m/s)	Ri_D
1	3	1.81
2	4.5	0.84
3	6	0.48
4	7.5	0.33
5	9	0.22

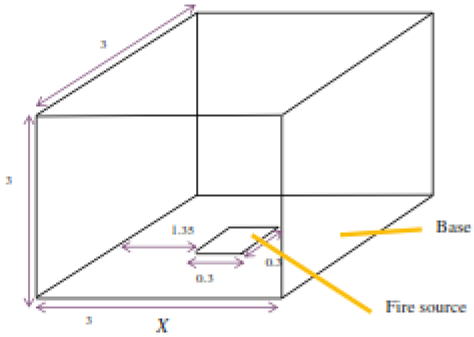

Fig. 2. Computational domain for validation of numerical results against experimental data presented by McCaffrey (1979). The dimensions are in meter.

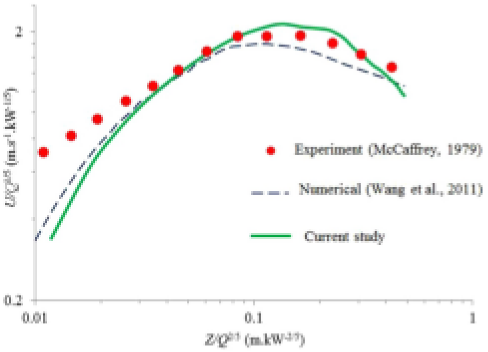

Fig. 3. Comparison of normalized centreline velocity profile of the current study with numerical (Wang et al., 2011) and experimental data (McCaffrey, 1979) available in the literature.

Considering symetry in the spanwise direction, a 2-D model was used in the current study to solve the governing equations [Eqs. (1)–(5)] in Cartesian coordinates. Ali et al., 2010) also used a 2-D approach to validate their numerical model with the experimental data of Hirano and Kinoshita (1975).

A 2-D rectangular dimensionally shown in Fig. 4 was used as a computational domain. In order to satisfy both the solution accuracy and computational cost, a uniform grid of approximately 550 × 400 cells in streamwise (x) and spanwise (y) directions was implemented.

At the inlet, a smooth and uniform fixed velocity of air was imposed, while the outflow boundary condition was suggested for the domain outlet. As for the initial condition, a constant temperature of 300 K was set. The no-slip velocity condition and the adiabatic condition were set at the top and bottom walls. Hirano and Kinoshita (1975) used thick quartz for the chamber sides which makes the assumption of adiabatic condition reasonable.

Fig. 5 shows both the measured and CFD results of downstream velocity profiles of the leading flame edge across the boundary layer over liquid methanol fuel with flame. This figure presents the distortion of the upstream velocity profile due to created flow enhancement and local pressure gradient (Hirano and Kinoshita, 1975).

Moreover, the aerodynamic structure of the region closer to the trailing flame edge indicating a shift in its shape change and the maximum velocity in this higher velocity region rises with downstream distance x (Hirano and Kinoshita, 1975).

Fig. 6 compares the temperature profiles of experimental data of Hirano and Kinoshita (1975) and the current CFD results downstream of the fire source.

3.2. Grid sensitivity analysis

A grid sensitivity analysis with three grid sizes of course, medium and fine was carried out for the simulation scenario #1. The grid sizes were defined as 360 k (50 × 80 × 90) for coarse, 2.4 million (127 × 149 × 130) for medium and 7 million (197 × 163 × 220) for fine. The non-uniform structured grid was used to generate smaller computational cells near the fire source so that the smallest cell takes the volume of 0.000013 m^3 (1.7 × 2.9 × 2.5 cm) for the medium case. Fig. 7 compares the normalized longitudinal velocity and density of simulation #1 for the three grid sizes at $X^* = 3$. There is negligible difference between the medium and fine grid for both velocity and density profiles. The average difference ratio of the corresponding velocity between fine and medium cases is 0.32% while this value for the medium and fine case is 7.24%. For the density parameter, the abovementioned values are 0.36% and 7.4%, respectively. Therefore, the medium grid size is chosen for this study.

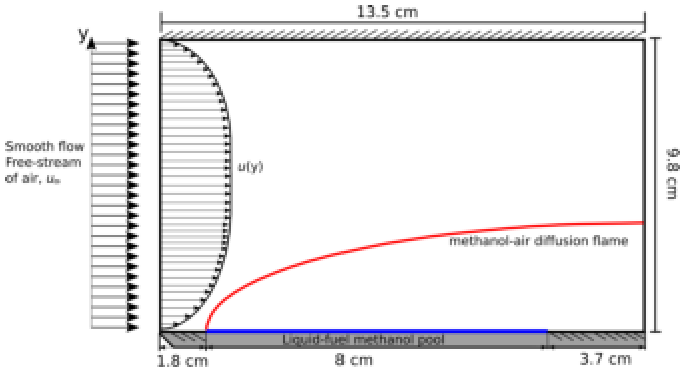

Fig. 4. 2-D schematic diagram of numerical validation of Hirano and Kinoshita's experiment (Hirano and Kinoshita, 1975).

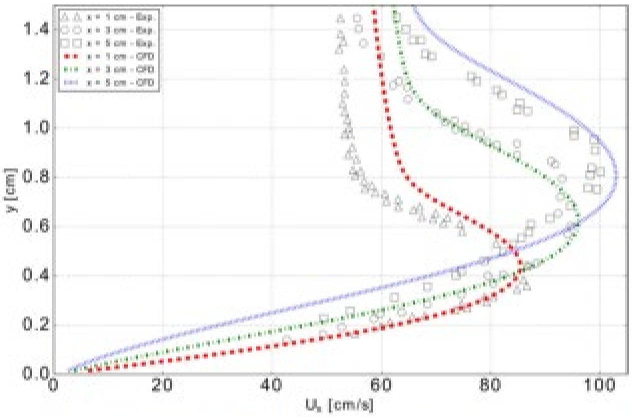

Fig. 5. Comparison between experiment (Hirano and Kinoshita, 1975) and CFD of the velocity profiles taken downstream the boundary layer of methanol-air diffusion flame, $u_\infty = 0.5$ m/s.

3.3. Details of LES analysis and uncertainties

In order to check if the chosen (i.e., the medium) grid is fine enough to appropriately resolve a high fraction of turbulent kinetic energy, it is necessary to define turbulent length scale and the corresponding wave number for the flow largest eddies, Kolmogorov length scale and the smallest eddies captured by the grid. The flow largest eddies are limited by the domain physical boundary (Vilfayeau, 2015), here we consider the fire bed width as the characteristic length (0.3 m). The corresponding wave number for the physical domain boundary length scale is 20.93 (m^{-1}). Kolmogorov length scale can be calculated by $\eta_k = (\frac{\nu^3}{\varepsilon})^{(1/4)}$ (Landahl et al., 1992). The Kolmogorov length scale and the corresponding wave number would be respectively 7×10^{-4} m and 8971.42 m^{-1}. The grid spacing is calculated based on the grid size in the plume region: $\Delta = (\Delta_x \Delta_y \Delta_z)^{(1/3)}$. The corresponding wave number for this grid spacing is 314 m^{-1}.

The credibility of LES model for a computational grid depends on the extent to which turbulent structures of large eddies is resolved. In other words, the grid spacing should be fine enough to resolve the dominant eddy structures in the model. The sizes of large eddies are determined based on integral of turbulent length scale. For buoyant diffusion of methane flame in a finite fire source, integral length scale can be approximated based on the fire source width. In Vilfayeau et al. (2016), it was shown that for buoyant diffusion of methane turbulent flame the results can be considered to be independent of the grid size for $\frac{W}{\Delta} > 12$, where W is the fire source width and Δ is the grid spacing. In our case, this ratio is 15 in the plume region for the chosen grid structure.

Another method to verify the functionality of the LES for a given computational model is to check if 80% of total turbulent kinetic energy is resolved by the chosen grid for the LES simulation (Pope and Pope, 2000). Fig. 8 presents the plots of the ratio of resolved turbulent kinetic energy (k_{res}) to the total turbulent kinetic energy ($k_{res} + k_{sgs}$), in which the latter is the summation of resolved turbulent kinetic energy (k_{res}) and sub-grid turbulent kinetic energy (k_{sgs}). Fig. 8 shows that within the plume region, at almost all distances downstream of the fire source, more than 70% of turbulent kinetic energy is resolved, except very close to the wall. This is because we used a wall function for near-

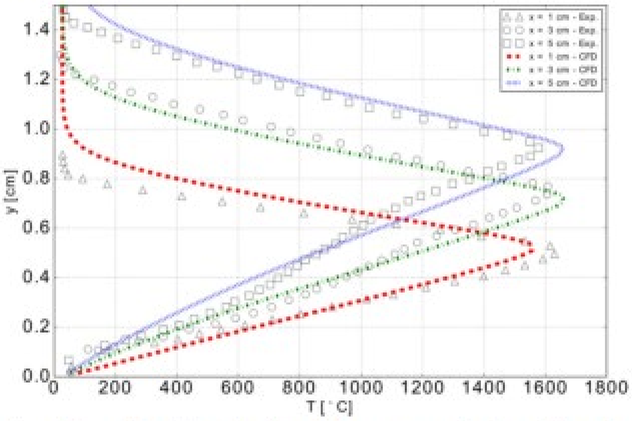

Fig. 6. Comparison between experiment (Hirano and Kinoshita, 1975) and CFD of the temperature profiles taken at different distances downstream the boundary layer of methanol-air diffusion flame, $u_\infty = 0.5$ m/s.

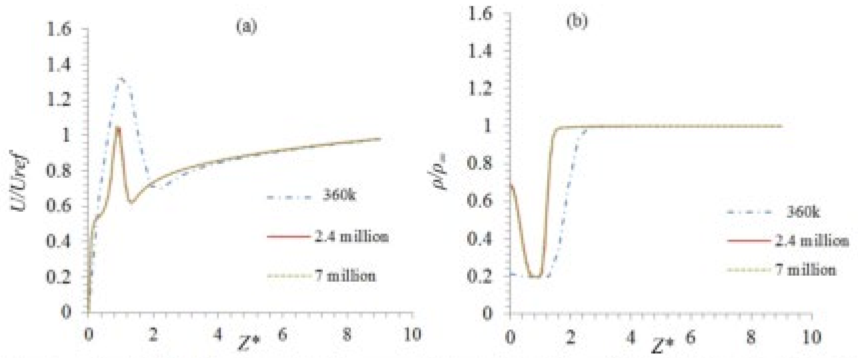

Fig. 7. Comparison of vertical distribution of normalized time-averaged (a) longitudinal velocity and (b) density at $X^* = 3$ for different grid sizes.

ground turbulent shear stresses. However, if one focuses on the plume region, the turbulent kinetic energy is satisfactorily (more than 90%) resolved. This trend is consistent with that reported in Vilfayeau et al. (2016).

Power spectra is another important flow characteristic in turbulent flows. Normalized power spectra density of the longitudinal velocity ($nS_{uu}/<U>^2$) along a horizontal line (Y^*, Z^*) = (0, 1.6) at upstream ($X^* = -7$) and downstream of the fire source ($X^* = 6$) are plotted in Fig. 9. Here n is the frequency, S_{uu} is the power spectra density. The power spectra and frequency plotted in Fig. 9 are normalized with the mean velocity (time-averaged velocity) ($<U>$) which is the mean velocity of the point where the data is collected. It is worth mentioning that the chosen point downstream of the fire source (6D, 0, 1.6D) falls within the plume region which is affected by fire. Fig. 9 shows that the chosen grid size is fine enough to capture the large eddy structures up to the normalized frequency of 10^{-2}. Fig. 9 also demonstrates the effects of fire on energy content of the spectrum. It is believed that fire increases the velocity fluctuations which lead to the increase of power spectra amplitude by almost two orders of magnitude as shown in Fig. 9. It should be noted that the first 115 s of the simulation time was considered as the transition period and the data were collected in the following 160 s for statistical analysis.

3.4. vortex method and turbulent intensity

Vortex method (Mathey et al., 2006) is shown to be an effective method for generating synthetic turbulent fluctuations at the inlet of the computational domain in LES simulations which can be found in the work of Xie et al. (2018), Montorfano et al. (2013) and Penttinen and Nilsson (2015).

In the current work, the turbulent intensity is about 11% at the inlet at the height of $Z^* = 10$. This, in turn, produces approximately 5% turbulent intensity at the target height location (1D upstream of the fire source).

4. Fire-wind interaction simulation results and discussion

The findings of this research are presented into two parts. The first part is a fundamental analysis of how fire-wind interaction leads to distortion of the wind velocity profile. Furthermore, the effect of wind velocity variation on velocity distortion downstream of the fire is explained. Simulation scenarios with different free-stream wind velocities were performed to investigate the issue. Table. 1 contains a summary of the considered simulation scenarios.

The second part of the research investigates how distortion in the wind velocity profile varies in different longitudinal distances downstream of the fire.

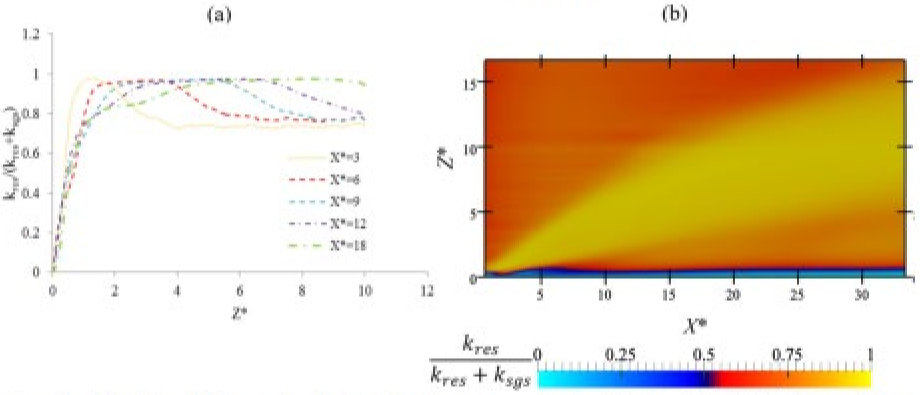

Fig. 8. Fraction of resolved turbulent kinetic energy $k_{res}/(k_{res}+k_{sgs})$ along domain center plane ($Y = 0$) for S#1. (a) vertical distribution at different distances downstream of the fire and (b) planar distribution.

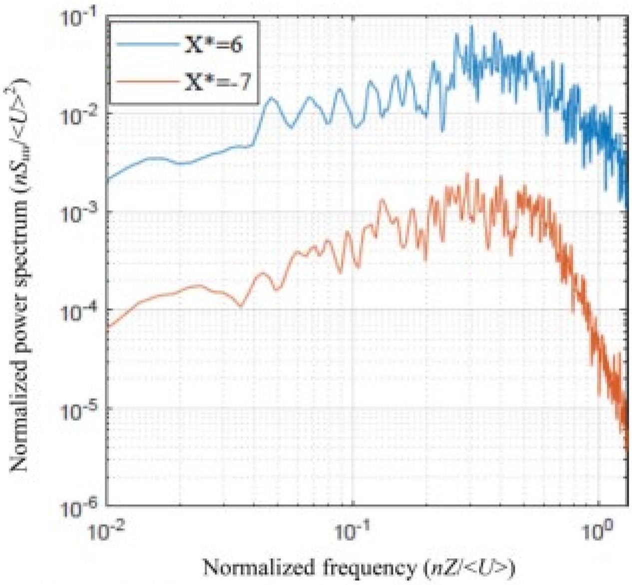

Fig. 9. Normalised power spectra density of longitudinal velocity on a horizontal line (Y^*, Z^*) = (0, 1.6) at $X^* = -7$ (upstream of the fire source) and $X^* = 6$ (downstream of the fire source within the plume region) for S#1.

All the presented results are based on the time averaging data in the quasi-steady condition.

4.1. The effects of fire-induced forces

A comparison between the normalized longitudinal velocities for different wind reference velocities (described in Table 1) at $X^* = -3$ and $X^* = 6$ are respectively shown in Fig. 10(a) and (b). Fig. 10(a) includes free-stream ($X^* = -3$) wind velocity profiles for different simulation scenarios. As observed in Fig. 10(a), normalized free-stream wind velocity profile for all simulation scenarios are almost identical and therefore, one of these profiles (S#1) is selected for comparison with the longitudinal velocity profile downstream of the fire, as shown in Fig. 10(b). Local Richardson number (Eq. (10)) has been calculated for all the simulation scenarios as shown in Fig. 10(b). The distance x at Eq. (10) is $x = X\text{-}D/2$. T_f in Eq. (10) is the maximum flame temperature at distance the x. Therefore, because of the absence of flame, $Ri = 0$ for all $x^* \leq -1$, or $X^* \leq -0.5$. Fig. 10(b) shows that longitudinal velocity is enhanced for the simulation scenarios with the higher Richardson number at the specified x distance. The effects of fire on wind velocity distortion can be vividly observed in Fig. 10(b). Fig. 10(b) shows that the longitudinal wind velocity decreases in the region very close to the ground before it is subjected to a significant enhancement. Wind velocity undergoes an enhancement in a comparatively thin region above the ground and then experiences a reduction, possessing a lower velocity than the condition where the fire is non-existent (the upstream velocity profile), as shown in Fig. 10(b). The wind velocity profile undergoes a distortion due to the presence of the fire. The distorted profile possesses a local peak whose magnitude and vertical location are seen to vary with the local Richardson number. Fig. 10(b) also demonstrates

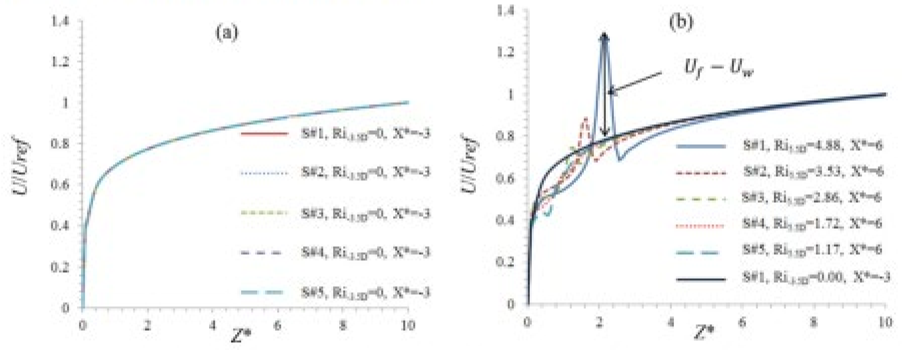

Fig. 10. Comparison of longitudinal time-averaged normalized velocity profiles at (a) $X^* = -3$ and (b) $X^* = 6$ for different simulation scenarios.

that the higher level of velocity enhancement happens in simulation scenarios with a higher Richardson number. The level of enhancement (*LE*) is defined as:

$$LE = \frac{U_f - U_w}{U_w} \tag{12}$$

where, U_f is the enhanced velocity at the specific height Z^* and U_w is the corresponding upstream wind velocity. Note that LE is a function of U_∞, Q, X^* and Z^*. $U_f - U_w$ for S#1 is shown in Fig. 10(b).

To explain the observed trend that lower wind velocities undergo a higher variation in the velocity profile subjected to the same fire intensity, it is necessary first to explain the mechanism through which wind is enhanced by fire. Comparison of Figs. 11(a) and (b) shows that wind enhancement happens within the plume region where density is comparatively low. This is because due to the effects of buoyancy and thermal expansion, a negative longitudinal pressure gradient is generated along the fire plume, accelerating the flow. Since the interaction between wind and fire causes the fire plume to be tilted towards the downstream direction (as shown in Fig. 11) a longitudinal component of the pressure gradient is generated, driving the flow in the longitudinal direction. The tilt angle, γ, is defined as the angle between the plume centreline and vertical axis. Plume region can be defined based on the density distribution (Eftekharian et al., 2019) which includes the area of the domain where the density is comparatively lower than the free-stream density ($\rho \le 0.5\rho_\infty$ according to Eftekharian et al. (2019)). Fig. 11 shows that although fire-induced pressure force is asymmetrical, density distribution shows almost a symmetrical trend. Thus, the plume axis can be defined as an axis passing the plume region centreline as shown in Fig. 11(b). This way, the angle between the plume axis and vertical direction can be considered as the plume tilt angle. This longitudinal force imposed on the flow due to the longitudinal fire-induced pressure gradient is referred to

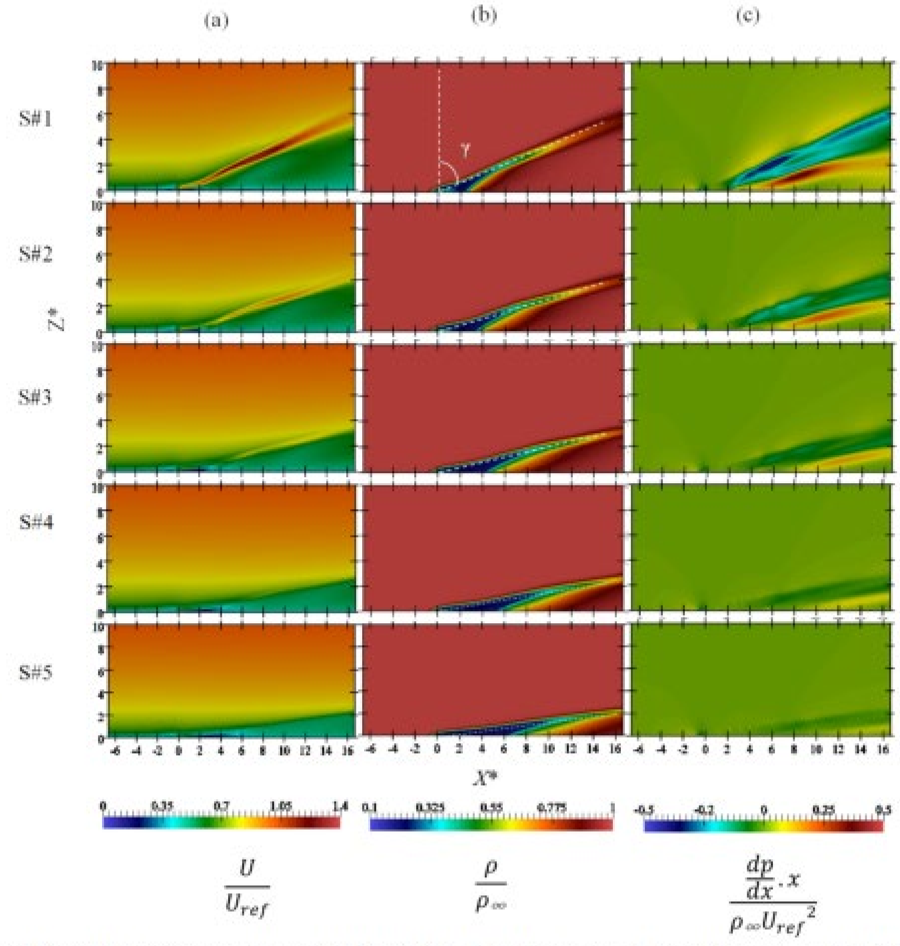

Fig. 11. Normalized distribution of time-averaged (a) longitudinal velocity (first column), (b) density (second column) and (c) pressure gradient (third column) for different simulation scenarios at $Y = 0$.Vertical and horizontal axis indicates normalized vertical and longitudinal distance. Plume tilt angle (γ) is the angle between the dash lines.

as "fire-induced longitudinal pressure force" in the rest discussion of this paper. In other words, as a result of the fire-wind interaction, flow accelerates within the plume region and causes an increase of flow momentum in the longitudinal direction that culminates in wind velocity enhancement, as shown in Figs. 11(a)–(c). Fire or a heat source induces the buoyancy force in the vertical direction only. Fire-induced force in the longitudinal direction is the ensemble effect of the rise of the fire plume and the deflection of it due to the wind. This component appears in the form of pressure and viscous force. The fire-induced pressure force happens due to the pressure gradient generated in the fire plume as shown in Fig. 11(c). The pressure gradient along the longitudinal direction accelerates the flow longitudinally. Based on Eq. (7), this longitudinal acceleration is also reciprocally proportional to flow density. Therefore, since in the plume region density is low and fire-induced pressure force is high, in all considered scenarios, the highest distortion in the velocity profile appears within the plume region.

Fig. 11 also depicts that immediately downstream of the fire source, the fire plume is attached to the ground due to the entrainment restriction which is a manifestation of Coanda effects. When the wind interacts with fire, the fire plume is tilted toward the ground surface and restricts flow entrainment in the near-ground region. Therefore, flow accelerates to balance the momentum transfer which eventually results in the plume attachment to the ground. However, in further downstream of the fire source where the buoyancy force becomes dominant, the flow starts to lift up from the ground and create a near-ground low-velocity region downstream of the fire source as observed in Fig. 11. This effect has been observed and reported in previous studies (Eftekharian et al., 2019, 2019; He et al., 2011; Hu et al., 2017).

Fig. 11 also illustrates that the plume tilt angle increases with the increase of upstream wind velocity profile. Fig. 11 shows that in contrast to the density distribution, the *U*-velocity and longitudinal pressure gradient distributions are not symmetrical about the plume axis. The main reason why *U*-velocity and longitudinal pressure gradient distributions are not symmetrical is because of unbalanced flow entrainment at each side of the plume axis caused by Coanda effects. In further downstream of the fire plume, flow velocity gradient on the down-side region of the plume axis is higher than that of its up-side region. Consequently, the flow is more inclined to be entrained and decelerated from down-side of the plume axis than the up-side, causing the asymmetrical distribution of longitudinal velocity and pressure gradient at each side of the plume axis. However, as density is a thermodynamic property of the flow and is less affected by the entrainment process, it preserves its symmetrical configuration about the plume axis.

Fig. 11 also shows that in contrast to the normalized density distribution which does not change significantly with the increase of inertia force (wind velocity), the normalized pressure gradient decreases with the increase of upstream wind momentum. Thus, wind velocity distortion decreases with the increase of wind velocity profile as shown in Fig. 10(b).

In order to quantify the variation of plume tilt angle with the increase of free-stream wind velocity, changes of tilt angle with free-stream wind velocity were plotted in Fig. 12. Fig. 12(a) and (b) show how plume tilt angle changes with variation of the incoming flow momentum. Fig. 12(a) demonstrates that as the incoming flow increases, Ri number which implies the ratio of vertical buoyancy force to the horizontal inertia force decreases; consequently tilt angle increases and plume axis becomes closer to ground as shown in Fig. 12(b). As enhancement of wind by fire happens in the fire plume region (Eftekharian et al., 2019), it is expected that wind enhancement in the scenarios with higher momentum happens in the relatively closer area to the ground as confirmed in Fig. 11(a). Fig. 12 shows that for the Ri $(D) \geq 0.5$, tilt angle almost linearly decreases with the increase of Ri number. This reduction in tilt angle is approximately equivalent to 3° for each 1 m/s reduction of free-stream wind velocity, under a constant fire intensity.

In fluid dynamics and wind engineering, pressure is conventionally normalized by dynamic pressure i.e. $(\frac{1}{2}\rho_\infty {U_{ref}}^2)$. Hence, here, the fire-induced pressure force $(\vec{f_p})$ in Eq. (9) can be normalized with dynamic pressure as below:

Normalized fire-induced pressure force (stress):

$$\left(\vec{f_p}\right)_N = \frac{\rho\vec{a}_p D}{\frac{1}{2}\rho_\infty {U_{ref}}^2} = \frac{-\frac{dp}{dx}D}{\frac{1}{2}\rho_\infty {U_{ref}}^2} \tag{13}$$

Similarly, other forces can be normalized by the same factor:

Normalized viscous force (stress):

$$\left(\vec{f_v}\right)_N = \frac{\rho\vec{a}_v D}{\frac{1}{2}\rho_\infty {U_{ref}}^2} \tag{14}$$

Normalized total force (stress):

$$\left(\vec{f_T}\right)_N = \frac{\rho\vec{a}_T D}{\frac{1}{2}\rho_\infty {U_{ref}}^2} \tag{15}$$

While Eq. (13) physically represents the extent to which the interaction of wind and fire can increase the incoming flow momentum, Eq. (14) shows how viscous forces can decelerate and counteract fire-wind enhancement. Eq. (15) takes into account the combined effects of fire-induced pressure and viscous forces.

Eq. (13) is highly similar to the Euler number which represents the ratio of pressure force to the inertia force (Batchelor, 2000):

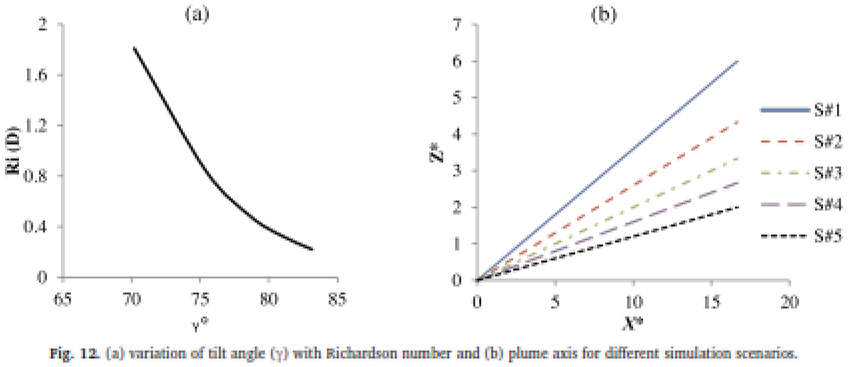

Fig. 12. (a) variation of tilt angle (γ) with Richardson number and (b) plume axis for different simulation scenarios.

$$Eu = \frac{\Delta P}{\rho U^2} \tag{16}$$

where ρ is fluid density, ΔP is the pressure difference and U is the characteristic velocity of the flow. Here instead of ΔP, we use $\frac{-dp}{dx}x$, where $\frac{-dp}{dx}$ takes into account the induced longitudinal pressure force due to the fire-wind interaction and x is the downstream distance from fire source:

$$Eu_x = \frac{\frac{-dp}{dx}x}{\rho_\infty U_{ref}^2} \tag{17}$$

where Eu_x is the modified local Euler number. The replacement of ΔP with $\frac{-dp}{dx}x$ is on the basis of dimension analysis and also an analogy

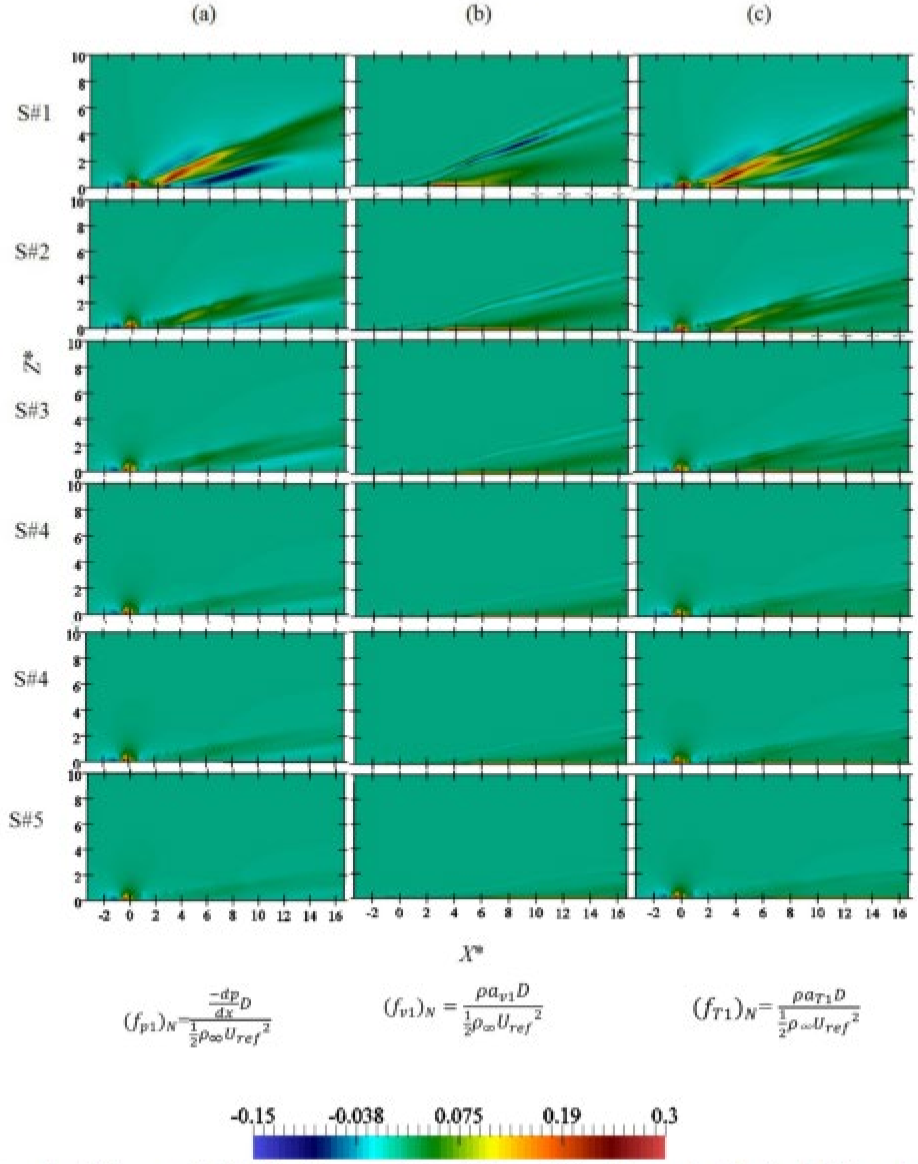

Fig. 13. Comparison of different normalized fire-induced time-averaged longitudinal forces, including (a) pressure force (first column), (b) viscous force (second column) and (c) total force (third column) in different simulation scenarios. Vertical and horizontal axis indicates normalized vertical and longitudinal distances.

between the Richardson number [Eq. (10)] and Euler number [Eq. (16)].

As shown in Fig. 11, longitudinal fire-induced pressure force in the form of Euler number plays a significant role in the enhancement of wind velocity. However, it should be noted that although buoyancy force applies in the vertical direction, it is prerequisite for generation of fire-induced pressure force. Therefore, indirectly, buoyancy force affects the longitudinal fire-wind enhancement phenomenon. In the following discussion of this study, it will be shown that fire-induced viscous forces play a minor role in wind enhancement phenomenon. Hence, the modified Euler number [Eq. (17)] and Richardson number [Eq. (10)] are incorporating all the important forces (buoyancy, fire-induced pressure, and wind inertia force) that contribute to the fire-wind enhancement phenomenon. It is then considered that modified Euler number and Richardson number are appropriate non-dimensional groups to study the mechanisms involved in fire-wind enhancement phenomenon.

The distribution contours of the longitudinal components of the normalized fire-induced pressure, viscous and total forces along the surface passing through the domain centreline ($Y = 0$, Fig. 1) for all simulation scenarios are plotted in Fig. 13.

Fig. 13 shows that fire-induced pressure forces are dominant within the plume region while fire-induced viscous forces prevail in near-ground (boundary layer) region. A comparison between Fig. 13(a, b) and (c) reveals that fire-induced pressure force is the dominant force which causes wind enhancement within the plume region.

Fig. 13(a) also indicates that the normalized fire-induced longitudinal pressure force decreases with the increase of free-stream wind velocity. It means that under constant fire intensity, the free-stream wind velocity is less influenced by the fire when the wind velocity increases, or Ri_D decreases. Under a constant fire intensity, fire-induced pressure force value does not change significantly with the increase of

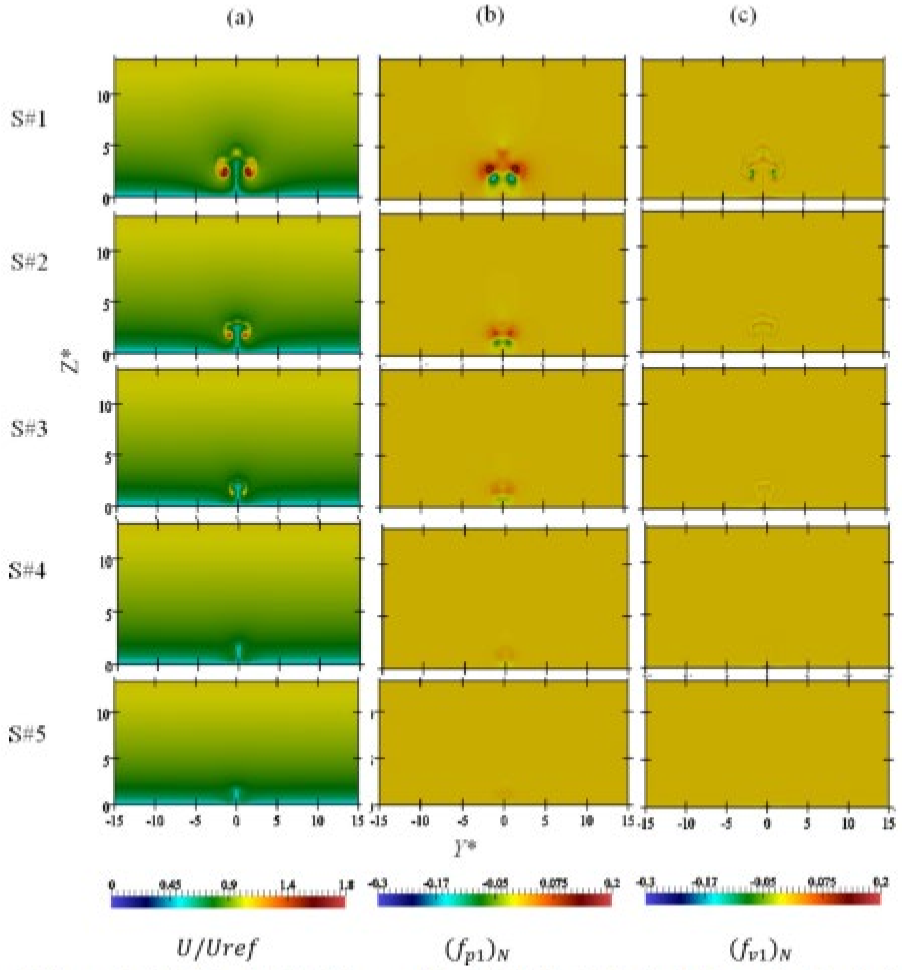

Fig. 14. normalized cross-sectional distribution of fire-induced time-averaged longitudinal (a) velocity (first column), (b) pressure force (second column) and (c) viscous force (third column) for different upstream wind velocities at $X^* = 12$. The vertical and horizontal axis indicates normalized vertical and spanwise distance.

upstream wind velocity. However, the flow momentum upstream of the fire source increases when wind velocity increases. Therefore, $(\vec{f_p})_N$, or the ratio of fire-induced pressure force to free-stream momentum force diminishes. Consequently, an upstream flow with higher momentum is less affected by the fire-induced pressure force.

As can be seen in Fig. 13(b), fire-induced viscous forces appear in two regions: in boundary layer region near the ground and within the plume region. It was shown that fire-induced pressure forces distort the velocity profile within the plume region. This distortion creates a velocity gradient in the flow field. According to the Eq. (2), this velocity gradient generates viscous forces within the plume region as shown in Fig. 13(b). Accordingly, fire-induced viscous forces within the plume region are indirectly generated due to fire-induced pressure forces. In other words, pressure force controls the generation of velocity enhancement, and velocity enhancement controls viscous force. Therefore, both normalized longitudinal fire-induced pressure and viscous forces follow the same trend of reduction when free-stream wind velocity increases.

Fig. 14 shows a cross-sectional view (at $X^* = 12$) of normalized longitudinal velocity, fire-induced pressure, and viscous forces for different simulation scenarios. For all simulation scenarios, longitudinal velocity enhancement distribution has a horse-saddle shape which is due to the counter-rotating vortices generated as a result of the interaction of longitudinal wind velocity and vertical buoyant plume. A similar trend can be seen in the previous studies (Eftekharian et al., 2019; Fric and Roshko, 1994; Margason, Apr. 1993). Moreover, Fig. 14

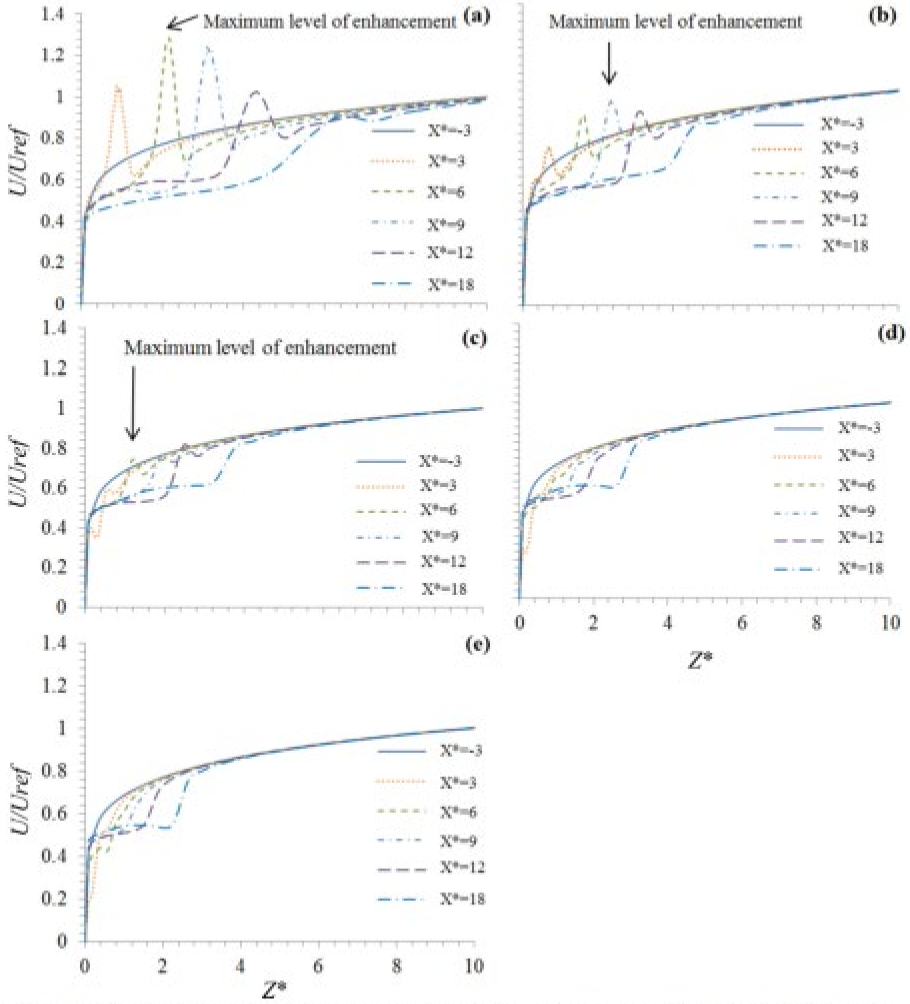

Fig. 15. Vertical distribution of normalized time-averaged longitudinal velocity in different distances downstream of the fire source for (a) simulation scenario #1 (U_{ref} = 3 m/s) and (b) simulation scenario #2 (U_{ref} = 4.5 m/s), (c) simulation scenario #3 (U_{ref} = 6 m/s), (d) simulation scenario #4 (U_{ref} = 7.5 m/s), (e) simulation scenario #5 (U_{ref} = 9 m/s). The arrows in the figure indicate the location corresponding to the maximum level of enhancement at each simulation scenario.

explicitly shows the role of fire-induced pressure force on the longitudinal wind enhancement which confirms the trend observed in Figs. 11 and 13. Fig. 14 also demonstrates that a negative fire-induced pressure force is generated just below the region of enhancement where positive fire-induced pressure force exists. This is due to the flow entrainment process which causes flow deceleration just below the fire plume.

Fig. 14 confirms the trend of fire-wind enhancement reduction with the increase in free-stream wind velocity, as observed in Fig. 11. As discussed earlier, this is because as wind velocity increases, the flow becomes more dominant by inertial force and the buoyant plume which causes the generation of fire-induced pressure forces does not play a significant role in forming the flow field. Therefore, as wind velocity increases under constant fire intensity, the corresponding Euler number becomes smaller and therefore the effective fire-induced pressure forces decreases and consequently, the level of wind enhancement reduces.

4.2. Longitudinal changes in longitudinal velocity profile

In Fig. 10, the variation in U profile is due to the variation in U_{ref}. In contrast, the variation in U profile in each plot of Fig. 15 is due to the variation in X, or in x. The results shown in Fig. 15 confirm the trend observed in Fig. 11. It is seen that longitudinal velocity in the region just above and below the plume is weakened in comparison to the free-stream profile at the same elevation. The amount of reduction seems proportional to U_{ref}, or reversely proportional to Ri_D. This is mainly because the flow entrainment process happens around the plume region and decelerates the flow surrounding the plume region. In other words, as shown in Figs. 11(c) and (b), flow entrainment around the plume region causes the generation of an adverse (positive) pressure gradient and decelerates the flow surrounding the plume region which eventually ends up to the reduction of longitudinal velocity in those regions. As can be observed in Figs. 11 and 15, in far enough vertical distance from the plume region (e.g., $Z^* \approx 10$) where the effects of entrainment disappear, wind velocity downstream of the fire source converges to the corresponding velocity at the upstream of fire source.

Variation of the level of enhancement for different wind reference velocities at different distances downstream of the fire source is plotted in Fig. 16. Fig. 16 confirms that the level of enhancement is highly affected by the upstream wind velocity and experiences a considerable reduction as free-stream wind velocity increases, as shown in Fig. 16. Fig. 16 also highlights that the level of enhancement also highly depends on the distance from the fire source, as depicted in Fig. 15. Fig. 16 indicates that for all simulation scenarios, the level of enhancement first increases longitudinally reaching a peak value and then undergoes a reduction further downstream of the fire source.

The corresponding Ri_x and Eu_x number for each simulation scenario at different distances downstream of the fire source are plotted in Fig. 17. Comparison of Fig. 17 with Fig. 15 shows that in each simulation scenario, the longitudinal distance corresponding to the maximum level of enhancement and maximum Eu_x number are the same, at about $X^* = 6$, $X^* = 9$, and $X^* = 6$ for simulation scenarios # 1, #2 and #3, respectively.

Fig. 17 also reveals that with the increase of free-stream wind velocity, both Ri_x and Eu_x number decreases for a given X^*, and consequently the level of enhancement decreases significantly. Fig. 17 also shows that with the increase of wind momentum, generally, the ratio of Eu_x number to Ri_x number reduces. For example, for free-stream wind velocity of 3 m/s, the graph corresponding to the Eu_x number is entirely above the Ri_x number and gradually with the increase of wind velocity, the graph related to Eu_x number falls behind that of Ri_x number and for reference velocity of 9 m/s, Eu_x number graph entirely falls behind the corresponding Ri_x number graph.

5. Conclusion

This study employed LES results to fundamentally investigate the mechanisms involved in fire-wind enhancement phenomenon, caused by the interaction between the fire-induced buoyancy flow and momentum wind flow. The effects of change in Richardson number due to variation in free-stream wind velocity on fire-wind enhancement were investigated for pool fire wind scenarios. A module was implemented to the Fire-FOAM solver to explicitly calculate the fire-induced force components under different free-stream wind velocity conditions. Below are the main conclusions of this study.

(1) It was shown that the interaction of wind and fire causes the generation of longitudinal fire-induced pressure and viscous forces. Longitudinal fire-induced pressure forces accelerate the flow and create distortion/enhancement in the velocity profile.
(2) LES results also indicated that with the increase of wind velocity, the normalized fire-induced pressure force decreases, resulting in a reduction in the level of wind enhancement.
(3) Richardson number and the modified Euler number were utilized in the analysis to predict the patterns for the level of enhancement at different distances from the fire in different free-stream wind velocity conditions. It was revealed that although the level of wind enhancement depends on both Richardson and the modified Euler number, the maximum level of enhancement in each simulation scenario (free-stream wind velocity) happens in the longitudinal location where the modified Euler number has the highest value.
(4) Plume tilt angle which represents the region of generation of fire-

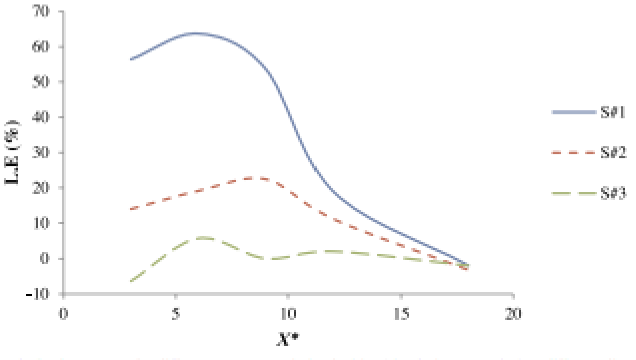

Fig. 16. Comparison of the level of enhancement for different upstream wind velocities (simulation scenarios) at different distances downstream of the fire.

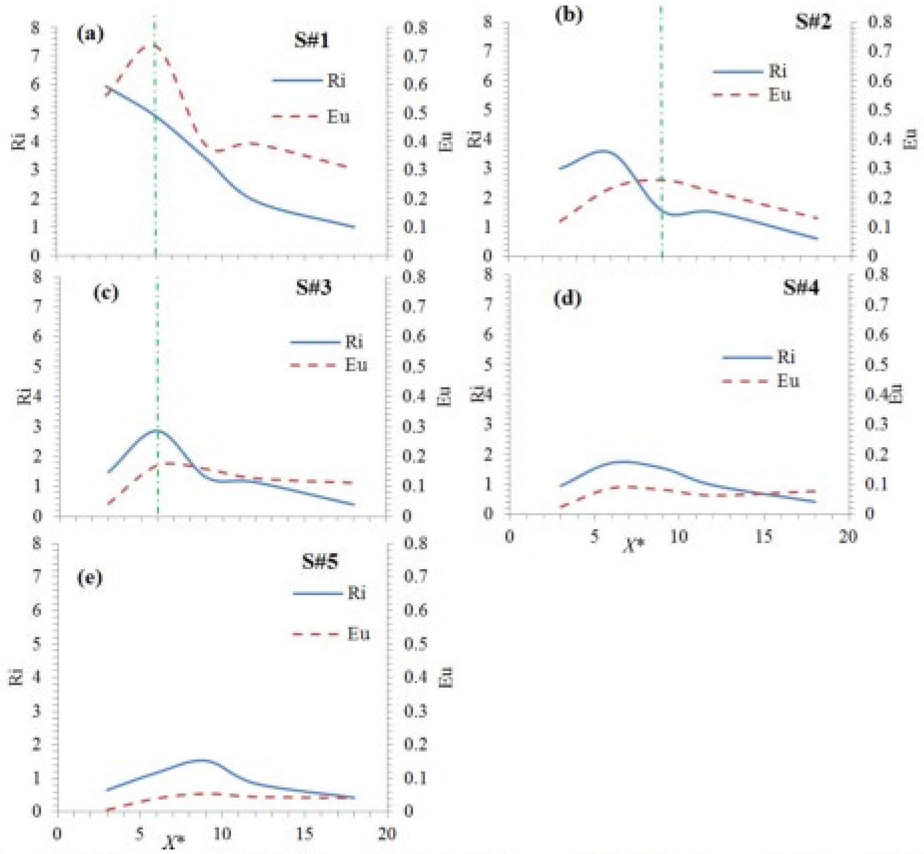

Fig. 17. Comparison of Ri_x and Eu_x number at different distances downstream of the fire source for different simulation scenarios. The green dash line is corresponding to the location at which maximum velocity enhancement happens in the specified scenario.

induced pressure force and wind enhancement was also investigated and it was shown that for the $\mathrm{Ri}(D) \geq 0.5$, an increase of 1 m/s of the incoming wind velocity corresponds to 3° increase in plume tilt angle under a constant fire intensity.

Acknowledgment

This project is funded by Australian Research Council grant ARC-DP160103248. The authors gratefully acknowledge OpenFOAM foundations for the provision of an open-source CFD platform.

References

Ali, S.M., Raghavan, V., Tiwari, S., 2010. A study of steady laminar diffusion flame over methanol pool surface. Int. J. Heat Mass Transfer 53 (21–22), 4696–4706. https://doi.org/10.1016/j.ijheatmasstransfer.2010.06.022.

Almeida, Y.P., Lage, P.L.C., Silva, L.F.L.R., 2015. Large eddy simulation of a turbulent diffusion flame including thermal radiation heat transfer. Appl. Therm. Eng. 81, 412–425. https://doi.org/10.1016/j.applthermaleng.2015.02.027.

Batchelor, G.K., 2000. An introduction to fluid dynamics. Cambridge University Press.

Boirlaud, M., Couton, D., Plourde, F., 2012. Direct numerical simulation of the turbulent wake behind a heated cylinder. Int. J. Heat Fluid Flow 38, 82–93. https://doi.org/10.1016/j.ijheatfluidflow.2012.09.005.

Chen, Z., Wen, J., Xu, B., Dembele, S., 2014. Large eddy simulation of a medium-scale methanol pool fire using the extended eddy dissipation concept. Int. J. Heat Mass Transfer 70, 389–408. https://doi.org/10.1016/j.ijheatmasstransfer.2013.11.010.

Eftekharian, E., Ghodrat, M., He, Y., Ong, R.H., Kwok, K.C.S., Zhao, M., Samali, B., 2019. Investigation of terrain slope effects on wind enhancement by a line source fire. Case Stud. Therm. Eng. 14 (September), 100467. https://doi.org/10.1016/j.csite.2019.100467.

Eftekharian, E., He, Y., Kwok, K.C.S., Ong, R.H., Yuan, J., 2019. Investigation of fire-driven cross-wind velocity enhancement. Int. J. Therm. Sci. 141 (July), 84–95. https://doi.org/10.1016/j.ijthermalsci.2019.03.033.

Fang, J., Jiang, C., Wang, J.-w., Guan, J.-f., Zhang, Y.-m., Wang, J.-j., 2016. Oscillation frequency of buoyant diffusion flame in cross-wind. Fuel 184 (December), 856–863. https://doi.org/10.1016/j.fuel.2016.07.084.

Fric, T.F., Roshko, A., 1994. Vortical structure in the wake of a transverse jet. J. Fluid Mech. 279, 1–47. https://doi.org/10.1017/S0022112094003800.

Fuaad, P.A., Baig, M.F., Khan, B.A., 2016. Turbulent drag reduction using active control of buoyancy forces. Int. J. Heat Fluid Flow 61, 585–598. https://doi.org/10.1016/j.ijheatfluidflow.2016.07.003.

Gould, J., McCaw, W., Cheney, N., Vesta, Project, 2007. Fire in Dry Eucalypt Forest: Fuel Structure, Fuel Dynamics and Fire Behaviour. Ensis-CSIRO, Canberra, Australia and WA Department of Environment and Conservation.

Greenshields, C.J., 2019. Openfoam User Guide. OpenFOAM Foundation Ltd [Online] Available. https://www.openfoam.com/documentation/user-guide Accessed July. 3, 2019.

He, Y., Kwok, K., Douglas, G., Razali, I., 2011. Numerical investigation of bushfire-wind interaction and its impact on building structure. In: Fire Safety Science: Proceedings of the Tenth International Symposium. 10. pp. 1449–1462. https://doi.org/10.3801/iafss.fss.10-1449.

Hirano, T., Kanno, Y., 1973. Aerodynamic and thermal structures of the laminarboundary layer over a flat plate with a diffusion flame. Symp. (Int.) Combust. 14 (1), 391–398. https://doi.org/10.1016/S0082-0784(73)80038-4.

Hirano, T., Kinoshita, M., 1975. Gas velocity and temperature profiles of a diffusion flame stabilized in the stream over liquid fuel. Symp. (Int.) Combust. 15 (January(1)), 379–387. https://doi.org/10.1016/S0082-0784(75)80312-2.

Hu, L., Liu, S., Xu, Y., Li, D., 2011. A wind tunnel experimental study on burning rate enhancement behavior of gasoline pool fires by cross air flow. Combust. Flame 158 (3), 586–591. https://doi.org/10.1016/j.combustflame.2010.10.013.

Hu, L., Wu, L., Liu, S., 2013. Flame length elongation behavior of medium hydrocarbon pool fires in cross air flow. Fuel 111 (September), 613–620. https://doi.org/10.1016/j.fuel.2013.03.025.

Hu, L., Zhang, X., Delichatsios, M.A., Wu, L., Kuang, C., 2017. Pool fire flame base drag behavior with cross flow in a sub-atmospheric pressure. Proc. Combust. Inst. 36 (2)), 3105–3112. https://doi.org/10.1016/j.proci.2016.06.139.

Kwok, K., He, Y., Douglas, G., 2012. Bushfire-enhanced wind load on structures. Proc. Inst. Civil Eng.-Eng. Comput. Mech. 165 (4), 253–263. https://doi.org/10.1680/eacm.11.00022.

Kwok, K.C., He, Y., Douglas, G.B., 2010. Wind impacts on fire spread and structural failure during bushfire in complex terrain. In: Proceedings of 9th United Kingdom Conference on Wind Engineering, Sep. 20-22.

Landahl, M.T., Landahl, M., Mollo-Christensen, E., 1992. Turbulence and Random Processes in Fluid Mechanics. Cambridge University Press.

Lawal, M., Fairweather, M., Ingham, D., Ma, L., Pourkashanian, M., Williams, A., 2010. Numerical study of emission characteristics of a jet flame in cross-flow. Combust. Sci. Technol. 182 (10), 1491–1510. https://doi.org/10.1080/00102202.2010.496379.

Li, Y.Z., Huang, C., Anderson, J., Svensson, R., Ingason, H., Husted, B., Runefors, M., Wahlqvist, J., 2017. Verification, validation and evaluation of FireFOAM as a tool for performance design. Lund University Rep 3208.

Magnussen, B.F., 2005. The eddy dissipation concept—a bridge between science and technology. In: ECCOMAS Thematic Conference on Computational Combustion. Lisbon, Portugal. June 21-24.

Majeski, A.J., Wilson, D.J., Kostiuk, L.W., 2004. Predicting the length of low-momentum jet diffusion flames in crossflow. Combust. Sci. Technol. 176 (12), 2001–2025. https://doi.org/10.1080/00102200490514769.

Maragkos, G., Beji, T., Merci, B., 2017. Advances in modelling in CFD simulations of turbulent gaseous pool fires. Combust. Flame 181 (July), 22–38. https://doi.org/10.1016/j.combustflame.2017.03.012.

Margason, R.J., Apr. 1993. Fifty years of jet in cross flow research. In: Proceedings of the AGARD Symposium on Computational and Experimental Assessment of Jets in Cross Flow. Winchester, UK. AGARD-CP-534.

Mathey, F., Cokljat, D., Bertoglio, J.P., Sergent, E., 2006. Assessment of the vortex method for large eddy simulation inlet conditions. Prog. Comput. Fluid Dyn. 6 (1–3), 58–67. https://doi.org/10.1504/PCFD.2006.009483.

McCaffrey, B.J., 1979. Purely buoyant diffusion flames: aSome experimental results. Center for Fire Research National Engineering Laboratory National Bureau of Standards NBSIR 79-1910.

Meroney, R.N., 2011. Wind effects on atria fires. J. Wind Eng. Ind. Aerodyn. 99 (4), 443–447. https://doi.org/10.1016/j.jweia.2010.11.003.

Montorfano, A., Piscaglia, F., Ferrari, G., 2013. Inlet boundary conditions for incompressible LES: a comparative study. Math. Comput. Model 57 (7), 1640–1647. https://doi.org/10.1016/j.mcm.2011.10.077.

Nelson, R.M., Butler, B.W., Weise, D.R., 2012. Entrainment regimes and flame characteristics of wildland fires. Int. J Wildland Fire 21 (2), 127–140. https://doi.org/10.1071/WF10034.

Penttinen, O., Nilsson, H., 2015. A fully synthetic turbulent boundary condition with a homogeneous vortex distribution. Comput. Phys. Commun. 190, 23–32. https://doi.org/10.1016/j.cpc.2015.01.002.

Pope, S.B., Pope, S.B., 2000. Turbulent flows. Cambridge University Press.

Scesa, S., 1957. Transfer of Heat By Forced Convection from a Line Combustion Source–The Influence of Atmospheric Stability and Surface Roughness. Forest service, Washington DC.

Scesa, S., 2019. Transfer of Heat By Forced Convection from a Line Combustion Source. U.S. Department of Agriculture, National Agricultural Library Available. https://archive.org/details/CAT31365328/page/n1 Accessed: July. 17, 2019.

Scesa, S., Sauer, F., 1954. Possible Effects of Free Convection on Fire Behavior-Laminar and Turbulent Line and Point Sources of Heat. Possible Effects of Free Convection on Fire Behavior-Laminar and Turbulent Line and Point Sources of Heat 12 US Department of Agriculture, Forest Service, California Forest and Range Experiment Station, Berkeley, CA Tech. Pap. 12.

Sikanen, T., Hostikka, S., 2016. Modeling and simulation of liquid pool fires with in-depth radiation absorption and heat transfer. Fire Saf. J. 80 (February), 95–109.

Sun, B., Guo, K., Pareek, V.K., 2014. Computational fluid dynamics simulation of LNG pool fire radiation for hazard analysis. J. Loss Prev. Process Ind. 29 (May), 92–102. https://doi.org/10.1016/j.jlp.2014.02.003.

Tang, F., Li, L.J., Zhu, K.J., Qiu, Z.W., Tao, C.F., 2015. Experimental study and global correlation on burning rates and flame tilt characteristics of acetone pool fires under cross air flow. Int. J. Heat Mass Transfer 87 (August), 369–375. https://doi.org/10.1016/j.ijheatmasstransfer.2015.04.019.

Tang, W., Miller, C.H., Gollner, M.J., 2017. Local flame attachment and heat fluxes in wind-driven line fires. Proc. Combust. Inst. 36 (2), 3253–3261. https://doi.org/10.1016/j.proci.2016.06.064.

Thomas, P.H., 1963. The size of flames from natural fires. Symp. (Int.) Combust. 9 (January(1)), 844–859. https://doi.org/10.1016/S0082-0784(63)80091-0.

Vasanth, S., Tauseef, S.M., Abbasi, T., Abbasi, S.A., 2013. Assessment of four turbulence models in simulation of large-scale pool fires in the presence of wind using computational fluid dynamics (CFD). J. Loss Prev. Process Ind. 26 (November (6)), 1071–1084. https://doi.org/10.1016/j.jlp.2013.04.001.

Vasanth, S., Tauseef, S.M., Abbasi, T., Abbasi, S.A., 2015. CFD simulation of pool fires situated at differing elevation. Process Saf. Environ. Protect. 94 (March), 89–95. https://doi.org/10.1016/j.psep.2015.01.001.

Vasanth, S., Tauseef, S.M., Abbasi, T., Abbasi, S.A., 2017. Simulation of multiple pool fires involving two different fuels. J. Loss Prev. Process Ind. 48 (July), 289–296. https://doi.org/10.1016/j.jlp.2017.04.031.

Vilfayeau, S., 2015. Large eddy simulation of fire extinction phenomena. University of Maryland.

Vilfayeau, S., White, J.P., Sunderland, P.B., Marshall, A.W., Trouvé, A., 2016. Large eddy simulation of flame extinction in a turbulent line fire exposed to air-nitrogen co-flow. Fire Saf. J. 86, 16–31. https://doi.org/10.1016/j.firesaf.2016.09.003.

Volchkov, E., Terekhov, V., Terekhov, V., 2004. Flow structure and heat and mass transfer in boundary layers with injection of chemically reacting substances. Combust. Explosion Shock Waves 40 (1), 1–16. https://doi.org/10.1023/b:cesw.0000013663.27112.ab.

Wang, C.J., Liu, H.R., Wen, J.X., 2018. An improved PaSR-based soot model for turbulent fires. Appl. Therm. Eng. 129, 1435–1446. https://doi.org/10.1016/j.applthermaleng.2017.10.129.

Wang, C.J., Wen, J.X., Chen, Z.B., Dembele, S., 2014. Predicting radiative characteristics of hydrogen and hydrogen/methane jet fires using FireFOAM. Int. J. Hydrogen Energy 39 (March(35)), 20560–20569. https://doi.org/10.1016/j.ijhydene.2014.04.062.

Wang, H., 2006. Ember attack: its role in the destruction of houses during ACT bushfire. In: 2003," Life in A Fire-Prone Environment: Translating Science into Practice, Proceedings of Bushfire Conference. Brisbane, Australia. Griffith University [Online]. Available: http://www.griffith.edu.au/conference/.

Wang, Y., Chatterjee, P., de Ris, J.L., 2011. Large eddy simulation of fire plumes. Proc. Combust. Inst. 33 (2), 2473–2480. https://doi.org/10.1016/j.proci.2010.07.031.

Wang, Y.F., Sun, X.F., Liu, S., Yan, P.N., Qin, T., Zhang, B., 2016. Simulation of back-layering length in tunnel fire with vertical shafts. Appl. Therm. Eng. 109, 344–350. https://doi.org/10.1016/j.applthermaleng.2016.08.081.

Xie, B., Gao, F., Boudet, J., Shao, L., Lu, L., 2018. Improved vortex method for large-eddy simulation inflow generation. Comput. Fluids 168, 87–100. https://doi.org/10.1016/j.compfluid.2018.03.069.

Yeoh, G.-H., Yuen, K.K., 2009. Computational Fluid Dynamics in Fire Engineering: Theory, Modelling and Practice. Butterworth-Heinemann.

Yoshizawa, A., 1986. Statistical theory for compressible turbulent shear flows, with the application to subgrid modeling. Phys. Fluids 29 (7), 2152–2164. https://doi.org/10.1063/1.865552.

Appendix A3

Esmaeel Eftekharian, Maryam Ghodrat , Yaping He, Robert H. Ong, Kenny C. S. Kwok, Ming Zhao **Numerical analysis of the effect of fire source configuration on fire-wind enhancement ,** *Heat Transfer Engineering.* 2019, Volume 42, pages 1-20 issue 1 https://doi.org/10.1080/01457632.2019.1685249

Taylor & Francis

Heat Transfer Engineering

ISSN: 0145-7632 (Print) 1521-0537 (Online) Journal homepage: https://www.tandfonline.com/loi/uhte20

Numerical Analysis of the Effect of Fire Source Configuration on Fire-Wind Enhancement

Esmaeel Eftekharian, Maryam Ghodrat, Yaping He, Robert H. Ong, Kenny C. S. Kwok & Ming Zhao

To cite this article: Esmaeel Eftekharian, Maryam Ghodrat, Yaping He, Robert H. Ong, Kenny C. S. Kwok & Ming Zhao (2019): Numerical Analysis of the Effect of Fire Source Configuration on Fire-Wind Enhancement, Heat Transfer Engineering, DOI: 10.1080/01457632.2019.1685249

To link to this article: https://doi.org/10.1080/01457632.2019.1685249

[redacted]

[redacted]

[redacted]

[redacted]

[redacted]

[redacted]

[redacted]

[redacted]

[redacted]

[redacted]

[redacted]

[redacted]

[redacted]

[redacted]

[redacted]

[redacted]

[redacted]

[redacted]

[redacted]

[redacted]

Appendix A4

Esmaeel Eftekharian, Maryam Ghodrat, Yaping He, Robert H. Ong, Kenny C. S. Kwok, Ming Zhao, **Correlations for fire-wind enhancement flow characteristics based on LES simulations,** *International Journal of Heat and Fluid Flow.* 2020; Volume 82, Article No: 108558. https://doi.org/10.1016/j.ijheatfluidflow.2020.108558.

International Journal of Heat and Fluid Flow 82 (2020) 108558

Contents lists available at ScienceDirect

International Journal of Heat and Fluid Flow

journal homepage: www.elsevier.com/locate/ijhff

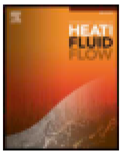

Correlations for fire-wind enhancement flow characteristics based on LES simulations

Esmaeel Eftekharian[a,*], Maryam Ghodrat[b], Yaping He[a], Robert H. Ong[c], Kenny C.S. Kwok[c], Ming Zhao[a]

[a] Center for Infrastructure Engineering, School of Computing Engineering and Mathematics, Western Sydney University, Penrith, NSW, 2751, Australia
[b] University of New South Wales Canberra, Canberra, 2610, ACT, Australia
[c] School of Civil Engineering, The University of Sydney, NSW, 2006, Australia

ARTICLE INFO

Keywords:
Fire-wind enhancement
Fire intensity
Wind velocity
Correlation
LES

ABSTRACT

Unraveling the physics of fire-wind interaction has long been a subject of interest. Among all the physics involved, enhancement of wind by fire deserves great attention due to its potential effects on building structures downstream of the fire source in bushfire attack events. Predominantly, two contributing factors determine the extent to which wind is enhanced by fire: freestream wind velocity and fire intensity. This study employs Large-Eddy Simulation (LES) to fundamentally investigate the combined effects of freestream wind velocity and fire intensity on fire-wind enhancement. An added module was implemented to an open-source transient fire solver in order to analyze the effects of freestream wind velocity and fire intensity based on the analysis of interactions between momentum and fire-induced buoyancy forces. Simulations are performed for parametric combinations of wind velocity and fire intensity. The LES results demonstrate that the normalized maximum wind enhancement increases with a reduction of freestream wind velocity and an increase in fire intensity. The non-dimensional Froude number, Fr, and normalized fire intensity, I^*, were employed to quantify the effects of freestream wind velocity and fire intensity, respectively. A correlation was developed to determine the maximum wind enhancement as a function of Fr and I^*. The location corresponding to maximum wind enhancement occurs further downstream of the fire source as freestream wind velocity or fire intensity increases. A correlation based on the Fr number and I^* was developed for the location at which maximum wind enhancement occurs. Furthermore, the concept of wind enhancement plume line was defined as a line along which the local wind enhancement occurs at a given longitudinal location downstream of the fire source, for which a correlation was also developed. Moreover, a gradual decaying trend is observed in wind enhancement after reaching a peak along the wind enhancement plume line in all simulation scenarios for which a correlation was also developed as a function normalized longitudinal direction.

1. Introduction

Wind-driven fires are complex phenomena as a result of various compound processes. On the other hand, the understanding of wildland fire is of great importance to lessen the risk of bushfire attacks and to increase our capability to predict their behaviour (Hu, 2017). A detailed understanding of the dominant feature and the behaviour of wind-driven fire assists us to better manage fire-induced changes in flow aerodynamics which plays a pivotal role in measuring potential fire threats.

Theoretical investigation offers a decent comprehension of buoyant diffusion flames from axisymmetric, line and pool fire sources in no-wind condition (Quintiere and Grove, 1998). However, the knowledge behind wind-blown diffusion flames requires more robust theoretical framework combining the semi-empirical flame-geometry correlations attained from the broad number of wind tunnel data (Thomas, 1963; Thomas et al., 1963; Nelson Jr and Adkins; 1986; Lin et al., 2019; Wang et al., 2019; Zhang et al., 2016; Sun et al., 2019; Tang et al., 2017; Lin et al., 2018; Lam and Weckman, 2015; Hu et al., 2017; Tang et al., 2015; Hu et al., 2017).

The comprehensive numerical models (Morvan and Dupuy, 2001; Morvan and Dupuy, 2004; Zhou et al., 2005; Mell et al., 2013; Aboje et al., 2017; Nmira et al., 2010; Ali et al., 2010) can be helpful to enhance the knowledge behind the mechanisms that are accountable

---

[*] Corresponding author.
E-mail address: e.eftekharian@westernsydney.edu.au (E. Eftekharian).

https://doi.org/10.1016/j.ijheatfluidflow.2020.108558
Received 4 October 2019; Received in revised form 3 February 2020; Accepted 4 February 2020

Nomenclature

a	acceleration (m/s^2)
a'	non-dimensional coefficient in Eq. (18)
a_p	acceleration due to pressure force (m/s^2)
a_v	acceleration due to viscous force (m/s^2)
b'	non-dimensional power constant in Eq. (18)
c_p	specific heat (kJ/kgK)
c'	non-dimensional power constant in Eq. (18)
C_k	sub-grid scale coefficient
C_ϵ	sub-grid scale coefficient
C_{EDC}	time scale coefficient
C_{diff}	molecular diffusion coefficient in Eddy Dissipation Model
CFD	computational fluid dynamics
d'	constant coefficient in Eq. (23)
D	fuel bed depth (m)
D_c	diffusion coefficient (m^2/s)
exp	exponential function
E_r	unit energy release rate of the fire (kW)
F	force (N)
Fr	Froude number
f	force per unit volume (N/m^3)
f^*	Function defined in Eq. (22)
g	gravitational acceleration (9.81 m/s^2)
g'	constant coefficient in Eq. (23)
h	total enthalpy (kJ/m^3)
H_{f0}	constant coefficient in Eq. (23)
H_f	flame height in presence of wind (m)
H_{f0}	flame height in absence of wind (m)
I	fire intensity (MW/m)
I^*	normalised fire intensity defined in Eq. (19)
k_{res}	resolved turbulent kinetic energy (m^2/s^2)
k_{sgs}	sub-grid scale turbulent kinetic energy (m^2/s^2)
LES	large eddy simulation
m	mass (kg)
m'	constant coefficient in Eq. (25)
$\dot{m}''^*$	non-dimensional burning intensity defined in Eq. (2)
$\dot{m}''$	burning rate per unit area (kg/m^2)
n'	constant coefficient in Eq. (25)
p	static pressure (Pa)
p_d	dynamic pressure of the ambient wind (Pa)
Pr$_t$	turbulent Prandtl number
$\dot{q}_r''$	radiant heat flux (W/m^2)
$\dot{q}'''$	heat release rate per unit volume (W/m^3)
R	gas constant (J/kgK)
r^2	Pearson correlation coefficient
r'	coefficient defined in Eq. (28)
S#	scenario number
s'	constant coefficient in Eq. (25)
T	temperature (K)
t	time (s)
t'	constant in Eq. (28)
U	velocity (m/s)
U^*_{enh}	normalized wind enhancement
U_{t_max}	maximum enhanced wind velocity (global value) (m/s)
$U^*_{t\_max}$	normalized quantity of U_{t_max}
$U^*_{max\_l}$	normalized maximum wind enhancement (local value)
U_p	wind enhancement plume line velocity (m/s)
U^*_p	normalized wind enhancement plume line velocity
u_f	fuel injection velocity (m/s)
$\forall$	volume (m^3)
X, Y, Z	coordinates of computational domain (m)
X^*	normalized X position
$X^*_{t\_max}$	normalized location corresponding to the maximum wind enhancement
x_i	coordinate in i direction
Z^*_m	coordinate in j direction
Y_m	mass fraction of species m
Z^*	normalized Z position
Z^*_m	Z^*corresponding to $U^*_{max\_l}$

Greek symbols

α	terrain coefficient
α_T	thermal diffusion coefficient (m^2/s)
δ	Kronecker delta
ρ	density (kg/m^3)
σ	stress (Pa)
ν	kinematic viscosity (m^2/s)
Φ	viscous stress tensor (kg/m^{2}s^2)
ω_m	mass rate of production of species (kg/m^{3}s)

Subscripts

1, 2, 3	correspond to X, Y and Z direction respectively
ref	reference value
pred	predicted by the presented correlation
∞	freestream
g	gravitational
i, j, k	direction or component indices
P	pressure
t	turbulent
T	total
v	viscous

Superscripts

*	normalized
—	spatial filtering
→	vector variable
~	Favre filtering

for the fire-wind interaction and the geometric properties of the flame but these models are highly computationally demanding which make them less attractive particularly for estimating large fire characteristics. Some simplified models have been proposed by other researchers (Margerit and Séro-Guillaume, 2002; Balbi et al., 2007; Koo et al., 2005) in this regard. These models commonly need input parameters, which depend on fire profile itself such as the flame length and tilt angle. The value of these input parameters is generally identified from experimental measurements (Koo et al., 2005; Weise et al., 2016) and outputs of these models help to deliver detailed insight into fire behaviour. These physics-based models have the potential to be used as a substitute method to regulate and generalize experimental model parameters.

In spite of the abundance of simplified models/correlations for flame geometry, the literature lacks model development for flame flow characteristics. This study aims at filling the knowledge gap in this regard by presenting correlations for flow velocity affected by fire-wind interaction. The appropriate non-dimensional groups (Froude number and non-dimensional fire intensity) reflecting the contributing forces in fire-wind interaction scenarios are employed to develop these correlations. Bushfire-wind enhancement is one of the implications of the current study in which the wind enhancement by bushfire causes increase of pressure coefficient around the buildings, damaging building structures downstream of the bushfire source.

2. Fire-wind interaction

The spread rate of wildland fire escalates with growth in wind speed, which clarifies the great importance of wind-blown flames in the bushfire. Laboratory-scale (Nelson Jr and Adkins, 1986; Mendes-Lopes et al., 2003) and field-scale (Butler et al., 2004; Gould et al., 2007) experiments showed that the fire spread rate was intensified with wind speed. It was also noted that even though the general behaviour of the fire spread observed was consistent, the scattered data measured in the experiment make it hard for the case to case comparison with the numerical modelling (Mendes-Lopes et al., 2003).

The pioneer studies by Thomas (1963) and Thomas et al., (1963) on the effect of wind on flame characteristics of finite burning surface area (natural fire) revealed that the dimensionless flame length is governed by the dimensionless burning intensity (or burning rate per unit area) and the modified Froude number as:

$$L_f^* = 70\dot{m}'^{*0.86}\mathrm{Fr}_D^{-0.11} \tag{1}$$

where $\dot{m}'^{'*}$ is the non-dimensional burning intensity; defined as:

$$\dot{m}'^{'*} = \dot{m}''/(\rho_\infty\sqrt{gD}) \tag{2}$$

in which $\dot{m}''$ is the burning rate per unit area (kg m^{-2} s^{-1}), g is gravitational acceleration and D is flame depth (m). The modified Froude number Fr_D is defined on the basis of the freestream velocity and characteristic buoyancy force:

$$\mathrm{Fr}_D = U_\infty^2/(gD) \tag{3}$$

The low value of the exponent of the modified Froude number (−0.11) in Eq. (1) suggests a small direct effect of wind velocity on flame length. However, the observed reduction in flame length with an increase in wind velocity is believed to stem from more effective plume entrainment (Thomas et al., 1963). From fire experiments in pine needle fuel beds, Hilton et al. (2015) suggested an exponent factor of 0.86 instead of 0.97 in Eq. (1). Furthermore, they proposed that the tangent of the flame tilt angle (hereafter called tilt coefficient of the flame) is proportional to $p_d U_\infty/E_r$, where p_d is the dynamic pressure of the ambient wind and E_r the equivalent unit energy release rate of the fire.

Putnam (1965) derived formula for calculating flame heights and horizontal extensions of the flame for natural-gas line fires using experimental data. Normalizing the flame height in wind presence (H_f) with that in the absence of wind, H_{f0}, Putnam presented a correlation for flame height under wind condition:

$$\frac{H_f}{H_{f0}} = (1 + 4U_\infty^2/gH_{f0})^{-1/2} \tag{4}$$

while the tilt coefficient of the flame is found to be proportional to $(U_\infty^2/gH_{f0})^{-1/2}$, the tangent of the flame angle varied directly with the square root of the Froude number.

Using fuel beds of pine needles with different widths, Rossa et al. (2015) showed that flame width (corresponding to the width of the fuel bed) has a considerable effect on the total radiation emitted by the flame and then significantly influences the rate of spread.

By conducting experiments of fires propagating with wind through beds of pine needles, Nelson Jr and Adkins, (1986) found that the flame length and the tilt coefficient of the flame correlate roughly with the square root of the fire intensity and the Froude number. In the fire experiments concerning individual plant species of hummocks and eucalyptus, Bradstock and Gill (1993) focused on the flammability of individual plant species in relation to flame height or length. Flame length is defined as the distance from the base of the fire source to the tip of the flame and flame height is the vertical distance measured from the ground to the tip of the flame. In the case of no wind, flames are vertical and height equates to flame length; whereas with wind, flame height is less than flame length.

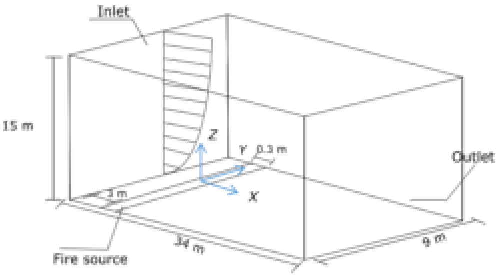

Fig. 1. Schematic view of the computational domain.

One of the primary numerical studies is that of Albini, (1981), who developed a one dimensional model for the structure of wind-blown, turbulent flame from a line fire. The model was built based on some assumptions. One assumption is that wind speed was constant, homogeneous combustion happened only above the fuel bed, and combustion products were integrated as a pure gaseous fuel added to the top of the fuel bed with an insignificant speed compared to wind speed. Simulations were conducted for an extended range of Fr_D. Another assumption used in the simulation was that the flame tip was the height at which the mean temperature inclined below 500 K and the air entrained up to this height is roughly 10 times as much as the stoichiometric air prerequisite (Albini, 1981). Analysing the numerical outcomes, Albini (1981) suggested that the square of tilt coefficient of the flame from vertical is equal to 1.5 of the Froude number defined based on flame height ($\mathrm{Fr}_{Hf} = U_\infty^2/gH_f$) where the numerical factor was found to be dependent on the flame tip temperature only.

Other researchers such as Sinai and Owens (1995) utilized a commercial code, namely FLOW3D, to simulate large-scale unconstrained pool fires exposed to a cross-wind highlighting the flame geometry. Their model was founded on the buoyancy-modified k-ε turbulence model, the Eddy-Break-Up combustion model (Sinai and Owens, 1995) and a grey medium estimate for thermal radiation. Morandini et al. (2005) numerically analyzed the impacts of wind on fire plumes by replacing the fuel bed with a 0.25 m × 0.4 m propane burner. The combustion route was disregarded in their model with the assumption of uniform heat release within the flame. Morvan et al. (1998) adopted a multicomponent k- ε turbulent reacting flow and numerically investigated the effect of a cross-wind upon the buoyant turbulent flow induced by a diffusion flame. Their outcomes revealed that the flow is characterized by oscillations which influences the flame behaviour. These authors also concluded that as the cross-wind velocity escalates, a transition from buoyancy dominated flow to cross-wind dominated flow can be realized along with a cut in oscillation (Morvan et al., 1998).

Of late, Snegirev (2004) used a Computational Fluid Dynamics (CFD) model and simulated the pool fire and crosswind interactions. In his model, Monte Carlo method combined with the Weighted Sum of Gray Gases model was utilized to capture the thermal radiation effects. Snegriev also concluded that the burning rate rises with wind velocity. These results were found to be in good agreement with experimental observations (Souil et al., 1984).

In more recent work, Yoshihara et al. (2013) examined flame characteristics of small pool fires in the downslope and upslope angled winds and stated that the alteration between horizontal and angled wind flow is due to the presence of both horizontal and vertical momentum components. Yoshihara and his co-authors suggested a set of reformed semi-empirical correlations for flame length and flame tilt angle calculation for low wind speeds. At the same time,

Table 1
List of simulation scenarios based on freestream wind velocity and fire line intensity.

Simulation number (S#)	U_{ref} (m/s)	I (MW/m)	u_f (m/s)	Simulation number (S#)	U_{ref} (m/s)	I (MW/m)	u_f (m/s)
1	3	2	0.18	13	7.5	2	0.18
2	3	3	0.27	14	7.5	3	0.27
3	3	4	0.36	15	7.5	4	0.36
4	3	6	0.55	16	7.5	6	0.55
5	4.5	2	0.18	17	9	2	0.18
6	4.5	3	0.27	18	9	3	0.27
7	4.5	4	0.36	19	9	4	0.36
8	4.5	6	0.55	20	9	6	0.55
9	6	2	0.18	21	3	1	0.09
10	6	3	0.27	22	4.5	0.66	0.06
11	6	4	0.36	23	6	0.66	0.06
12	6	6	0.55	24	2	1	0.09

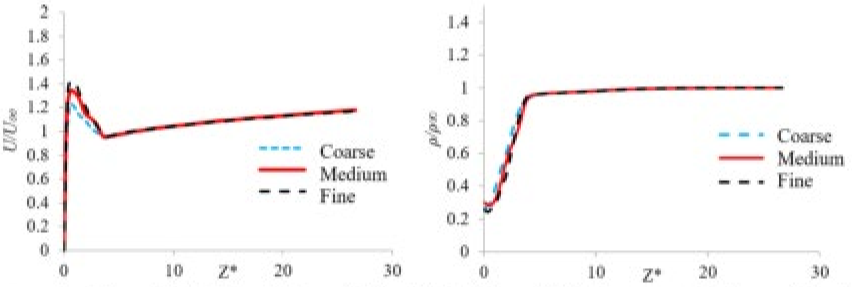

Fig. 2. Comparison of the vertical distribution of (a) normalized longitudinal velocity and (b) density at $X^* = 12$ for different grid sizes in S#5.

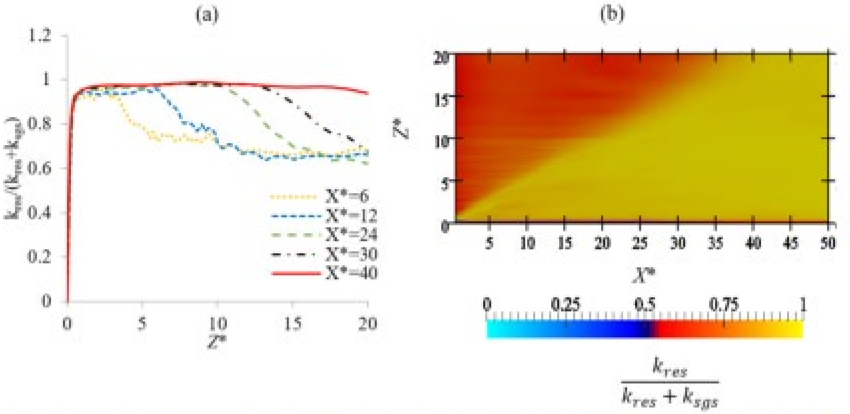

Fig. 3. Ratio of the resolved turbulent kinetic energy to total turbulent kinetic energy for S#2 (a) vertical distribution at different distances downstream of the fire source; and (b) planar distribution ($Y = 0$).

Hu et al. (2013) developed a novel mathematical model based on experiments to establish a correlation for the flame tilt angle of small pool fires. A dimensionless global parameter, linking the wind speed by a characteristic rising velocity of the flame underpinned by the buoyancy strength of the pool fire sources, was suggested, which is shown to better converge and correlate the flame tilt angle data comparing to the previous models.

Tang et al. (2015) also developed a global relation to identify the burning behaviour of acetone pool fire-cross-wind conditions. They showed that an increase in cross airflow speed leads to a higher mass burning rate in relatively smaller pool fires.

The influence of cross-wind on flame drag base length was also examined experimentally (Lin et al., 2018; Lam and Weckman, 2015; Tang et al., 2019). The flame drag base length is associated with the unburnt fuel adjacent to the burner surface and dragged towards the downwind direction. Dimensionless correlations for the flame base drag length have been suggested by several researchers (Tang et al., 2017; Hu et al., 2017; Raj, 2010). Flame sag is another phenomenon during fire-wind interaction that was studied in previous works (Zhang et al., 2019; Lautkaski, 1992; Rew et al., 1997).

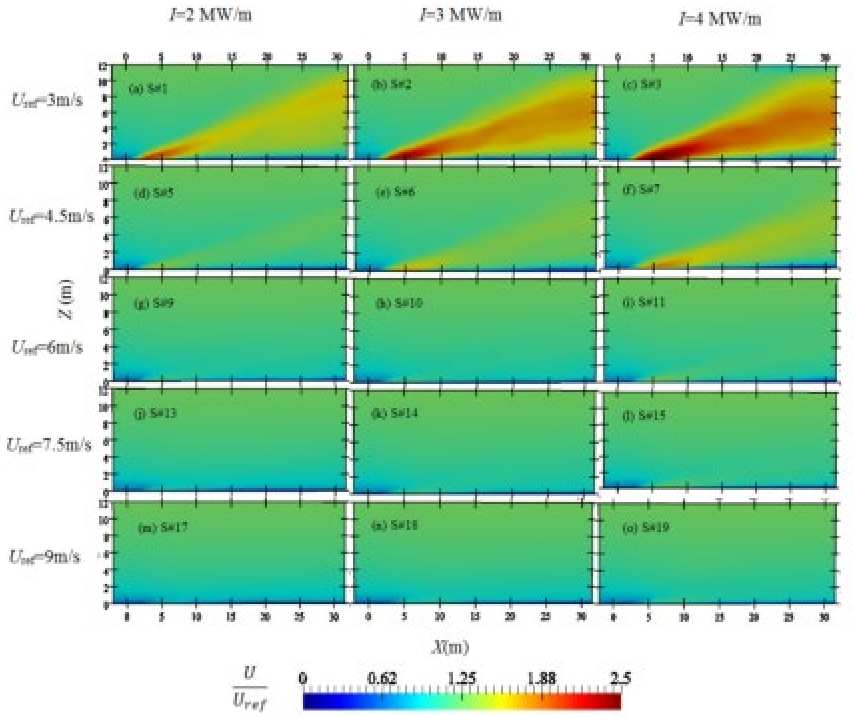

Fig. 4. Distribution of normalized longitudinal velocity for different simulation scenarios at a vertical plane passing the centreline ($Y = 0$).

The previous studies presented correlations for flame geometries such as flame length, flame height, and flame tilt angle under cross-flow conditions Lin et al., 2019; Wang et al., 2019; Hu et al., 2011; Liu and Hu, 2019; Lu et al., 2019; Ping et al., 2018). However, no correlations have been reported in the literature for aerodynamic characteristics of the flame. Nmira et al (2010) showed that Froude number (which takes into account wind effects) and dimensionless heat release rate (for point source fire) and dimensionless fire intensity (for line source fire) are appropriate non-dimensional groups [Eqs. (5) and ((6)] to develop correlations for flame geometrical features such as flame length, height, and tilt angle in fire-wind interaction scenarios:

$$\mathrm{Fr} = \frac{U_{ref}^2}{gD} \tag{5}$$

$$I^* = \frac{I}{\rho_\infty c_p T_\infty \sqrt{g} D^{(3/2)}} \tag{6}$$

It is hypothesized that flame aerodynamic characteristics can also be correlated as a function of these non-dimensional groups as they take into account the important contributing forces (inertia and buoyancy and thermal expansion) during fire-wind interaction:

The interactions between wind and fire are not limited to changes in the burning rate and flame geometry. Previous numerical simulation studies showed that interaction of wind and fire can also lead to the increases of wind velocities and pressure load on buildings downstream of a line fire source (He et al., 2011; Kwok et al., 2012). Recently Eftekharian et al. (2019) performed LES studies to fundamentally investigate the enhancement of wind by pool fire sources and expounded in detail of how the interaction of buoyant plume with wind results in augmentation of wind downstream of the fire source. They revealed that the enhancement of wind by fire is triggered by the generation of a negative longitudinal pressure gradient in the low-density region due to fire-wind interaction. In other studies by the same group (Eftekharian et al., 2019, 2018), the influence of freestream wind velocity on the alteration of velocity profile downstream of a point (Eftekharian et al., 2019) and line (Eftekharian et al., 2018) fire source was investigated. Eftekharian et al., (2019, 2018) showed that the effects wind velocity enhancement downstream of the fire source is reduced as freestream wind velocity increases. Moreover, Eftekharian et al investigated the effects of fire source configuration of the wind enhanced by fire (Eftekharian et al., 2019). It was found that the wind enhanced by a line source of fire is considerably higher than that induced by a point source under the same fire intensity condition. The stronger fire-induced pressure force in line source fire scenario than the point source case was considered as the reason behind this trend (Eftekharian et al., 2019). Eftekharian et al., (2019, 2020a, 2020b) also investigated the effects of terrain both in upslope and downslope conditions on fire-wind enhancement. They showed that in contrast to the downslope cases, in upslope scenarios an additional component of buoyancy force in wind direction is generated which assists fire-induced pressure force and causes stronger wind enhancement.

The presented literature review confirms that in spite of these recent studies performed in unravelling the physics of the fire-wind enhancement phenomenon, there is still a gap in formulating wind enhancement by fire based on the major contributing factors (wind velocity and fire intensity). This work aims to fill the gap by developing correlations to determine the enhancement of wind by fire as a function the contributing non-dimensional groups (Froude number and

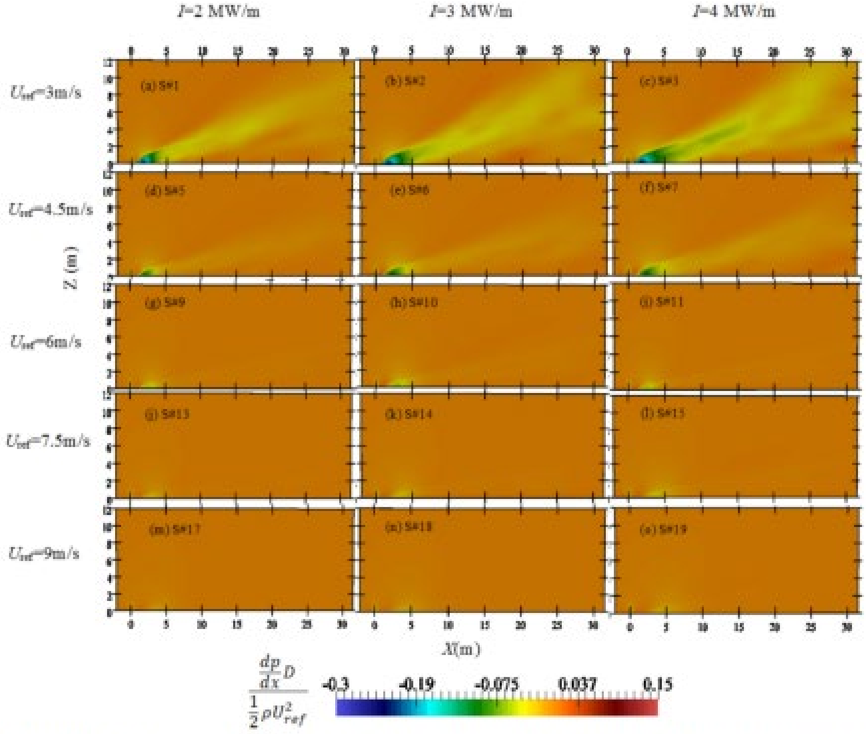

$$\frac{\frac{dp}{dx}D}{\frac{1}{2}\rho U_{ref}^2}$$

Fig. 5. Planar distribution of normalized longitudinal pressure gradient for different simulation scenarios at a vertical plane passing the domain centreline ($Y = 0$).

normalized fire intensity).

The main objective of this study hence is to provide a comprehensive and fundamental understanding of fire-wind enhancement behaviour under a range of freestream wind velocity and line-fire intensity conditions. The final goal is to develop correlations to predict maximum fire-wind enhancement as well as the decay of wind velocity enhancement by fire as a function of the contributing non-dimensional groups.

In summary, flow characteristics can be correlated with the controlling non-dimensional groups (Fr, I^* and X^*). In other words, there exist correlations in the form of multi-variant functions:

$$U^* = f\,(\mathrm{Fr},\ I^*,\ X^*) \tag{7}$$

where U^* represent generally a flow characteristic. Fr, I^* and X^* are respectively Froude number, normalized fire intensity and normalized longitudinal location from the fire source.

3. Numerical modelling

3.1. Overall methodology and simulation strategy

In order to establish the correlations of the form given by Eq. (7), a data set (U^*_{enh}, Fr, I^*, X^*) of reasonable size needs to be obtained. A number of simulation scenarios with different freestream wind velocity and fire intensity inputs were defined to generate sufficient data set of $U_{enh}{}^*$, Fr, I^*, X^* with the aim to develop trends and correlations between fire-wind enhancement flow characteristics and the appropriate non-dimensional groups (Fr, I^*, X^*). These characteristics include maximum wind enhancement by fire, the corresponding location at which maximum wind enhancement occurs, wind enhancement plume line and the decay of wind velocity enhancement along the plume line. These concepts and parameters will be defined and explained in the following sections.

3.2. Modelling software and governing equations

The CFD solver utilized in this research was FireFOAM which is a derivative of OpenFOAM 4.1 platform (Greenshields, 2015). This solver is mainly designed for fire dynamics simulations. OpenFOAM is an entirely open-source software platform using an object-oriented C + + design that has custom-written solvers and easy access to model extension and modification.

FireFOAM uses LES (Large Eddy Simulation) to model turbulent structures in buoyant plumes. LES was proved to perform well for turbulent combustion modelling (Malalasekera et al., 2013). Different solvers of OpenFOAM such as FireFOAM have been benchmarked with several experimental fire-related data including large eddy simulation of fire plumes, small-scale pool fire (Wang et al., 2011) and medium-scale methanol pool fire (Maragkos et al., 2017). FireFOAM is also benchmarked with an analytical solution as well as real fire tests (Li et al., 2017).

FireFOAM solves the Favre filtered fully compressible Navier–Stokes equations (Eftekharian et al., 2019; Wang et al., 2011) to capture turbulent structures of the flow. Continuity, momentum, energy, state and species equations solved by FireFOAM are as below:

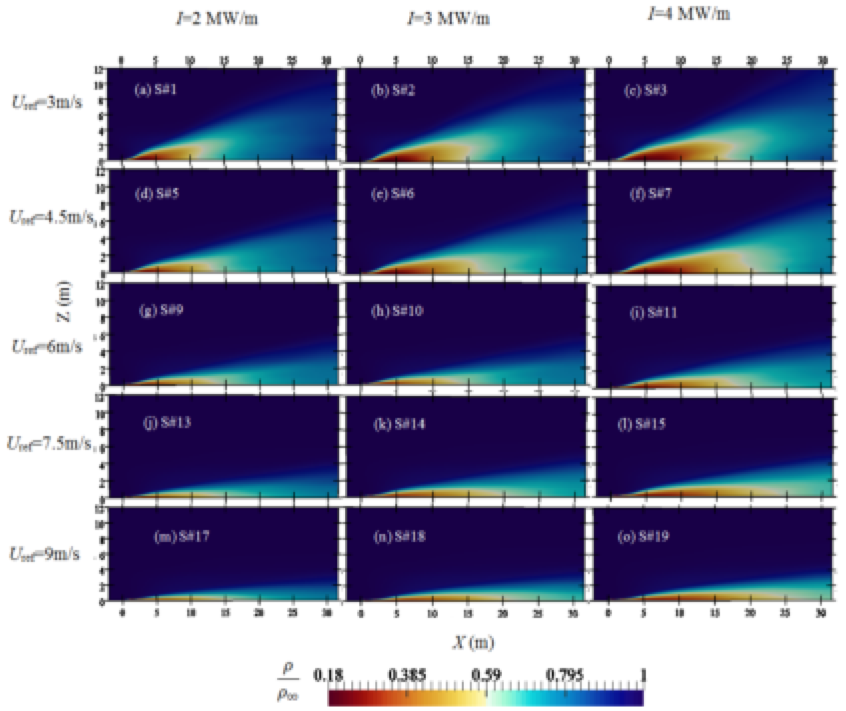

Fig. 6. Distribution of normalized density for different simulation scenarios at a vertical plane passing the domain centreline ($Y = 0$).

$$\frac{\partial \bar{\rho}}{\partial t} + \frac{\partial(\bar{\rho}\tilde{u}_i)}{\partial x_i} = 0 \tag{8}$$

$$\frac{\partial(\bar{\rho}\tilde{u}_i)}{\partial t} + \frac{\partial(\bar{\rho}\tilde{u}_i\tilde{u}_j)}{\partial x_j} = -\frac{\partial \bar{p}}{\partial x_i} + \bar{\rho}g_i + \frac{\partial}{\partial x_j}\left[\bar{\rho}(\nu + \nu_t)\left(\frac{\partial(\tilde{u}_i)}{\partial x_j} + \frac{\partial(\tilde{u}_j)}{\partial x_i} - \frac{2}{3}\frac{\partial \tilde{u}_k}{\partial x_k}\delta_{ij}\right)\right] \tag{9}$$

$$\frac{\partial(\bar{\rho}\tilde{h})}{\partial t} + \frac{\partial(\bar{\rho}\tilde{u}_j\tilde{h})}{\partial x_j} = \frac{D\bar{p}}{Dt} + \frac{\partial}{\partial x_j}\left[\bar{\rho}\left(\alpha_T + \frac{\nu_t}{\mathrm{Pr}_t}\right)\left(\frac{\partial \tilde{h}}{\partial x_j}\right)\right] + \dot{q}''' - \nabla\cdot\dot{q}_r'' \tag{10}$$

$$\frac{\partial\bar{\rho}\widetilde{Y_m}}{\partial t} + \frac{\partial(\bar{\rho}\tilde{u}_j\widetilde{Y_m})}{\partial x_j} = \frac{\partial}{\partial x_j}\left[\bar{\rho}\left(D_c + \frac{\nu_t}{\mathrm{Sc}_t}\right)\frac{\partial(\widetilde{Y_m})}{\partial x_j}\right] + \omega_m \tag{11}$$

$$\bar{p} = \bar{\rho}R\tilde{T} \tag{12}$$

where the symbols "$-$" and "$\sim$" shows spatial and Favre filtering. Also, ρ, p, h, Y_m, g, ν, ν_t, D_c, R, α_T, Pr_t, Sc_t, δ and ω_m are respectively, density, static pressure, total enthalpy, mass fraction of species m in the gas mixture, gravitational acceleration, laminar viscosity, turbulent viscosity, laminar diffusion coefficient, gas constant, thermal diffusion coefficient, turbulent Prandtl number, turbulent Schmidt number, Kronecker delta and production/sink rate of species m due to gas reaction. ν_t is determined based on the subgrid-scale turbulence model. $\dot{q}'''$ is heat release rate per unit volume (W/m^3) from a chemical reaction and $\dot{q}_r''$ is the total radiation heat transfer emission intensity (W/m^2) of the gas mixture.

Based on the momentum equation, the force imposed on the infinitesimal fluid parcel is equal to the fluid parcel mass multiplied by the acceleration (Eftekharian et al., 2019):

$$d\vec{F} = \vec{a}\,dm = \rho\vec{a}\,d\forall = \rho(\vec{a}_p + \vec{g} + \vec{a}_v)d\forall = \vec{f}_p\,d\forall + \vec{f}_g\,d\forall + \vec{f}_v\,d\forall = d\vec{F}_P + d\vec{F}_g + d\vec{F}_v \tag{13}$$

where $\forall$ is volume and $\vec{a}$ is flow acceleration and f is the force per unit volume. Symbols $\vec{a}_p$, $\vec{g}$ and $\vec{a}_v$denote accelerations due to pressure force, gravitational force and viscous forces, respectively.

The flow acceleration based on the momentum equation in the Eulerian system can be expressed as (Eftekharian et al., 2019):

$$\vec{a} = \frac{D\vec{u}}{Dt} = \frac{-\nabla p}{\rho} + \vec{g} + \frac{\Phi}{\rho} = \vec{a}_p + \vec{g} + \vec{a}_v \tag{14}$$

where $\vec{u}$ is velocity vector, Φ is the viscous shear stress vector $(\Phi_i) = \frac{\partial(\sigma_{ij})}{\partial x_j}$ in which σ_{ij} is the components of stress. The first, second and third terms on the right-hand side (RHS) of Eq. (14) represents the accelerations due to pressure gradient, gravity, and viscous forces, respectively. The three components are referred to as pressure acceleration, gravitational acceleration, and viscous acceleration, respectively hereafter in this paper. Similarly, $\vec{f}_p$, $\vec{f}_g$ and $\vec{f}_v$ are referred to as pressure force, gravitational force and viscous force. The directional components of $\vec{f}$ and $\vec{a}$ and are presented separately (Eftekharian et al., 2019):

$$a_i = a_{pi} + g_i + a_{vi} \tag{15}$$

$$\vec{f}_i = \vec{f}_{pi} + \vec{f}_{gi} + \vec{f}_{vi} \tag{16}$$

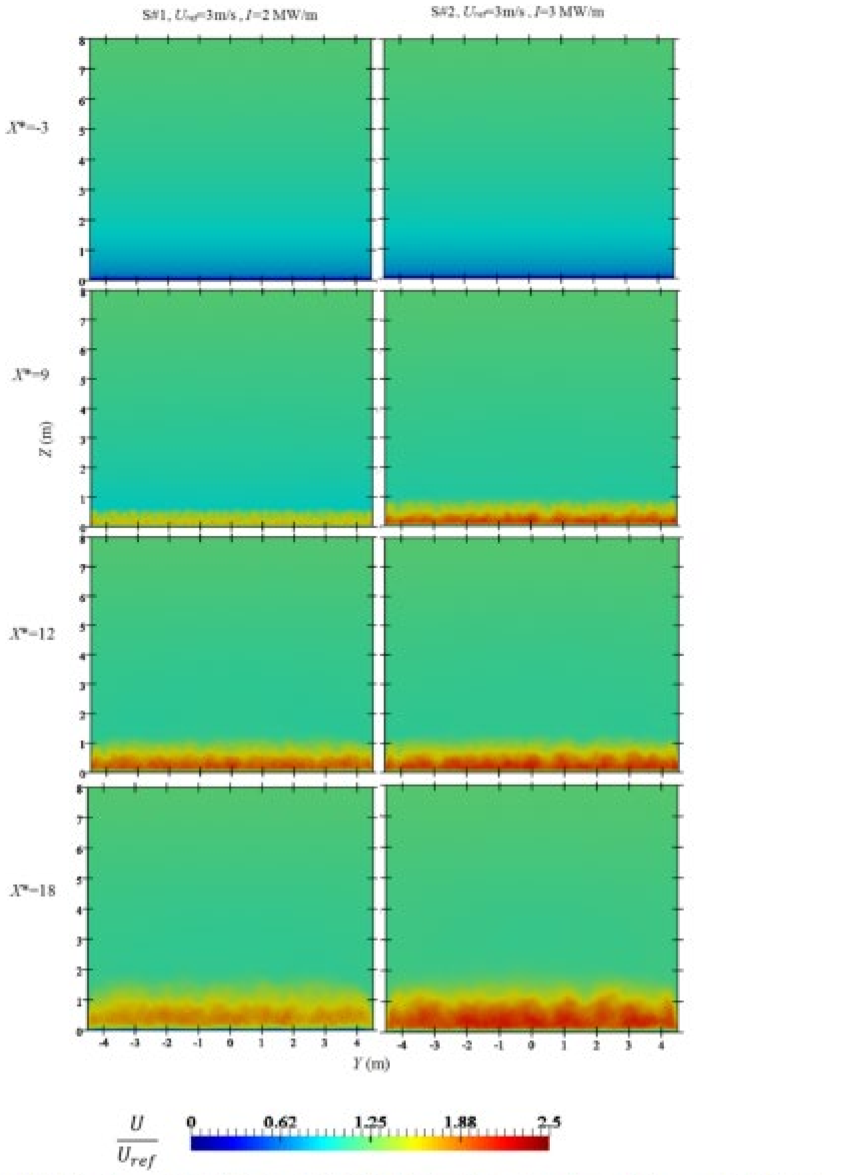

Fig. 7. Cross-sectional distribution of normalized longitudinal velocity (U/U_{ref}) at different distances downstream of the fire source for S#1, S#2.

Where index i = 1, 2, 3 accounts for forces and acceleration in X, Y and Z directions. In the current discussion, the focus is on velocity, force, and acceleration in the longitudinal (i = 1).

FireFOAM iteratively solves Eqs. (8)–(12) to identify the prime flow variables. It employs kEq model to treat sub-grid scale turbulence structures. The coefficients C_k and C_ε (Shi et al., 2016; Vilfayeau, 2015) used for the determination of sub-grid scale characteristics for sub-grid turbulent kinetic energy equation (k_{sgs}) are 0.07 and 1.05, respectively. The combustion is governed by eddy dissipation, and the infinitely-fast chemical reactions were presumed. Time scale coefficient (C_{EDC}) and molecular diffusion coefficient (C_{diff}) in Eddy Dissipation model were chosen to be 4 and 0.4 respectively, as suggested in Vilfayeau (2015). A module has been developed and attached to the FireFOAM platform to generate individual output

Table 2
Data related to the maximum wind enhancement predicted by CFD and the developed correlation for different simulation scenarios.

S#	U_{ref} (m/s)	I (MW/m)	Fr	I^*	$U^*_{f\_max}$		Error [Eq. (20)] (%)
					CFD	Eq. (20)	
1	3	2	3.058	11.06	2.03	2.05	0.99
2	3	3	3.058	16.59	2.37	2.34	1.1
3	3	4	3.058	22.12	2.51	2.57	2.67
4	3	6	3.058	33.18	3.01	2.94	2.12
5	4.5	2	6.88	11.06	1.38	1.44	4.82
6	4.5	3	6.88	16.59	1.64	1.65	0.83
7	4.5	4	6.88	22.12	1.8	1.81	1.02
8	4.5	6	6.88	33.18	2.05	2.07	3.93
9	6	2	12.23	11.06	1.08	1.12	4.58
10	6	3	12.23	16.59	1.25	1.29	3.3
11	6	4	12.23	22.12	1.36	1.41	4.4
12	6	6	12.23	33.18	1.59	1.62	1.57
13	7.5	2	19.11	11.06	0.93	0.93	0.24
14	7.5	3	19.11	16.59	1.06	1.06	0.54
15	7.5	4	19.11	22.12	1.12	1.17	0.16
16	7.5	6	19.11	33.18	1.3	1.33	3.05
17	9	2	27.52	11.06	0.88	0.79	9.42
18	9	3	27.52	16.59	0.98	0.91	7.02
19	9	4	27.52	22.12	1.06	1	5.48
20	9	6	27.52	33.18	1.19	1.14	3.75
Testing Data							
21	3	1	3.058	5.53	1.62	1.63	0.67
22	4.5	0.66	6.88	3.68	0.93	1	8.24
23	6	0.66	12.23	3.68	0.76	0.78	3.42
24	2	1	1.35	5.53	2.56	2.31	9.7

components of the total fire-induced forces and acceleration [Eqs. (13) and (14)] at the end of each computational time step. FireFOAM solves the radiative heat transfer equation based on the grey gas assumption (Vilfayeau, 2015) and uses finite volume discrete ordinates model (fvDOM) (Chai and Rath, 2006) to solve the radiation heat transfer equation. In this study, the radiant fraction of 0.2 was considered as it has been used in previous studies for the simulation of methane-diffusion flame (Eftekharian et al., 2019; Wang et al., 2011).

More details about how FireFOAM treats radiation heat transfer can be found in Vilfayeau (2015). A comparison between different radiation heat transfer models for pool fire scenario can also be found in Krishnamoorthy (2012).

4. Computational domain and simulation conditions

The computational domain consists of a rectangular box with the dimension of 9 × 15 × 34 m as shown in Fig. 1. A line source of fire with the depth of 0.3 m was placed 3 m downstream of the inlet as shown in Fig. 1. The origin of the x-y-z coordinate is set at 3.15 m downstream of the inlet along with domain centreline (at the middle of fire source) as shown in Fig. 1.

Methane was chosen as the fuel source to be injected from the fire source. Bushfire intensity (I) is usually described as the heat release rate per unit width (here 9 m) of bushfire front (Byram, 1959), which in this study is 2,3, 4 and 6 MW/m depending on the simulation scenario.

A power law velocity profile representing atmospheric boundary layer profile was used at the inlet on the left side of the domain:

$$U(Z) = U_{ref}\left(\frac{Z}{Z_{ref}}\right)^{\alpha} \tag{17}$$

where, U_{ref} and Z_{ref} are, respectively, the reference velocity (free-stream velocity at the the height of Z_{ref}) and reference height (3 m); α is determined based on terrain category (here 0.16). In this study simulations with a range of different reference velocities including 3, 4.5, 6, 7.5 and 9 m/s were performed to investigate the effects of wind velocity on fire-wind enhancement. The injected fuel velocity (u_f) is negligible compared to the incoming cross-wind velocity as shown in Table 1. A summary of the simulation scenarios performed in this study can be found in Table 1.

The range of values used for wind velocity and fire intensity is consistent with those suggested in previous studies (Nmira et al., 2010) in which the vegetation fire characteristics under the wind condition were studied. In order to consider turbulent fluctuations in the domain inlet, the "2D vortex method" (Sergent, 2002) was used so that the turbulent intensity of approximately 5% is obtained at the target location. As for the other domain boundaries, outflow and open boundary conditions were prescribed for domain outlet on the right and ceiling, respectively. Slip and no-slip boundary conditions were applied respectively to the domain sides and base. The initial and the incoming freestream flow temperature was set to be 300 K, while the adiabatic boundary was suggested for the domain base.

5. Numerical uncertainty analysis

5.1. Grid sensitivity analysis

A grid sensitivity analysis was conducted using three grid sizes. The three grid sizes were 600 k (70 × 90 × 98), 8.7 million (127 × 527 × 130) and 23 million (197 × 550 × 220) for coarse, medium and fine grids, respectively. The non-uniform structured grid was used to create smaller computational cells close to the fire source so that the grid size of the fire source would be 1 cm.

Fig. 2. compares normalized velocity and density for the three grid sizes at $X^* = 12$ for S#5, where $X^* = X/D$. The negligible difference (approximately 1%) is observed between the medium and fine grid for both velocity and density profiles. Hence, the medium grid was chosen for all simulation scenarios in the current study.

5.2. LES uncertainty analysis

Evaluating the ratio of resolved turbulent kinetic energy (k_{res}) to the total turbulent kinetic energy ($k_{res} + k_{sgs}$) is one of the criteria to assess the credibility of the applied LES model and appropriateness of the applied grid size in numerical simulations (Pope and Pope, 2000). According to Pope and Pope (2000), resolving 80% of turbulent kinetic energy shows the reliability of LES in a numerical model. Fig. 3 (a) and (b) depict this ratio for S#2 of the chosen (medium) grid along the plane $Y = 0$. It can be seen that more than 70% of turbulent kinetic energy is resolved for almost all distances downstream of the fire source. However, in the plume region, which is the region of focus in this study, turbulent kinetic energy is satisfactorily (more than 95%) resolved. This trend is consistent with that presented in previous studies (Vilfayeau et al., 2016). More information and analysis about reliability of the performed LES simulations can be found in our previous studies (Eftekharian et al., 2019) employing similar numerical approach.

5.3. Validation

The developed numerical model has been validated against two sets of experimental data in our previous work (Eftekharian et al., 2019). The first set includes experimental data of McCaffrey (McCaffrey, 1979) and the second set is associated with that of Hirano and Kinoshita (Hirano and Kinoshita, 1975). McCaffrey experiment (McCaffrey, 1979) includes experimental data of buoyant diffusion flame in the still environment. McCaffrey (McCaffrey, 1979) utilized a natural gas burner and measured the centreline of flow velocity for various heat release rates. The simulation results were then assessed against the numerical results of (Wang et al., 2011) and experimental data of (McCaffrey, 1979). A reasonable agreement with the experimental data was obtained (Eftekharian et al., 2019).

The second validation is associated with experimental data of Hirano and Kinoshita (1975) who measured velocity and temperature

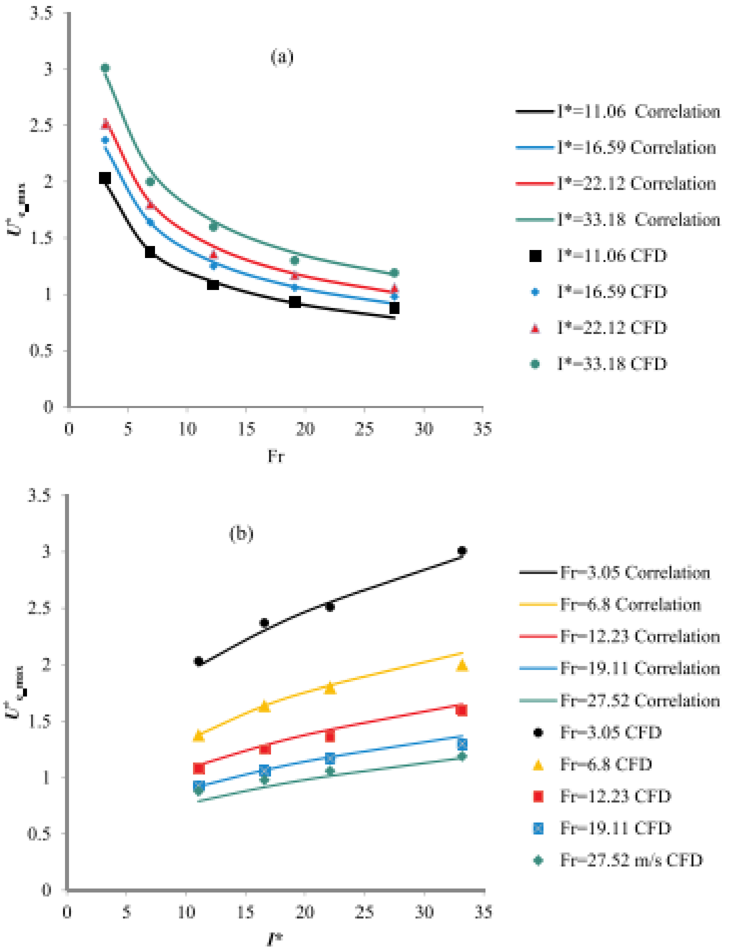

Fig. 8. Comparison of the maximum wind enhancement by between the results of Eq. (20) and CFD data of the first 20 simulation scenarios.

distribution at different distances downstream of the fire source. Their experiment involved a steady burning of a liquid-fuel methanol pool in a forced convective channel flow with a velocity of 0.5 m/s. The schematics of their experimental setup and the details of the validation of the model used in the current study can be found in our previous work (Eftekharian et al., 2019). A reasonable agreement between numerical and experimental data was reported in (Eftekharian et al., 2019) (with the overall error of approximately 7% and 8 % with experimental data respectively for velocity and temperature distribution in the plume region) (Eftekharian et al., 2019). More details of the validation set up can be found in our previous work (Eftekharian et al., 2019).

6. Results and discussion

All simulation scenarios were performed for 70 s. The first 35 s were considered as the transition period and the results were averaged over the last 35 s. Fig. 4 shows the planar distribution of normalized longitudinal wind velocity for different combinations of freestream wind velocity and fire intensity. This figure explains how the wind enhancement changes with variation of freestream wind velocity and fire intensity. As can be observed in Fig. 4, when wind interacts with fire, there would be an enhancement in wind velocity downstream of the fire. An explanation provided by Eftekharian et al. (2019a,2019b,2018) is that when wind interacts with fire, a longitudinal negative pressure gradient is generated in the low-density region (plume area) which accelerates the flow and cause enhancement of wind by fire in the near ground region. This can be observed by comparing Figs. 4 with 5 and 6. When freestream wind velocity increases and/or fire intensity decreases, the normalized longitudinal pressure gradient generated by fire-wind interaction undergoes a reduction, causing a reduction in flow enhancement by fire, as shown in Fig. 4. As a consequence, wind enhancement is shown in Fig. 4 to increase with an increase in fire intensity and/or a reduction in freestream wind velocity.

Fig. 6 shows the extent to which density distribution is affected by

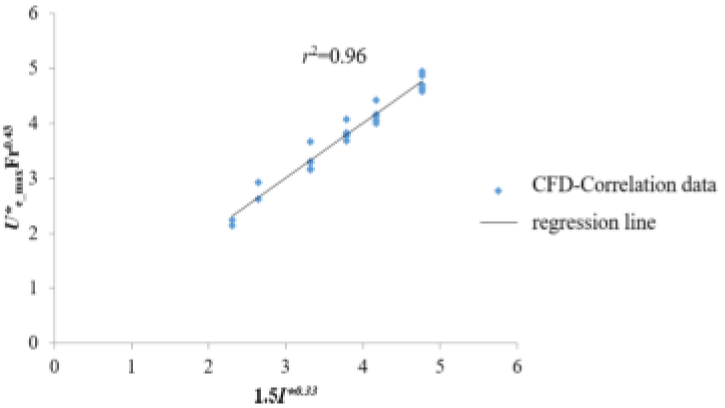

Fig. 9. Comparison of Eq. (21) with all CFD data.

the variation of freestream wind velocity and fire intensity at the domain centre plane ($Y = 0$). It is seen that when fire intensity and/or wind velocity increases, the core of the plume region (where the minimum density occurs) is extended further downstream of the fire source. Also, when freestream wind velocity increases under a constant fire intensity, it can be seen that the plume region becomes thinner and more inclined to attach to the ground. These results are consistent with the findings of (Nmira et al., 2010). Considerable reductions in the broadness of the plume region and flame height with the increase of wind velocity are observed in Fig. 6. The fire intensity I, on the other hand, appears to have the opposite effect, i.e., the broadness of the flame region and the flame height tend to increase with increasing fire intensity. This is mainly because strong wind velocity causes great flow horizontal inertia forces which renders flame to bend significantly toward the ground, increasing flame tilt angle and reducing flame height. This trend of reduction of flame height with the increase of upstream wind velocity was also observed in previous experimental studies (Lin et al., 2019; Tang et al., 2015). High inclination of fire plume for ground attachment in strong freestream wind velocity is a manifestation of the increase of Froude number which indicates the ratio of freestream inertia to buoyancy effects (Nmira et al., 2010).

Fig. 7. demonstrates the cross-sectional distribution of normalized longitudinal flow velocity at different distances downstream of the fire source for two simulation scenarios (S#1, S#2). It shows that the wind is enhanced along a belt-shaped region parallel to the fire source and the region of wind enhancement is shifted above the ground with the increase of distance from the fire source. Moreover, immediately downstream of the fire source, the wind enhancement starts to increase longitudinally, reaching its maximum value and then undergoes a reduction further downstream of the fire source. This observation is consistent with the trend observed in Fig. 4. Fig. 7 also indicates the homogeneous distribution of wind enhancement along the spanwise (Y) direction. Hence the behaviour of fire-wind enhancement along the domain centre plane ($Y = 0$) can be generalized to other span wise locations.

Maximum wind enhancement is the most critical velocity information in fire-wind interaction scenarios as it can create the highest pressure load on buildings located downstream of the fire source. Figs. 4 and 7 confirm that the maximum wind enhancement by fire for each simulation scenario happens at near ground region somewhere downstream of the fire source. Therefore, the maximum wind enhancement normalized by the freestream wind reference velocity, ($U^*_{\varepsilon\_max} = \frac{U_{\varepsilon\_max}}{U_{ref}}$), can be considered to be a function of freestream wind velocity and fire intensity or the non-dimensional groups (Fr and I^*) reflecting these quantities.

In order to predict wind velocity enhancement in different combinations of freestream wind velocity and fire intensity, corresponding data is tabulated in Table 2. Table 2 summarizes the maximum wind enhancement in different simulation scenarios.

On the one hand, Froude number (Fr) and normalized fire intensity (I^*) have been shown to be appropriate non-dimensional groups to characterize line fire flame features under cross-wind fire scenarios (Nmira et al., 2010). On the other, Froude number (Fr) and normalized fire intensity (I^*) take into account the effects of respectively freestream wind velocity and fire intensity which are influential factors affecting fire-wind enhancement as shown Figs. 4–7. Hence, it is postulated that the normalized maximum enhanced velocity ($U^*_{\varepsilon\_max}$) correlates with the Fr and I^* in the following form:

$$U^*_{\varepsilon-max} = a'\mathrm{Fr}^{b'}I^{*c'} \tag{18}$$

where a', b' and c' are constants and

$$U^*_{\varepsilon\_max} = U_{\varepsilon\_max}/U_{ref}, \tag{19a}$$

$$\mathrm{Fr} = \frac{U_{ref}{}^2}{gD} \tag{19b}$$

$$I^* = \frac{I}{\rho_\infty c_p T_\infty \sqrt{g}\, D^{3/2}} \tag{19c}$$

where c_p (kJ/kg K) is the specific heat of air at constant pressure, D (m) is the fire source depth, ρ_∞ (kg/m^3) is the ambient density, T_∞ (K) is the ambient temperature and g is the gravitational acceleration (m/s^2). The Matlab (Inc, 2016) regression method/software was used to determine the values of parameter a', b' and c' for the best fit to the simulation results. Eq. (18) becomes:

$$U^*_{\varepsilon\_max} = 1.5\mathrm{Fr}^{-0.43}I^{*0.33} \tag{20}$$

Eq. (20) is plotted in Fig. 8 together with the CFD simulation results. It is seen that the regression function of Eq. (20) produces a very good agreement with CFD data (with the average error of about 3%).

The developed correlation was based on the CFD simulation result within the parameter ranges of $3.05 \le \mathrm{Fr} \le 27.72$ and $11.06 \le I^* \le 33.18$. In order to examine if the correlation is able to well predict wind velocity enhancement under a freestream wind velocity and fire intensity for wider ranges of the input parameters, we performed four extra simulations whose results are shown as Testing Data in Table 2. It is seen that the errors related to the testing data are marginal and comparable with that associated with the original set of

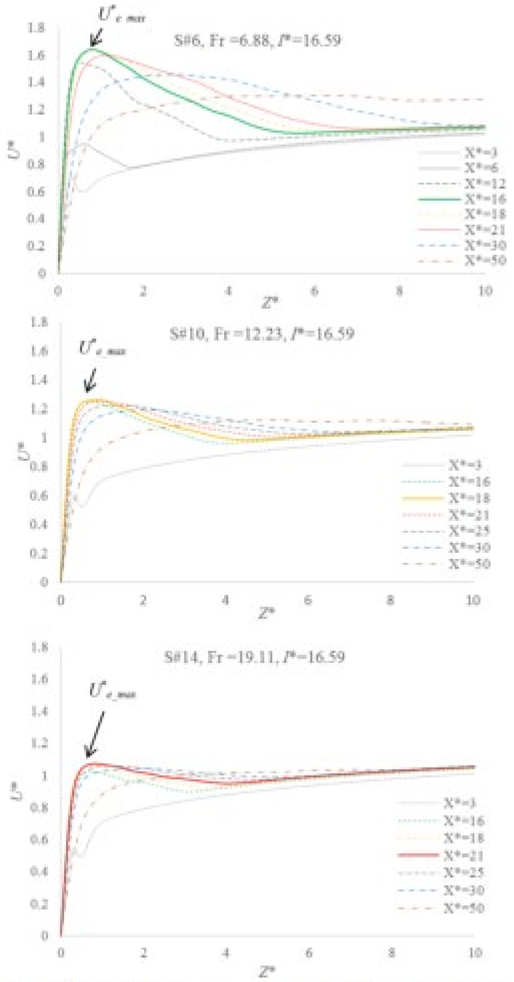

Fig. 10. Vertical distribution of normalized longitudinal velocity at different distances downstream of the fire source for three different simulation scenarios. (The line and position corresponding to $U^*_{e\_max}$ is shown by an arrow for each simulation scenario).

scenarios, confirming the capability of the presented correlation in predicting the extended range of the simulation conditions.

To check the agreement between the correlation function and the CFD simulation results, Eq. (20) is re-arranged into:

$$U^*_{e\_max}\mathrm{Fr}^{0.43} = 1.5I^{*0.33} \tag{21}$$

This equation is plotted in Fig. 9 and compared with the CFD simulation results, including that of the additional simulations runs.

Comparison of Fig. 8 (a) and (b) confirms the trend observed in Fig. 4 which indicates that the maximum wind enhancement by fire has a direct and reverse relation with fire intensity and freestream wind velocity, respectively.

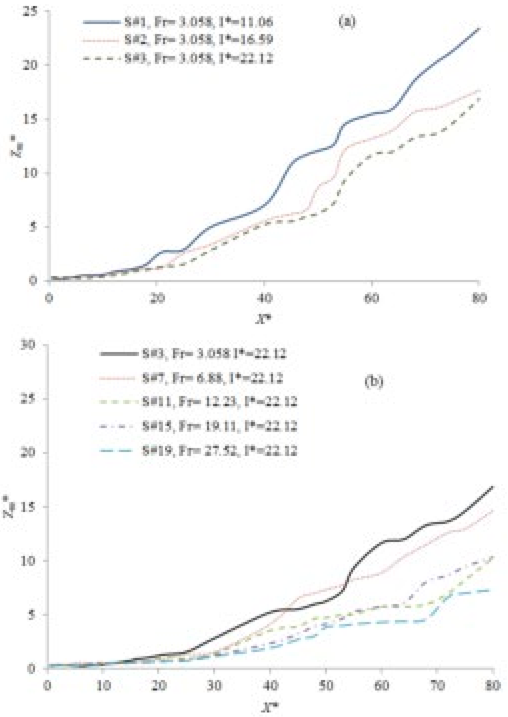

Fig. 11. Comparison of wind enhancement plume line in different simulation scenarios: (a) the effects of I^* under constant Fr, (b) the effects of Fr under constant I^*.

Fig. 10 presents vertical distribution of normalized longitudinal velocity at different normalized distances ($X^* = \frac{X}{D}$) downstream of the fire source for three different simulation scenarios. Fig. 10 shows that at a given X^*, there exists a local wind enhancement, $U^*_{max\_l}$ (X^*, Z^*_m), where Z^*_m represents the normalized z-coordinate ($Z^* = \frac{Z}{D}$) at which the local U_{max_l} occurs. Z^*_m is a function of X^*, or $Z^*_m = Z^*_m(X^*)$. This function in the x-z coordinate is called the wind enhancement plume line. Note that the parameter U_{e_max} refers to the global maximum wind enhancement. Fig. 11 is the plot of wind enhancement plume line for different simulation scenarios. Fig. 11 (a) and (b) show that in all simulation scenarios, immediately downstream of the fire source, wind enhancement plume line is horizontally extended at the near ground region and then is levelled up from the ground under a curved line in further downstream. This trend is consistent with previous observation of fire plume under cross-flow conditions (He et al., 2011). Fig. 11 (a) and (b) also illustrate respectively the effects of I^* [Fig. 11 (a)] and Fr number [Fig. 11 (b)] on the wind enhancement plume line. Fig. 11 (a) and (b) show that as Fr number and/or I^* increases, the wind enhancement plume line is more inclined to the ground. This is mainly due to the Coanda effects which necessitate the plume attachment to the ground immediately downstream of the fire source. With the increase of Fr number and/or I^*, the unbalanced flow entrainment downstream of the fire source at each side of the plume increases, strengthening the Coanda effects that consequently increases the plume inclination to the ground attachment. High inclination of plume line toward the ground in high cross-wind velocities observed in Fig. 11 (b) also manifests the increase of flame tilt angle with the increase of wind inertia force. This trend is observed in the previous experimental (Lin et al., 2019; Lam and Weckman, 2015; Tang et al., 2015; Hu et al.,

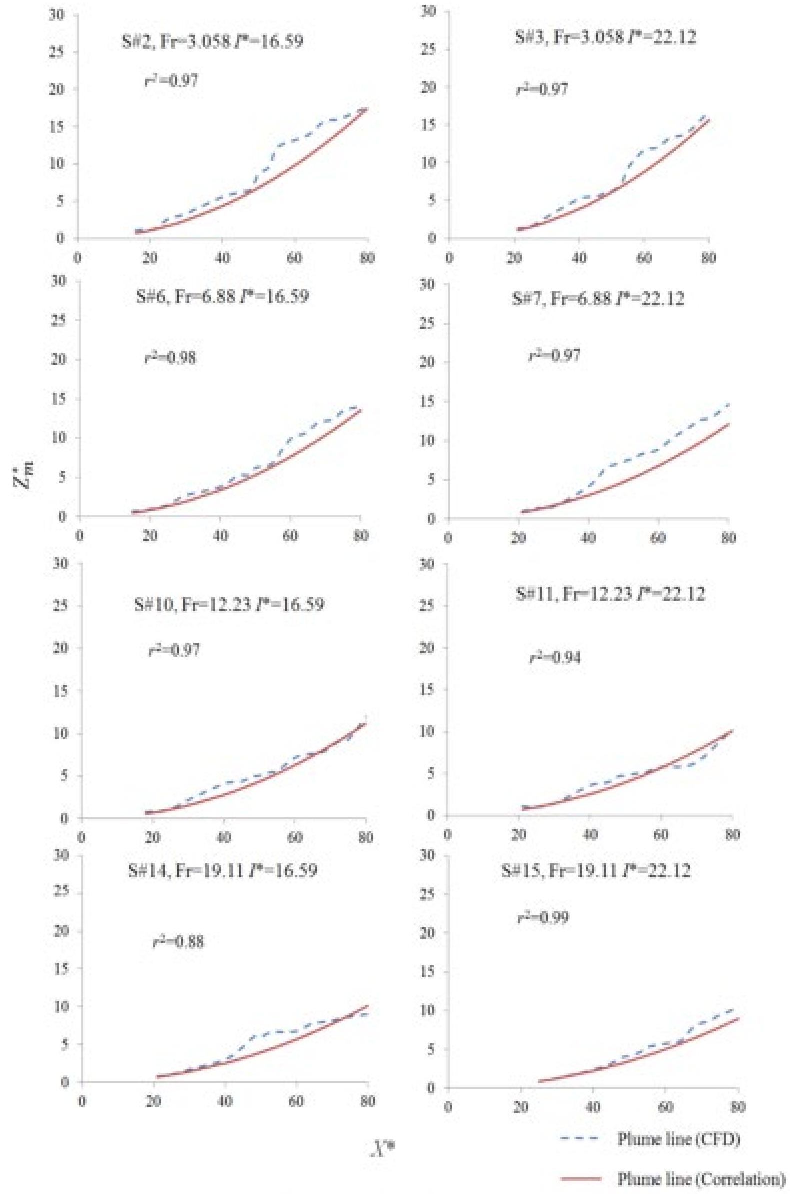

Fig. 12. Comparison of wind enhancement plume line between CFD data and that of correlation [Eq. (24)] for different simulation scenarios.

2017; Ping et al., 2018) and numerical (Nmira et al., 2010; Eftekharian et al., 2019) studies investigating flame tilt angle. On the other hand, Fig. 11 (a) also indicates that under a constant cross-wind velocity, with the reduction of fire heat release rate (fire intensity), wind enhancement plume line becomes closer to the ground, or the tilt angle increases. This is mainly because vertical buoyancy reduces causing the increase of tilt angle. This trend is in agreement with that observed in (Lin et al., 2019). Fig. 11 (b) also indicates the horizontal extension of plume line immediately downstream of the fire source. This phenomenon was referred to as flame base drag and has been observed in previous studies (Lin et al., 2018; Hu et al., 2017; Tang et al., 2019). This horizontal extension increases with the increase

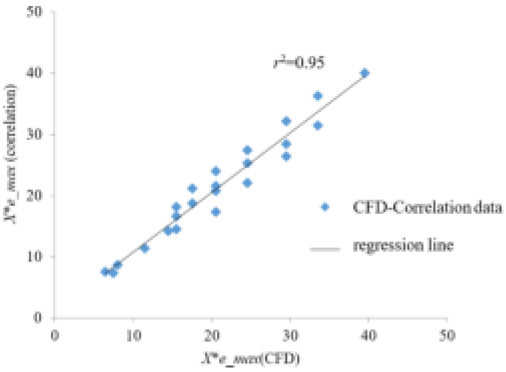

Fig. 13. Comparison of $X^*_{e\_max}$ values by CFD and by correlation Eq. (26)

of cross-wind velocity as observed in Fig. 11 (b).

Another review of the entire Fig. 11 also reveals that the wind enhancement plume lines could be approximated with functions of the parabolic form. It is then postulated that the wind enhancement plume line can be correlated in the following form:

$$Z^*_m = f'(\mathrm{Fr}, I^*)X^{*2} \tag{22}$$

where f' is a function of Fr number and I^* and can be written in the form of:

$$f' = d'\mathrm{Fr}^{g'}I^{*h'} \tag{23}$$

in which d', g' and $h'$are constants that were determined using Matlab (Inc, 2016) regression method. Eq. (22) becomes:

$$Z^*_m = 0.011\mathrm{Fr}^{-0.31}I^{*-0.37}X^{*2} \tag{24}$$

To check the agreement between the correlation function Eq. (24) and the CFD simulation results, Fig. 12 is plotted which compares the wind enhancement plume line predicted by CFD and the developed correlation [Eq. (24)]. Fig. 12 shows that there is a reasonable agreement (with average regression coefficient of $r^2 = 0.95$) between CFD results that those predicted by Eq. (24).

It was also found that a correlation can be developed for the longitudinal location at which maximum wind enhancement happens as a function of Fr number and I^*:

$$X^*_{e\_max} = m'\mathrm{Fr}^{n'}I^{*s'} \tag{25}$$

where, $X^*_{e\_max}$ is the location corresponding to the maximum wind enhancement ($U^*_{e\_max}$) and m', $n'$and s' are constant values determined by regression using Matlab (Inc, 2016) regression tool. Eq. (25) becomes:

$$X^*_{e\_max} = 2\mathrm{Fr}^{0.27}I^{*0.6} \tag{26}$$

Comparison of $X^*_{e\_max}$ of CFD results and that predicted by Eq. (26) is shown in Fig. 13 which reveals there is a good agreement (regression coefficient of 0.95 and the average error of around 8%) between CFD data and the correlation prediction.

Although the investigation of the global maximum wind enhancement ($U^*_{e\_max}$) is the most critical velocity information in fire-wind interaction scenarios, the variation of local enhanced velocity along the longitudinal direction is worth investigating. Here also we define the normalized plume velocity as:

$$U^*_p = \frac{U_p}{U_{e\_max}} = \frac{U_{max\_l}}{U_{e\_max}} = \frac{U^*_{max\_l}}{U^*_{e-max}} \tag{27}$$

where Up is the U-component velocity along the plume line. In other words, U_p represents the local maximum wind enhancement at given X^*.

Fig. 14 shows the variation of normalized plume velocity (U^*_p) along the wind enhancement plume line [Eq. (24)] for different simulation scenarios. The vertical axis represents the local wind enhancement velocity along the plume line (U_{max_l}) normalized with the global maximum wind enhancement velocity (U_{e_max}), while the horizontal

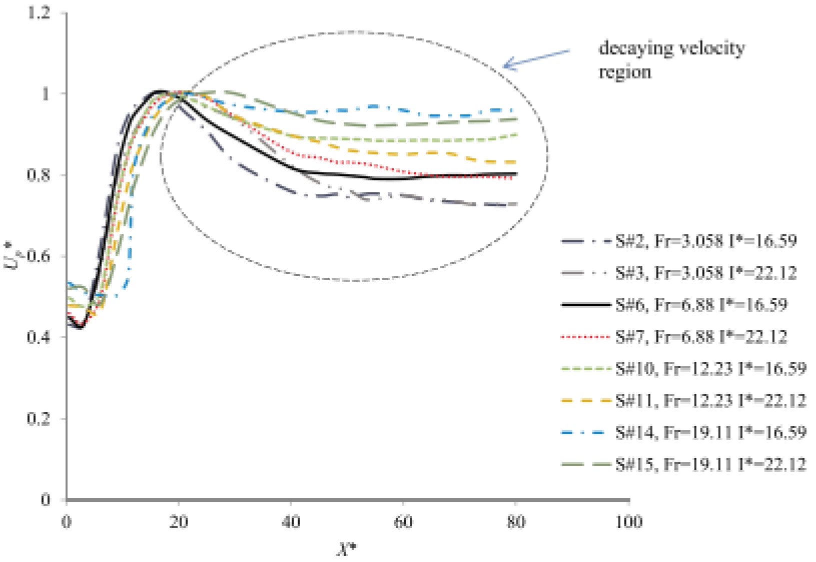

Fig. 14. Variation of normalized plume velocity along the wind enhancement plume line.

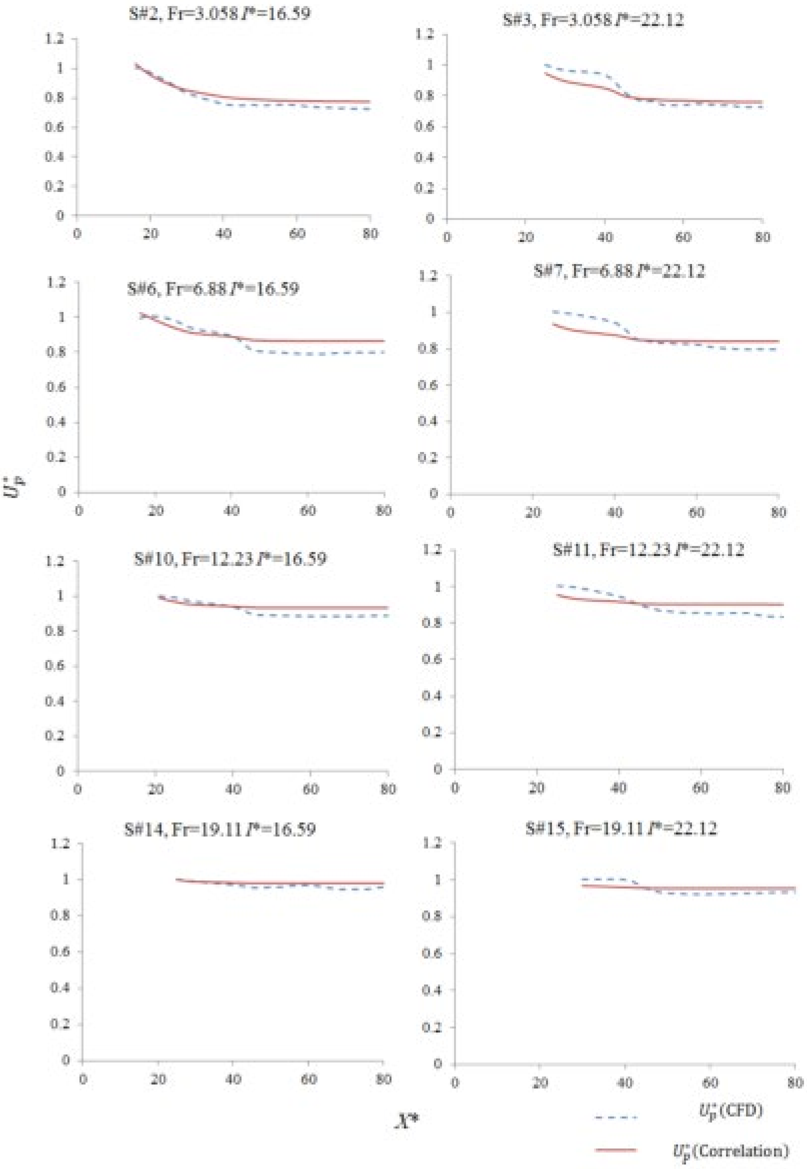

Fig. 15. Comparison of normalized plume velocity (U_p^* for $X^* > X^*_{e\_max}$) between CFD data and the developed correlation [Eq. (28)].

axis indicates the normalized longitudinal position (X^*) corresponding to the plume line. Fig. 14 shows that for all examined simulation scenarios, the normalized enhanced velocity first increases and then reaches the maximum wind enhancement (U_{e_max}) followed by the decaying trend. To explain why wind enhancement undergoes decay after reaching a peak, it is necessary to address mechanisms through which wind is enhanced by fire. According to Eftekharian et al. (2019), wind enhancement occurs due to the combined effects of fire-induced pressure gradient and density. Strongest wind enhancement happens in a region where fire-induced pressure force has the highest value and air density is minimum. Figs. 5 and 6 confirm that in all simulation scenarios, strongest fire-induced pressure gradient occurs in low density region immediately downstream of the fire source, causing occurrence of maximum wind enhancement. Further downstream, gradually fire-induced pressure force starts to decrease and density increases along the plume line, causing decay of wind enhancement. Fig. 14 reveals that the higher rate of decay velocity happens in the scenarios with the greater maximum wind enhancement. For example, the highest decay rate of velocity is observed in S#2 and S#3 possessing comparatively higher wind enhancement values (see Fig. 4 and also Table 2).

The results obtained from the decaying velocity of different simulation scenarios were also fit to a correlation:

$$U_p^* = \exp(-r'X^*) + t', \text{ for } X^*>X^*_{(\varepsilon\_max)} \tag{28}$$

where r' is the decay rate and t' is the asymptotic limit of decay such that when $X^* \to \infty$, $U_p^* \to t'$.

These two parameters are functions of normalized maximum wind enhancement as expressed below:

$$r' = 0.2(U^*_{\varepsilon\_max})^{-1} \tag{29}$$

$$t' = (U^*_{\varepsilon\_max})^{-0.3} \tag{30}$$

Fig. 15. compares the normalized plume velocity of the CFD results and that predicted by the developed correlation [Eq. (28)]. Fig. 15 shows that there is a good agreement (average error of less than 4%) between CFD results that those predicted by Eq. (28). Fig. 15 also confirms that there is a higher decay of velocity in scenarios with a higher maximum wind enhancement.

7. Conclusion

LES study was conducted to determine the effects of freestream wind velocity and fire intensity on the enhancement of wind by fire. A number of simulation scenarios with different combinations of freestream wind velocity and fire intensity were performed to quantitatively determine the flow behaviour under different wind and fire intensity conditions. Correlations were developed for fire-wind enhancement flow characteristics based on the predominant non-dimensional groups (Fr and I^*). Below are the main conclusions of this study.

- LES results showed that fire-wind enhancement increases with the increase of fire intensity and reduction of freestream wind velocity.
- A correlation was developed for maximum wind enhancement ($U^*_{\varepsilon\_max}$) by fire as a function of non-dimensional groups (Fr and I^*). LES results showed that maximum wind enhancement by fire increases with the increase of I^* and reduction in Fr number.
- A correlation was also developed as a function of Fr number and I^* to represent the longitudinal location (($X^*_{\varepsilon\_max}$) at which maximum wind enhancement by fire occurs.
- It was observed that at a given distance downstream of the fire source, there exists a local maximum wind enhancement, $U^*_{max,l}$ (X^*, Z^*_m), whose vertical location (Z^*_m) was correlated with the normalized longitudinal distance X^* that represents the wind enhancement plume line.
- It was found that the wind enhancement gradually decays longitudinally along the plume line after reaching a peak downstream of the fire source. A correlation was also developed to determine the decay of the enhanced velocity as a function of the longitudinal distance downstream of the fire surface.

Acknowledgment

This project is financially supported by Australian Research Council grant ARC-DP160103248. We acknowledge the OpenFOAM Foundation for the provision of an open-source CFD platform.

References

Aboje, A.A., Hughes, K.J., Ingham, D.B., Ma, L., Williams, A., Pourkashanian, M., 2017. Numerical study of a wake-stabilized propane flame in a cross-flow of air. J. Energy Inst. 90 (1), 145–158 2017/02/01/.

Albini, F.A., 1981. A model for the wind-blown flame from a line fire. Combust. Flame 43, 155–174 1981/01/01.

Ali, S.M., Raghavan, V., Tiwari, S., 2010. A study of steady laminar diffusion flame over methanol pool surface. Int. J. Heat Mass Transf. 53 (21-22), 4696–4706.

Balbi, J.-H., Rossi, J.-L., Marcelli, T., Santoni, P.-A., 2007. A 3D physical real-time model of surface fires across fuel beds. Combust. Sci. Technol. 179 (12), 2511–2537.

Bradstock, R., Gill, A., 1993. Fire in semiarid, mallee shrublands-size of flames from discrete fuel arrays and their role in the spread of fire. Int. J. Wildland Fire 3 (1), 3–12.

Butler, B., et al., 2004. Measurements of radiant emissive power and temperatures in crown fires. Can. J. For. Res. 34 (8), 1577–1587.

Byram, G.M., 1959. Combustion of forest fuels. Forest Fire 61–89.

J. Chai and P. Rath, "Discrete-ordinates and finite-volume methods for radiation heat transfer," 2006.

Eftekharian, E., et al., 2019. Investigation of terrain slope effects on wind enhancement by a line source fire. Case Stud. Therm. Eng. 14 2019/09/01/Art100467.

Eftekharian, E., Ghodrat, M., He, Y., Ong, R.H., Kwok, K.C.S., Samali, B., 2020b. Numerical Simulation of the Effect of Terrain Slope on Fire-Wind Enhancement. ACMSM25. Springer, Singapore, pp. 1087–1096 Singapore.

Eftekharian, E., Ghodrat, M., He, Y., Ong, R.H., Kwok, K.C.S., Zhao, M., 2019. Numerical analysis of the effect of fire source configuration on fire-wind enhancement. Heat Transf. Eng. 42 (1).

Eftekharian, E., Ghodrat, M., He, Y., Ong, R.H., Kwok, K.C.S., Zhao, M., 2019b. Numerical analysis of wind velocity effects on fire-wind enhancement. Int. J. Heat Fluid Flow 80, 108471 2019/12/01/.

Eftekharian, E., Ghodrat, M., Ong, R., He, Y., Kwok, K., 2018. CFD investigation of cross-flow effects on fire-wind enhancement. In: Australasian Fluid Mechanics Conference. Adelaide, Australia.

Eftekharian, E., He, Y., Kwok, K.C.S., Ong, R.H., Yuan, J., 2019a. Investigation of fire-driven cross-wind velocity enhancement. Int. J. Therm. Sci. 141, 84–95 2019/07/01/.

Eftekharian, E., Rashidi, M., Ghodrat, M., He, Y., Kwok, K.C.S., 2020a. LES simulation of terrain slope effects on wind enhancement by a point source fire. Case Stud. Therm. Eng. 18, 100588 2020/04/01/.

J. S. Gould et al., *Project Vesta: Fire in Dry Eucalypt Forest: Fuel Structure, Fuel Dynamics and Fire Behaviour*. Ensis, 2007.

Greenshields, C.J., 2015. Openfoam User Guide 3 OpenFOAM Foundation Ltd version.

He, Y., Kwok, K.C.S., Douglas, G., Razali, I.M., 2011. Numerical Investigation of Bushfire-Wind Interaction and its Impact on Building Structure. Fire Safety Science 1449–1462.

Hilton, J., Miller, C., Sullivan, A., Rucinski, C., 2015. Effects of spatial and temporal variation in environmental conditions on simulation of wildfire spread. Environ. Model. Softw. 67, 118–127.

Hirano, T., Kinoshita, M., 1975. Gas velocity and temperature profiles of a diffusion flame stabilized in the stream over liquid fuel. Symp. (Int.) Combust. 15 (1), 379–387 1975/01/01/.

Hu, L., 2017. A review of physics and correlations of pool fire behaviour in wind and future challenges. Fire Saf. J. 91 (Supplement C), 41–55 2017/07/01/.

Hu, L., Kuang, C., Zhong, X., Ren, F., Zhang, X., Ding, H., 2017. An experimental study on burning rate and flame tilt of optical-thin heptane pool fires in cross flows. Proc. Combust. Inst. 36 (2), 3089–3096 2017/01/01/.

Hu, L., Liu, S., de Ris, J.L., Wu, L., 2013. A new mathematical quantification of wind-blown flame tilt angle of hydrocarbon pool fires with a new global correlation model. Fuel 106, 730–736 4//.

Hu, L., Liu, S., Xu, Y., Li, D., 2011. A wind tunnel experimental study on burning rate enhancement behaviour of gasoline pool fires by cross air flow. Combust. Flame 158 (3), 586–591.

Hu, L., Zhang, X., Delichatsios, M.A., Wu, L., Kuang, C., 2017. Pool fire flame base drag behaviour with cross flow in a sub-atmospheric pressure. Proc. Combust. Inst. 36 (2), 3105–3112 2017/01/01/.

M. Inc, "MATLAB–MathWorks," 2016.

Koo, E., Pagni, P., Stephens, S., Huff, J., Woycheese, J., Weise, D., 2005. A simple physical model for forest fire spread rate. Fire Saf. Sci. 8, 851–862.

Krishnamoorthy, G., 2012. A comparison of angular discretization strategies for modeling radiative transfer in pool fire simulations. Heat Transf. Eng. 33 (12), 1040–1051.

Kwok, K., He, Y., Douglas, G., 2012. Bushfire-enhanced wind load on structures. Proc. Inst. Civil Eng.-Eng. Comput. Mech. 165 (4), 253–263.

Lam, C.S., Weckman, E.J., 2015. Wind-blown pool fire, Part II: Comparison of measured flame geometry with semi-empirical correlations. Fire Saf. J. 78, 130–141 11//.

Lautkaski, R., 1992. Validation of flame drag correlations with data from large pool fires. J. Loss. Prev. Process. Ind. 5 (3), 175–180.

Li, Y.Z., et al., 2017. Verification, Validation and Evaluation of FireFOAM as a Tool for Performance Design, ed. .

Lin, Y., Delichatsios, M.A., Zhang, X., Hu, L., 2019. Experimental study and physical analysis of flame geometry in pool fires under relatively strong cross flows. Combust. Flame 205, 422–433 2019/07/01/.

Lin, Y., Zhang, X., Hu, L., 2018. An experimental study and analysis on maximum horizontal extents of buoyant turbulent diffusion flames subject to relative strong cross flows. Fuel 234, 508–515.

Liu, S., Hu, L., 2019. An experimental study on flame envelope morphologic characteristics of downward-orientated buoyant turbulent jet fires. In: Proceedings of the Combustion Institute. 37. pp. 3935–3942 2019/01/01/.

Lu, Y., Huang, X., Hu, L., Fernandez-Pello, C., 2019. The interaction between fuel inclination and horizontal wind: Experimental study using thin wire. In: Proceedings of the Combustion Institute. 37. pp. 3809–3816 2019/01/01/.

Malalasekera, W., Ibrahim, S.S., Masri, A.R., Gubba, S.R., Sadasivuni, S., 2013. Experience with the large eddy simulation (LES) technique for the modeling of premixed and non-premixed combustion. Heat Transf. Eng. 34 (14), 1156–1170.

Maragkos, G., Beji, T., Merci, B., 2017. Advances in modelling in CFD simulations of turbulent gaseous pool fires. Combust. Flame 181, 22–38 2017/07/01/.

Margerit, J., Séro-Guillaume, O., 2002. Modelling forest fires. Part II: reduction to two-dimensional models and simulation of propagation. Int. J. Heat Mass Transf. 45 (8), 1723–1737 2002/04/01/.

B. J. McCaffrey, "Purely buoyant diffusion flames: some experimental results," vol. NBSIR79–1910, 1979.

Mell, W., Charney, J., Jenkins, M.A., Cheney, P., Gould, J., 2013. Numerical simulations of grassland fire behaviour from the LANL-FIRETEC and NIST-WFDS models. Remote Sensing and Modeling Applications to Wildland Fires. Springer, pp. 209–225.

Mendes-Lopes, J.M., Ventura, J.M., Amaral, J.M., 2003. Flame characteristics, temperature–time curves, and rate of spread in fires propagating in a bed of Pinus pinaster needles. Int. J. Wildland Fire 12 (1), 67–84.

Morandini, F., Simeoni, A., Santoni, P.-A., Balbi, J.-H., 2005. A model for the spread of fire across a fuel bed incorporating the effects of wind and slope. Combust. Sci. Technol. 177 (7), 1381–1418.

Morvan, D., Dupuy, J.L., 2004. Modeling the propagation of a wildfire through a Mediterranean shrub using a multiphase formulation. Combust. Flame 138 (3), 199–210 2004/08/01/.

Morvan, D., Dupuy, J., 2001. Modeling of fire spread through a forest fuel bed using a multiphase formulation. Combust. Flame 127 (1-2), 1981–1994.

Morvan, D., Porterie, B., Larini, M., Loraud, J.C., 1998. Numerical simulation of turbulent diffusion flame in cross flow. Combust. Sci. Technol. 140 (1-6), 93–122.

Nelson Jr, R.M., Adkins, C.W., 1986. Flame characteristics of wind-driven surface fires. Can. J. For. Res. 16 (6), 1293–1300.

Nmira, F., Consalvi, J., Boulet, P., Porterie, B., 2010. Numerical study of wind effects on the characteristics of flames from non-propagating vegetation fires. Fire Saf. J. 45 (2), 129–141.

Ping, P., He, X., Kong, D., Wen, R., Zhang, Z., Liu, P., 2018. An experimental investigation of burning rate and flame tilt of the boilover fire under cross air flows. Appl. Therm. Eng. 133, 501–511 2018/03/25/.

Pope, S.B., Pope, S.B., 2000. Turbulent Flows. Cambridge University Press.

Putnam, A.A., 1965. A model study of wind-blown free-burning fires. Symp. (Int.) Combust. 10 (1), 1039–1046.

Quintiere, J.G., Grove, B.S., 1998. A unified analysis for fire plumes. Symp. (Int.) Combust. 27 (2), 2757–2766 1998/01/01/.

Raj, P.K., 2010. A physical model and improved experimental data correlation for wind induced flame drag in pool fires. Fire Technol. 46 (3), 579–609.

Rew, P., Hulbert, W., Deaves, D., 1997. Modelling of thermal radiation from external hydrocarbon pool fires. Process Saf. Environ. Prot. 75 (2), 81–89.

Rossa, C.G., Davim, D.A., Viegas, D.X., 2015. Behaviour of slope and wind backing fires. Int. J. Wildland Fire 24 (8), 1085–1097.

Sergent, M.E., 2002. Vers une Méthodologie de Couplage Entre la Simulation des Grandes Echelles et les Modèles Statistiques. Ecole Central de Lyon Phd Thesis.

Shi, L., Shi, L., Yeo, D., 2016. OpenFOAM large-eddy simulations of atmospheric boundary layer turbulence for wind engineering applications. US Department of Commerce. National Institute of Standards and Technology.

Sinai, Y.L., Owens, M.P., 1995. Validation of CFD modelling of unconfined pool fires with cross-wind: Flame geometry. Fire Saf. J. 24 (1), 1–34.

Snegirev, A.Y., 2004. Statistical modeling of thermal radiation transfer in buoyant turbulent diffusion flames. Combust. Flame 136 (1-2), 51–71.

Souil, J.M., Joulain, P., Gengembre, E., 1984. Experimental and theoretical study of thermal radiation from turbulent diffusion flames to vertical target surfaces. Combust. Sci. Technol. 41 (1-2), 69–81 1984/09/20.

Sun, X., Zhang, X., Hu, L., Kuwana, K., 2019. Temperature evolution and transition inside fire compartment with an opening subject to external sideward wind. In: Proceedings of the Combustion Institute. 37. pp. 3869–3877 2019/01/01/.

Tang, F., He, Q., Wen, J., 2019. Effects of crosswind and burner aspect ratio on flame characteristics and flame base drag length of diffusion flames. Combust. Flame 200, 265–275.

Tang, F., Hu, L., Zhang, X., Zhang, X., Dong, M., 2015. Burning rate and flame tilt characteristics of radiation-controlled rectangular hydrocarbon pool fires with cross air flows in a reduced pressure. Fuel 139, 18–25 2015/01/01/.

Tang, F., Li, L.J., Zhu, K.J., Qiu, Z.W., Tao, C.F., 2015. Experimental study and global correlation on burning rates and flame tilt characteristics of acetone pool fires under cross air flow. Int. J. Heat Mass Transf. 87, 369–375 8//.

Tang, W., Miller, C.H., Gollner, M.J., 2017. Local flame attachment and heat fluxes in wind-driven line fires. In: Proceedings of the Combustion Institute. 36. pp. 3253–3261.

Thomas, P.H., 1963. The size of flames from natural fires. Symp. (Int.) Combust. 9 (1), 844–859 1963/01/01/.

Thomas, P., Pickard, R., Wraight, H., 1963. On the size and orientation of buoyant diffusion flames and the effect of wind. Fire Saf. Sci. 516 1–1.

Vilfayeau, S., 2015. Large Eddy Simulation of Fire Extinction Phenomena. University of Maryland College Park.

Vilfayeau, S., White, J.P., Sunderland, P.B., Marshall, A.W., Trouvé, A., 2016. Large eddy simulation of flame extinction in a turbulent line fire exposed to air-nitrogen co-flow. Fire Saf. J. 86, 16–31 11//.

Wang, J., et al., 2019. Sooting tendencies of propane jet diffusion flame under crossflow. Fuel 245, 247–252 2019/06/01/.

Wang, Y., Chatterjee, P., de Ris, J.L., 2011. Large eddy simulation of fire plumes. Proc. Combust. Inst. 33 (2), 2473–2480 //.

Weise, D.R., Koo, E., Zhou, X., Mahalingam, S., Morandini, F., Balbi, J.-H., 2016. Fire spread in chaparral–a comparison of laboratory data and model predictions in burning live fuels. Int. J. Wildland Fire 25 (9), 980–994.

Yoshihara, N., Ito, A., Torikai, H., 2013. Flame characteristics of small-scale pool fires under low gravity environments. In: Proceedings of the Combustion Institute. 34. pp. 2599–2606.

Zhang, X., Xu, W., Hu, L., Liu, X., Zhang, X., Xu, W., 2016. A new mathematical method for quantifying trajectory of buoyant line-source gaseous fuel jet diffusion flames in cross air flows. Fuel 177, 107–112 8/1/.

Zhang, X., Zhang, X., Hu, L., Tu, R., Delichatsios, M.A., 2019. An experimental investigation and scaling analysis on flame sag of pool fire in cross flow. Fuel 241, 845–850 2019/04/01/.

Zhou, X., Mahalingam, S., Weise, D., 2005. Modeling of marginal burning state of fire spread in live chaparral shrub fuel bed. Combust. Flame 143 (3), 183–198.

Appendix A5

Esmaeel Eftekharian, Maryam Ghodrat, Yaping He, Robert H. Ong, Kenny C. S. Kwok, Ming Zhao, Bijan Samali, **Investigation of terrain slope effects on wind enhancement by a line source fire,** *Case Studies in Thermal Engineering.* 2019; Volume 14, Article No: 100467. https://doi.org/10.1016/j.csite.2019.100467.

Case Studies in Thermal Engineering 14 (2019) 100467

Contents lists available at ScienceDirect

Case Studies in Thermal Engineering

journal homepage: www.elsevier.com/locate/csite

Investigation of terrain slope effects on wind enhancement by a line source fire

E. Eftekharian[a,*], M. Ghodrat[a], Y. He[a], R.H. Ong[b], K.C.S. Kwok[b], M. Zhao[a], B. Samali[a]

[a] *Center for Infrastructure Engineering, School of Computing Engineering and Mathematics, Western Sydney University, Penrith, NSW, 2751, Australia*
[b] *School of Civil Engineering, The University of Sydney, NSW, Australia*

ARTICLE INFO

Keywords:
Upslope
Downslope
Wind enhancement
Fire
CFD
Coanda effects

ABSTRACT

Wind enhancement triggered by fire-wind interaction can potentially pose significant damage to structures built in bushfire prone areas. The effect of terrain slope is one of the parameters contributing to the enhancement of wind by fire that needs to be taken into account. This study employs a validated model of Computational Fluid Dynamics to assess the effects of terrain slope on this phenomenon. A module was developed and appended to the FireFOAM solver to output individual component of flow acceleration. Multiple analyses were used to explain the effects of terrain upslope and downslope on the phenomenon. The results reveal that although the enhancement of wind velocity due to fire increases with an increase in terrain upslope, a terrain downslope reduces flow enhancement by fire. The results also established that while an upslope terrain reinforces the Coanda effects and intensifies attachment of the plume to the ground, the downslope condition mitigates Coanda effects and reduces the flow's tendency to attach to the ground downstream of the fire source. Furthermore, under a constant heat release rate and upstream wind velocity, the maximum magnitude of wind enhancement linearly increases with the increase of upslope angle.

1. Introduction

Interaction of wind and fire is a two-sided issue. On the one hand, wind leads to a change of fire plume geometrical structures and on the other, fire also influences the freestream (wind) aerodynamics. Many researchers have investigated the effects of wind on fire plume geometrical properties, such as fire plume tilt angle and flame length under the conditions of flat ground [1–3] as well as sloped ground [4,5] and unveiled a number of interesting fire behavior under the influence of wind [6–15].

Flame base drag is one of the important phenomena that happens during fire-wind interaction in which flame is horizontally extended downstream of the fire source [6]. Experimental studies have been conducted to quantitatively investigate flame base drag phenomenon and it was found that flame extension first increases and then decreases with the increase of upstream wind velocity [7]. Correlations were developed for flame base drag length [7,8]. The combined effects of cross-flow and sub-atmospheric pressure on flame base drag length were also investigated [9].

Flame sag is another phenomenon that occurs due to the interaction of cross-wind with pool fire above the ground surface [10]. In this phenomenon, the flame is deflected toward the ground at the leeward side of the lifted fire source [10] primarily due to the complex pressure field in the wake flow in the lee of the pool. Flame sag phenomenon was initially reported in Refs. [11,12], however, a comprehensive experimental study has only recently been conducted to determine flame sag behavior under different

---

[*] Corresponding author.
E-mail address: E.Eftekharian@westernsydney.edu.au (E. Eftekharian).

https://doi.org/10.1016/j.csite.2019.100467
Received 2 April 2019; Received in revised form 13 May 2019; Accepted 17 May 2019
Available online 17 May 2019

wind velocity, fire heat release rate and pool fire height conditions [10].

Another phenomenon involved in fire-wind interaction with more relevant industrial applications is flame downwash which is referred to as flame pulling by the wake produced at the burner nozzle leeward side [13]. Flame downwash length is of great importance in designing industrial burners [14]. Recently, experimental investigations have been carried out to determine flame downwash length for different cross-wind and fuel jet velocities as well as nozzle diameters and a correlation for these parameters has been developed [13]. A correlation was also developed for maximum flame downwash length [15].

The aforementioned studies primarily focused on the effects of wind on pool fire or point source fires. Some studies [4,5] focused on the effect of terrain slope and wind on fire behavior. However, very few studies could be found in the literature that address the effects of terrain slope on aerodynamics change of wind during fire-wind interaction, particularly involving a line source fire setting that resembles bushfire (wildland fire) front.

Fire-wind enhancement is one of the detrimental effects of major bushfire attacks. Lambert [16] and McRae et al. [17] identified that wind can be magnified because of its interaction with bushfire. He et al. [18] and Kwok et al. [19] studied bushfire-wind interaction numerically and revealed that it may elevate the near ground wind velocity downstream of the bushfire source to a considerable extent. Owing to the escalation of wind velocity because of wind-fire interaction, the pressure coefficient around buildings downstream of the bush-fire source will be correspondingly increased. Recently, using numerical simulation, Eftekharian et al. [20] fundamentally investigated the fire-wind enhancement phenomenon and revealed that as a result of the interaction of wind with fire, a negative streamwise pressure gradient is generated in the fire plume region which causes flow acceleration and increase of wind velocity downstream of the fire source. They also investigated the effects of heat release rate on the phenomenon and showed that wind enhancement is intensified as fire heat release rate increases. In a separate study, Eftekharian et al. [21], investigated the effects of wind velocity on the enhancement of wind by fire. It was shown that under a constant fire heat release rate, the magnitude of flow enhancement decreases as the freestream wind velocity increases.

It has long been recognized that wildfire spread on uphill slopes is faster than on flat grounds [22,23]. The rise in the fire spread rate was usually thought to be associated with the flames tilting towards or in direct contact with the ground fuel bed [23,24], but in fact, the total flame streamwise velocity profile and fire-induced flow are subjected to more fundamental variations in which the sloped terrain and some dangerous fire behavior were reported [24].

Some experimental studies have shed light on the effect of terrain slope on the kinematics of bushfires such as fire front shape and the relative fire propagation rate. The aforementioned terrain slope effects have commonly been assessed in conjunction with wind for various fuels [25–27]. Other studies produced useful sets of data to validate semi-empirical fire spread models [25,28]. Lately, Dupuy et al. [29] analyzed the influence of terrain slope and fuel bed geometry on the kinematics of the fire front to explain the mechanisms behind fire front shape and the pattern of line source fire. These researchers found that the fire-induced wind behind the fire was more intense when the terrain angle enlarged. Wind–slope correction models were developed by some researchers such as Sharples [30]. These models are central to the idea of wind-slope corrections of fire spread rates based on the concepts of wind vector, topographic slope and other topographic aspects of the studied area. Their study [30] includes a systematic review of the techniques for merging the slope correction models with the rate of spread calculations and specified two main methods which can be applied to either empirical [31] or semi-physical models [32] of fire spread and slope interactions.

The effects of terrain slope in bushfire modeling approaches have been taken into account for years. Currently, with the development of computational fluid dynamics methods for simulating fire propagation scenarios [33–35], there has been a renewed focus on developing an in-depth understanding of the effect of slope on fire-wind enhancement [30–32]. However, predicting the influence of terrain slope on fire-wind enhancement has been a challenging task which has neither been accurately identified nor sufficiently understood. Some researchers indicated air flow acceleration on windward terrain slopes may be responsible for fire propagation [36,37], whereas others claimed reduced angles between fuel and buoyant plume leads to an increase in heat flux [38,39]. Some other researchers such as Wu et al. [40] proposed the attachment of flames to the slope as the underlying mechanism for the rate of fire spread variation on slope terrain.

Although studies into this matter have been limited, yet, a number of laboratory scale researches have been carried out aiming at developing techniques to quantify the impact of terrain slope on propagation rate [40–42]. In spite of enhancement in computer simulation of the fire spread edge and improvements in three-dimensional information systems on geomorphology facilitated prediction of bushfire spread [43–47], fundamental understanding of the flow aerodynamics identifying the influences of terrain slope on the behavior of wind-fire enhancement is still in its early observation and empirical modeling stages.

One of the parameters that influence fire spread rate on the hilly terrains is the attachment of flames to the slope by the Coanda effect [40,41]. In fact, the Coanda effect is a reaction to the pressure difference induced by changes in the capacity for entrainment of air upslope and downslope of the fire and is considered as the main cause of plume attachment to the ground [48]. For locations with a slope of about 40°–42°, there is a possibility for an unexpected wind to happen due to the Coanda effect. In other words, it is likely that the wind felt by firefighters in Tuolumne Fire event in California on a steep hill was actually sourced by flow within the buoyant plume itself as stated by Sharples et al. [48]. They concluded that the experienced abrupt wind change in upslope terrain is compatible with what observed in the initial stage of plume attachment due to the Coanda effect.

The principal aim of this research is to shed light on the effects of sloped terrain on fire-wind enhancement and to investigate how flow accelerates during fire-wind interaction on hilly terrain.

This study attempts to fundamentally explain how the terrain slope affects the interaction between streamwise wind and vertical buoyant plume and alter the velocity profile near the ground. For this purpose, the flow acceleration is explicitly expressed in terms of contributions from pressure gradient, body force, and shear stress. A computational fluid dynamics method is used to quantitatively define the contribution of these terms.

2. Numerical approach

FireFOAM was used as a CFD solver in this study. This solver is a derivative of OpenFOAM [49] platform, specifically designed for the fire dynamic simulations. OpenFOAM is an object-oriented open-source platform which allows the users to add self-developed modules to the main code. FireFOAM employs the LES (Large Eddy Simulation) scheme to solve Favre-filtered continuity, momentum, energy, species and state equations for compressible-flows [50].

$$\frac{\partial\bar{\rho}}{\partial t}+\frac{\partial(\bar{\rho}\tilde{u}_i)}{\partial x_i}=0 \tag{1}$$

$$\frac{\partial(\bar{\rho}\tilde{u}_i)}{\partial t}+\frac{\partial(\bar{\rho}\tilde{u}_i\tilde{u}_j)}{\partial x_j}=\frac{\partial}{\partial x_j}\left[\bar{\rho}(\nu+\nu_t)\left(\frac{\partial(\tilde{u}_i)}{\partial x_j}+\frac{\partial(\tilde{u}_j)}{\partial x_i}-\frac{2}{3}\frac{\partial\tilde{u}_k}{\partial x_k}\delta_{ij}\right)\right]-\frac{\partial\bar{p}}{\partial x_i}+\bar{\rho}g_i \tag{2}$$

$$\frac{\partial(\bar{\rho}\tilde{h})}{\partial t}+\frac{\partial(\bar{\rho}\tilde{u}_j\tilde{h})}{\partial x_j}=\frac{D\bar{p}}{Dt}+\frac{\partial}{\partial x_j}\left[\bar{\rho}\left(\alpha_t+\frac{\nu_t}{\mathrm{Pr}_t}\right)\left(\frac{\partial\tilde{h}}{\partial x_j}\right)\right]+\dot{q}'''-\nabla\cdot\dot{q}_r'' \tag{3}$$

$$\frac{\partial\bar{\rho}\widetilde{Y_m}}{\partial t}+\frac{\partial(\bar{\rho}\tilde{u}_j\widetilde{Y_m})}{\partial x_j}=\frac{\partial}{\partial x_j}\left[\bar{\rho}\left(D_c+\frac{\nu_t}{\mathrm{Sc}_t}\right)\frac{\partial(\widetilde{Y_m})}{\partial x_j}\right]+\omega_m \tag{4}$$

$$\bar{p}=\bar{\rho}R\tilde{T} \tag{5}$$

here the symbols "$-$" and "$\sim$" indicate spatial and Favre filtering. p is the static pressure, h is total enthalpy, Y_m is the mass fraction of species m, g is gravitational acceleration, ρ, ν, ν_t, D_c, R, α_t, Pr_t, Sc_t δ and ω_m, are density, laminar viscosity, turbulent viscosity, laminar diffusion coefficient, gas constant, thermal diffusion coefficient, turbulent Prandtl number, turbulent Schmidt number, Kronecker delta and production/sink rate of species m due to gas reaction respectively. $\dot{q}'''$ is heat release rate per unit volume (W/m^3) from a chemical reaction and $\dot{q}_r''$ is the total radiation emission intensity (W/m^2) of the gas mixture. 20% of the radiant fraction was used in this study. FireFOAM uses PIMPLE scheme to couple velocity and pressure field. First order upwind was used as the differencing scheme and kEq model was used to model sub-grid scale turbulent structures. Eddy Dissipation Model (EDM) was applied as the combustion model.

Momentum equation [Eq. (2)] can be written based on the flow acceleration as:

$$\vec{a}=\frac{D\vec{u}}{Dt}=\frac{-\nabla p}{\rho}+\vec{g}+\frac{\Phi}{\rho} \tag{6}$$

in which $\vec{a}$ is the flow acceleration, u is the flow velocity, ∇p is pressure gradient (N/m^2.s), ρ is density (m^3/s), $\vec{g}$ is gravitational acceleration and Φ is the viscous shear stress vector or $(\Phi_i)=\frac{\partial(\sigma_{ji})}{\partial x_j}$ in which σ_{ji} is the components of stress. Eq. (6) shows that the flow acceleration can be decomposed into three components, namely, pressure acceleration$\left(\frac{-\nabla p}{\rho}\right)$, gravitational acceleration ($\vec{g}$) and viscous acceleration $\left(\frac{\Phi}{\rho}\right)$.

2.1. Model description and boundary conditions

The computational domain consists of a rectangular box with the dimension of 34 × 9 × 15 m as shown in Fig. 1. The origin of the computational coordinate system is set at the center of the firebed which has a depth D of 0.3 m and a width W of 9 m extending to

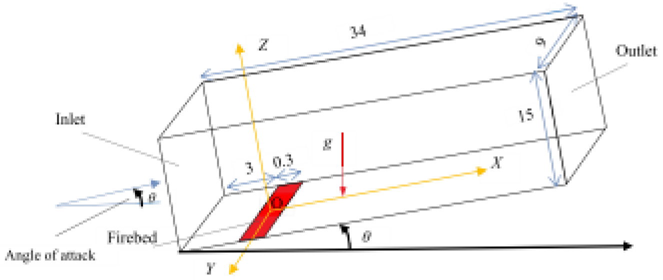

Fig. 1. A schematic view of the computational domain at a slope angle θ from Earth horizontal direction ($\theta > 0$: upslope; $\theta = 0$: no slope; and $\theta < 0$: downslope). Dimensions are in meter.

the full width of the computation domain. The firebed is flush with the ground and its leading edge is 3 m from the inlet of the domain. The domain inclination angle to the Earth horizontal, θ, is specified through the angle of gravitational acceleration to the z-coordinate of the computation domain. A negative value of θ indicates downslope. In such a specified computation domain, gravitational acceleration has two non-zero components:

$$g_x = -g\sin(\theta) \text{ and } g_z = -g\cos(\theta) \tag{7}$$

Since buoyancy force is in opposite direction to gravitation acceleration, the heated fire plume will experience positive acceleration in x and z-direction under the upslope condition ($\theta > 0$); but the deceleration in x-direction and acceleration in z-direction under the downslope condition ($\theta < 0$).

A line source of fire with a width of 0.3 m is introduced 3 m downstream of the domain inlet. Methane was used as the fuel in the burner (fire source) to generate a 6.6 MW/m^2 heat release rate intensity which corresponds to a fire line intensity of $I = 1.98$ MW/m. Atmospheric boundary layer condition with power-law velocity profile was considered as in Eq. (8) for the domain inlet.

$$U(Z) = U_{ref}\left(\frac{Z}{Z_{ref}}\right)^{\alpha} \tag{8}$$

in which U_{ref} and Z_{ref} are respectively the reference velocity (4.5 m/s) and reference height (3 m). The value of the power exponent α is determined according to the terrain category and for the current study is taken to be 0.16. The two dimensional vortex method [51] was used to take into account turbulent structures at the domain inlet. The initial temperature and velocity inside the whole domain were set to be 300 K and 0 m/s respectively.

Simulations were performed for no slope condition ($\theta = 0^\circ$), four different terrain upslope angles ($\theta = 5^\circ, 15^\circ, 10^\circ, 20^\circ$) and four terrain downslope angles ($\theta = -5^\circ, -15^\circ, -10^\circ, -20^\circ$) to evaluate the impact of terrain slope on fire-wind enhancement. The incoming flow direction for all cases is parallel with respect to the slope angle as shown in Fig. 1; in other words, the angle of attack for incoming flow in each case is equal to the slope angle. Adiabatic boundary condition was used for the domain base.

No-slip wall boundary condition was prescribed for the domain base, while slip boundary was assigned to the domain sides. To treat the wall-bounded flow over the domain base, wall-function approach [52] was used. Open boundary condition was prescribed for the domain top to allow flows cross the boundary and a typical outflow boundary was applied to the domain outlet.

2.2. *Grid sensitivity analysis*

The grid sensitivity study was conducted with a grid similar to that used in our previous works [20,21]. The grid system includes a structured non-uniform grid with the smaller cell size in the critical fire plume region. The three different grid sizes including coarse [600 k (70 × 90 × 98)], medium [2.4 million, (127 × 149 × 130)] and fine [7 million, (197 × 163 × 220)] were tested. The results showed that negligible differences (< 1%) in both streamwise velocity and density distributions were found between the results of the medium and fine grid, while the corresponding differences between the coarse and medium grid were about 1.7%. Hence, the medium grid was chosen for simulation in this study.

2.3. *Model validation*

The numerical model has been validated with two sets of experimental data, one involves diffusion flame in still air [53] and the other in cross-flow [54] conditions. The details of the validation exercise were reported in our previous studies [20,21].

3. Result and discussion

3.1. *Upslope fire spread*

Simulated flow duration for all simulation cases is 24 s. The first 12 s is considered as the transition period for the simulation to reach a quasi-steady condition. Therefore, all the presented results are established on the average of the last 12 s of the quasi-steady period. The streamwise velocity is defined as the velocity in the X direction in Fig. 1.

Fig. 2 depicts the influence of terrain upslope on different flow aerodynamic features including normalized streamwise velocity, pressure gradient, acceleration and buoyancy force on a plane passing the domain centerline ($Y = 0$ in Fig. 1). The normalized streamwise buoyancy force is defined as:

$$(F_b)_x = \left(\frac{\rho_\infty - \rho}{\rho_\infty}\right)\sin\theta \tag{9}$$

Fig. 2 (a) indicates that even in no slope condition ($\theta = 0^\circ$) where the buoyancy force does not have any component in the streamwise direction, streamwise velocity is enhanced downstream of the fire source. This is mainly because when wind interacts with fire, a streamwise pressure gradient is generated along the wind direction and the fire-generated buoyant plume is tilted [20]. This fire-induced favorable pressure gradient according to Eq. (6) accelerates the flow and causes enhancement of the streamwise velocity.

Comparison of Fig. 2 (b) and (c) with (a) reveals that the streamwise buoyancy force intensifies the streamwise negative pressure

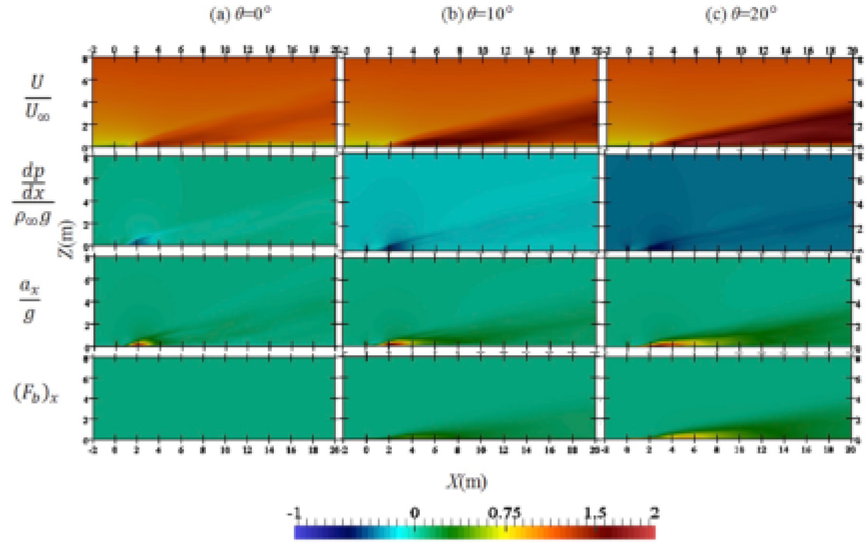

Fig. 2. Comparison of normalized streamwise velocity $\left(\frac{U}{U_{ref}}\right)$, normalized streamwise pressure gradient $\left(\frac{\frac{dp}{dx}}{\rho_\infty g}\right)$, normalized streamwise acceleration $\left(\frac{a_x}{g}\right)$ and normalized streamwise component of buoyancy force $(F_b)_x$ at $Y = 0$ for three inclination angles.

gradient which leads to a greater magnitude of wind enhancement. Fig. 2 also indicates that the higher upslope angle, the more intensified streamwise negative pressure gradient which culminates in a greater magnitude of wind enhancement.

Fig. 3 presents the cross-sectional streamwise normalized velocity at upstream and downstream of the fire source for no slope and upslope cases. The distance is normalized by the depth of the firebed. As shown in Fig. 3, for all cases, the wind velocity is enhanced at a near ground region parallel to the fire source. Fig. 3 also shows that fire plume is attached to the ground downstream of the fire source. Flame attachment to the ground downstream of the fire source was also observed in the previous studies investigating fire-wind interaction [7,9,20,21]. It is also seen that the enhanced zone of velocity is expanded with the increase of distance from the fire source. Moreover, it is observed that the higher upslope angle leads to more intensified wind enhancement. However, the region of wind enhancement is thinner when the slope angle increases. It is believed that this is due to the Coanda effect which necessitates the plume to be inclined to the ground immediately downstream of the fire source. The Coanda effects become stronger in higher upslope angles, because in these cases, in addition to the wind force, a component of buoyancy force is created in wind direction, strengthening the Coanda effects and causing more inclination for the plume to be attached to the ground.

3.2. Downslope fire spread

Fig. 4 shows the influence of terrain downslope on different flow aerodynamic characteristics. As can be observed, in contrast to the upslope, downslope terrain has an adverse effect on the enhanced wind by fire. The higher the downslope angle, the lower the wind enhancement. The reason behind is that in downslope scenarios, a component of buoyancy force acts against wind direction which tends to decelerate the flow. In fact, in downslope condition, the adverse effects of buoyancy force counteract the favorable pressure gradient being generated due to the fire-wind interaction. Immediately downstream of the fire source, the fire-induced pressure gradient (pressure force) which causes enhancement of wind by fire is strong. This pressure force prevails the adverse effects of buoyancy force and causes enhancement of wind as shown in Fig. 4 (b) and (c). However, further downstream of the fire source where the fire-induced pressure force becomes weaker, the adverse effects of buoyancy become dominant and significantly reduce the wind velocity. At some regions, the overall effects of fire-induced pressure gradient and adverse effects of buoyancy force cause flow deceleration which leads to the reduction of the wind velocity to even lower than the freestream wind velocity.

Fig. 5 shows how downslope affects streamwise velocity. Cross-sectional normalized streamwise velocity distribution on Fig. 5 shows that downslope may not only reduce the magnitude of flow enhancement by fire, but also the near ground flow velocity even lower than freestream wind velocity in relatively large downslope angles. For example, at 18D downstream of the fire source with the downslope angle of $\theta = -20^\circ$, the adverse buoyancy force causes a reduction in freestream wind velocity by almost 50%, creating a low-velocity region even lower than the freestream wind velocity. Moreover, in contrast to the upslope case, in the downslope

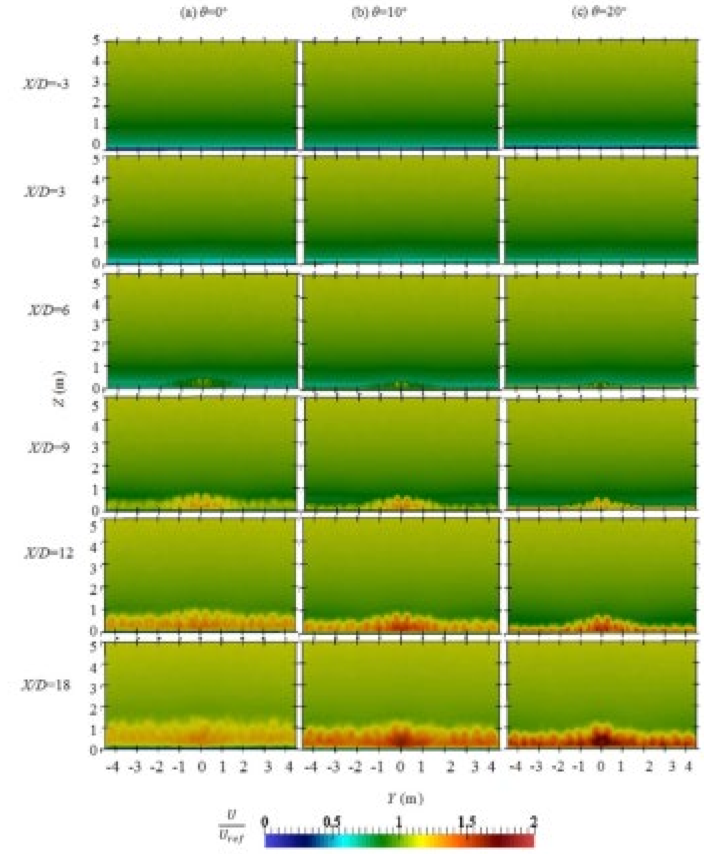

Fig. 3. Cross-sectional normalized streamwise velocity $\left(\frac{U}{U_{ref}}\right)$ at different distances (X/D) from the fire source subjected to different slope conditions.

scenario, the near-ground region of wind enhancement is thicker than that of no slope condition. This happens mainly because the adverse buoyancy force generated in downslope cases reduces the Coanda effects, the very effect which causes the attachment of plume to the ground immediately downstream of the fire source.

3.3. *Comparison of upslope and downslope*

The location and the magnitude of the maximum velocity enhancement were searched in the flow filed for all simulations fire scenarios. Let $U_{\max}$ denotes the maximum streamwise velocity observed in the domain, L_x and L_z denote the X and Z coordinates of the location where $U_{\max}$ is observed. The normalized quantities of the above are listed in Table 1. As can be seen, for all upslope angles, the vertical distance L_z does not significantly increase, despite the increase of buoyancy force with the slope angle. This is mainly because of the dominance of Coanda effects which causes the plume to be attached to the ground immediately downstream of the fire source. However, in downslope cases, this distance (L_z) increases noticeably as the magnitude of the downslope angle increases. The major reason for this trend is that Coanda effects are weakened by the buoyancy force component against the flow in the streamwise direction. Consequently, the flow is shifted upward due to the dominance of the buoyancy force component in the vertical direction.

The variation in L_x with θ appears to follow a similar trend. In order to visualize how the maximum magnitude of wind enhancement and the corresponding streamwise location change with the slope angle, these quantities are plotted in Fig. 6 (a). Fig. 6

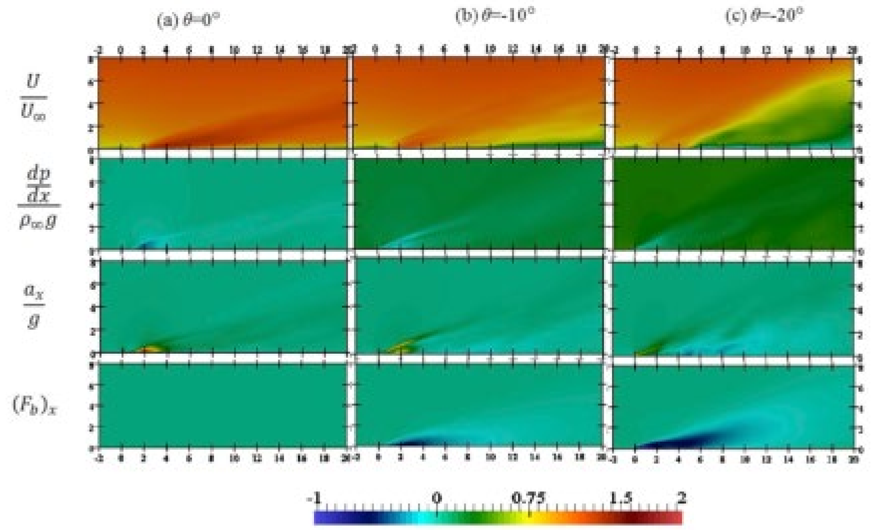

Fig. 4. Comparison of normalized streamwise velocity $\left(\frac{U}{U_\infty}\right)$, normalized streamwise pressure gradient $\left(\frac{\frac{dp}{dx}}{\rho_\infty g}\right)$, normalized streamwise acceleration $\left(\frac{a_x}{g}\right)$ and normalized streamwise component of buoyancy force $(F_b)_x$ for (a) without slope ($\theta = 0^\circ$), (b) middle downslope ($\theta = -10^\circ$), high downslope ($\theta = -20^\circ$).

(a$_1$) shows that the maximum magnitude of wind enhancement is insensitive to θ in the range $-20^\circ < \theta < -15^\circ$. However, for $\theta > -15^\circ$, $(U/U_{ref})_{max}$ increases with θ almost linearly. Under the given constant wind velocity and fire intensity, an increase of 1° in slope angle approximately causes the maximum magnitude of wind enhancement to increase by approximately 2%. The L_x/D curve, however, exhibits a trough at about $\theta = -5^\circ$ (See Fig. 6 (a$_2$)). It then increases almost linearly with θ for $\theta > 0^\circ$.

Fig. 6 (b) depicts the 3-D iso-contour of density distribution coloured by the streamwise normalized wind velocity U/U_{ref} for downslope, upslope and no slope cases in the plume region. In other words, Fig. 6 (b) shows a region of the domain where the flow density is lower than $0.5\rho_\infty$ (plume region) and these regions are coloured by normalized streamwise velocity.

Fig. 6 (b) reveals that the enhancement of wind by fire happens in the plume region. Moreover, the upslope intensifies the magnitude of wind enhancement by fire, whereas the downslope counteracts the flow enhancement. Additionally, in contrast to the upslope scenarios, thickness growth is observed in the downslope plume region which leads to the wind enhancement in higher altitudes. All these observations are in agreement with the results observed in Figs. 2–5.

4. Conclusion

The effects of terrain slope on fire-wind enhancement phenomenon were investigated using Computational Fluid Dynamics approach, based on FireFOAM solver. Simulations were performed for 9 different slope angles ranging from -20° (downslope) to $+20^\circ$ (upslope) under constant freestream velocity profile and constant fire intensity. It was shown that in the upslope scenarios, streamwise buoyancy force intensifies the streamwise fire-induced negative pressure gradient which leads to a greater magnitude of wind enhancement. More specifically, the following conclusions have been drawn.

- Upslope terrain can intensify enhancement of wind by fire through the generation of a component of buoyancy force in the wind direction. In contrast, downslope terrain reduces the effects of wind enhancement by fire. In this latter case, a component of buoyancy force is generated opposite to the wind direction, which causes flow deceleration.
- Upslope terrain reinforces the Coanda effects and causes the flow to be more inclined to stay attached to the ground immediately downstream of the fire, while downslope terrain mitigates the Coanda effects, culminating in the fire plume detaching from the ground earlier.
- The simulation results revealed that the maximum magnitude of wind enhancement increases almost linearly with an increase of upslope angle.

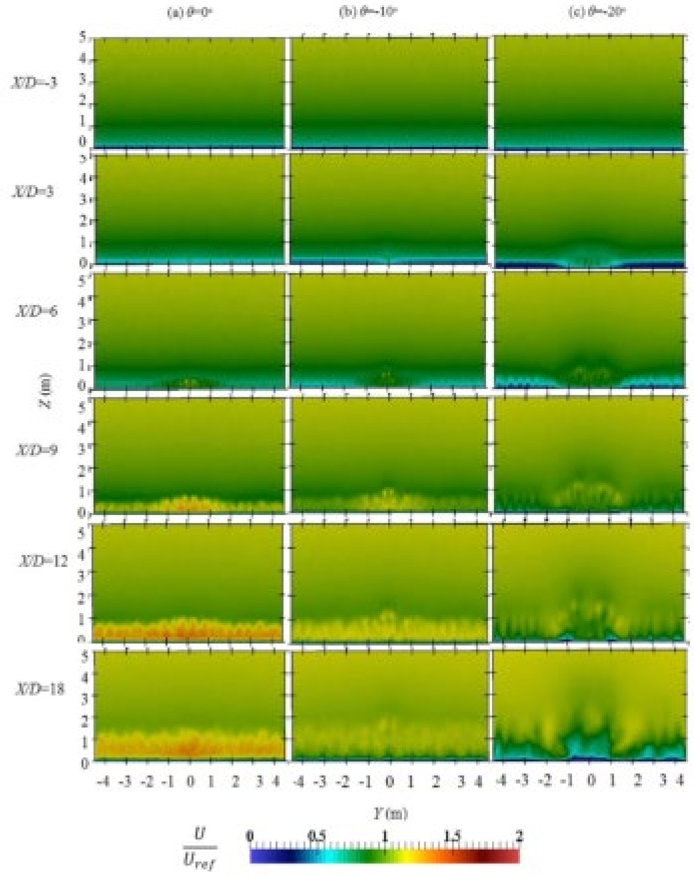

Fig. 5. Cross-sectional normalized streamwise velocity $\left(\frac{U}{U_{ref}}\right)$ at different distances (X/D) from the fire source for the case without slope ($\theta = 0^\circ$) and downslope ($\theta = -10^\circ$, $\theta = -20^\circ$) scenarios.

Table 1
Variation of maximum wind velocity enhancement and the corresponding location for different slope angles (degrees).

θ (°)	$U_{max}/Uref$	L_x/D (± 0.38)[a]	L_z/D (± 0.19)
−20	1.02	20.0	7.80
−15	1.04	14.0	4.43
−10	1.13	11.6	1.30
−5	1.22	11.0	1.06
0	1.34	12.5	0.65
5	1.47	16.0	0.85
10	1.58	19.5	1.00
15	1.77	22.5	1.30
20	1.90	26.0	1.60

[a] The half error band is determined by $\delta_x/(2D)$, where δ_x is the cell size.

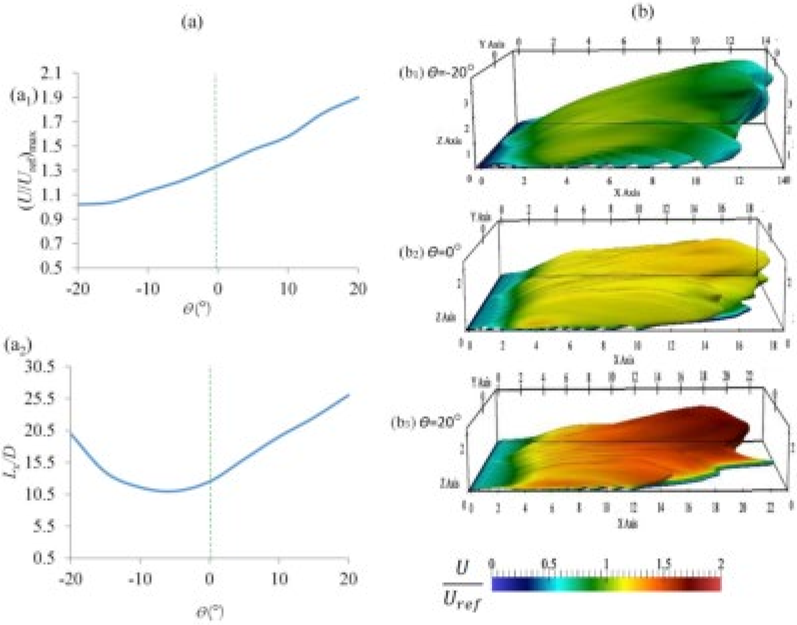

Fig. 6. Left column (a): the trend of (a_1) maximum velocity enhancement and (a_2) its corresponding location with slope angle for all simulation cases; right column (b): Contour of plume region (the domain region where the density is less than half of the freestream density ($0.5\rho_\infty$)) coloured by normalized streamwise velocity $\left(\frac{U}{U_{ref}}\right)$ for downslope (b_1), no-slope (b_2) and upslope (b_3) conditions.

The current study is limited to the idealized situation where the firebed is flush with the ground. In reality, both the firebed and the ground can be very rough. Their roughness and firebed protrusion above ground may have a strong influence on the turbulence intensity of the boundary layer flow, which, in turn, may alter the velocity profile downstream of the fire. These topics will be the subject of future studies.

Acknowledgment

This project is financially supported by an Australian Research Council Discovery Project grant ARC DP160103248. We gratefully acknowledge OpenFOAM and FM-Global Foundation which provides an open-source CFD platform.

References

[1] L. Hu, A review of physics and correlations of pool fire behaviour in wind and future challenges, Fire Saf. J. 91 (Supplement C) (2017) 41–55.
[2] L. Hu, S. Liu, J.L. de Ris, L. Wu, A new mathematical quantification of wind-blown flame tilt angle of hydrocarbon pool fires with a new global correlation model, Fuel 106 (2013) 730–736.
[3] L. Hu, L. Wu, S. Liu, Flame length elongation behavior of medium hydrocarbon pool fires in cross air flow, Fuel 111 (2013) 613–620.
[4] P. Zhu, X.S. Wang, Y.P. He, C.F. Tao, X.M. Ni, Flame characteristics and burning rate of small pool fires under downslope and upslope oblique winds, Fuel 184 (2016) 725–734.
[5] N. Liu, J. Wu, H. Chen, X. Xie, L. Zhang, B. Yao, J. Zhu, Y. Shan, Effect of slope on spread of a linear flame front over a pine needle fuel bed: experiments and modelling, Int. J. Wildland Fire 23 (8) (2014) 1087–1096.
[6] J. Welker, C. Sliepcevich, Bending of wind-blown flames from liquid pools, Fire Technol. 2 (2) (1966) 127–135.
[7] Y. Lin, X. Zhang, L. Hu, An experimental study and analysis on maximum horizontal extents of buoyant turbulent diffusion flames subject to relative strong cross flows, Fuel 234 (2018) 508–515.
[8] F. Tang, Q. He, J. Wen, Effects of crosswind and burner aspect ratio on flame characteristics and flame base drag length of diffusion flames, Combust. Flame 200 (2019) 265–275.
[9] L. Hu, X. Zhang, M.A. Delichatsios, L. Wu, C. Kuang, Pool fire flame base drag behavior with cross flow in a sub-atmospheric pressure, Proc. Combust. Inst. 36 (2) (2017) 3105–3112.
[10] X. Zhang, X. Zhang, L. Hu, R. Tu, M.A. Delichatsios, An experimental investigation and scaling analysis on flame sag of pool fire in cross flow, Fuel 241 (2019) 845–850.
[11] R. Lautkaski, Validation of flame drag correlations with data from large pool fires, J. Loss Prev. Process. Ind. 5 (3) (1992) 175–180.

[12] P. Kew, W. Hulbert, D. Deaves, Modelling of thermal radiation from external hydrocarbon pool fires, Process Saf. Environ. Protect. 75 (2) (1997) 81–89.
[13] F. Shang, L. Hu, X. Sun, Q. Wang, A. Palacios, Flame downwash length evolution of non-premixed gaseous fuel jets in cross-flow: experiments and a new correlation, Appl. Energy 198 (2017) 99–107.
[14] H.S. Zhen, Y.S. Choy, C.W. Leung, C.S. Cheung, Effects of nozzle length on flame and emission behaviors of multi-fuel-jet inverse diffusion flame burner, Appl. Energy 88 (9) (2011) 2917–2924.
[15] X. Li, L. Hu, F. Shang, Flame downwash transition and its maximum length with increasing fuel supply of non-premixed jet in cross flow, Energy 164 (2018) 298–305.
[16] K. Lambert, Extreme bushfire/firestorm impact and the bush/urban interface, Black Saturday 7th February 2009, Submission to the 2009 Victorian Bushfires Royal Commission, 2010Available online www.royalcommission.vic.gov.au/Submissions/SubmissionDocuments/SUBM-002-059-0366_01_R.pdf , Accessed date: 13 February 2014.
[17] R.H.D. McRae, J.J. Sharples, S.R. Wilkes, A. Walker, An Australian pyro-tornadogenesis event, Nat. Hazards 65 (3) (2013) 1801–1811.
[18] Y. He, K. Kwok, G. Douglas, I. Razali, Numerical investigation of bushfire-wind interaction and its impact on building structure, Fire Saf. Sci. 10 (2011) 1449–1462.
[19] K. Kwok, Y. He, G. Douglas, Bushfire-enhanced wind load on structures, Proc. Instit. Civil Eng.-Eng. Computat. Mech. 165 (4) (2012) 253–263.
[20] E. Eftekharian, Y. He, K.C.S. Kwok, R.H. Ong, J. Yuan, Investigation of fire-driven cross-wind velocity enhancement, Int. J. Therm. Sci. 141 (2019) 84–95.
[21] E. Eftekharian, M. Ghodrat, R. Ong, Y. He, K. Kwok, CFD Investigation of Cross-Flow Effects on Fire-Wind Enhancement, Australasian Fluid Mechanics Conference, Adelaide, Australia, 10-13 Dec, 2018, 2018 Adelaide, Australia.
[22] L.F. Hawley, Theoretical considerations regarding factors which influence forest fires, J. For. 24 (7) (1926) 756–763.
[23] S.B. Show, Climate and forest fires in northern California, J. For. 17 (8) (1919) 965–979.
[24] J.J. Sharples, An overview of mountain meteorological effects relevant to fire behaviour and bushfire risk, Int. J. Wildland Fire 18 (7) (2009) 737–754.
[25] J.M. Mendes-Lopes, J.M. Ventura, J.M. Amaral, Flame characteristics, temperature–time curves, and rate of spread in fires propagating in a bed of Pinus pinaster needles, Int. J. Wildland Fire 12 (1) (2003) 67–84.
[26] D.X. Viegas, Slope and wind effects on fire propagation, Int. J. Wildland Fire 13 (2) (2004) 143–156.
[27] D.R. Weise, B. G.S, Effects of wind velocity and slope on flame properties, Can. J. For. Res. 26 (1996) 1849–1858.
[28] J.H. Balbi, F. Morandini, X. Silvani, J.B. Filippi, F. Rinieri, A physical model for wildland fires, Combust. Flame 156 (12) (2009) 2217–2230.
[29] J.-L. Dupuy, J. Maréchal, D. Portier, J.-C. Valette, The effects of slope and fuel bed width on laboratory fire behaviour, Int. J. Wildland Fire 20 (2) (2011) 272–288.
[30] J.J. Sharples, Review of formal methodologies for wind–slope correction of wildfire rate of spread, Int. J. Wildland Fire 17 (2) (2008) 179–193.
[31] A.L. Sullivan, Wildland surface fire spread modelling, 1990–2007. 3: simulation and mathematical analogue models, Int. J. Wildland Fire 18 (4) (2009) 387–403.
[32] A.L. Sullivan, Wildland surface fire spread modelling, 1990–2007. 2: empirical and quasi-empirical models, Int. J. Wildland Fire 18 (4) (2009) 369–386.
[33] J.-L. Dupuy, D. Morvan, Numerical study of a crown fire spreading toward a fuel break using a multiphase physical model, Int. J. Wildland Fire 14 (2) (2005) 141–151.
[34] R.R. Linn, P. Cunningham, Numerical simulations of grass fires using a coupled atmosphere–fire model: basic fire behavior and dependence on wind speed, J. Geophys. Res.: Atmosphere 110 (D13) (2005).
[35] W.E. Mell, S.L. Manzello, A. Maranghides, D. Butry, R.G. Rehm, The wildland–urban interface fire problem–current approaches and research needs, Int. J. Wildland Fire 19 (2) (2010) 238–251.
[36] F. Albini, Estimating Upslope Convective Windspeeds for Predicting Wildland Fire Behavior vol. 24, (1982) 1982.
[37] P. Jackson, J. Hunt, Turbulent wind flow over a low hill, Q. J. R. Meteorol. Soc. 101 (430) (1975) 929–955.
[38] R.H. Luke, A.G. McArthur, Bushfires in Australia, Australian Government Publishing Service, Canberra, 1978, p. 367.
[39] S. Pyne, P. Andrews, R.D. Laven, Introduction to Wildland Fire, John Wiley and Sons, New York, 1996.
[40] Y. Wu, H. Xing, G. Atkinson, Interaction of fire plume with inclined surface, Fire Saf. J. 35 (4) (2000) 391–403.
[41] D. Tritton, Physical Fluid Dynamics, Clarendon, Oxford, 1988.
[42] C. Van Wagner, Effect of slope on fire spread rate, Can. Forest. Serv. Bi-monthly Res. Notes 33 (1) (1977).
[43] J.R. Coleman, A.L. Sullivan, A real-time computer application for the prediction of fire spread across the Australian landscape, Simulation 67 (4) (1996) 230–240.
[44] M. Finney, Fire Area Simulator-Model Development and Evaluation: Technical Report: RMRS-RP-4, USDA, UT, Ogden, 2004.
[45] P. Johnston, J. Kelso, G.J. Milne, Efficient simulation of wildfire spread on an irregular grid, Int. J. Wildland Fire 17 (5) (2008) 614–627.
[46] K. Tolhurst, B. Shields, D. Chong, Phoenix: development and application of a bushfire risk management tool, Aust. J. Emerg. Manag. 23 (4) (2008) 47.
[47] C. Tymstra, R. Bryce, B. Wotton, S. Taylor, O. Armitage, Development and Structure of Prometheus: the Canadian Wildland Fire Growth Simulation Model, Natural Resources Canada, Canadian Forest Service, Northern Forestry Centre, 2010 Information Report NOR-X-417.(Edmonton, AB).
[48] J.J. Sharples, A.M. Gill, J.W. Dold, The trench effect and eruptive wildfires: lessons from the King's cross underground disaster, Proceedings of Australian Fire and Emergency Service Authorities Council 2010 Conference, 2010, 2010, pp. 8–10.
[49] C.J. Greenshields, Openfoam User Guide vol. 3, OpenFOAM Foundation Ltd, 2015 (1).
[50] Y. Wang, P. Chatterjee, J.L. de Ris, Large eddy simulation of fire plumes, Proc. Combust. Inst. 33 (2) (2011) 2473–2480.
[51] F. Mathey, D. Cokljat, J.P. Bertoglio, E. Sergent, Assessment of the vortex method for large eddy simulation inlet conditions, Prog. Comput. Fluid Dynam. Int. J. 6 (1–3) (2006) 58–67.
[52] D. Spalding, A single formula for the "law of the wall", J. Appl. Mech. 28 (3) (1961) 455–458.
[53] B.J. McCaffrey, Purely Buoyant Diffusion Flames: Some Experimental Results, NBSIR (1979) 79–1910.
[54] T. Hirano, M. Kinoshita, Gas velocity and temperature profiles of a diffusion flame stabilized in the stream over liquid fuel, Symp. Combust. Proc. 15 (1) (1975) 379–387.